

**A. Dargys  
J. Kundrotas**

**HANDBOOK  
on  
PHYSICAL  
PROPERTIES  
of  
Ge  
Si  
GaAs  
and  
InP**

# Physical constants

Quantity	SI	CGS
Electronic charge $e$	$1.602\,177 \cdot 10^{-19} \text{ C}$	$4.803\,206 \cdot 10^{-10} \text{ esu}$
Electron mass $m_0$	$9.109\,389 \cdot 10^{-31} \text{ kg}$	$9.109\,389 \cdot 10^{-28} \text{ g}$
Light velocity $c$	$2.997\,924 \cdot 10^8 \text{ m/s}$	$2.997\,924 \cdot 10^{10} \text{ cm/s}$
Electric constant $\epsilon_0$	$8.854\,187 \cdot 10^{-12} \text{ F/m}$	1
Magnetic constant $\mu_0$	$4\pi \cdot 10^{-7} \text{ H/m} =$ $12.566\,370 \cdot 10^{-7} \text{ H/m}$	1
Planck constant $h$	$6.626\,075 \cdot 10^{-34} \text{ J}\cdot\text{s}$	$6.626\,075 \cdot 10^{-27} \text{ erg}\cdot\text{s}$
$\hbar = h/2\pi$	$1.054\,572 \cdot 10^{-34} \text{ J}\cdot\text{s}$	$1.054\,572 \cdot 10^{-27} \text{ erg}\cdot\text{s}$
Boltzmann constant $k$	$1.380\,658 \cdot 10^{-23} \text{ J/K}$	$1.380\,658 \cdot 10^{-16} \text{ erg/K}$
Bohr magneton $\mu_B$	$9.274\,015 \cdot 10^{-24} \text{ J/T}$	$9.274\,015 \cdot 10^{-21} \text{ erg/Gs}$
Electron g-factor	2.002 319	2.002 319

## Nonsystemic:

$$h = 4.135\,669 \cdot 10^{-15} \text{ eV}\cdot\text{s}$$

$$\hbar = 6.582\,122 \cdot 10^{-16} \text{ eV}\cdot\text{s}$$

$$k = 8.617\,385 \cdot 10^{-5} \text{ eV/K}$$

$$\mu_B = 5.788\,382 \cdot 10^{-5} \text{ eV/T}$$

## Relations between photon wavelength $\lambda$ , energy $E$ and wave number $k$

---

$$\lambda [\mu\text{m}] = \frac{1.239.502}{E[\text{eV}]} \quad \text{in air with refractive index } n_a = 1.000\,274\,9,$$

$$\frac{1.239\,842}{E[\text{eV}]} \quad \text{in vacuum.}$$

$$k [\text{cm}^{-1}] = 8\,065.54 \, E[\text{eV}] \quad \text{in vacuum.}$$

$$1 \, \text{eV} = 8\,065.54 \, \text{cm}^{-1} \quad \text{in vacuum.}$$

$$1 \, \text{meV} = 8.065\,54 \, \text{cm}^{-1} \quad \text{in vacuum.}$$

$$1 \, \text{cm}^{-1} = 0.123\,98 \, \text{meV} \quad \text{in vacuum.}$$

$$1 \, \text{eV} = 2.417\,988 \cdot 10^{14} \, \text{Hz},$$

$$1.602\,177 \cdot 10^{-19} \, \text{J},$$

$$1.602\,177 \cdot 10^{-12} \, \text{erg.}$$

$$1 \, \text{K} = 8.617\,385 \cdot 10^{-5} \, \text{eV.}$$

$$1 \, \text{eV} = 1.160\,445 \cdot 10^4 \, \text{K.}$$





A. Dargys and J. Kundrotas

**HANDBOOK**  
**on**  
**PHYSICAL PROPERTIES**  
**of**  
**Ge, Si, GaAs and InP**



Vilnius, Science and Encyclopedia Publishers, 1994

UDK 621.315

Da 326

Adolfas Dargys  
Jurgis Kundrotas

Semiconductor Physics Institute  
Goštauto 11, Vilnius  
Lithuania

SCIENCE AND ENCYCLOPEDIA PUBLISHERS  
Žvaigždžių 23, Vilnius, Lithuania

## Preface

The data on main physical properties of technologically important semiconductor crystals, germanium, silicon, gallium arsenide, and indium phosphide, are presented. The choice of the semiconductors was dictated by two motives. First, they are the most thoroughly investigated materials and, second, they are of great importance for the semiconductor device fabrication. There exists a tremendous amount of information scattered in the physical literature on the properties of these semiconductors. The handbook contains only the most fundamental bulk properties of the single crystals.

A few words about the use of the handbook may be helpful. Introduction (Chapter A) is followed by the main Chapter B of the physical data. The latter is divided into four Sections. The Section number and the first number of a Figure or Table in Chapter B indicates the semiconductor, namely:

- 1 – germanium,
- 2 – silicon,
- 3 – gallium arsenide,
- 4 – indium phosphide.

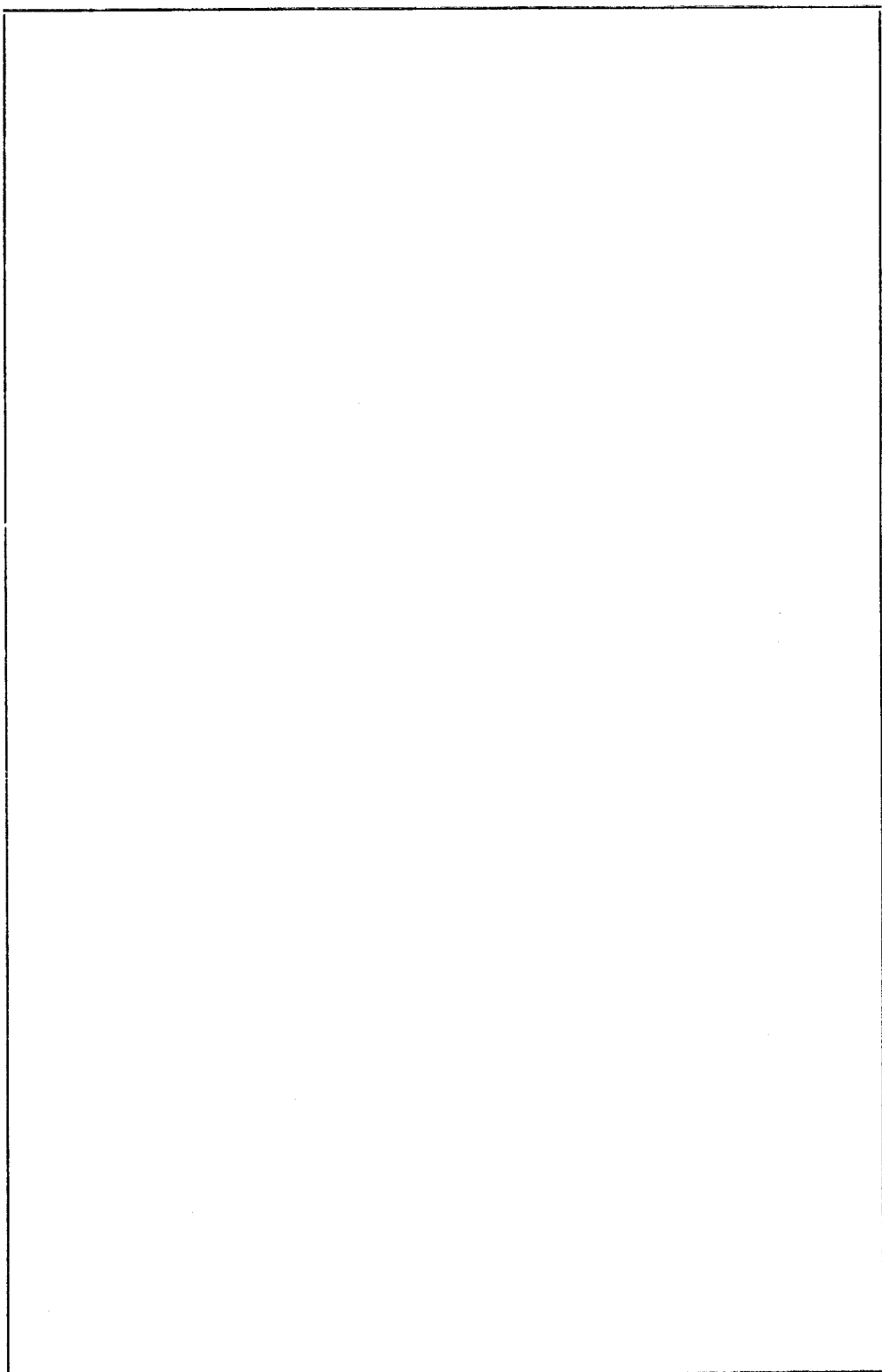
To present the physical properties of different semiconductors as uniformly as possible, the headings of the Subsections and their numbering in the Chapter B, as one may see from the Contents, are divided into six main groups:

- 1 – lattice properties,
- 2 – band properties,
- 3 – optical properties,
- 4 – electrical properties,
- 5 – piezoelectric, thermoelectric and magnetic properties,
- 6 – impurity properties.

The definitions of the physical properties presented in the handbook are given in the Introduction. Apart from English, the Subject index is also given in Lithuanian (Chapter C).

In selecting the data for the handbook the preference was given to those physical properties which are directly accessible to an experimenter. Where it was possible the presented data have been approximated by empirical formulas. The handbook is intended for solid state physicists, postgraduates and students and can serve as a laboratory reference guide. The engineers who are interested in semiconductor material application will find the handbook useful too.

Finally, we are grateful to the authors and publishers who granted permission for the use of particular figures and tables. Most figures and tables that are included in this handbook are in modified form to produce a uniform format. Sources are quoted with the individual captions.



## Contents

### A. Introduction. General remarks on the semiconductor properties and their definition

1. Lattice properties . . . . .	9
2. Band properties . . . . .	12
3. Optical properties . . . . .	17
4. Electrical properties . . . . .	21
5. Piezoelectric, thermoelectric and magnetic properties . . . . .	23
6. Impurity properties . . . . .	25
7. Restrictions on the tensor components in the cubic semiconductors . . . . .	26
8. Physical constants . . . . .	27

### B. Physical data

#### 1. Physical data for germanium

1.1. Ge lattice properties . . . . .	31
1.2. Ge band properties . . . . .	38
1.3. Ge optical properties . . . . .	46
1.4. Ge electrical properties . . . . .	55
1.5. Ge piezoelectric, thermoelectric and magnetic properties . . . . .	66
1.6. Ge impurity properties . . . . .	73

#### 2. Physical data for silicon

2.1. Si lattice properties . . . . .	83
2.2. Si band properties . . . . .	91
2.3. Si optical properties . . . . .	98
2.4. Si electrical properties . . . . .	109
2.5. Si piezoelectric, thermoelectric and magnetic properties . . . . .	124
2.6. Si impurity properties . . . . .	130

#### 3. Physical data for gallium arsenide

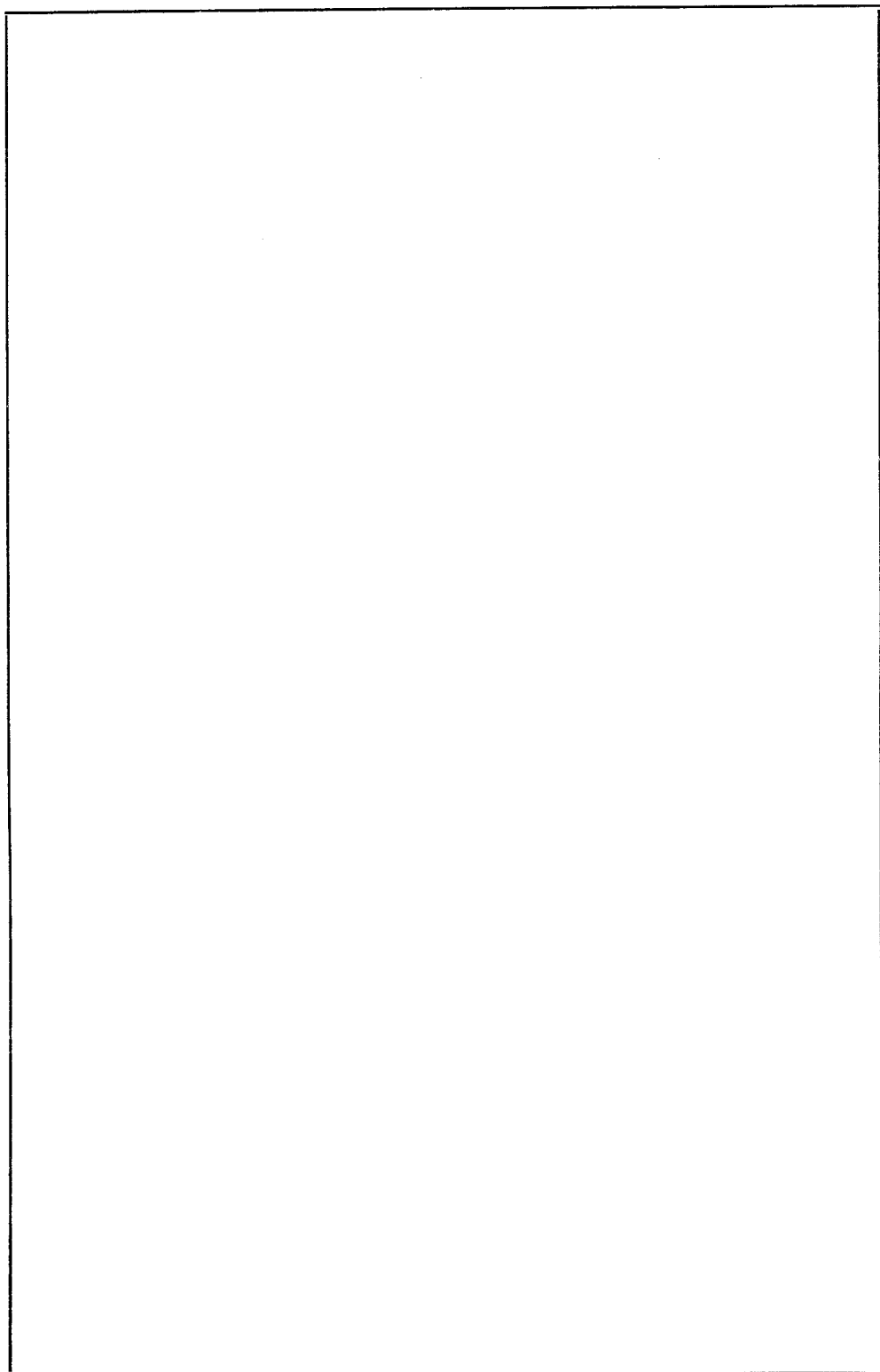
3.1. GaAs lattice properties . . . . .	143
3.2. GaAs band properties . . . . .	150
3.3. GaAs optical properties . . . . .	158
3.4. GaAs electrical properties . . . . .	170
3.5. GaAs piezoelectric, thermoelectric and magnetic properties . . . . .	179
3.6. GaAs impurity properties . . . . .	182

#### **4. Physical data for indium phosphide**

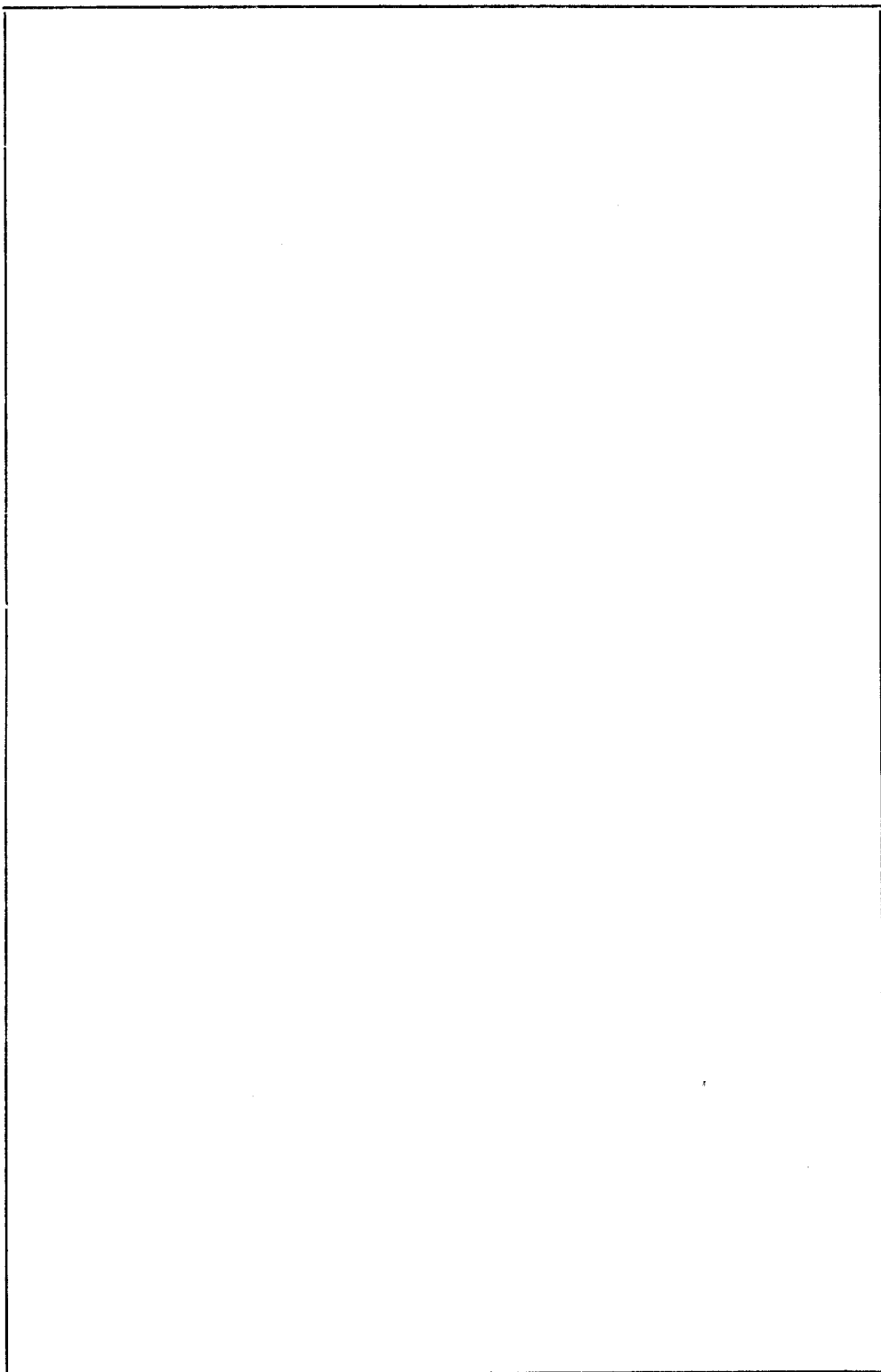
4.1. InP lattice properties . . . . .	189
4.2. InP band properties . . . . .	196
4.3. InP optical properties . . . . .	202
4.4. InP electrical properties . . . . .	211
4.5. InP piezoelectric, thermoelectric and magnetic properties . . . . .	219
4.6. InP impurity properties . . . . .	222

#### **C. References and subject index**

1. References . . . . .	229
2. Subject index . . . . .	247
3. Subject index in Lithuanian . . . . .	255







# A. Introduction. General remarks on the semiconductor properties and their definition

## 1. Lattice properties

**Phonon dispersion relation.** Lattice waves are characterized by wave vector  $\mathbf{q}$  and frequency  $\omega_j$ . The function  $\omega_j(\mathbf{q})$  is called the phonon dispersion relation of the  $j$ -th branch. If  $\omega_j \rightarrow 0$  when  $\mathbf{q} \rightarrow 0$ , the branch  $j$  is called acoustic. If  $\omega_j$  is nonzero when  $\mathbf{q} \rightarrow 0$ , the branch  $j$  is called optical. In addition, depending on polarization of the wave, the branch may be longitudinal or transverse. Phonons belonging to these branches are consequently cited as longitudinal acoustic (*LA*), transverse acoustic (*TA*), longitudinal optical (*LO*) and transverse optical (*TO*). If necessary, a subscript is added, for example, to indicate two orthogonal polarizations of transverse acoustic waves:  $TA_1$ ,  $TA_2$ .

The first Brillouin zone, nomenclature of high symmetry points and lines for the phonon branches are the same as for the electronic bands, Fig. 1.

**Stress and strain tensors.** For small deformations, when Hooke's law holds, the second-rank stress tensor  $\sigma_{ij}$  and strain tensor  $\varepsilon_{ij}$  are related by the fourth-rank compliance tensor  $s_{ijkl}$  and elastic tensor  $c_{ijkl}$  [1]

$$\varepsilon_{ij} = \sum_{kl} s_{ijkl} \sigma_{kl},$$

$$\sigma_{ij} = \sum_{kl} c_{ijkl} \varepsilon_{kl}.$$

For cubic semiconductors these tensorial equations can be put into the following matrix form:

$$\begin{vmatrix} \varepsilon_{xx} \\ \varepsilon_{yy} \\ \varepsilon_{zz} \\ \varepsilon_{yz} \\ \varepsilon_{zx} \\ \varepsilon_{xy} \end{vmatrix} = \begin{vmatrix} s_{11} & s_{12} & s_{12} & 0 & 0 & 0 \\ s_{12} & s_{11} & s_{12} & 0 & 0 & 0 \\ s_{12} & s_{12} & s_{11} & 0 & 0 & 0 \\ 0 & 0 & 0 & s_{44} & 0 & 0 \\ 0 & 0 & 0 & 0 & s_{44} & 0 \\ 0 & 0 & 0 & 0 & 0 & s_{44} \end{vmatrix} \begin{vmatrix} \sigma_{xx} \\ \sigma_{yy} \\ \sigma_{zz} \\ \sigma_{yz} \\ \sigma_{zx} \\ \sigma_{xy} \end{vmatrix}$$

$$\begin{vmatrix} \sigma_{xx} \\ \sigma_{yy} \\ \sigma_{zz} \\ \sigma_{yz} \\ \sigma_{zx} \\ \sigma_{xy} \end{vmatrix} = \begin{vmatrix} c_{11} & c_{12} & c_{12} & 0 & 0 & 0 \\ c_{12} & c_{11} & c_{12} & 0 & 0 & 0 \\ c_{12} & c_{12} & c_{11} & 0 & 0 & 0 \\ 0 & 0 & 0 & c_{44} & 0 & 0 \\ 0 & 0 & 0 & 0 & c_{44} & 0 \\ 0 & 0 & 0 & 0 & 0 & c_{44} \end{vmatrix} \begin{vmatrix} \varepsilon_{xx} \\ \varepsilon_{yy} \\ \varepsilon_{zz} \\ \varepsilon_{yz} \\ \varepsilon_{zx} \\ \varepsilon_{xy} \end{vmatrix}$$

Here  $x, y, z$  are directed along the crystallographic axes. The tensors  $s_{ijkl}$  and  $c_{ijkl}$  are written in the abbreviated form (see Section 7 for notation).

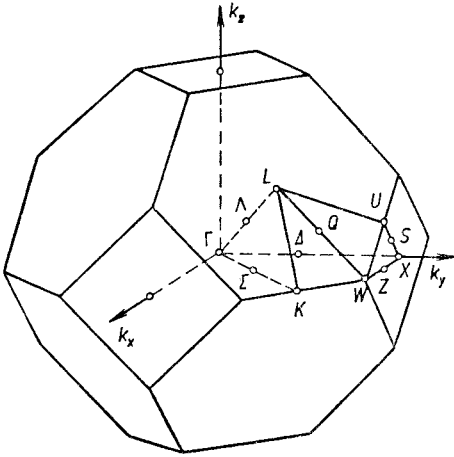


Fig. 1. The first Brillouin zone for Ge, Si, GaAs and InP lattices with high symmetry points (\$\Gamma\$, \$K\$, \$L\$, \$U\$, \$X\$, \$W\$) and lines (\$\Lambda\$, \$\Delta\$, \$\Sigma\$, \$Q\$, \$S\$, \$Z\$) indicated.

For cubic semiconductors the following relations exist between the elastic and compliance tensor components:

$$s_{11} = \frac{c_{11} + c_{12}}{(c_{11} - c_{12})(c_{11} + 2c_{12})}, \quad s_{12} = \frac{-c_{12}}{(c_{11} - c_{12})(c_{11} + 2c_{12})}, \quad s_{44} = \frac{1}{c_{44}}.$$

Below the various parameters characterizing the cubic lattice are listed.

#### Elastic anisotropy factor:

$$a = (c_{11} - c_{12}) / (2c_{44}).$$

For isotropic media \$a=1\$.

**Poisson ratio** \$\nu\$ characterizes the response of the lattice to the shear deformation as compared to the compressional one

$$\nu = -s_{12}/s_{11}.$$

**Young's modulus** \$E\$ characterizes the ability of the lattice to resist the deformation in the particular direction [qrt]:

$$E_{[100]} = \frac{1}{s_{11}}, \quad E_{[110]} = \frac{4}{2s_{11} + 2s_{12} + s_{44}}, \quad E_{[111]} = \frac{3}{s_{11} + 2s_{12} + s_{44}}.$$

For isotropic media, \$2c\_{44} = c\_{11} - c\_{12}\$, the Young's modulus is independent of the direction.

**Isothermal compressibility** \$K\$ defines the relative differential change in a volume at the constant temperature, \$(dV/V)\_T\$, after hydrostatic pressure increment \$dp\$

$$(dV/V)_T = -K dp.$$

The compressibility is an inverse of the isothermal bulk modulus \$B\_0\$,

$$K = 1/B_0.$$

**Isothermal bulk modulus** \$B\_0\$ is related to the elastic constants in the following way

$$B_0 = (c_{11} + 2c_{12})/3.$$

**Murnaghan equation** describes the relation between the hydrostatic pressure \$p\$ and the lattice constant \$a\_p\$ [2]

**TABLE 1** Relations between acoustic wave longitudinal ( $L$ ) and transverse ( $T$ ) velocities and adiabatic elastic constants for the main crystallographic directions in cubic semiconductors

Wave propagation direction	Direction or plane of particle motion	Sound velocity as a function of crystal density $\rho$ and elastic constants $c_{ij}$
[100]	[100] (100) plane	$v_L = (c_{11}/\rho)^{1/2}$ $v_T = (c_{44}/\rho)^{1/2}$
[110]	[110] [001] [1 $\bar{1}$ 0]	$v_L = [(c_{11} + c_{12} + 2c_{44})/2\rho]^{1/2}$ $v_{T_1} = (c_{44}/\rho)^{1/2}$ $v_{T_2} = [(c_{11} - c_{12})/2\rho]^{1/2}$
[111]	[111] (111) plane	$v_L = [(c_{11} + 2c_{12} + 4c_{44})/3\rho]^{1/2}$ $v_T = [(c_{11} - c_{12} + c_{44})/3\rho]^{1/2}$

$$p = \frac{B_0}{B'_0} \left[ \left( \frac{a}{a_0} \right)^{3B'_0} - 1 \right],$$

where  $B'_0 = dB_0/dp$  and  $a$  is the lattice constant at  $p=0$ .

**Grüneisen parameter**  $\gamma_j$  characterizes the shift of phonon energy with the pressure  $p$  or volume  $V$  [3, 4]. This parameter for quasi-harmonic lattice mode  $j$  of frequency  $\omega_j$  is defined by the relation

$$\gamma_j = - \frac{\partial \ln \omega_j}{\partial \ln V} = \frac{1}{K} \frac{\partial \ln \omega_j}{\partial p} = \frac{1}{K\omega_j} \frac{\partial \omega_j}{\partial p},$$

where  $K$  is the isothermal compressibility. Derivatives are defined at zero hydrostatic pressure. Averaged (thermodynamic) Grüneisen parameter is

$$\gamma_{av} = C_V^{-1} \sum_j \gamma_j c_V(j) = \frac{\beta V}{C_V K},$$

where  $c_V(j)$  is the heat capacity of the mode  $j$  and  $C_V$  is the heat capacity of the crystal at the constant volume.

**Velocities of elastic waves** are slopes of the acoustic phonon branches at  $\mathbf{q}=0$ . The slope  $d\omega_j/dq$  gives the velocity of longitudinal waves for the  $LA$ -branch and the velocity of transverse waves for the  $TA$ -branches. Table 1 gives relations between sound wave velocities and elastic constants.

**Acoustic wave attenuation coefficient** is defined by the relation

$$\alpha_{ac} [\text{dB/cm}] = \frac{1}{l_2 - l_1} 20 \log_{10} \frac{P(l_1)}{P(l_2)},$$

where  $P(l_1)$  and  $P(l_2)$  are the acoustic wave intensities at distances  $l_1$  and  $l_2$ . Relation between attenuation coefficients in units  $[\text{dB}/\mu\text{s}]$  and  $[\text{dB/cm}]$ :

$$\alpha_{ac} [\text{dB}/\mu\text{s}] = \alpha_{ac} [\text{dB/cm}] \cdot 10^{-6} v [\text{cm/s}],$$

where  $v$  is an appropriate sound velocity of the elastic wave.

The **heat capacity**  $C$  relates the increment in sample energy  $\Delta E_T$  at the temperature  $T$  upon temperature increment  $\Delta T$

$$C = \Delta E_T / \Delta T.$$

The relation between heat capacity at constant pressure  $C_p$  [J/K] and constant volume  $C_v$  [J/K] is

$$C_p = C_v + \beta^2 B_0 V T.$$

Here  $B_0$  is the isothermal bulk modulus,  $V$  is the volume, and  $\beta$  is the **volume coefficient of thermal expansion** at constant pressure,

$$\beta = V^{-1} (\partial V / \partial T)_p,$$

which for cubic semiconductors can be expressed through **differential thermal expansivity**  $(1/l) (\partial l / \partial T)_p$ :

$$\beta = \frac{3}{l} \left( \frac{\partial l}{\partial T} \right)_p.$$

The handbook gives the heat capacity at constant pressure for unit weight,  $C_p$  [J/(g · K)].

The **Debye characteristic temperature**  $\Theta$  is defined through the equation [5]

$$C_v = 9Nk \left( \frac{T}{\Theta} \right)^3 \int_0^{\Theta/T} \frac{x^4 e^x}{(e^x - 1)^2} dx,$$

where  $C_v$  is the experimentally measured heat capacity at constant volume,  $N$  is the total number of atoms in the specimen, and  $k$  is the Boltzmann constant.

**Thermal conductivity**  $\chi$  relates the power  $P$  transmitted through the sample of the cross sectional area  $S$  when the temperature difference  $\Delta T = T_2 - T_1$  is maintained over the sample length  $\Delta l = l_2 - l_1$

$$P = \chi S \Delta T / \Delta l.$$

## 2. Band properties

**Nomenclature of high symmetry points and lines.** Points and axes of high symmetry in the Brillouin zone for Ge, Si, GaAs and InP are shown in Fig. 1. The wave vector components  $k_x$ ,  $k_y$ ,  $k_z$  are assumed to be parallel to the crystallographic directions [100], [010], [001], respectively.

The dependence of carrier energy  $E_n(\mathbf{k})$  on the wave vector  $\mathbf{k}$  is a multivalued function. The index  $n$  determines the band. Bands are further characterized by irreducible representations of the respective symmetry group according to which the wave functions transform. Tables 2 and 3 give standard notation of irreducible representations of single and double groups used for diamond and zinc blende lattices. If necessary, a subscript or superscript is added to mark whether the state belongs to the conduction or valence band. For example,  $\Gamma_1^-$ ,  $\Gamma_1^+$  and  $\Gamma_{6c}^+$ ,  $\Gamma_{6c}^-$  indicate the same state in the valence and conduction bands when spin-orbit interaction is neglected ( $\Gamma_1^-$ ) and included ( $\Gamma_1^+$ ).

**Relationship of energy to wave vector.** The energy-wave vector relationship, also called the dispersion relation,  $E = E(\mathbf{k})$  around a minimum (valley) in a conduction band or around a maximum in a valence band may assume three forms characterized by spherical, ellipsoidal or warped constant energy surfaces, Fig. 2.

**TABLE 2** The comparison of nomenclatures of high symmetry points and lines in the Brillouin zone of Ge and Si when spin-orbit interaction is neglected ( $\Gamma, X, L, \Delta, \Lambda, \Sigma$ ) and included ( $\Gamma, X, L, \Delta, \Lambda, \Sigma$ )  $\times D^{(1/2)}$ . In fact, the points and lines are irreducible representations of single and double  $O_h^7$  space group of diamond lattice [6]

Point, line	Coordinate in $\mathbf{k}$ -space	Symmetry point, line				
$\Gamma$	$(0, 0, 0)$	$\Gamma_1$	$\Gamma_2$	$\Gamma_{12}$	$\Gamma'_{15}$	$\Gamma'_{25}$
$\Gamma \times D^{(1/2)}$		$\Gamma_6^+$	$\Gamma_7^+$	$\Gamma_8^+$	$(\Gamma_6^+, \Gamma_8^+)$	$(\Gamma_7^+, \Gamma_8^+)$
$\Gamma$	$(0, 0, 0)$	$\Gamma'_1$	$\Gamma'_2$	$\Gamma'_{12}$	$\Gamma_{15}$	$\Gamma_{25}$
$\Gamma \times D^{(1/2)}$		$\Gamma_6^-$	$\Gamma_7^-$	$\Gamma_8^-$	$(\Gamma_6^-, \Gamma_8^-)$	$(\Gamma_7^-, \Gamma_8^-)$
$X$	$(1, 0, 0) \frac{2\pi}{a}$	$X_1$		$X_2$	$X_3$	$X_4$
$X \times D^{(1/2)}$		$X_5$		$X_5$	$X_5$	$X_5$
$L$	$\left(\frac{1}{2}, \frac{1}{2}, \frac{1}{2}\right) \frac{2\pi}{a}$	$L_1, L_2$	$L_3$	$L'_1, L'_2$	$L'_3$	
$L \times D^{(1/2)}$		$L_6^+, L_6^+$	$(L_4^+, L_5^+), L_6^+$	$L_6^-, L_6^-$	$(L_4^-, L_5^-), L_6^-$	
$\Delta$	$(q, 0, 0) \frac{2\pi}{a}$	$\Delta_1$	$\Delta'_1, \Delta_2$	$\Delta'_2$	$\Delta_5$	
$\Delta \times D^{(1/2)}$	$0 < q < 1$	$\Delta_6$	$\Delta_6, \Delta_7$	$\Delta_7$	$(\Delta_6, \Delta_7)$	
$\Lambda$	$(q, q, q) \frac{2\pi}{a}$	$\Lambda_1$	$\Lambda_2$		$\Lambda_3$	
$\Lambda \times D^{(1/2)}$	$0 < q < 1/2$	$\Lambda_6$	$\Lambda_6$		$(\Lambda_4, \Lambda_5), \Lambda_6$	
$\Sigma$	$(q, q, 0) \frac{2\pi}{a}$	$\Sigma_1$	$\Sigma_2$	$\Sigma_3$	$\Sigma_4$	
$\Sigma \times D^{(1/2)}$	$0 < q < 1/2$	$\Sigma_5$	$\Sigma_5$	$\Sigma_5$	$\Sigma_5$	

$a$  is the lattice constant.

**TABLE 3** The comparison of nomenclatures of high symmetry points and lines in the Brillouin zone of GaAs and InP when spin-orbit interaction is neglected ( $\Gamma$ ,  $X$ ,  $L$ ,  $\Delta$ ,  $\Lambda$ ,  $\Sigma$ ) and included ( $\Gamma$ ,  $X$ ,  $L$ ,  $\Delta$ ,  $\Lambda$ ,  $\Sigma$ )  $\times D^{(1/2)}$ . In fact, the points and lines are irreducible representations of single and double  $T_d^2$  space group of zinc blende lattice [7]

Point, line	Coordinate in $\mathbf{k}$ -space	Symmetry point, line
$\Gamma$ $\Gamma \times D^{(1/2)}$	(0, 0, 0)	$\Gamma_1$ $\Gamma_2$ $\Gamma_{12}$ $\Gamma_{15}$ $\Gamma_{25}$ $\Gamma_6$ $\Gamma_7$ $\Gamma_8$ ( $\Gamma_7$ , $\Gamma_8$ ) ( $\Gamma_6$ , $\Gamma_8$ )
$X$ $X \times D^{(1/2)}$	(1, 0, 0) $\frac{2\pi}{a}$	$X_1$ $X_2$ $X_3$ $X_4$ $X_5$ $X_6$ $X_7$ $X_7$ $X_6$ ( $X_6$ , $X_7$ )
$L$ $L \times D^{(1/2)}$	$\left(\frac{1}{2}, \frac{1}{2}, \frac{1}{2}\right) \frac{2\pi}{a}$	$L_1$ $L_2$ $L_3$ $L_6$ $L_6$ ( $L_4$ , $L_5$ ), $L_6$
$\Delta$ $\Delta \times D^{(1/2)}$	( $q$ , 0, 0) $\frac{2\pi}{a}$ $0 < q < 1$	$\Delta_1$ $\Delta_2$ $\Delta_3$ $\Delta_4$ $\Delta_5$ $\Delta_5$ $\Delta_5$ $\Delta_5$
$\Lambda$ $\Lambda \times D^{(1/2)}$	( $q$ , $q$ , $q$ ) $\frac{2\pi}{a}$ $0 < q < 1/2$	$\Lambda_1$ $\Lambda_2$ $\Lambda_3$ $\Lambda_6$ $\Lambda_6$ ( $\Lambda_4$ , $\Lambda_5$ ), $\Lambda_6$
$\Sigma$ $\Sigma \times D^{(1/2)}$	( $q$ , $q$ , 0) $\frac{2\pi}{a}$ $0 < q < 1/2$	$\Sigma_1$ $\Sigma_2$ ( $\Sigma_3$ , $\Sigma_4$ ) ( $\Sigma_3$ , $\Sigma_4$ )

$a$  is the lattice constant. The points  $L_4$  and  $L_5$  and lines  $\Delta_3$  and  $\Delta_4$  are degenerate by time reversal.

**Spherical constant energy surfaces** are characteristic of conduction band. They are located in the center of the Brillouin zone at the points  $\Gamma_6$  and  $\Gamma_7$  and are described by the following dispersion relation:

$$E(\mathbf{k}) = \frac{\hbar^2 (k_x^2 + k_y^2 + k_z^2)}{2m_n} = \frac{\hbar^2 \mathbf{k}^2}{2m_n}.$$

The parameter  $m_n$  is called scalar effective mass.

**Ellipsoidal constant energy surfaces** are described by two parameters, longitudinal  $m_l$  and transverse  $m_t$  effective masses, and are connected with the dispersion relation of the form

$$E(\mathbf{k}) = \frac{\hbar^2}{2} \left( \frac{k_l^2}{m_l} + 2 \frac{k_t^2}{m_t} \right).$$

Ellipsoidal surfaces are appropriate for energy minima located at  $L$  and  $X$  points or along  $\Delta$  and  $\Lambda$  axes. For symmetry reasons, as a rule, there are several equiva-



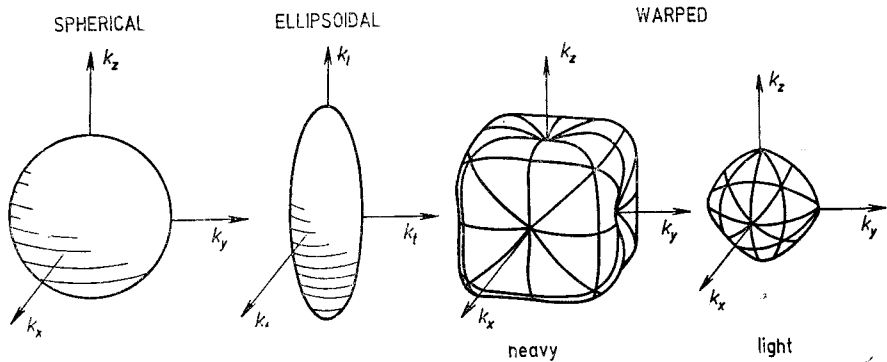


Fig. 2. Shapes of constant energy surfaces for electrons and holes in cubic semiconductors.

lent valleys (many-valley model). The conductivity mass  $m_c$  and the density-of-states mass  $m_d$  are described by the formulas

$$\frac{1}{m_c} = \frac{1}{3} \left( \frac{1}{m_i} + \frac{2}{m_t} \right), \quad m_d = (m_i \cdot m_t^2)^{1/3}.$$

**Warped constant energy surfaces** are typical to valence bands which are degenerate at  $\mathbf{k}=0$ . Energies of holes for parabolic warped heavy  $h$  and light  $l$  mass bands are

$$E_{h,l}(\mathbf{k}) = \frac{\hbar^2}{2m_0} \left[ \gamma_1 (k_x^2 + k_y^2 + k_z^2) \pm 2 \sqrt{\gamma_2^2 (k_x^4 + k_y^4 + k_z^4) + (3\gamma_3^2 - \gamma_2^2) (k_x^2 k_y^2 + k_x^2 k_z^2 + k_y^2 k_z^2)} \right],$$

where  $k_x, k_y, k_z$  are the wave vector components defined with reference to crystallographic axes and  $\gamma_1, \gamma_2, \gamma_3$  are the valence band parameters (also called Luttinger parameters). The plus and minus signs refer to light and heavy hole mass bands, respectively. For GaAs and InP the lack of inversion symmetry gives an additional term in the dispersion which is linear in a wave vector. The latter term is small and is not taken into account most often.

The valence band warping is characterized by nonsphericity parameter [8]

$$\delta = (\gamma_3 - \gamma_2)/\gamma_1.$$

For spherical valence bands  $\gamma_2 = \gamma_3$ .

Frequently the band warping is neglected, then the dispersion laws for heavy and light mass bands reduce to

$$E_{h,l}(\mathbf{k}) = \hbar^2 (k_x^2 + k_y^2 + k_z^2) / (2m_{h,l}) = \hbar^2 \mathbf{k}^2 / (2m_{h,l}),$$

where  $m_h$  and  $m_l$  are the averaged heavy and light hole masses [8]:

$$m_h/m_0 = 1/(\gamma_1 - 2\bar{\gamma}),$$

$$m_l/m_0 = 1/(\gamma_1 + 2\bar{\gamma}),$$

where

$$\bar{\gamma} = (3\gamma_3 + 2\gamma_2)/5.$$

Density-of-states mass for parabolic and spherical valence band is

$$m_d = (m_h^{3/2} + m_l^{3/2})^{2/3}.$$

Another set of parameters is sometimes used instead of  $\gamma_1, \gamma_2, \gamma_3$ :

$$A = -\gamma_1,$$

$$B = -2\gamma_2,$$

$$|C| = 2\sqrt{3} \sqrt{\gamma_2^2 - \gamma_1^2}.$$

If  $E(\mathbf{k})$  is proportional to  $|\mathbf{k}|^2$  the dispersion law is called parabolic. The deviation from parabolicity is characterized by **nonparabolicity parameter**  $\alpha$ :

$$E(1 + \alpha E) = \hbar^2 k^2 / 2m.$$

**Splitting of the spin degeneracy.** The energies of Ge and Si are at least doubly spin degenerate at any point of the Brillouin zone.

The lack of inversion symmetry in GaAs and InP results in lifting of the spin degeneracy except for  $\mathbf{k}$  along [100] directions and for  $\Gamma$  and  $L$  points. For the bands originating from the points  $\Gamma_6$  and  $\Gamma_7$ , and for the light hole band  $\Gamma_8$  the double degeneracy is preserved also in [111] directions [9]. In GaAs, for example, the spin splitting of the lowest conduction band in [110] directions is the largest in the middle of  $\Sigma$ -line, Fig. 1, and reaches 0.075 eV [10]. The valence band spin splitting is smaller by an order of magnitude, therefore, it is often neglected.

**Band structure in a magnetic field.** The orbital motion of carriers is quantized in the presence of a magnetic field  $\mathbf{B}$ . The orbital motion is characterized by the cyclotron frequency which can be expressed by the same set of parameters as the quasi-particle motion in the absence of the magnetic field, i. e. by the longitudinal and transverse effective masses  $m_l, m_t$  in case of the conduction band, or the Luttinger parameters  $\gamma_1, \gamma_2, \gamma_3$  in case of the valence band.

The band states which are degenerate with respect to spin will suffer additional quantization. For isotropic parabolic conduction band the additional band splitting is

$$\Delta E = \mu_B g B,$$

where  $\mu_B$  is the Bohr magneton and  $g$  is the effective  $g$ -factor. For ellipsoidal surface the  $g$ -factor is characterized by longitudinal and transverse parts:  $g_l, g_t$ . For valence bands degenerate at  $\mathbf{k}=0$  the  $g$ -factor depends on the polar angles  $\varphi, \theta$  with reference to the crystallographic axes

$$g_v = 2k + qf(\varphi, \theta),$$

where  $k, q$  describe isotropic and anisotropic parts, respectively [11, 12]. For Ge and Si the factor  $q$  is very small and is neglected most often.

The bands for GaAs and InP, except the points of high symmetry, are not spin degenerate, therefore, the  $g$ -factor is meaningful in the very vicinity of the points  $\Gamma_8, \Gamma_7$ .

**Deformation potentials.** Application of an external stress changes the band structure of the semiconductor. The hydrostatic (isotropic) stress shifts the energies of the extrema relative to one another. A rate of change of energy separation  $\Delta E_{ij}$  between the energy extrema  $i$  and  $j$  is described by the parameter  $d\Delta E_{ij}/dp$ , where  $p$  is the hydrostatic pressure. For example, in case of forbidden energy gap:  $d\Delta E_{ij}/dp = dE_g/dp$ .

Uniaxial stress, in addition, gives rise to splitting of degenerate bands. The strength of the splitting is described by uniaxial deformation potentials:  $\Xi_u$  in case of ellipsoidal energy surfaces, and  $D_u, D'_u$  or  $b, d$  in case of degenerate valence band. The last ones are connected by the relations

$$D_u = -\frac{3}{2} b, \quad D'_u = -\frac{\sqrt{3}}{2} d.$$

For isotropic materials  $D_u = D'_u$ . For details of the conduction band splitting at  $X$  and  $L$  points and of the valence band splitting under uniaxial stress see Figs 1.13, 2.12 and Table 1.8.

### 3. Optical properties

**Parameters which characterize optical properties** of semiconductors:

complex dielectric permittivity

$$\varepsilon(\omega) = \varepsilon_1(\omega) - i\varepsilon_2(\omega),$$

complex refractive index

$$\tilde{n}(\omega) = n(\omega) - ik(\omega),$$

where  $n(\omega)$  is the real part of the refractive index and  $k(\omega)$  is the extinction coefficient;  $i = \sqrt{-1}$ .

The ratio of the electric (magnetic) field reflected from a semi-infinite sample to the normally incident electric (magnetic) field, in general, is a complex quantity

$$r = |r| e^{i\theta} = \frac{n - ik - 1}{n - ik + 1}.$$

The reflection coefficient (reflectance) from a semi-infinite sample for the normal incidence is

$$R = \frac{I_{\text{inc}}}{I_{\text{refl}}} = |r|^2 = \frac{(n-1)^2 + k^2}{(n+1)^2 + k^2},$$

where  $I_{\text{inc}}$  and  $I_{\text{refl}}$  are the intensities of the incident and reflected light.

Reflectance phase shift:

$$\theta = \tan^{-1} \left( \frac{-2k}{n^2 + k^2 - 1} \right).$$

Absorption coefficient:

$$\alpha = 4\pi k / \lambda,$$

where  $\lambda$  is the wavelength in free space.  $\alpha$  is related to the light intensity  $I$  in the semi-infinite sample at the points  $x_1$  and  $x_2$  in the following way:

$$\alpha = -\frac{1}{x_2 - x_1} \ln \frac{I(x_2)}{I(x_1)}.$$

Relation between absorption coefficient  $\alpha$  [ $\text{cm}^{-1}$ ], concentration of absorbers  $N$  [ $\text{cm}^{-3}$ ] and absorption cross section  $\sigma$  [ $\text{cm}^2$ ]:

$$\alpha = N \sigma.$$

Various relations:

$$\begin{cases} \varepsilon_1 = n^2 - k^2, \\ \varepsilon_2 = 2nk. \end{cases}$$

$$\begin{cases} n = 2^{-1/2} [(\varepsilon_1^2 + \varepsilon_2^2)^{1/2} + \varepsilon_1]^{1/2}, \\ k = 2^{-1/2} [(\varepsilon_1^2 + \varepsilon_2^2)^{1/2} - \varepsilon_1]^{1/2}. \end{cases}$$

$$\begin{cases} n = \frac{1-R}{(1-\sqrt{R})^2 + 4\sqrt{R} \sin^2 \frac{\theta}{2}} = \frac{1-R}{1+R-2\sqrt{R} \cos \theta}, \\ k = \frac{2\sqrt{R} \sin \theta}{(1-\sqrt{R})^2 + 4\sqrt{R} \sin^2 \frac{\theta}{2}} = \frac{2\sqrt{R} \sin \theta}{1+R-2\sqrt{R} \cos \theta}. \end{cases}$$

**Luminescence.** The main radiative recombination channels are shown in Table 4 and Fig. 3.

**TABLE 4** Main radiative recombination channels

Recombination channel	Reaction
Donor—acceptor pair recombination ( <i>D-A</i> transition)	$[D^0 A^0] \rightarrow [D^+ A^-] + h\nu$
Free electron and hole recombination ( <i>e-h</i> transition)	$e + h \rightarrow h\nu$ $e + h \rightarrow h\nu + \text{phonon}$
Free electron and neutral acceptor recombination ( <i>e-A</i> transition)	$e + A^0 \rightarrow A^- + h\nu$
Free hole and neutral donor recombination ( <i>h-D</i> transition)	$h + D^0 \rightarrow D^+ + h\nu$
Free exciton decay	$X \rightarrow h\nu$ $X_{\text{ph}} \rightarrow h\nu + \text{phonon}$
Excitonic complex decay	$[D^0 X] \rightarrow D^0 + h\nu$ $[D^0 X]_{\text{ph}} \rightarrow D^0 + h\nu + \text{phonon}$ $[A^0 X] \rightarrow A^0 + h\nu$ $[A^0 X]_{\text{ph}} \rightarrow A^0 + h\nu + \text{phonon}$
Multiexcitonic complex decay	$[D^0 X_n] \rightarrow [D^0 X_{n-1}] + h\nu$ $[D^0 X_n]_{\text{ph}} \rightarrow [D^0 X_{n-1}] + h\nu + \text{phonon}$

Subscript ph indicates that phonons participate in the decay.

**Symbols of particles and complexes** participating in various generation and recombination processes:

*e* — conduction band electron;

*h* — valence band hole;

*hν* — photon;

*D*<sup>0</sup>, *D*<sup>+</sup> — neutral, positively charged donor, for example, As<sup>0</sup>, As<sup>+</sup>, Sb<sup>0</sup>, Sb<sup>+</sup>;

*A*<sup>0</sup>, *A*<sup>−</sup> — neutral, negatively charged acceptor, for example, Ga<sup>0</sup>, Ga<sup>−</sup>, B<sup>0</sup>, B<sup>−</sup>;

*D*<sup>0</sup>(*n*), *A*<sup>0</sup>(*n*) — *n*-th excited state of neutral donor, neutral acceptor, for example, Sb<sup>0</sup>(2*p*<sub>0</sub>), Ga<sup>0</sup>(8+1);

*D*<sub>*T*</sub>, *A*<sub>*T*</sub> — donor, acceptor which replaces lattice atom of type *T*, for example, when gallium atom in GaAs lattice is replaced by silicon, then *D*<sub>*T*</sub> is Si<sub>Ga</sub>;

*V* — vacancy;

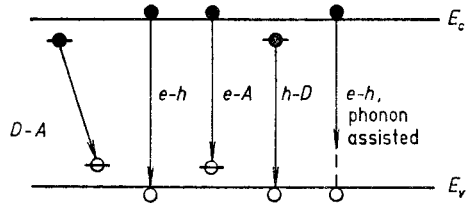
*V*<sub>Ga</sub>, *V*<sub>As</sub> — gallium, arsenic vacancies;

*X* — free exciton;

*X*(*n*) — free exciton in the excited *n*-th state;

*X*<sub>2</sub> — free excitonic molecule (biexciton);

Fig. 3. Radiative recombination channels for electrons (full circles) and holes (open circles).  $E_c$  and  $E_v$  are the conduction and valence band edges. For details see Table 4.



$[D^0X]$  – excitonic complex, i. e. exciton bound to neutral donor, for example,  $[As^0X]$ ;

$[D^0X](n)$  –  $n$ -th excited state of the excitonic complex, for example,  $[As^0X](2)$ ;

$[D^+X]$  – charged excitonic complex, i. e. exciton bound to a charged donor, for example,  $[As^+X]$ ;

$[D^0X_n]$  – multiexcitonic complex, i. e.  $n$  excitons bound to a single donor  $D^0$ ,  $n=1, 2, 3, \dots$ ;

$[D_n^0X]$  – single exciton bound to  $n$  neutral donors,  $n=1, 2, 3, \dots$ ;

$[D^0A^0]$  – donor–acceptor complex, for example,  $[In^0Sb^0]$ ;

$[Cu_{Ga}V_{As}]$  – complex consisting of copper atom and vacancy, which replace Ga and As atoms in GaAs lattice;

$[Ge_{As}X]$  – complex which consists of the exciton bound to germanium, the latter replaces lattice As atom;

$LA, LO, TA, TO$  – longitudinal acoustic, longitudinal optical, transverse acoustic, transverse optical phonons or phonon branches.

**Piezooptic and elasto-optic coefficients.** By elasto-optic and piezooptic effects are meant the phenomena of change in the refractive index of the crystal under linear mechanical stress. Dimensionless fourth-rank elasto-optic tensor components  $p_{ijkl}$  are defined as the first terms in the tensorial series

$$\Delta \eta_{ij} = \sum_{kl} p_{ijkl} \varepsilon_{kl},$$

where  $\Delta \eta_{ij}$  is the change in the optical impermeability tensor  $\Delta \eta_{ij} = \Delta (\varepsilon_0/\varepsilon)_{ij} = \Delta (1/n^2)$ .  $\varepsilon$  and  $n$  is the dielectric constant and refractive index, respectively, and  $\varepsilon_{kl}$  is the strain tensor. Here, it is assumed that the extinction coefficient is negligible.  $\Delta \eta_{ij}$  can also be expressed through the stress tensor  $\sigma_{kl}$ :

$$\Delta \eta_{ij} = \sum_{kl} \pi_{ijkl} \sigma_{kl}.$$

The components  $\pi_{ijkl}$  make up a fourth-rank piezooptic tensor.

For cubic semiconductors the nonvanishing components of  $p_{ijkl}$  and  $\pi_{ijkl}$  reduce to three coefficients, traditionally denoted as  $p_{11}, p_{12}, p_{44}$  and  $\pi_{11}, \pi_{12}, \pi_{44}$  (see Section 7 for notation).

Elasto-optic and piezooptic tensors are related by compliance  $s_{ijkl}$  and elastic  $p_{ijkl}$  tensors

$$p_{ijrs} = \sum_{kl} \pi_{ijkl} c_{klrs},$$

$$\pi_{ijkl} = \sum_{rs} p_{ijrs} s_{rskl}.$$

In case of cubic semiconductors the uniaxial stresses  $X_{[100]}$  and  $X_{[111]}$  in [100] and [111] directions, piezooptic coefficients and dielectric permittivities are related by the formulas

$$\frac{\varepsilon_{\parallel} - \varepsilon_{\perp}}{X_{[100]}} = -n^4(\pi_{11} - \pi_{12}),$$

$$\frac{\varepsilon_{\parallel} - \varepsilon_{\perp}}{X_{[111]}} = -n^4\pi_{44},$$

where  $n$  is the refractive index in the absence of stress and  $\varepsilon_{\parallel}$ ,  $\varepsilon_{\perp}$  are the real parts of the relative dielectric permittivity for radiation polarized parallel and perpendicular to the applied stress.

Relative change of the refractive index under hydrostatic pressure  $p$ :

$$\frac{dn}{dp} = -\frac{1}{2} n^3 (\pi_{11} + 2\pi_{12}).$$

**Electrooptic coefficients.** By electrooptic effect is meant the phenomenon of change in the refractive index of the crystal under electric field  $\mathbf{E}$ . Electrooptic tensor is defined through tensorial series

$$\eta_{ij}(\mathbf{E}) - \eta_{ij}(0) \equiv \Delta\eta_{ij} = \sum_k r_{ijk} E_k + \sum_{kl} s_{ijkl} E_k E_l + \dots,$$

where  $\eta_{ij}$  are the impermeability tensor components (for isotropic media  $\eta = \varepsilon_0/\varepsilon$ ),  $r_{ijk}$  are the linear electrooptic tensor components (Pockels coefficients), and  $s_{ijkl}$  are the quadratic electrooptic tensor components (Kerr coefficients).

For centrosymmetric crystals, Ge and Si,  $r_{ijk}=0$ , i. e. all Pockels coefficients are equal zero. For GaAs and InP nonvanishing components of  $r_{ijk}$  reduce to a single component traditionally denoted by  $r_{14}$ .

For Ge, Si, GaAs and InP nonvanishing components of  $s_{ijkl}$  reduce to two Kerr coefficients  $s_{11} \equiv s_{1111}$  and  $s_{12} \equiv s_{1122}$ .

**Nonlinear optics.** The polarization induced by the electric field in the nonlinear media is

$$P_i = P_i^{(1)} + P_i^{(2)} + P_i^{(3)} + \dots = \varepsilon_0 \left( \sum_j \chi_{ij} E_j + \sum_{jk} d_{ijk} E_j E_k + \sum_{jkl} c_{ijkl} E_j E_k E_l + \dots \right),$$

where  $P_i$  and  $E_i$  are  $i$ -th components of momentary polarization and electric field in the media, respectively.

Linear polarization:

$$P_i^{(1)} = \varepsilon_0 \sum_j \chi_{ij} E_j.$$

In this case the linear susceptibility  $\chi_{ij}$  for Ge, Si, GaAs and InP reduces to a scalar,  $\chi_{ij} = \chi$ , which can be expressed through dielectric permittivity

$$\varepsilon = \varepsilon_0 (1 + \chi).$$

Second-order nonlinear polarization:

$$P_i^{(2)} = \varepsilon_0 \sum_{jk} d_{ijk} E_j E_k.$$

Now the third-rank tensor components  $d_{ijk}$  [m/V] describe the second-order nonlinear susceptibility. For Ge and Si, which are centrosymmetric crystals, all com-

ponents are equal to zero,  $d_{ijk}=0$ . For GaAs and InP the nonvanishing components of  $d_{ijk}$  reduce to a single component traditionally denoted by  $d_{14}$ . Then, the equation for  $P_i^{(2)}$  with reference to the cubic crystallographic axes  $x, y, z$  assumes the following form:

$$P_x^{(2)} = 2d_{14}\epsilon_0 E_y E_z,$$

$$P_y^{(2)} = 2d_{14}\epsilon_0 E_z E_x,$$

$$P_z^{(2)} = 2d_{14}\epsilon_0 E_x E_y.$$

Third-order nonlinear polarization:

$$P_i^{(3)} = \epsilon_0 \sum_{jkl} c_{ijkl} E_j E_k E_l.$$

Here the fourth-rank tensor components  $c_{ijkl}$  [ $\text{m}^2/\text{V}^2$ ] describe the third-order nonlinear susceptibility. For Ge, Si, GaAs and InP nonvanishing components of  $c_{ijkl}$  reduce to two coefficients,  $c_{11} \equiv c_{1111}$  and  $c_{12} \equiv c_{1122}$ . Then the equation for  $P_i^{(3)}$  with reference to the cubic crystallographic axes  $x, y, z$  assumes the following form:

$$P_x^{(3)} = c_{1111}\epsilon_0 E_x^3 + 3c_{1122}\epsilon_0 E_x(E_y^2 + E_z^2),$$

$$P_y^{(3)} = c_{1111}\epsilon_0 E_y^3 + 3c_{1122}\epsilon_0 E_y(E_z^2 + E_x^2),$$

$$P_z^{(3)} = c_{1111}\epsilon_0 E_z^3 + 3c_{1122}\epsilon_0 E_z(E_x^2 + E_y^2).$$

The anisotropy of the susceptibility is characterized by

$$\sigma = (1 + 3c_{1122}/c_{1111})/2.$$

For isotropic materials:  $c_{1122}/c_{1111}=1/3$ , and  $\sigma=1$ .

## 4. Electrical properties

**Carrier concentrations.** If  $n$  is the electron concentration in the conduction band and  $p$  is the hole concentration in the valence band the semiconductor is said to be

- intrinsic if  $n=p=n_i$ ,
- $n$ -type if  $n \gg p$ ,
- $p$ -type if  $p \gg n$ .

For doped and undoped nondegenerate semiconductors the mass-of-action law,  $np=n_i^2$ , holds.

**Drift velocity, drift mobility, current density and conductivity.** The drift velocity of the carrier in the electric field  $E$  is defined through the distance  $d$  and the transit time  $t_{tr}$  which is needed for the carrier to cross this distance:

$$v = d/t_{tr}.$$

The drift mobility is defined by

$$\mu_d = v/E.$$

The current density (due to electrons) is

$$J = env = en\mu_d E = \sigma E = E/\rho,$$

where  $e$  is the elementary charge,  $n$  is the electron concentration,  $\sigma$  is the conductivity and  $\rho$  is the resistivity.

In cubic semiconductors, in a weak electric field limit  $v$  is parallel and proportio-



nal to  $E$ , as a result  $\mu_d$ ,  $\sigma$ ,  $\rho$  are scalars. At high electric fields  $v$  is not parallel to  $E$  except when  $E$  is parallel to the high symmetry directions, such as  $\langle 100 \rangle$  or  $\langle 111 \rangle$ .

**Hall coefficient, Hall mobility and Hall factor.** The Hall coefficient  $R_H$  is the proportionality coefficient between the current density  $J$  along a long sample and the transverse electric field  $E_H$  (Hall field) which arises in the sample placed in a magnetic field with induction  $B$ :

$$E_H = R_H (J \times B).$$

$R_H$  is inversely proportional to the carrier concentration  $n$  in the sample if the carrier free-flight duration between collisions can be introduced

$$R_H = r_H / (en).$$

The constant  $r_H$  is called the Hall factor. It depends on the scattering mechanism: for acoustic scattering  $r_H = (3/8)\pi = 1.18$ ; for ionized impurity scattering  $r_H = (315/312)\pi = 1.93$ ; for degenerate semiconductors  $r_H = 1$ ; in the limit of high magnetic field ( $\mu_H B \gg 1$ )  $r_H = 1$ .

If one defines the carrier concentration by the relation

$$n_H = 1 / (eR_H),$$

then Hall velocity and mobility are

$$v_H = R_H J, \quad \mu_H = v_H / E,$$

where  $E$  is the applied electric field. The Hall factor can be expressed through the ratio of Hall to drift mobilities or velocities

$$r_H = \mu_H / \mu = v_H / v.$$

**Diffusion coefficient.** The gradient of carrier concentration in a sample causes the diffusion current of density

$$J_D = eD \operatorname{grad}_r n,$$

where  $D$  is the diffusion coefficient.  $D$  also describes the range (called diffusion length) the carrier can diffuse during the time interval  $\Delta t$

$$l_D = \sqrt{D \cdot \Delta t}.$$

At weak electric fields  $D$  and drift mobility  $\mu_d$  are related by the Einstein formula

$$D = \frac{kT}{e} \mu_d,$$

where  $T$  is the temperature in K,  $k$  is the Boltzmann constant and  $e$  is the elementary charge. In the presence of high electric fields, when hot carrier effects come into play, the diffusion current densities along and perpendicular to the electric field are different, and are characterized by  $D_{\parallel}$  and  $D_{\perp}$ , the longitudinal and transverse diffusion coefficients. In a weak field limit  $D_{\parallel} = D_{\perp} = D$ .

**Band-band impact ionization rates.** Experimentally measured impact ionization rates per unit length for electrons  $\alpha'(x)$  and for holes  $\beta'(x)$  at the point with the coordinate  $x$  are defined by equations

$$\begin{cases} -\frac{dJ_n}{dx} = \alpha'(x) J_n(x) + \beta'(x) J_p(x), \\ \frac{dJ_p}{dx} = \alpha'(x) J_n(x) + \beta'(x) J_p(x), \end{cases}$$

where  $J_n$  and  $J_p$  are the electron and hole current densities.

Theoretically calculated impact ionization rates are

$$\alpha = \frac{1}{|v_n| \tau_{in}}, \quad \beta = \frac{1}{|v_p| \tau_{ip}},$$

where  $\tau_{in}$  and  $\tau_{ip}$  are the characteristic times for creation of one electron-hole pair by an electron and a hole, respectively, and  $v_n$  and  $v_p$  are the electron and hole drift velocities.

The following relations exist between  $\alpha'$ ,  $\beta'$  and  $\alpha$ ,  $\beta$  [13]:

$$\alpha' = \alpha - \frac{1}{v_n} \frac{dv_n}{dE} \frac{dE}{dx},$$

$$\beta' = \beta + \frac{1}{v_p} \frac{dv_p}{dE} \frac{dE}{dx}.$$

If the electric field is homogeneous ( $dE/dx=0$ ) or velocity saturates ( $dv_{n,p}/dE=0$ ), then  $\alpha'=\alpha$  and  $\beta'=\beta$ .

**Energy relaxation time**  $\tau_e$  characterizes the rate of energy dissipation to the lattice by charge carriers.  $\tau_e$  appears in the power balance equation

$$d\varepsilon/dt = e v E - (\varepsilon_E - \varepsilon_0)/\tau_e,$$

where the first term on the right hand side describes the power gained by the electrons (holes) from the electric field  $E$  and the second one describes the power lost to the lattice. Here  $\varepsilon_E$  and  $\varepsilon_0$  are the carrier energies averaged over the distribution function in the presence and absence of the field, and  $v$  is their drift velocity.

The charge carriers are called warm if  $\varepsilon_E \gtrsim \varepsilon_0$ .

The charge carriers are called hot if  $\varepsilon_E \gg \varepsilon_0$ .

**Intervalley relaxation time**  $\tau_i$  characterizes the rate of change of carrier concentration in the  $i$ -th energy valley

$$dn_i/dt = G_i - (n_i - n_{i0})/\tau_i.$$

Here  $n_i$  and  $n_{i0}$  are the nonequilibrium and equilibrium carrier concentrations, and  $G_i$  is the carrier number generation rate in the considered  $i$ -th valley.

## 5. Piezoelectric, thermoelectric and magnetic properties

**Piezoresistance.** The most general linear change of resistance tensor  $\rho_{ij}$  on stress tensor  $\sigma_{kl}$  is expressed through (isothermal) piezoresistance tensor  $\pi_{ijkl}$

$$(\rho_{ij} - \rho_0)/\rho_0 \equiv \Delta\rho_{ij}/\rho_0 = \sum_{kl} \pi_{ijkl} \sigma_{kl},$$

where  $\rho_0$  is the resistance at zero stress, which for cubic semiconductors is scalar. For cubic semiconductors all  $\pi_{ijkl}$  components can be expressed through three independent coefficients traditionally denoted by  $\pi_{11}$ ,  $\pi_{12}$ ,  $\pi_{44}$  (see Section 7).  $\Delta\rho_{ij}/\rho_0$  can also be expressed through the strain tensor  $\varepsilon_{kl}$

$$\Delta\rho_{ij}/\rho_0 = \sum_{kl} m_{ijkl} \varepsilon_{kl},$$

where  $m_{ijkl}$  are the elastoresistance tensor coefficients which, similarly to the piezoresistance tensor, can be reduced to three independent coefficients  $m_{11}$ ,  $m_{12}$ ,  $m_{44}$ .

**TABLE 5** Orientations of the uniaxial stress  $X$  and current  $I$  with respects to the crystallographic axes, which yield experimentally measured combinations of piezoresistance tensors in cubic semiconductors. The piezoresistance is positive if tensile stress reduces the resistance [14, 15]

Direction of stress $X$	Direction of current $I$	$-\frac{\Delta\rho}{\rho_0 X} \Big _{X \rightarrow 0}$
Longitudinal configuration		
[100]	[100]	$\pi_{11}$
[110]	[110]	$(\pi_{11} + \pi_{12} + \pi_{44})/2$
[111]	[111]	$(\pi_{11} + 2\pi_{12} + 2\pi_{44})/3$
Transverse configuration		
[100]	[010]	$\pi_{12}$
[110]	[1 $\bar{1}$ 0]	$(\pi_{11} + \pi_{12} - \pi_{44})/2$
Hydrostatic pressure $p$		
$-\frac{\Delta\rho}{\rho_0 p} = \pi_{11} + 2\pi_{12}$		

Conversion formulas from  $\pi_{ij}$  to  $m_{ij}$  for cubic semiconductors [14]:

$$m_{44} = \pi_{44} c_{44},$$

$$(m_{11} - m_{12})/2 = (\pi_{11} - \pi_{12})(c_{11} - c_{12})/2,$$

$$(m_{11} + 2m_{12})/3 = (\pi_{11} + 2\pi_{12})(c_{11} + 2c_{12})/3,$$

where  $c_{ij}$  are the elastic tensor components described in Section 1 of this Chapter.

Theory shows that under some conditions the piezoresistance coefficients satisfy:

$\pi_{11} - \pi_{12} = \pi_{44} = 0$  if the band edge is isotropic and situated at the wave vector  $\mathbf{k} = 0$ ;

$\pi_{11} - \pi_{12} \neq 0, \pi_{44} = 0$  if the energy ellipsoids are situated on the  $\Delta$ -axes;

$\pi_{11} - \pi_{12} = 0, \pi_{44} \neq 0$  if the ellipsoids are situated on the  $\Lambda$ -axes.

Table 5 shows the relations between piezoresistance tensor combinations and orientation of stress and current.

**Piezoelectric tensor** relates the components of electric field  $E_i$  or polarization  $P_i$  of the crystal and the components of strain  $\varepsilon_{jk}$  or stress  $\sigma_{jk}$  tensor

$$P_i = \sum_{ij} d_{ij} \sigma_{ij}, \quad P_i = - \sum_{jk} e_{ijk} \varepsilon_{jk},$$

$$E_i = - \sum_{jk} g_{ijk} \sigma_{jk}, \quad E_i = - \sum_{ij} h_{ij} \varepsilon_{ij},$$

$d_{ij}, e_{ijk}, g_{ijk}, h_{ij}$  are the piezoelectric tensor components.

For Si and Ge, centrosymmetric crystals, all piezoelectric components are equal zero.

For GaAs and InP all nonvanishing components of  $d_{ijj}$ ,  $e_{ijk}$ ,  $g_{ijk}$ ,  $h_{ijj}$  reduce to a single constant usually denoted by  $d_{14}$ ,  $e_{14}$ ,  $g_{14}$ ,  $h_{14}$ , respectively (see Section 7).

**Seebeck coefficient  $S$**  (also called thermoelectric power) is a measure of thermoelectric voltage  $\Delta V$  which develops between the specimen ends when the temperature difference  $\Delta T$  is maintained between them

$$S = \Delta V / \Delta T.$$

**Magnetoresistance.** In general, the magnetoresistance is a fourth-rank tensor. The magnetoresistance is sensitive to the sample geometry and the direction of the magnetic induction  $\mathbf{B}$  and the current  $\mathbf{I}$  with reference to the crystallographic axes. In practice two components are frequently defined for the specimens whose dimensions in the current direction are much larger than in the other directions: the longitudinal magnetoresistance when  $\mathbf{I} \parallel \mathbf{B}$ , and the transverse magnetoresistance when  $\mathbf{I} \perp \mathbf{B}$ . Experimentally one measures the change of specimen resistivity in the direction of the current flow under the action of parallel or perpendicular magnetic field

$$\Delta \rho / \rho_0 = [\rho(B) - \rho_0] / \rho_0,$$

where  $\rho_0 \equiv \rho(B=0)$ . The quantity  $\Delta \rho / (\rho_0 B^2)$  is called the magnetoresistance coefficient.

**Magnetic susceptibility  $\chi_m$** , magnetic permeability of vacuum  $\mu_0$  and relative magnetic permeability  $\mu_r$  are related to magnetic induction  $\mathbf{B}$ , magnetic field  $\mathbf{H}$  and magnetization  $\mathbf{M}$  by equalities

$$\mathbf{B} = \mu_0 \mu_r \mathbf{H} = \mu_0 (1 + \chi_m) \mathbf{H} = \mu_0 (\mathbf{H} + \mathbf{M}).$$

## 6. Impurity properties

Positively (negatively) charged states of an impurity are defined as donor (acceptor) states. Neutral states bear no other distinctive name. Impurity which can have only one or more donor (acceptor) states is referred to as a donor (acceptor). The above mentioned states are denoted by symbols  $D^+$ ,  $D^{2+}$  etc ( $A^-$ ,  $A^{2-}$  etc). The corresponding neutral state of the donor (acceptor) is denoted by symbol  $D^0$  or  $D$  ( $A^0$  or  $A$ ). Impurity which can have both the donor and the acceptor states is referred to as an amphoteric impurity.

**Elementary carrier capture and emission processes** are shown in Fig. 4. Electron or hole capture time  $\tau_{n,p}$  and capture rate  $c_{n,p}$  due to centers of concentration  $N$  are

$$\tau_n = \frac{1}{N \sigma_n v_{th}}, \quad \tau_p = \frac{1}{N \sigma_p v_{th}},$$

$$c_n = \sigma_n v_{th}, \quad c_p = \sigma_p v_{th},$$

where  $\sigma_n$  and  $\sigma_p$  are the electron and hole capture cross sections by the center and  $v_{th}$  is the thermal electron or hole velocity

$$v_{th} = \sqrt{\frac{8kT}{\pi m_d}} = 6.25 \cdot 10^5 \sqrt{\frac{T [K]}{m_d/m_0}} \left[ \frac{\text{cm}}{\text{s}} \right].$$

Here  $m_d$  is the density-of-states mass.

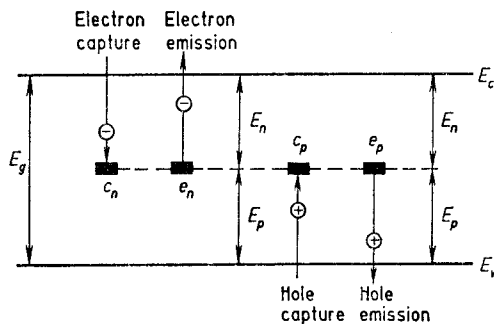


Fig. 4. Elementary capture and emission processes.  $E_n$  and  $E_p$  are the activation energies for electrons and holes.  $E_c$  and  $E_v$  are the conduction and valence band edges.

Small deviations from electron and hole equilibrium concentrations can be described by an exponential law

$$n_T(t) = n_T(0) \exp(-t/\tau_{en}),$$

$$p_T(t) = p_T(0) \exp(-t/\tau_{ep}).$$

Here  $t$  is time,  $n_T(0)$  and  $p_T(0)$  are the excess electron and hole concentrations at  $t=0$ . Assuming the detailed balance, the thermal emission rates for electrons and holes are (see Fig. 4)

$$\tau_{en}^{-1} = e_n = g_n \sigma_n v_{th} N_c \exp(-E_n/kT),$$

$$\tau_{ep}^{-1} = e_p = g_p \sigma_p v_{th} N_v \exp(-E_p/kT),$$

where  $g_n, g_p$  are the respective degeneracy factors, which are frequently assumed to be equal to unity.  $E_n$  and  $E_p$  are the activation energies for electrons and holes.  $N_c$  and  $N_v$  are densities of states in the conduction and valence bands

$$N_{c,v} = 2M \left[ \frac{2\pi m_d kT}{h^2} \right]^{3/2} = 4.83 \cdot 10^{15} M \left( \frac{m_d}{m_0} \right)^{3/2} T^{3/2} [\text{cm}^{-3}].$$

Here  $M$  is the number of equivalent valleys.

**Impurity impact ionization coefficient**  $A_i$  characterizes the rate of increase of free carrier concentration  $n$  due to impact ionization of impurities of concentration  $N$ :

$$dn/dt = A_i N n.$$

**Principles of the measurement** of semiconductor properties discussed in the Introduction can be found, for example, in [16–26].

## 7. Restrictions on the tensor components in the cubic semiconductors

By symmetry considerations the following restrictions are imposed on the second-, third- and fourth-rank tensors for diamond and zinc blende lattices.

**Second-rank tensors** (electrical conductivity and resistivity, heat conductivity and resistivity):

$$T_{xx} = T_{yy} = T_{zz} \neq 0, \quad T_{ik} = 0 \text{ if } i \neq k.$$

**Third-rank tensors** (piezoelectricity, nonlinear susceptibility for second harmonic generation, Pockels effect, parametric generation). For Ge and Si, which possess the center of symmetry, all components are equal zero.

For GaAs and InP:

$$T_{xyz} = T_{xzy} = T_{yxz} = T_{yzx} = T_{zxy} = T_{zyx},$$

which are traditionally written as a single coefficient  $T_{14}$ . All other components are equal zero.

**Fourth-rank tensors** (magnetoresistance, piezoresistance, elastic constants, Kerr effect). To simplify notation the following abbreviation is introduced:  $xx=1$ ,  $yy=2$ ,  $zz=3$ ,  $yz=zy=4$ ,  $xz=zx=5$ ,  $xy=yx=6$ . Then the fourth-rank tensor components reduce to the following nonvanishing terms:

$$T_{11} = T_{22} = T_{33}, \quad T_{44} = T_{55} = T_{66},$$

$$T_{12} = T_{21} = T_{13} = T_{31} = T_{23} = T_{32}.$$

All other components are equal zero.

The tensor component having the simplified notation will be called a constant or a coefficient.

## 8. Physical constants

**TABLE 6** Relations between photon wavelength  $\lambda$ , energy  $E$  and wave number  $k$  [27, 28]

$$\lambda [\mu\text{m}] = \frac{1.239\,502}{E[\text{eV}]} \quad \text{in air with refractive index } n_a = 1.000\,274\,9,$$

$$\frac{1.239\,842}{E[\text{eV}]} \quad \text{in vacuum.}$$

$$k [\text{cm}^{-1}] = 8\,065.54 \, E [\text{eV}] \quad \text{in vacuum.}$$

$$1 \, \text{eV} = 8\,065.54 \, \text{cm}^{-1} \quad \text{in vacuum.}$$

$$1 \, \text{meV} = 8.065\,54 \, \text{cm}^{-1} \quad \text{in vacuum.}$$

$$1 \, \text{cm}^{-1} = 0.123\,98 \, \text{meV} \quad \text{in vacuum.}$$

$$1 \, \text{eV} = 2.417\,988 \cdot 10^{14} \, \text{Hz},$$

$$1.602\,177 \cdot 10^{-19} \, \text{J},$$

$$1.602\,177 \cdot 10^{-12} \, \text{erg}.$$

$$1 \, \text{K} = 8.617\,385 \cdot 10^{-5} \, \text{eV}.$$

$$1 \, \text{eV} = 1.160\,445 \cdot 10^4 \, \text{K}.$$

TABLE 7 Physical constants [28]

Quantity	SI	CGS
Electronic charge $e$	$1.602\,177 \cdot 10^{-19}$ C	$4.803\,206 \cdot 10^{-10}$ esu
Electron mass $m_0$	$9.109\,389 \cdot 10^{-31}$ kg	$9.109\,389 \cdot 10^{-28}$ g
Light velocity $c$	$2.997\,924 \cdot 10^8$ m/s	$2.997\,924 \cdot 10^{10}$ cm/s
Electric constant $\epsilon_0$	$8.854\,187 \cdot 10^{-12}$ F/m	1
Magnetic constant $\mu_0$	$4\pi \cdot 10^{-7}$ H/m = $12.566\,370 \cdot 10^{-7}$ H/m	1
Planck constant $h$	$6.626\,075 \cdot 10^{-34}$ J·s	$6.626\,075 \cdot 10^{-27}$ erg·s
$\hbar = h/2\pi$	$1.054\,572 \cdot 10^{-34}$ J·s	$1.054\,572 \cdot 10^{-27}$ erg·s
Boltzmann constant $k$	$1.380\,658 \cdot 10^{-23}$ J/K	$1.380\,658 \cdot 10^{-16}$ erg/K
Bohr magneton $\mu_B$	$9.274\,015 \cdot 10^{-24}$ J/T	$9.274\,015 \cdot 10^{-21}$ erg/Gs
Electron g-factor	2.002 319	2.002 319

Nonsystemic:

$$h = 4.135\,669 \cdot 10^{-15} \text{ eV} \cdot \text{s},$$

$$\hbar = 6.582\,122 \cdot 10^{-16} \text{ eV} \cdot \text{s},$$

$$k = 8.617\,385 \cdot 10^{-5} \text{ eV/K},$$

$$\mu_B = 5.788\,382 \cdot 10^{-5} \text{ eV/T}.$$

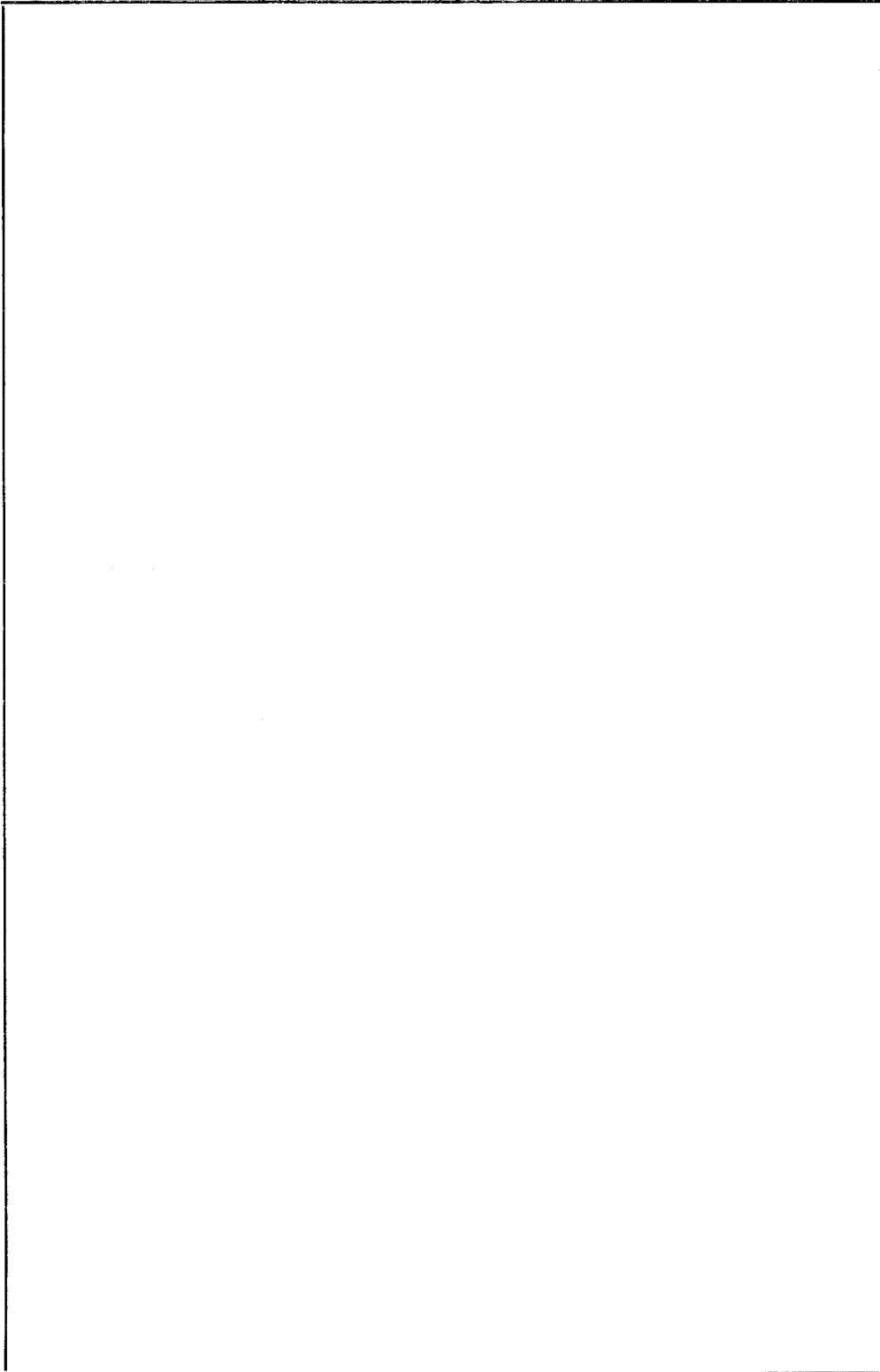


**TABLE 8** Translation of electrical quantities from CGS to SI units [29]

Quantity	CGS	SI
Relative dielectric permittivity	$\epsilon^*$	$\rightarrow \epsilon_r$
Relative magnetic permeability	$\mu^*$	$\rightarrow \mu_r$
Electric field intensity	$E^*$	$\rightarrow E \cdot (4\pi\epsilon_0)^{1/2}$
Electric induction	$D^*$	$\rightarrow D \cdot (4\pi/\epsilon_0)^{1/2}$
Magnetic field intensity	$H^*$	$\rightarrow H \cdot (4\pi\mu_0)^{1/2}$
Magnetic induction	$B^*$	$\rightarrow B \cdot (4\pi/\mu_0)^{1/2}$
Electron charge	$e^*$	$\rightarrow e/(4\pi\epsilon_0)^{1/2}$
Charge	$Q^*$	$\rightarrow Q/(4\pi\epsilon_0)^{1/2}$
Current density	$J^*$	$\rightarrow J/(4\pi\epsilon_0)^{1/2}$
Current	$I^*$	$\rightarrow I/(4\pi\epsilon_0)^{1/2}$
Voltage	$U^*$	$\rightarrow U \cdot (4\pi\epsilon_0)^{1/2}$
Vector potential	$A^*$	$\rightarrow A \cdot (4\pi/\mu_0)^{1/2}$
Polarization vector	$P^*$	$\rightarrow P/(4\pi\epsilon_0)^{1/2}$
Magnetization vector	$M^*$	$\rightarrow M/(4\pi/\mu_0)^{1/2}$
Resistance	$R^*$	$\rightarrow R \cdot (4\pi\epsilon_0)$
Conductivity	$\sigma^*$	$\rightarrow \sigma/(4\pi\epsilon_0)$
Capacity	$C^*$	$\rightarrow C/(4\pi\epsilon_0)$
Inductance	$L^*$	$\rightarrow L \cdot (4\pi/\mu_0)$
Mobility	$\mu^*$	$\rightarrow \mu/(4\pi\epsilon_0)^{1/2}$
Dielectric susceptibility	$\chi_e^*$	$\rightarrow \chi_e/(4\pi)$
Magnetic susceptibility	$\chi_m^*$	$\rightarrow \chi_m/(4\pi)$
Bohr magneton	$\mu_B^*$	$\rightarrow \mu_B/(4\pi/\mu_0)$
Light velocity in vacuum		$c = 1/(\epsilon_0 \mu_0)^{1/2}$

Example: cyclotron frequency

$$\omega_c^* = \frac{e^* H^*}{mc} \rightarrow \omega_c = \frac{e}{(4\pi\epsilon_0)^{1/2}} \cdot \frac{H (4\pi\mu_0)^{1/2}}{m} = \frac{(\epsilon_0 \mu_0)^{1/2}}{m} \cdot \frac{e\mu_0 H}{m} = \frac{eB}{m}.$$



## B. Physical data

### 1. Physical data for germanium

#### 1.1. Ge lattice properties

1. Ge consists of the following isotopes (as a result the translational symmetry of the lattice is not exact) [1.1]  

$^{70}\text{Ge}$	.....	20.5 %
$^{72}\text{Ge}$	.....	27.4 %
$^{73}\text{Ge}$	.....	7.8 %
$^{74}\text{Ge}$	.....	36.5 %
$^{76}\text{Ge}$	.....	7.8 %
2. Average atomic weight: 72.59 [1.2]
3. Ge has a diamond-type lattice. Space group is  $Fd\bar{3}m (O_h^f)$ . Lattice symmetry formula is  $3L^4 4L^3 6L^2 9PC$ , which means that there are 3 symmetry axes of the fourth-order, 4 symmetry axes of the third-order, 6 symmetry axes of the second-order, 9 symmetry planes and inversion center
4. Lattice constant:  $a=0.565\ 79\ \text{nm}$  at  $298.15\ \text{K}$  [1.3]
5. Density:  $5.326\ 74\ \text{g/cm}^3$  at  $298 \pm 0.01\ \text{K}$  [1.4]
6. Number of atoms in  $1\ \text{cm}^3$  is  $4.4 \cdot 10^{22}$
7. Melting temperature:  $1210\ \text{K}$  [1.5]
8. Transition to metallic phase occurs at the pressure  $10.5\ \text{GPa}$  [1.6]
9. Ge cleaves most readily on  $\{111\}$  family planes [1.7]

**TABLE 1.1** Elastic parameters of Ge at the lattice temperature 77 K, 300 K [1.8] and 973 K [1.9]

Parameter	Value		
	77 K	300 K	973 K
Elastic constants:			
$c_{11}$ , GPa	131.1	128.5	112.1
$c_{12}$ , GPa	49.2	48.3	37.3
$c_{44}$ , GPa	68.2	66.8	62.1
Sound velocity in the direction [100]:			
longitudinal $v_L$ , cm/s	$4.96 \cdot 10^5$	$4.91 \cdot 10^5$	$4.59 \cdot 10^5$
transverse $v_T$ , cm/s	$3.58 \cdot 10^5$	$3.54 \cdot 10^5$	$3.42 \cdot 10^5$
Sound velocity in the direction [111]:			
longitudinal $v_L$ , cm/s	$5.61 \cdot 10^5$	$5.55 \cdot 10^5$	$5.22 \cdot 10^5$
transverse $v_T$ , cm/s	$3.07 \cdot 10^5$	$3.03 \cdot 10^5$	$2.93 \cdot 10^5$
Elastic anisotropy factor $a$	0.6	0.6	0.6
Poisson ratio $\nu$	0.273	0.273	0.249
Young's modulus $E$ , GPa:			
direction [100]	104.2	102.1	93.4
direction [110]	139.8	136.9	124.4
direction [111]	157.7	154.5	139.8
Bulk modulus $B_0$ , GPa	76.5	75.0	62.2
$B'_0 = dB_0/dp$		4.35*	

\* - [1.10].

**TABLE 1.2** Ge phonon energies for high symmetry points  $\Gamma$ ,  $X$ ,  $L$  in the Brillouin zone at 300 K [1.11]

Phonon branch	Phonon energy, meV		
	$\Gamma$	$X$	$L$
<i>LO</i>	$37.3 \pm 0.08$	$29.5 \pm 0.08$	$30 \pm 0.08$
<i>TO</i>	$37.3 \pm 0.08$	$33.8 \pm 0.12$	$35.4 \pm 0.12$
<i>LA</i>	0	$29.5 \pm 0.08$	$27.4 \pm 0.16$
<i>TA</i>	0	$9.84 \pm 0.08$	$7.73 \pm 0.08$

**Temperature variation of phonon energies.** In Ge the phonon energies of all modes at 700 K are uniformly lower than those at 100 K by 3–5 % [1.12, 1.13].

**Optical phonon lifetime.** At the symmetry point  $\Gamma$  the half-widths of the first-order Raman line are  $3 \text{ cm}^{-1}$  at 77 K and  $4.1 \text{ cm}^{-1}$  at 300 K. These half-widths yield phonon lifetimes 1.7 ps and 1.3 ps, respectively [1.14].

**Raman activity.** Germanium has only one first-order Raman-active phonon of symmetry  $\Gamma_{25'}$  located at the Brillouin zone center and having energy 37.3 meV.

**TABLE 1.3** Grüneisen parameters for different phonon branches in Ge at  $X$ ,  $\Gamma$  ( $T=298 \text{ K}$ ) [3] and  $L$  ( $T=1.22 \text{ K}$ ) [1.15] critical points

Phonon branch	Grüneisen parameter		
	$X$	$\Gamma$	$L$
<i>LO</i>		1.12	1.2
<i>TO</i>		1.12	0.9
<i>LA</i>		$1.301^* [q00]$	0.5
<i>LA</i>		$1.294^* [qq0]$	
<i>LA</i>		$1.292^* [qqq]$	
<i>TA</i>	1.53	$0.612^* [q00]$	–0.4
<i>TA</i>		$0.367^* [qqq]$	
<i>TA<sub>1</sub></i>		$0.612^* [qq0]$	
<i>TA<sub>2</sub></i>		$0.161^* [qq0]$	

\* – Calculated from elastic parameters [1.16]. The direction of wave vector is given in parentheses;  $q \ll 2\pi/a$ , where  $a$  is the lattice constant.

#### Lattice dielectric permittivity.

Relative static [1.17]:

$$\varepsilon/\varepsilon_0 = 15.94 \text{ at } 300 \text{ K.}$$

Dependence on hydrostatic pressure  $p$  in GPa [1.17]:

$$\varepsilon/\varepsilon_0 = 15.94 - 0.36p + 0.014p^2.$$

Dependence on temperature [1.18]:

$$(1/\varepsilon)(d\varepsilon/dT) = 1.9 \cdot 10^{-4} \text{ K}^{-1}.$$

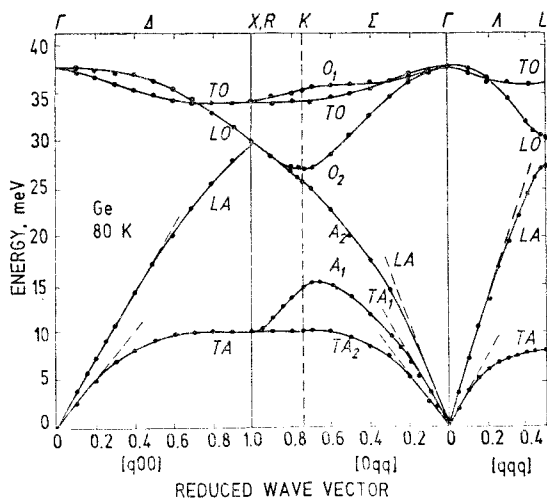


Fig. 1.1. Phonon dispersion curves for Ge in the main crystallographic directions at 80 K [1.19]. The dashed lines show the slopes for sound velocity in various directions.

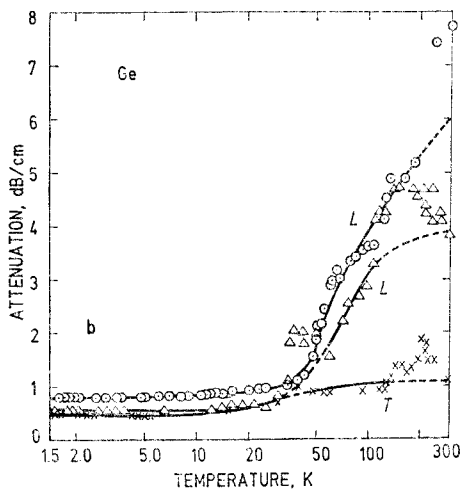
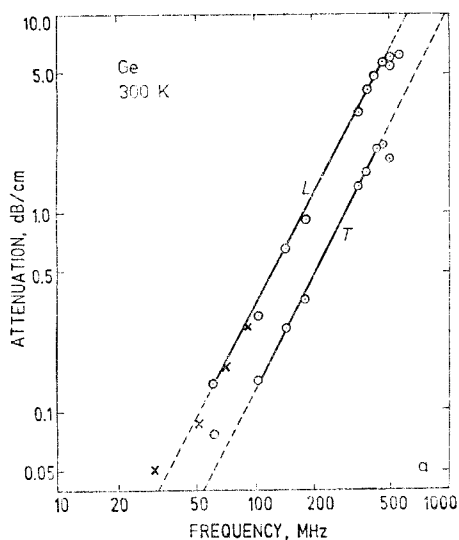


Fig. 1.2. Ultrasound attenuation. *a* – Frequency dependence of ultrasound attenuation coefficient for longitudinal, *L*, and transverse, *T*, ultrasound waves propagating in Ge lattice in [100] direction at room temperature. *b* – Dependence of attenuation of ultrasound waves propagating along [100] direction on the lattice temperature of Ge at fixed frequencies: *L*-wave at 508 MHz (circles), *L*-wave at 340 MHz (triangles), *T*-wave at 333 MHz (crosses) [1.20].

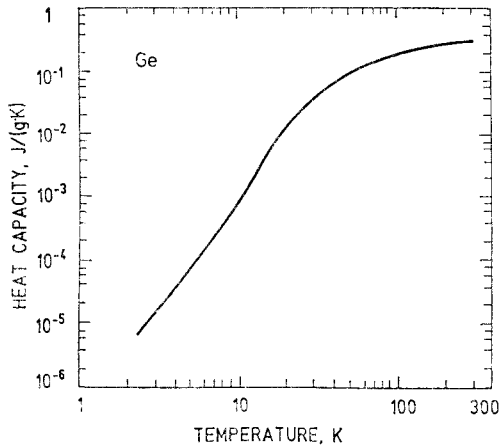


Fig. 1.3. Heat capacity  $C_p$  of pure Ge as a function of temperature [1.21].

Selected values:

$$C_p = 4 \cdot 10^{-5} \text{ J/(g} \cdot \text{K)} \text{ at } 4.2 \text{ K,}$$

$$0.147 \text{ J/(g} \cdot \text{K)} \text{ at } 77.4 \text{ K,}$$

$$0.322 \text{ J/(g} \cdot \text{K)} \text{ at } 295 \text{ K.}$$

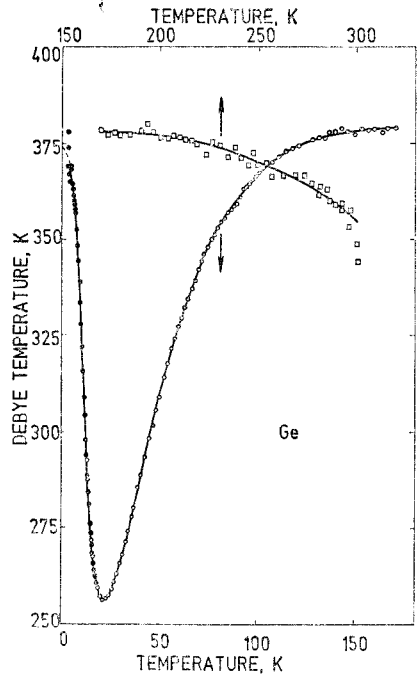


Fig. 1.4. Ge Debye temperature vs. lattice temperature [1.21].

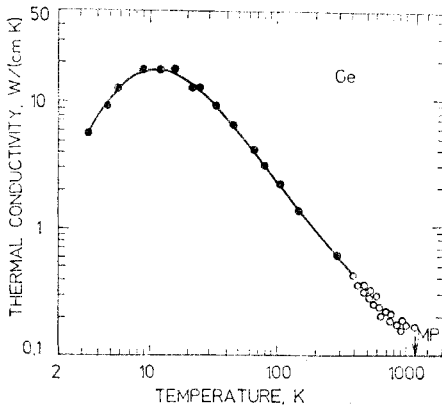


Fig. 1.5. Thermal conductivity  $\chi$  of Ge. MP indicates the melting point [1.22].

Selected values:

$$\chi = 15 \text{ W/(cm} \cdot \text{K)} \text{ at } 20 \text{ K,}$$

$$3.25 \text{ W/(cm} \cdot \text{K)} \text{ at } 77.4 \text{ K,}$$

$$0.60 \text{ W/(cm} \cdot \text{K)} \text{ at } 300 \text{ K.}$$

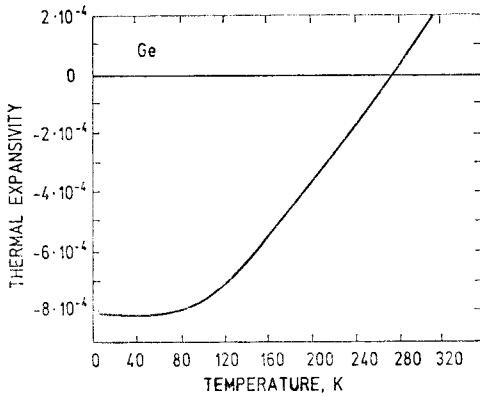


Fig. 1.6. Thermal expansivity,  $(l_T - l_{273.2})/l_{273.2}$ , as a function of the lattice temperature for Ge [1.23].  $l_{273.2}$  is a length at  $T = 273.2$  K.

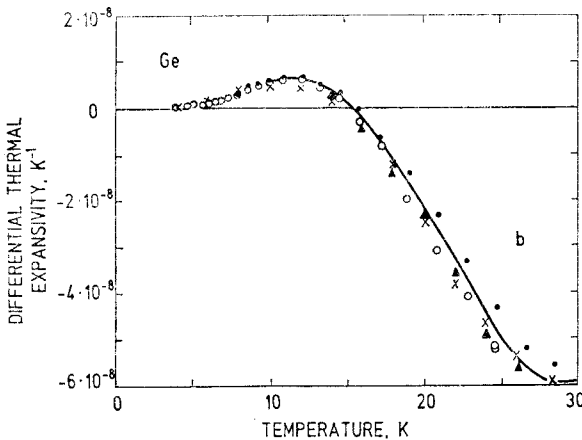
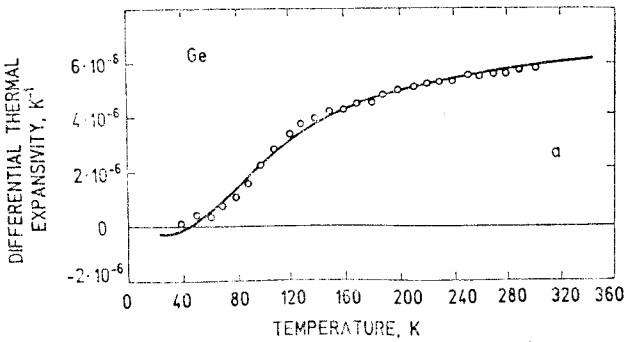


Fig. 1.7. Differential thermal expansivity,  $\alpha = (1/l_{273.2}) (dl/dT)$ , as a function of temperature for Ge. a - [1.23, 1.23a], b - [1.24].

Selected values:

- $\alpha = 5 \cdot 10^{-10} K^{-1}$  at 4 K [1.24],
- $1.3 \cdot 10^{-6} K^{-1}$  at 77.4 K [1.25],
- $5.9 \cdot 10^{-6} K^{-1}$  at 300 K [1.26].



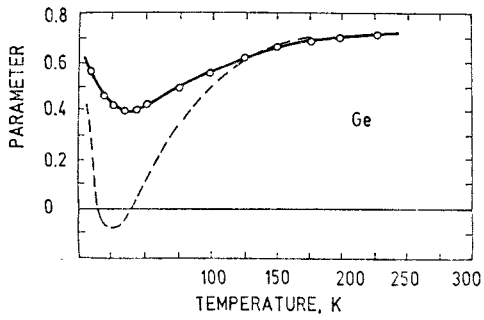


Fig. 1.8. Averaged Grüneisen parameter for Ge as a function of the lattice temperature. Solid line: from third-order elastic constants. Dashed line: from thermal expansion [1.27].

## 1.2. Ge band properties

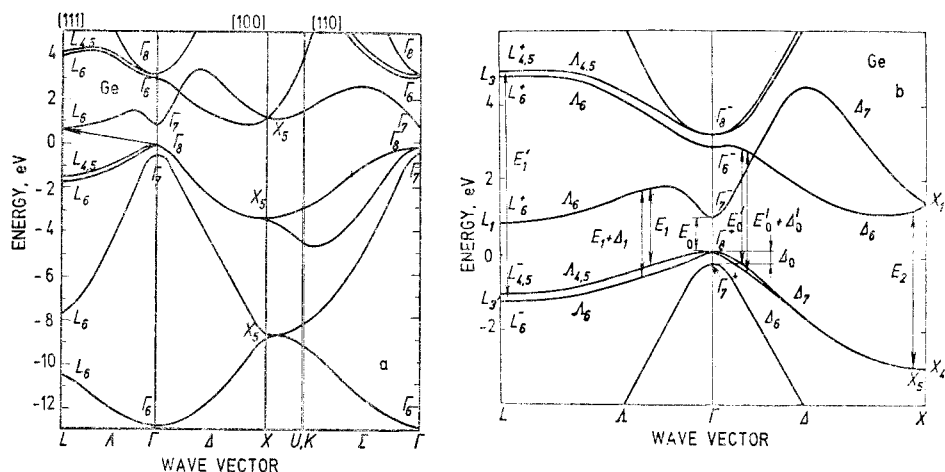


Fig. 1.9. Band structure for Ge with spin-orbit interaction included. *a* — General view [1.28]. The bands are at least doubly spin degenerate at any point of the Brillouin zone. Indirect gap between points  $\Gamma_{8v}^+$  and  $L_{6c}^+$  is shown by an arrow. *b* — Enlarged portion with main interband optical transitions indicated by vertical arrows [1.29].

**TABLE 1.4** Critical points associated with band-band transitions in Ge which are important in optical measurements (see also Fig. 1.9, *b*)

Critical point	Corresponding band-band transition with spin-orbit interaction		k-space location (units of $2\pi/a$ )
	included	neglected	
$E_0$	$\Gamma_{8v}^+ \rightarrow \Gamma_{7c}^-$		
$E_0 + \Delta$	$\Gamma_{7v}^+ \rightarrow \Gamma_{7c}^-$	$\Gamma_{25v}^+ \rightarrow \Gamma_{2c}^-$	(0, 0, 0)
$E'_0$	$\Gamma_{8v}^+ \rightarrow \Gamma_{6c}^-$		Large volume centered on (0.33, 0.24, 0.14)
$E'_0 + \Delta'_0$	$\Gamma_{8v}^+ \rightarrow \Gamma_{6c}^-$	$\Gamma_{25v}^+ \rightarrow \Gamma_{15c}^-$	
$E_1$	$(\Lambda_4, \Lambda_5) \rightarrow \Lambda_{8c}$		Wide region centered on (0.25, 0.25, 0.25)
$E_1 + \Delta_1$	$\Lambda_{6v} \rightarrow \Lambda_{8c}$	$\Lambda_3^+ \rightarrow \Lambda_1^c$	
$E'_1$	$(L_4^-, L_5^-)_v \rightarrow (L_4^+, L_5^+)_c$ and $L_{6v}^- \rightarrow L_{6c}^+$	$L_3^+ \rightarrow L_3^c$	Near <i>L</i> -face, centered on <i>L</i>
$E_2$	$X_{5v} \rightarrow X_{5c}$		Small region near
$E_2 + \Delta_2$	$X_{5v} \rightarrow X_{5c}$	$X_4^+ \rightarrow X_1^c$	(0.77, 0.29, 0.16)

**TABLE 1.5** Energetic distances between important critical points in the energy band of Ge at room temperature and respective hydrostatic pressure coefficients. For transition and critical point nomenclature see Fig. 1.9,b and Table 1.4

Energy separation and pressure coefficient	Value	Comment	Reference
$E_g = E(L_{6c}^+) - E(\Gamma_{8v}^+)$ , eV	0.665	Indirect forbidden energy gap	[1.30]
$E_{LT} = E(\Gamma_{7c}^-) - E(L_{6c}^+)$ , eV	0.14	$E_{LT} = E_0 - E_g$	[1.31]
$E_{LX} = E(\Delta_{8c}) - E(L_{6c}^+)$ , eV	0.186		[1.32]
$\Delta_0 = E(\Gamma_{8v}^+) - E(\Gamma_{7v}^+)$ , eV	0.289	Spin-orbit splitting of the valence band at $\mathbf{k}=0$	[1.33]
$E_0 = E(\Gamma_{7c}^-) - E(\Gamma_{8v}^+)$ , eV	0.798		[1.34]
$E_1$ , eV	2.11		[1.35]
$E_2$ , eV	4.37		[1.35]
$\Delta_1$ , eV	0.187		[1.35]
$dE_g/dp$ , eV/GPa	0.05	The plus sign indicates that the gap increases with hydrostatic pressure	[1.36, 1.37]
$dE_0/dp$ , eV/GPa	0.121		[1.33]
$dE_{LT}/dp$ , eV/GPa	0.07	$dE_{LT}/dp = dE_0/dp - dE_g/dp$	
$dE_X/dp$ , eV/GPa	-0.013	X valley relative to valence band edge	[1.37]
$dE_{LX}/dp$ , eV/GPa	-0.062		[1.37]
$dE_1/dp$ , eV/GPa	0.075		[1.38]
$dE_2/dp$ , eV/GPa	0.056		[1.38]

TABLE 1.6 Ge conduction band principal valley parameters

Parameter	$L$ valley*	$\Gamma$ valley	$X$ valley	Reference
Valley location in the Brillouin zone	$L_{6c}^+$ on the boundary of the zone in $\langle 111 \rangle$ direction	$\Gamma_{7c}^-$ in the center of the zone	$\Delta_{6c}$ in $\langle 100 \rangle$ direction	
Number of valleys	4	1	6	
Valley separation relative to $L$ valley, eV	0	0.14	0.186	[1.31, 1.32]
Electron masses:				
scalar $m_n/m_0$		0.038		[1.39]
longitudinal $m_l/m_0$	1.57		1.35	[1.40, 1.41]
transverse $m_t/m_0$	0.0807		0.29	[1.40, 1.41]
conductivity $m_c/m_0$	0.118	0.038	0.39	
density-of-states $m_d/m_0$	0.217	0.038	0.48	
Uniaxial deformation potential $\Xi_u$ , eV	16.4		10.4	[1.42, 1.43]
$g_c$ -factor		$-3.0 \pm 0.2$		[1.39]

\* — It is the most important valley in the transport property analysis.

**TABLE 1.7** Ge valence band parameters

Parameter	Value	Reference
<b>Light and heavy mass bands at <math>\Gamma_{8v}^+</math></b>		
Luttinger parameters:		
$\gamma_1$	$13.38 \pm 0.02$	[1.44]
$\gamma_2$	$4.24 \pm 0.03$	[1.44]
$\gamma_3$	$5.69 \pm 0.02$	[1.44]
Spherical part of $g_v$ -factor $2k$	$7.2 \pm 0.08$	[11]
Valence band nonsphericity $\delta$	0.108	
Average heavy hole mass for "spherical" bands $m_h/m_0$	0.316	
Average light hole mass for "spherical" bands $m_l/m_0$	0.0424	
Density-of-states mass $m_d/m_0$	0.326	
Light hole band nonparabolicity $\alpha$ , $\text{eV}^{-1}$	7	[1.45]
Uniaxial deformation potentials, eV		
$D_u$	$3.32 \pm 0.20$	[1.44]
$D'_u$	$3.81 \pm 0.25$	[1.44]
<b>Spin-orbit split-off valence band at <math>\Gamma_{7v}^+</math></b>		
$\Delta_0 = E(\Gamma_{8v}^+) - E(\Gamma_{7v}^+)$ , eV	0.289	[1.33]
Mass $m_{so}/m_0$	0.095	[1.39]
$g_{so}$ -factor	$-10 \pm 3$	[1.39]

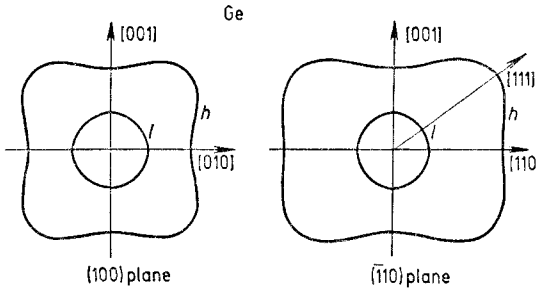


Fig. 1.10. Ge valence band warping. The contours are the constant energy surfaces of heavy (*h*) and light (*l*) mass bands in (100) and ( $\bar{1}10$ ) planes. The nonparabolicity is not included (cf. Fig. 2).

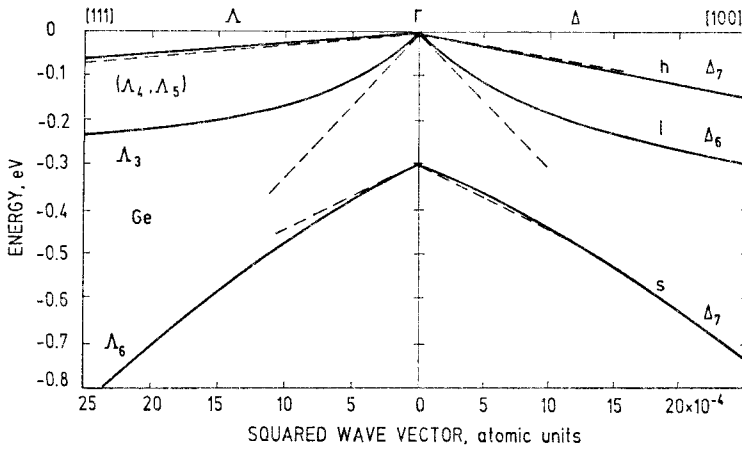


Fig. 1.11. Ge valence band nonparabolicity. Energies of holes in heavy (*h*), light (*l*) and split-off (*s*) valence bands are plotted as functions of squared wave vector. The dashed lines show parabolic bands. The wave vector range covered here is equivalent to about one tenth of the Brillouin zone radius [1.46].

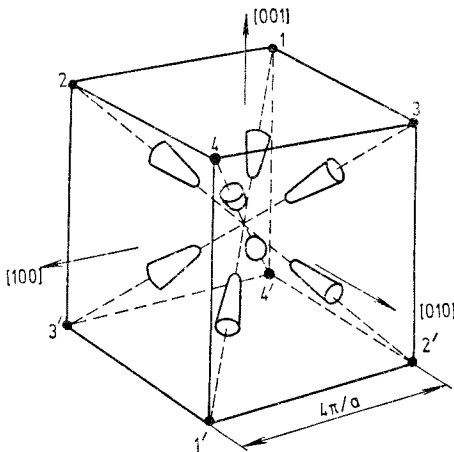


Fig. 1.12. Location of the lowest energies in the conduction band indicated by dots and constant energy surfaces (spheroids) in Ge. The dots are on the Brillouin zone boundaries at points  $L_0^+$ , therefore, two halves of the spheroids situated on the opposite ends of the diagonals, for example 1 and 1', make up a single constant energy ellipsoid.

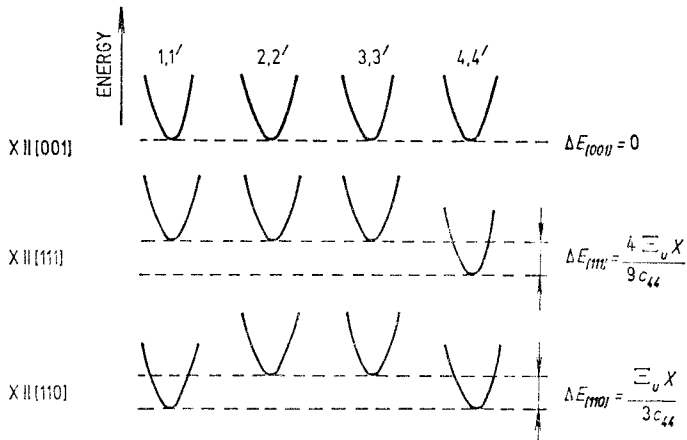


Fig. 1.13.  $L$  valley splitting under uniaxial compressive stress  $X$  (cf. Fig. 1.12). The stress removes fourfold degeneracy and, as a result, the energy difference  $\Delta E$  appears between different groups of valleys in the  $L_6^+$  point of the Brillouin zone.  $\Xi_u$  is the uniaxial deformation potential.  $\Xi_u = 16.4$  eV for  $n$ -Ge [1.42].

**TABLE 1.8** Valence band splitting under uniaxial stress  $X$ . The stress removes valence band degeneracy at the point  $\Gamma_{8v}^+$ , as a result the energy gap  $\Delta E$  appears in the vicinity of the wave vector  $\mathbf{k} = 0$  [1.44]

Direction of the uniaxial stress	Splitting $\Delta E$
[001]	$\Delta E_{[001]} = \frac{4}{3} \left  \frac{D_u X}{c_{11} - c_{12}} \right $
[111]	$\Delta E_{[111]} = \frac{2}{3} \left  \frac{D'_u X}{c_{44}} \right $
[110]	$\Delta E_{[110]} = \frac{1}{2} (\Delta E_{[001]}^2 + 3\Delta E_{[111]}^2)^{1/2}$

The valence band uniaxial deformation potential and elastic constant values can be found in Tables 1.1 and 1.7.

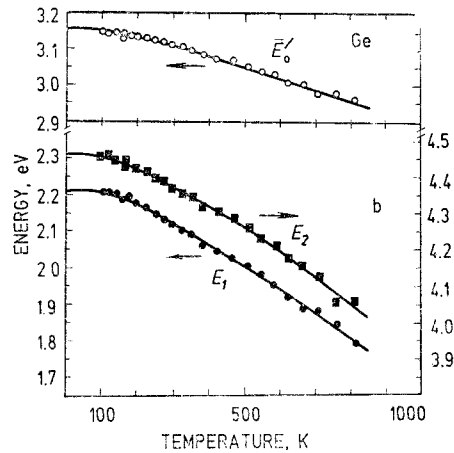
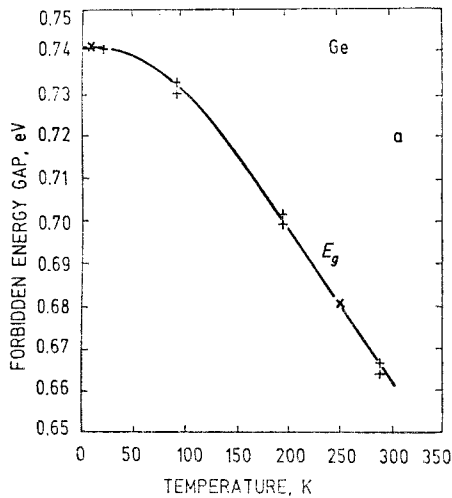


Fig. 1.14. Temperature dependence of *a* – forbidden energy gap  $E_g$  [1.30] and *b* – interband critical-point energies  $E_1$ ,  $E_2$ ,  $\bar{E}'_0$  [1.35] in Ge (see Fig. 1.9, *b* for the corresponding transitions). The solid lines are the best fits with the empirical formulas and parameter values listed in Table 1.9.

**TABLE 1.9** Values of the parameters *a*, *b* and  $\Theta$  in equation  $E(T) = a - b [1 + 2/(e^{\Theta/T} - 1)]$  obtained by fitting the critical point energies vs. absolute temperature *T* by solid lines in Fig. 1.14.  $\bar{E}'_0$  is average of  $E'_0$  and  $E'_0 + \Delta'_0$

Critical point	<i>a</i> , eV	<i>b</i> , eV	$\Theta$ , K
$E_1$	2.33	0.12	360
$\bar{E}'_0$	3.23	0.08	484
$E_2$	4.63	0.17	499

Dependence of the indirect energy gap on the absolute temperature can be fitted with the equation [1.47]:

$$E_g [\text{eV}] = 0.744 - 4.7 \cdot 10^{-4} T^2 / (235 + T).$$



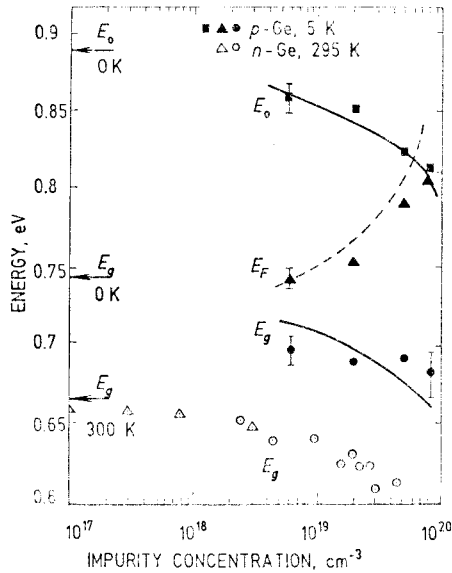


Fig. 1.15. Forbidden energy gap  $E_g$ , Fermi energy relative to the valence band edge  $E_F$  and critical transition energy  $E_0$  as functions of impurity concentration (cf. Table 1.5). Arrows on the energy scale indicate  $E_g$  and  $E_0$  of pure Ge at  $T=0$  and  $T=300$  K. Lines are theoretical calculations. Lattice temperature:  $T=5$  K for p-Ge (full squares, triangles and circles) [1.48] and  $T=295$  K for n-Ge (open triangles and circles) [1.49, 1.50].

### 1.3. Ge optical properties

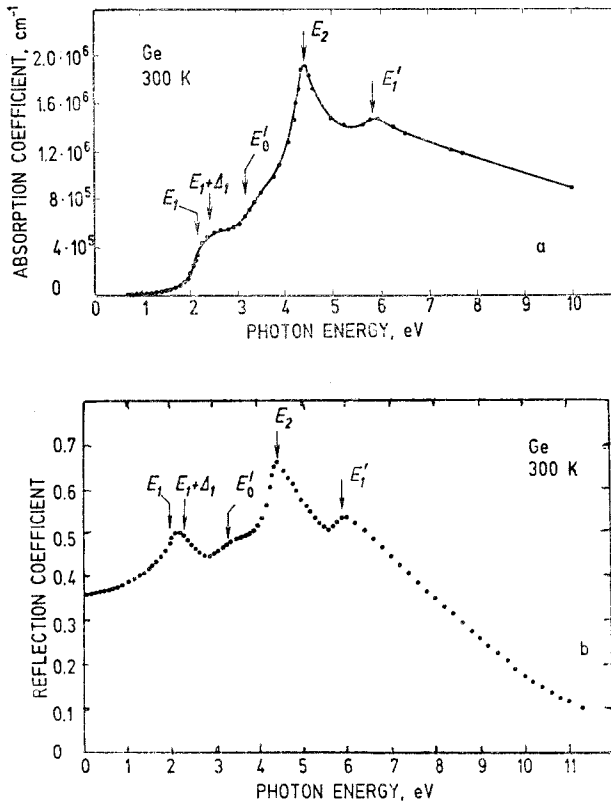


Fig. 1.16. Dependence of absorption (a) and reflection (b) coefficients of Ge on photon energy,  $T=300 \text{ K}$  [1.51].

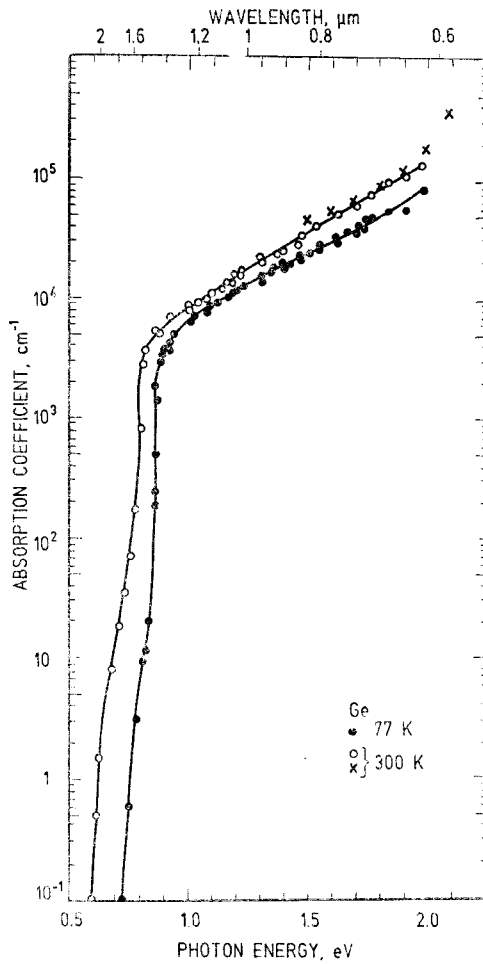


Fig. 1.17. Optical absorption coefficient of Ge at nitrogen and room temperatures. Open and full circles — [1.52], crosses — [1.53].

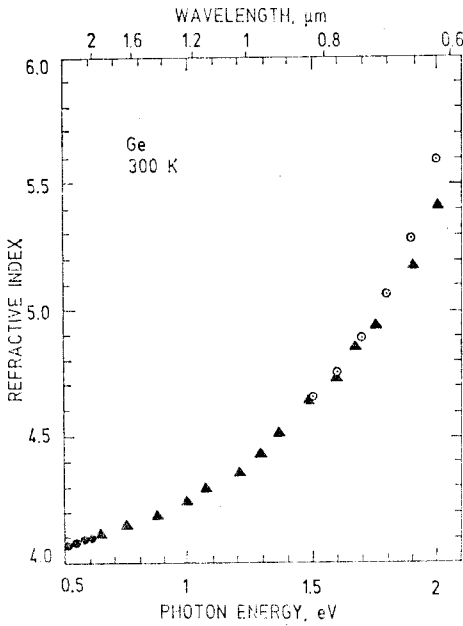


Fig. 1.18. Refractive index of Ge. Open circles — [1.53], full circles — [1.54], triangles — [1.51].

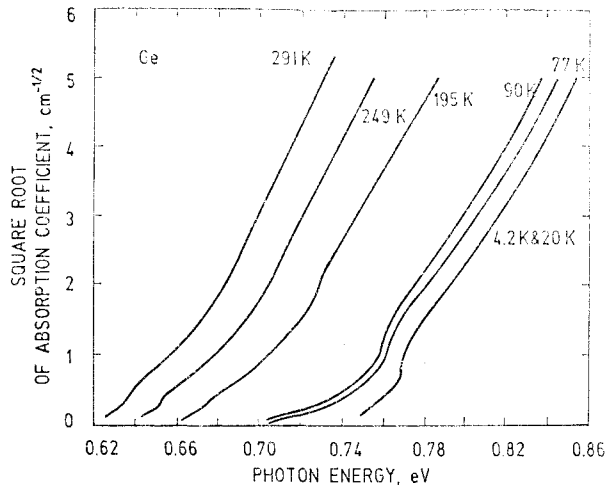


Fig. 1.19. Optical low-intensity absorption spectrum of high purity Ge near band gap energy at various temperatures [1.30].

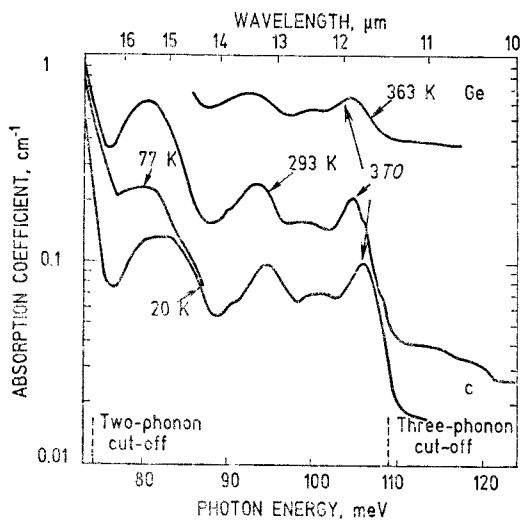
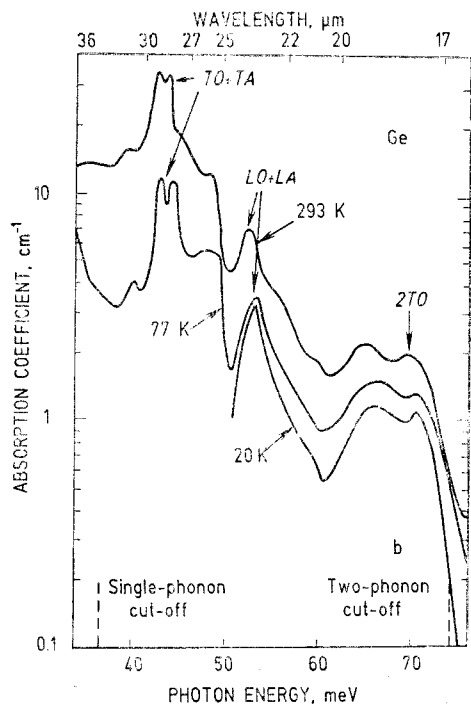
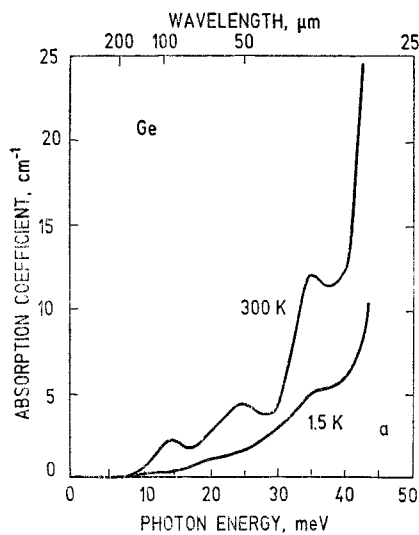


Fig. 1.20. Lattice optical absorption coefficient of Ge at different temperatures: *a* — [1.55], *b* and *c* — [1.56]. For phonon assignment see Table 1.2.

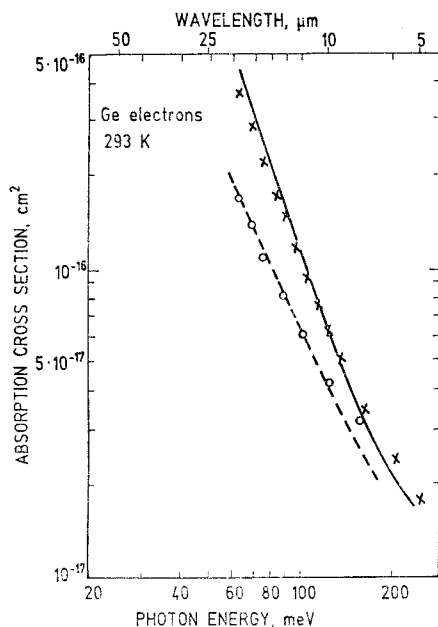


Fig. 1.21. Free electron absorption cross section vs. photon energy in *n*-Ge. Electron concentration: crosses —  $n = 1.59 \cdot 10^{18} \text{ cm}^{-3}$ , circles —  $n = 4.7 \cdot 10^{16} \text{ cm}^{-3}$ .  $T = 293 \text{ K}$  [1.57].

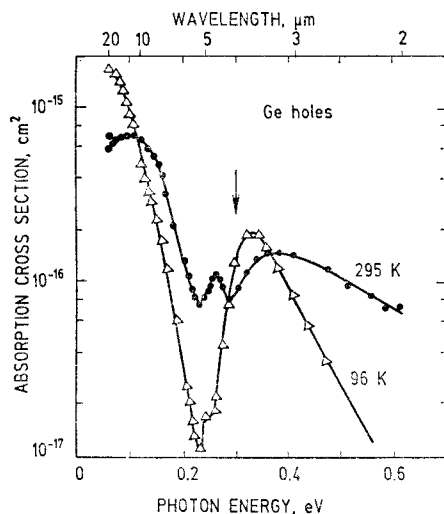


Fig. 1.22. Absorption cross section for free holes in *p*-Ge vs. photon energy at the lattice temperature 295 K (circles) and 96 K (triangles). The arrow indicates the onset of transitions to split-off valence band. The lattice absorption at long wavelengths (energies less than 0.1 eV) has been subtracted from the experimental absorption data [1.58].

**TABLE 1.10** Properties of free excitons and excitons bound to impurities in Ge as observed in luminescence experiments (see also Fig. 1.23)

Particle	Dissociation channel	Particle lifetime, $\mu\text{s}$	Luminescence energy, meV	Comments, reference
----------	----------------------	----------------------------------	--------------------------	---------------------

**Free exciton,  $X$**

$X_{LA}$	$h\nu + LA$		712.73 $\pm 0.04$	5.1 K, intense line [1.59]
$X_{TO}$	$h\nu + TO$		704.75	4.3 K, $N_D - N_A \approx 10^{16} \text{ cm}^{-3}$ [1.60]

**Exciton bound to donor,  $[DX]$**

$[\text{As}X]$	$\text{As} + h\nu$		739.08 $\pm 0.03$	5K, $N_{\text{As}} = 4 \cdot 10^{14} \text{ cm}^{-3}$ [1.61]
$[\text{As}X]$	$\text{As} + h\nu$	$\sim 30$		2K, $N_{\text{As}} = 2 \cdot 10^{16} \text{ cm}^{-3}$ , decay is nonexponential [1.62]

TABLE 1.10 (Continued)

Particle	Dissociation channel	Particle lifetime, $\mu\text{s}$	Luminescence energy, meV	Comments, reference
$[\text{As} X]_{TA}$	$\text{As} + h\nu + TA$	12	731.25	4.2 K [1.63]
$[\text{As} X]_{LA}$	$\text{As} + h\nu + LA$		711.3	4.2 K [1.63]
$[\text{As} X]_{LA}$	$\text{As} + h\nu + LA$			4.2 K, $N_{\text{As}} = 2 \cdot 10^{16} \text{ cm}^{-3}$ [1.62]
$[\text{As} X]_{TO}$	$\text{As} + h\nu + TO$		703.1	4.2 K, $N_{\text{As}} = (5-8) \cdot 10^{15} \text{ cm}^{-3}$ [1.64]
$[\text{P} X]$	$\text{P} + h\nu$	28	739.22 $\pm 0.02$	5 K, $N_{\text{P}} = 10^{15} \text{ cm}^{-3}$ [1.61]
$[\text{P} X]_{TA}$	$\text{P} + h\nu + TA$		731.4	4.2 K [1.63]
$[\text{P} X]_{LA}$	$\text{P} + h\nu + LA$		711.6	4.2 K [1.63]
$[\text{P} X]_{TO}$	$\text{P} + h\nu + TO$		703.2	4.2 K, $N_{\text{P}} = 8 \cdot 10^{15} \text{ cm}^{-3}$ [1.64]
$[\text{Sb} X]$	$\text{Sb} + h\nu$	28	739.5	Unobserved [1.64]
$[\text{Sb} X]_{LA}$	$\text{Sb} + h\nu + LA$		711.9	4.2 K, $N_{\text{Sb}} = 7 \cdot 10^{14} \text{ cm}^{-3}$ [1.64]
$[\text{Sb} X]_{LA}$	$\text{Sb} + h\nu + LA$			4.2 K, $N_{\text{Sb}} = 8 \cdot 10^{16} \text{ cm}^{-3}$ [1.62]
$[\text{Sb} X]_{TO}$	$\text{Sb} + h\nu + TO$		703.5	4.2 K, $N_{\text{Sb}} = 7 \cdot 10^{14} \text{ cm}^{-3}$ [1.64]
$[\text{Bi} X]$	$\text{Bi} + h\nu$		739.2	Unobserved [1.63]
$[\text{Bi} X]_{TA}$	$\text{Bi} + h\nu + TA$		731.5	4.2 K [1.63]
$[\text{Bi} X]_{LA}$	$\text{Bi} + h\nu + LA$		711.6	4.2 K [1.63]
$[\text{Li} X]$	$\text{Li} + h\nu$		739.45	4.2 K [1.63]
$[\text{Li} X]_{TA}$	$\text{Li} + h\nu + TA$		731.65	4.2 K [1.63]
$[\text{Li} X]_{LA}$	$\text{Li} + h\nu + LA$		711.75	4.2 K [1.63]

Exciton bound to acceptor,  $[AX]$ 

$[\text{Ga} X]$	$\text{Ga} + h\nu$		739.4	Unobserved [1.64]
$[\text{Ga} X]_{LA}$	$\text{Ga} + h\nu + LA$	20; 59	711.8	4.2 K, $N_{\text{Ga}} = 5 \cdot 10^{15} \text{ cm}^{-3}$ [1.64]
$[\text{Ga} X]_{LA}$	$\text{Ga} + h\nu + LA$			4.2 K, $N_{\text{Ga}} = 4 \cdot 10^{16} \text{ cm}^{-3}$ , decay is two-exponential [1.62]
$[\text{Ga} X]_{TO}$	$\text{Ga} + h\nu + TO$		703.4	4.2 K, $N_{\text{Ga}} = 5 \cdot 10^{15} \text{ cm}^{-3}$ [1.64]
$[\text{In} X]$	$\text{In} + h\nu$		739.3	Unobserved [1.64]
$[\text{In} X]_{LA}$	$\text{In} + h\nu + LA$		711.7	4.2 K, $N_{\text{In}} = 3 \cdot 10^{15} \text{ cm}^{-3}$ [1.64]
$[\text{In} X]_{TO}$	$\text{In} + h\nu + TO$		703.3	4.2 K, $N_{\text{In}} = 3 \cdot 10^{15} \text{ cm}^{-3}$ [1.64]

$LA$ ,  $TA$  and  $TO$  is longitudinal acoustic, transverse acoustic and transverse optic phonon energy, respectively.

Excitonic energy gap:  $E_{gX} = 740.46 \pm 0.03 \text{ meV}$  at  $T \lesssim 5 \text{ K}$  [1.59].

Exciton binding energy:  $E_X = 4.2 \text{ meV}$  [1.59a].

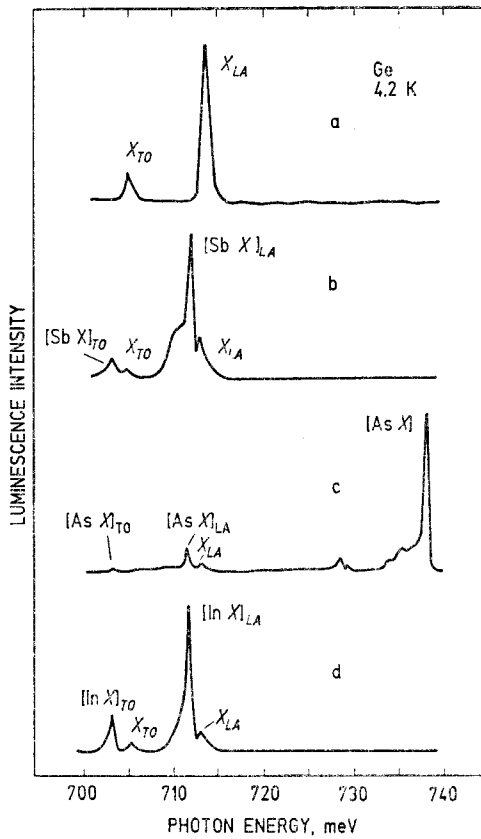


Fig. 1.23. Luminescence spectra of pure (a), Sb-doped (b), As-doped (c), In-doped (d) Ge crystals showing free and bound exciton recombination lines [1.64]. Impurity concentration: (a)  $N_A + N_D < 10^{13} \text{ cm}^{-3}$ , (b)  $N_{\text{Sb}} = (5-8) \cdot 10^{15} \text{ cm}^{-3}$ , (c)  $N_{\text{As}} = (5-8) \cdot 10^{15} \text{ cm}^{-3}$ , (d)  $N_{\text{In}} = 3 \cdot 10^{15} \text{ cm}^{-3}$ .

**Relative change of the refractive index with the hydrostatic pressure  $p$  [1.65]:**

$$(1/n)(dn/dp) = -0.0144 \text{ 1/GPa}$$

$$n = 4.006$$

at  $10.6 \text{ } \mu\text{m}$  and  $300 \text{ K}$ ,

$$(1/n)(dn/dp) = -0.0143 \text{ 1/GPa}$$

$$n = 4.037$$

at  $3.39 \text{ } \mu\text{m}$  and  $300 \text{ K}$ .

Temperature dependence of the refractive index in the wavelength range from  $2$  to  $20 \text{ } \mu\text{m}$  at room temperature [1.18]:

$$(1/n)(dn/dT) = 9.5 \cdot 10^{-5} \text{ K}^{-1}.$$



**TABLE 1.11** Elastooptic and piezooptic coefficients of Ge at lattice temperature  $T=300$  K and at two laser wavelengths [1.65]

Coefficient	3.39 $\mu\text{m}$	10.6 $\mu\text{m}$
Elastooptic, dimensionless		
$p_{11}$	-0.151	-0.154
$p_{12}$	-0.128	-0.126
$p_{44}$	-0.072	-0.073
Piezooptic, 1/GPa		
$\pi_{11}$	$-7.9 \cdot 10^{-4}$	$-8.4 \cdot 10^{-4}$
$\pi_{12}$	$-5.1 \cdot 10^{-4}$	$-4.8 \cdot 10^{-4}$
$\pi_{44}$	$-1.07 \cdot 10^{-3}$	$-1.09 \cdot 10^{-3}$

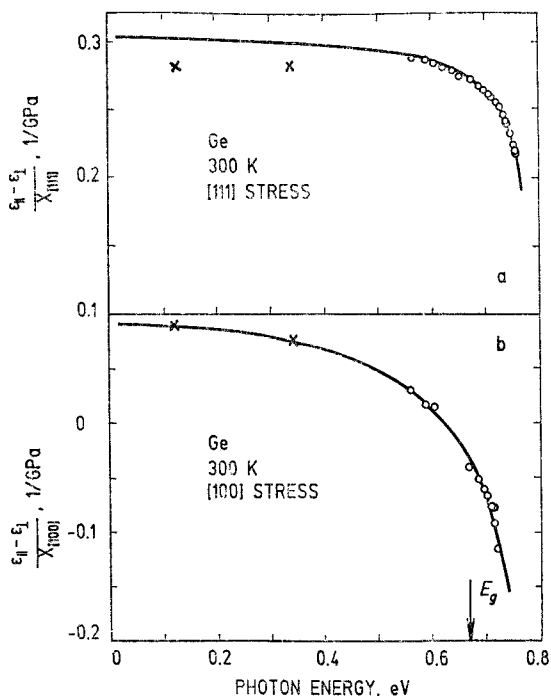


Fig. 1.24. Piezooptic effect. Measured values of  $(\epsilon_{\parallel} - \epsilon_{\perp})/X_{[111]} = -n^4 \pi_{44}$  and  $(\epsilon_{\parallel} - \epsilon_{\perp})/X_{[100]} = -n^4(\pi_{11} - \pi_{12})$  for Ge as a function of photon energy, where  $\epsilon_{\parallel}$  and  $\epsilon_{\perp}$  are relative dielectric permittivities for light polarized parallel and perpendicular to the uniaxial stress  $X$  applied in [111] and [100] directions.  $n$  is the refractive index and  $\pi_{ij}$  are the piezooptic coefficients.  $T=300$  K. Crosses - [1.65], circles - [1.66]. Solid lines are theoretical calculations.

**Electrooptic coefficients.** All linear electrooptic coefficients (Pockels coefficients) of Ge are equal to zero:  $r_{ijk}=0$ .

**Nonlinear susceptibility.** Ge is centrosymmetric, and the second-order nonlinear susceptibilities are equal to zero:  $d_{ijk}=0$ .

Valence electron contribution to the third-order nonlinear susceptibility  $c_{ijkl}(\omega_2-2\omega_1, \omega_1, \omega_1, -\omega_2)$  of Ge measured by mixing  $\lambda_1=10.6 \mu\text{m}$  and  $\lambda_2=9.5 \mu\text{m}$  radiation [1.67]:

$$|c_{1111}| = 1.4 \cdot 10^{-18} \text{ m}^2/\text{V}^2, \text{ 50 \% accuracy,}$$

$$c_{1122}/c_{1111} = 0.61 \pm 0.02.$$

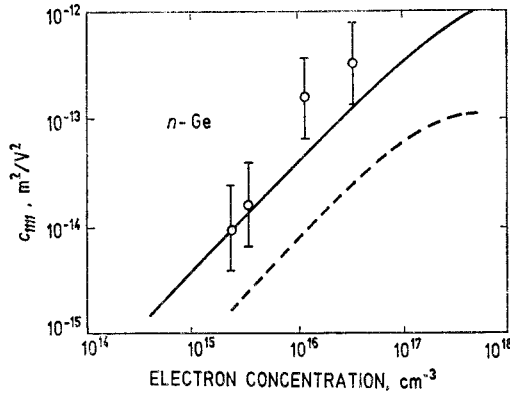


Fig. 1.25. Absolute values of third-order nonlinear susceptibility  $c_{1111}(3\omega, \omega, \omega, \omega)$  measured by frequency tripling of 0.5 mm radiation, vs. free electron concentration, for  $n$ -Ge at room temperature. The anisotropy of susceptibility is  $\sigma=(1+3c_{1122}/c_{1111})/2=1.16 \pm 0.05$ . The curves are theoretical predictions for the nonparabolicity (solid line) and relaxation (dashed line) contributions, respectively [1.68].

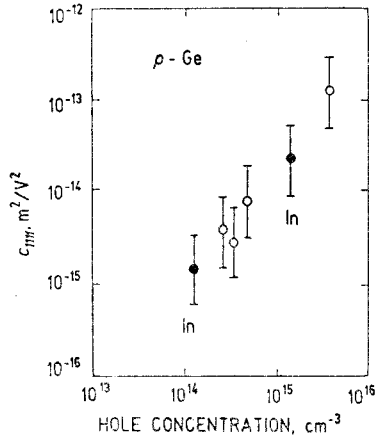


Fig. 1.26. Absolute values of third-order nonlinear susceptibility  $c_{1111}(3\omega, \omega, \omega, \omega)$  measured by frequency tripling of 0.5 mm radiation, vs. free-hole concentration, for  $p$ -Ge at room temperature [1.68].

## 1.4. Ge electrical properties

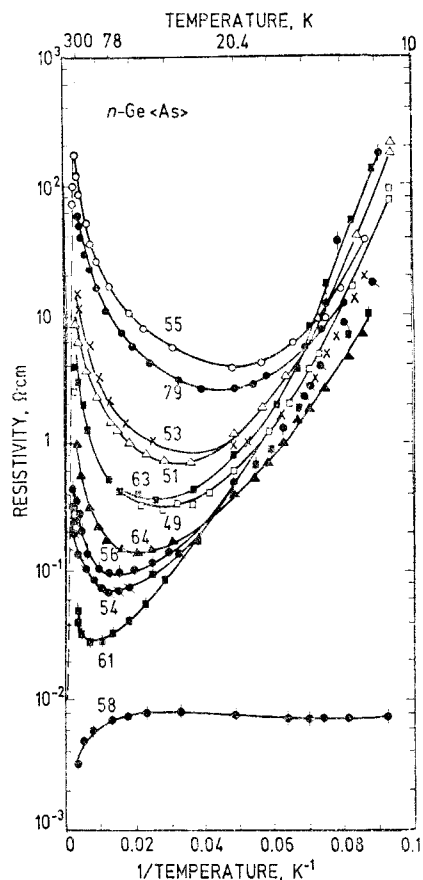


Fig. 1.27. Resistivity of a set of *n*-Ge samples (arsenic doped) as a function of inverse temperature. The intrinsic behaviour is indicated by a dashed line. For parameter values see Table 1.12 [1.69].

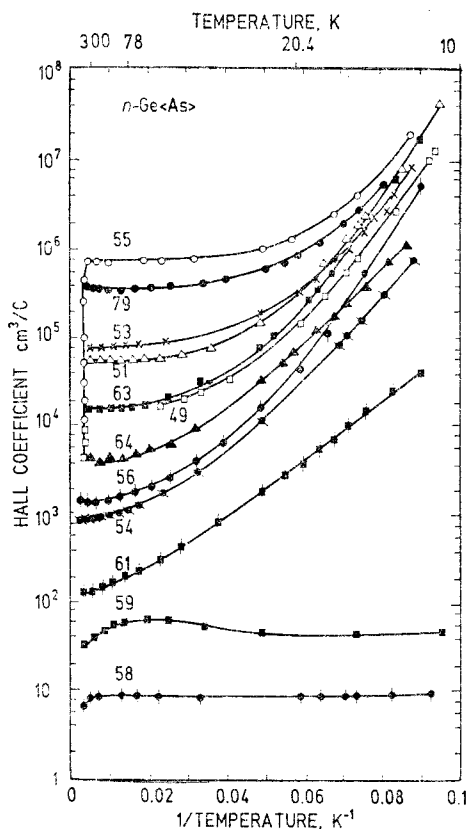


Fig. 1.28. Hall coefficient of a set of *n*-Ge samples (arsenic doped) as a function of inverse temperature. For parameter values see Table 1.12 [1.69].

**TABLE 1.12** Excess donor concentration  $N_D - N_A$  for samples in Figs. 1.27, 1.28 and 1.29

Sample	$N_D - N_A, \text{ cm}^{-3}$	Sample	$N_D - N_A, \text{ cm}^{-3}$
55	$1.0 \cdot 10^{13}$	64	$1.7 \cdot 10^{15}$
53	$9.4 \cdot 10^{13}$	56	$5.1 \cdot 10^{15}$
51	$1.4 \cdot 10^{14}$	54	$7.5 \cdot 10^{15}$
63	$4.6 \cdot 10^{14}$	61	$5.5 \cdot 10^{16}$
49	$4.8 \cdot 10^{14}$		

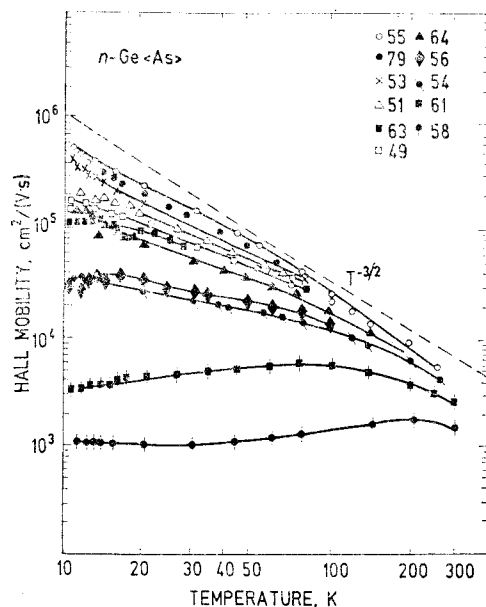


Fig. 1.29. Hall mobility of a set of *n*-Ge samples (arsenic doped) as a function of temperature. For parameter values see Table 1.12 [1.69].

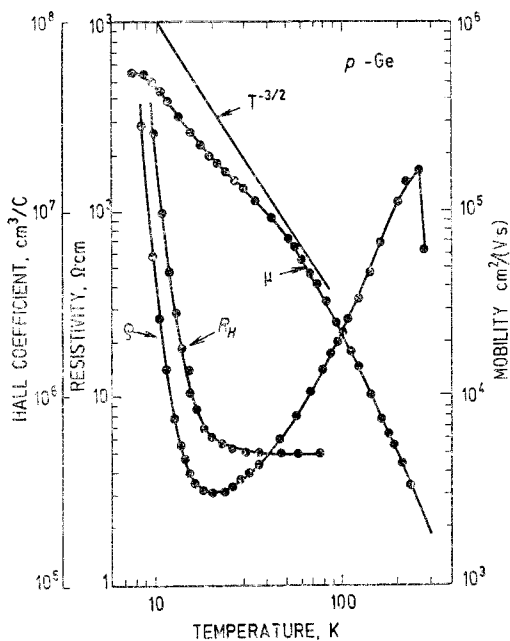
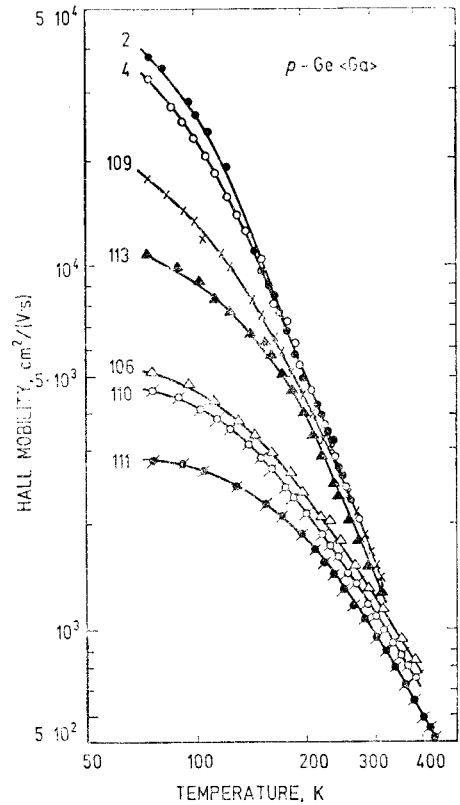


Fig. 1.30. Resistivity, Hall coefficient and mobility of holes in pure Ge as functions of the lattice temperature.  $N_A - N_D = 1.25 \cdot 10^{18} \text{ cm}^{-3}$  [1.70].

**TABLE 1.13** Excess hole concentration at 77 K for samples in Fig. 1.31

Sample	Hole concentration in $\text{cm}^{-3}$
2	$4.9 \cdot 10^{13}$
4	$2.1 \cdot 10^{14}$
109	$3.2 \cdot 10^{15}$
113	$8.7 \cdot 10^{15}$
106	$2.7 \cdot 10^{16}$
110	$3.2 \cdot 10^{16}$
111	$6.4 \cdot 10^{16}$

**Fig. 1.31.** The dependence of hole Hall mobility in *p*-Ge on temperature in the hole concentration range  $p = 4.9 \cdot 10^{13} - 6.4 \cdot 10^{16} \text{ cm}^{-3}$  [1.71]. For parameter values see Table 1.13.**TABLE 1.14** Excess hole concentration at 300 K for samples in Fig. 1.32

Sample	Hole concentration in $\text{cm}^{-3}$	Sample	Hole concentration in $\text{cm}^{-3}$
122	$1.2 \cdot 10^{17}$	100	$1.2 \cdot 10^{19}$
128	$2.8 \cdot 10^{17}$	38	$2.7 \cdot 10^{19}$
127	$6.8 \cdot 10^{17}$	87	$5.8 \cdot 10^{19}$
120	$1.1 \cdot 10^{18}$	77	$1 \cdot 10^{20}$
123	$2.2 \cdot 10^{18}$	71	$2 \cdot 10^{20}$
94	$4.9 \cdot 10^{18}$	7	$4.2 \cdot 10^{20}$
95	$6.9 \cdot 10^{18}$		

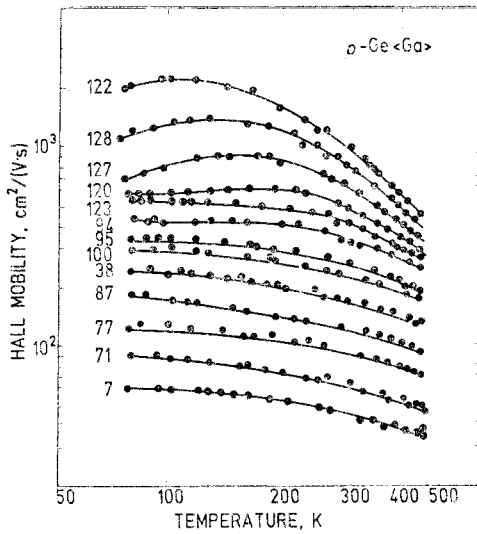


Fig. 1.32. The dependence of hole Hall mobility in  $p$ -Ge on temperature in the hole concentration range  $p=1.2 \cdot 10^{17} - 4.2 \cdot 10^{20} \text{ cm}^{-3}$  [1.71]. For parameter values see Table 1.14.

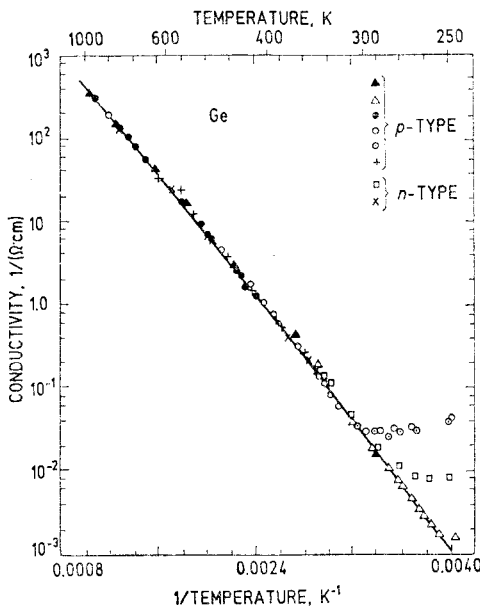


Fig. 1.33. Conductivity of Ge vs. inverse temperature in the intrinsic region [1.72]. At  $T=300 \text{ K}$   $\sigma_i=0.021 \text{ 1}/(\Omega \cdot \text{cm})$ .

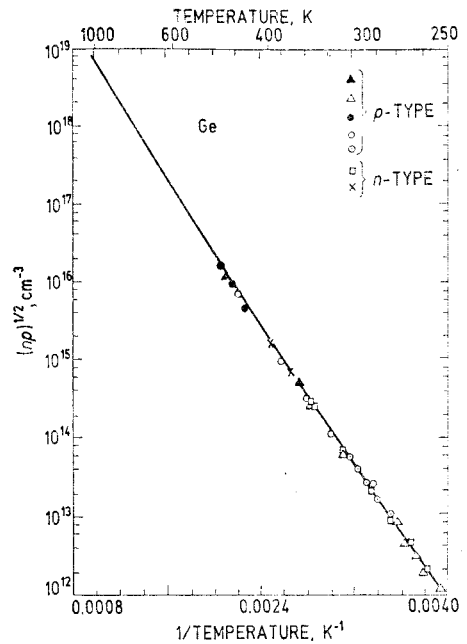


Fig. 1.34. Square root of the product of electron and hole concentration (intrinsic concentration) vs. inverse temperature for Ge in the intrinsic region [1.72]. The best fit to the curve is given by the empirical expression  $n_i = \sqrt{np} = 1.76 \cdot 10^{18} T^{1.5} \cdot \exp(-4555/T)$ ,  $n_i$  is in  $\text{cm}^{-3}$  and  $T$  is in K. At  $300 \text{ K}$   $n_i = 2.3 \cdot 10^{18} \text{ cm}^{-3}$ .

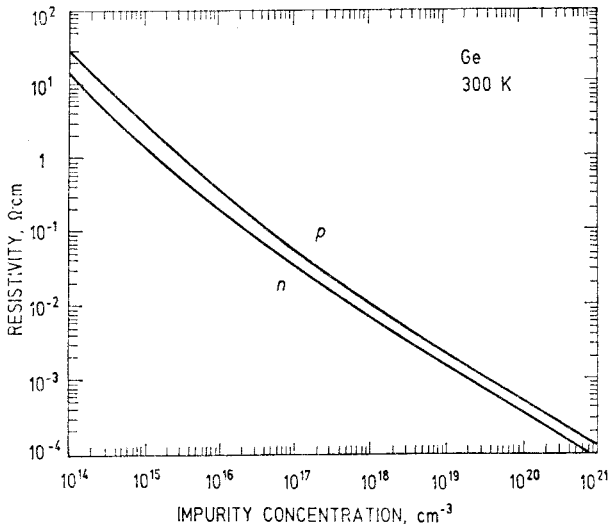


Fig. 1.35. Resistivity vs. shallow impurity concentration [for Ge at the lattice temperature 300 K [1.73].

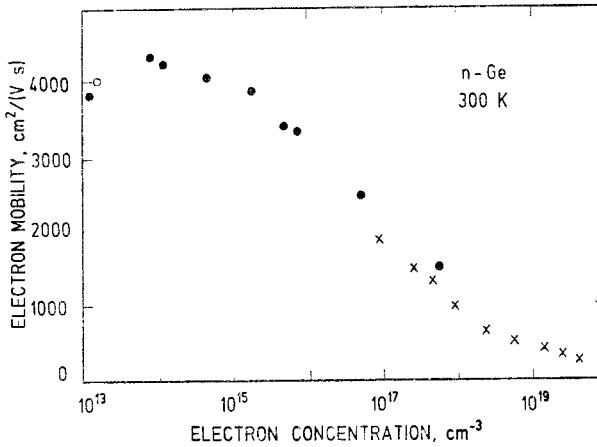


Fig. 1.36. Electron Hall mobility in  $n$ -Ge at 300 K as a function of electron concentration  $n = N_D - N_A$  [1.69, 1.72, 1.74].

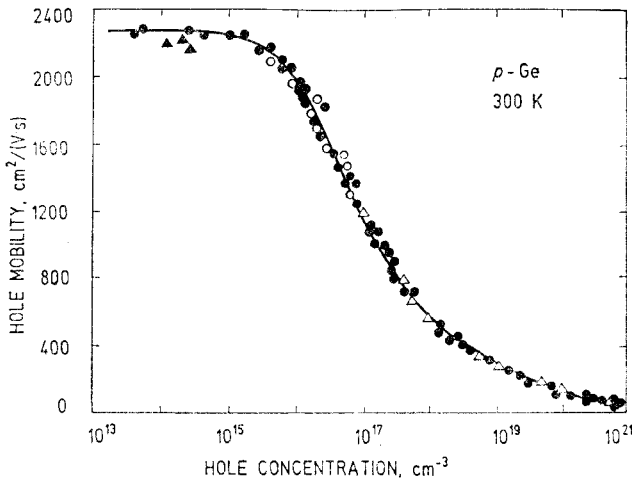


Fig. 1.37. Hole Hall mobility in *p*-Ge at 300 K as a function of hole concentration  $p = N_A - N_D$  [1.71].

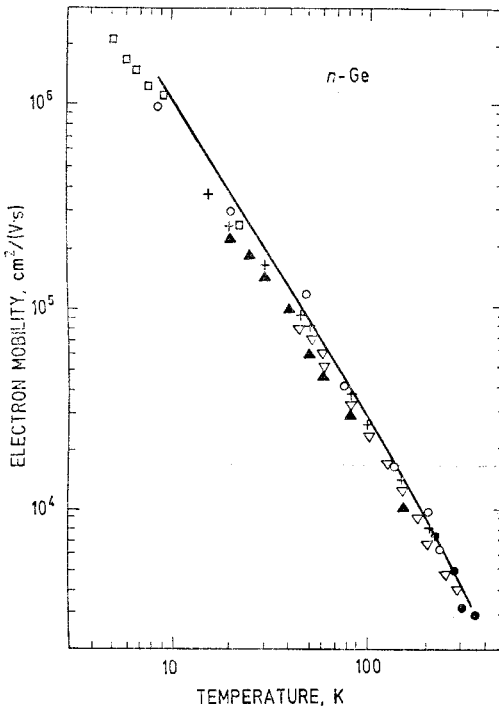


Fig. 1.38. Mobility of electrons in pure Ge as a function of temperature. The solid line indicates theoretical calculations due to lattice scattering [1.75].

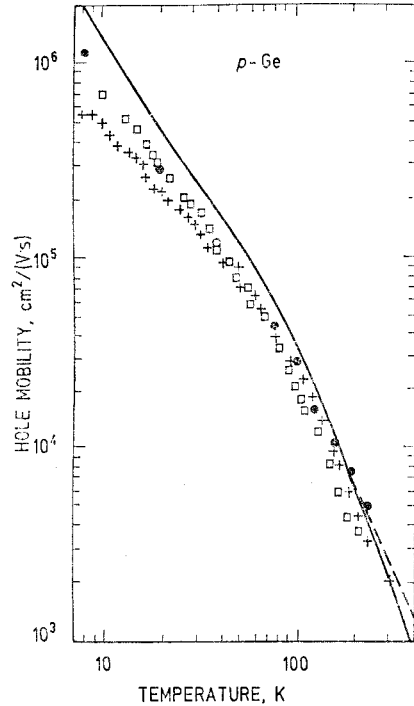


Fig. 1.39. Mobility of holes in pure Ge as a function of temperature. The solid and dashed lines show theoretical calculations due to lattice scattering [1.76].



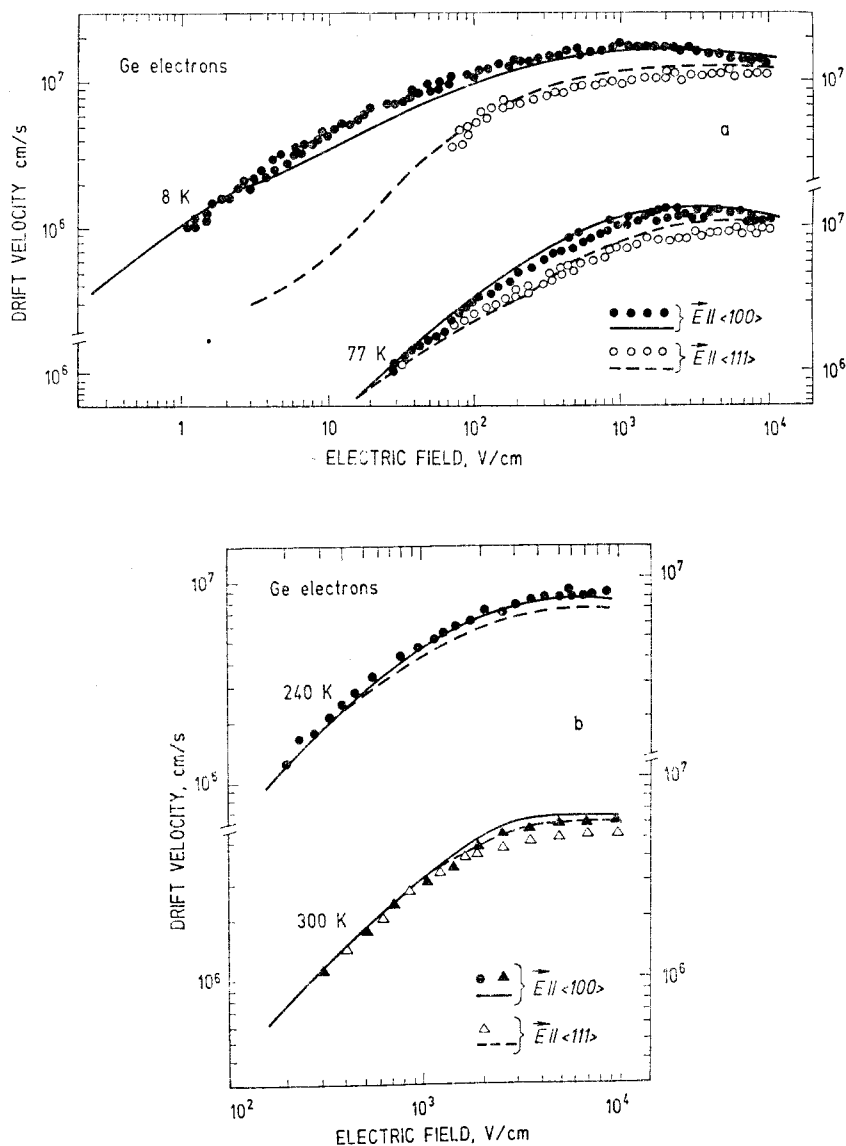


Fig. 1.40. Electron drift velocity in pure Ge as a function of electric field parallel to  $\langle 100 \rangle$  and  $\langle 111 \rangle$  crystallographic directions at (a) 8 K and 77 K, and (b) 240 K and 300 K. Points refer to the experimental data and solid and dashed lines indicate the theoretical results [1.75].

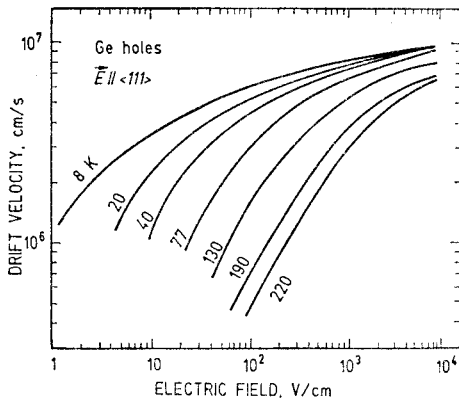


Fig. 1.41. Experimental hole drift velocity in pure Ge as a function of electric field applied parallel to  $\langle 111 \rangle$  direction at different temperatures [1.76].

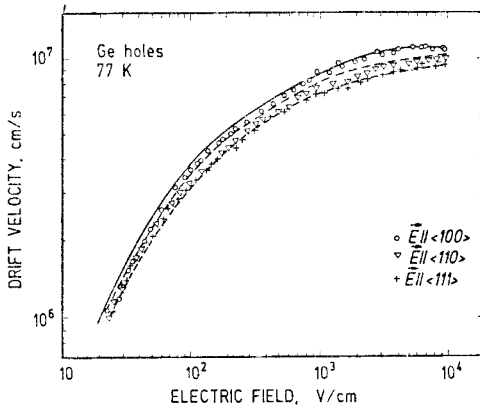


Fig. 1.42. Hole drift velocity in pure Ge in the main crystallographic directions as a function of electric field at the lattice temperature 77 K. Points refer to the experimental data and lines to the theoretical calculations [1.76].

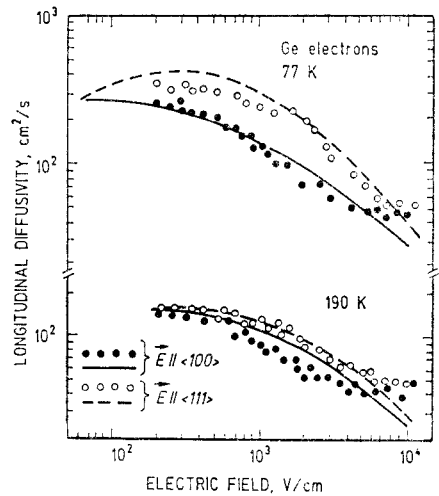


Fig. 1.43. Longitudinal diffusion coefficient (diffusivity) of electrons in pure Ge as a function of electric field applied parallel to  $\langle 111 \rangle$  and  $\langle 100 \rangle$  crystallographic directions at 77 K and 190 K. Points are experimental data. Lines are theoretical calculations [1.75].

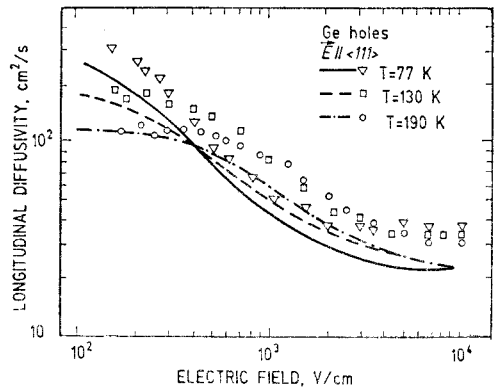


Fig. 1.44. Longitudinal diffusion coefficient as a function of electric field for holes in pure Ge at different lattice temperatures. Lines are theoretical calculations [1.77].

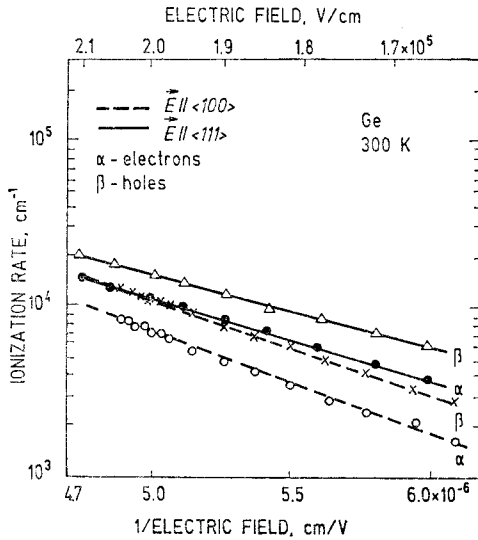


Fig. 1.45. Band-band ionization rates for electrons  $\alpha$  and holes  $\beta$  in Ge as functions of reciprocal electric field at room temperature with electric field parallel to  $\langle 111 \rangle$  and  $\langle 100 \rangle$  crystallographic directions [1.78].

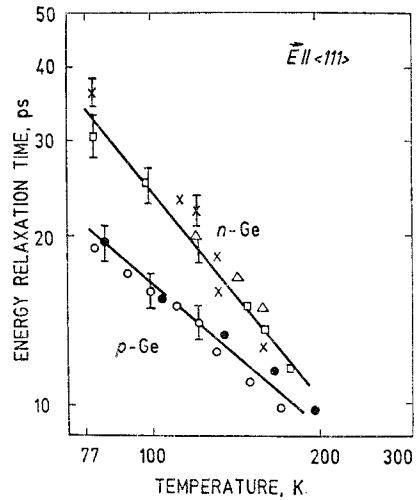


Fig. 1.46. Warm electron and hole energy relaxation times in Ge as functions of lattice temperature with electric field parallel to  $\langle 111 \rangle$  crystallographic direction. Room temperature resistivity: triangles —  $12 \Omega \cdot \text{cm}$ , squares —  $5 \Omega \cdot \text{cm}$ , crosses —  $30 \Omega \cdot \text{cm}$  for  $n\text{-Ge}$ ; open circles —  $55 \Omega \cdot \text{cm}$ , full circles —  $12 \Omega \cdot \text{cm}$  for  $p\text{-Ge}$  [1.79].

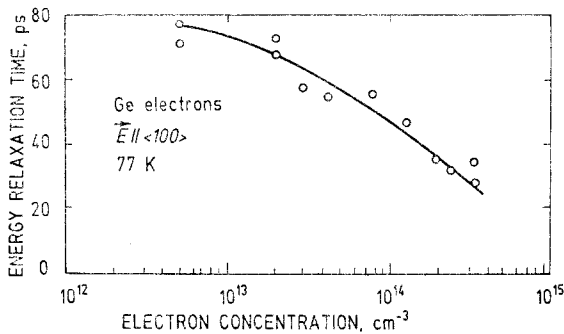


Fig. 1.47. Warm electron energy relaxation time in Ge vs. electron concentration at 77 K [1.80].

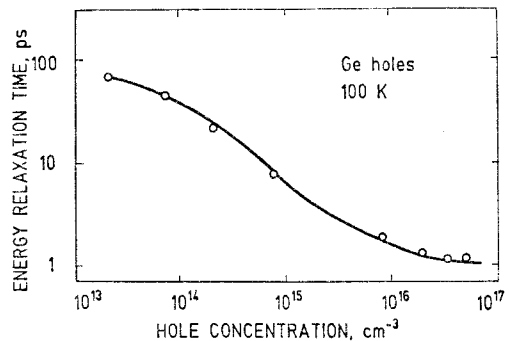


Fig. 1.48. Warm hole energy relaxation time in Ge vs. hole concentration at 100 K [1.81].

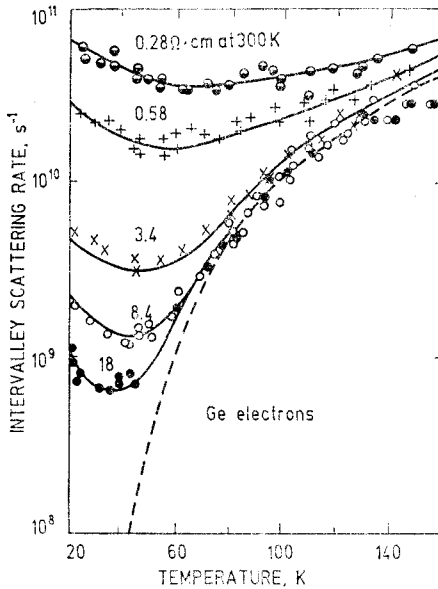


Fig. 1.49. Intervalley scattering rate as a function of temperature in *n*-Ge for samples having different room temperature resistivities. The circles are experimental points; the dashed line represents scattering due to phonons; the solid line includes contributions of ionized and neutral impurities [1.82].

Fig. 1.50. Electron energy relaxation time in pure Ge as a function of electric field applied along  $\langle 100 \rangle$  crystallographic direction at 77 K. Points are the experimental data [1.83] and the line is calculated [1.75].

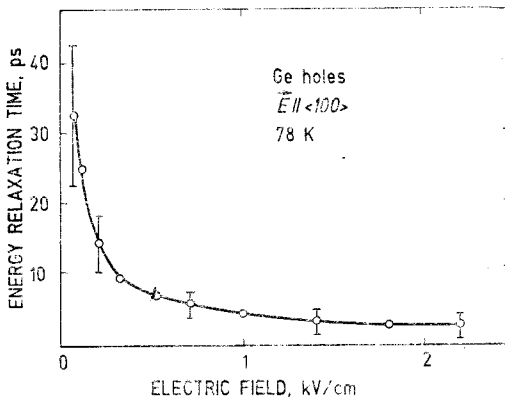
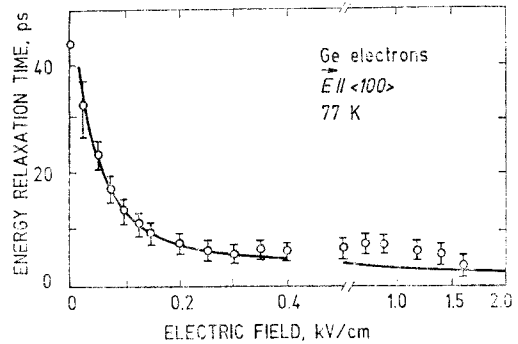


Fig. 1.51. Hole energy relaxation time in pure Ge as a function of electric field applied along  $\langle 100 \rangle$  crystallographic direction at 78 K [1.84].

**TABLE 1.15** Parameters for high field transport calculation in *n*-Ge [1.41]

Parameter	Value			
	Lattice	$\Gamma$ valley	<i>L</i> valley	<i>X</i> valley
Density, g/cm <sup>3</sup>	5.32			
Dielectric permittivity $\epsilon/\epsilon_0$	16			
<b>Intravalley properties</b>				
Number of valleys		1	4	6
Effective masses: $m_n/m_0$		0.04		
$m_l/m_0$			1.59	1.35
$m_t/m_0$			0.08	0.29
Nonparabolicity parameter, eV <sup>-1</sup>		0.3		
Valley separation with respect to <i>L</i> valley, eV		0.14	0	0.18
<b>Acoustic scattering parameters</b>				
Sound velocity, cm/s	5.4 · 10 <sup>5</sup>			
Deformation potential, eV		5	11	9
<b>Optical scattering parameters</b>				
Coupling constant, eV/cm			5.5 · 10 <sup>8</sup>	
Phonon energy, meV			37	
<b>Intervalley properties</b>				
Transition	Coupling constant	Phonon energy	Type	
$\Gamma - L$	2.0 · 10 <sup>8</sup> eV/cm	27.6 meV	<i>LA</i>	
$\Gamma - X$	10.0 · 10 <sup>8</sup> eV/cm	27.6 meV	<i>LA</i>	
<i>L</i> — <i>L</i>	3.0 · 10 <sup>8</sup> eV/cm	27.6 meV	<i>LA, LO</i>	
<i>L</i> — <i>L</i>	0.2 · 10 <sup>8</sup> eV/cm	10.3 meV	<i>TA</i>	
<i>L</i> — <i>X</i>	4.1 · 10 <sup>8</sup> eV/cm	27.6 meV	<i>LA</i>	
<i>X</i> — <i>X</i>	0.8 · 10 <sup>8</sup> eV/cm	8.6 meV	<i>LA g-type</i>	
<i>X</i> — <i>X</i>	9.5 · 10 <sup>8</sup> eV/cm	37.0 meV	<i>LO g-type</i>	

### 1.5. Ge piezoelectric, thermoelectric and magnetic properties

**Piezoelectric tensor.** For germanium, which possesses the center of symmetry, all piezoelectric tensor components are equal to zero.

**TABLE 1.16** Piezoresistance coefficients of Ge in 1/GPa. For physical

Experimental conditions	$\pi_{11}$	$\pi_{12}$	$\pi_{44}$
<b><i>n</i>-type</b>			
$\rho = 5.7 \, \Omega \cdot \text{cm}$ , 300 K	-0.027	-0.039	-1.368
$\rho = 16.6 \, \Omega \cdot \text{cm}$ , 300 K	-0.052	-0.055	-1.387
$n = (0.78\text{---}16.5) \cdot 10^{13} \, \text{cm}^{-3}$ , 78 K			
$n = 4.5 \cdot 10^{17} \, \text{cm}^{-3}$ , 78 K			
300 K			
$n = 8 \cdot 10^{18} \, \text{cm}^{-3}$ , 78 K			
300 K			
$n = 6 \cdot 10^{15} \, \text{cm}^{-3}$ , 78 K			-6.4
300 K			-1.62
$n = 5 \cdot 10^{17} \, \text{cm}^{-3}$ , 78 K			-5.5
300 K			-1.56
$n = 6.8 \cdot 10^{18} \, \text{cm}^{-3}$ , 78 K			-2.4
300 K			-1.28
<b><i>p</i>-type</b>			
$\rho = 1.1 \, \Omega \cdot \text{cm}$ , 300 K	-0.037	0.032	0.967
$\rho = 15 \, \Omega \cdot \text{cm}$ , 300 K	-0.106	0.05	0.986
$p = (2.3\text{---}150) \cdot 10^{13} \, \text{cm}^{-3}$ , 78 K			
$p = 5.5 \cdot 10^{13} \, \text{cm}^{-3}$ , 78 K	-0.25		
$p = 6.8 \cdot 10^{15} \, \text{cm}^{-3}$ , 78 K	0.3		
$\rho = 0.3 \, \Omega \cdot \text{cm}$ , 78 K			
300 K			

interpretation refer Table 5

$\frac{\pi_{11}+\pi_{12}+\pi_{44}}{2}$	$\frac{\pi_{11}+\pi_{12}-\pi_{44}}{2}$	$\pi_{11}+2\pi_{12}$	Reference
-0.717	0.62	-0.088	[14]
-0.747	0.679	-0.179	[14]
-2.7			[1.85]
-2.6			
-0.78			[1.86]
-1.37			
-0.71			[1.86]
			[1.87]
			[1.87]
			[1.87]
0.481		0.052	[14]
0.465		0.019	[14]
1.3			[1.85]
			[1.85]
			[1.85]
1.02			
0.45			[1.86]

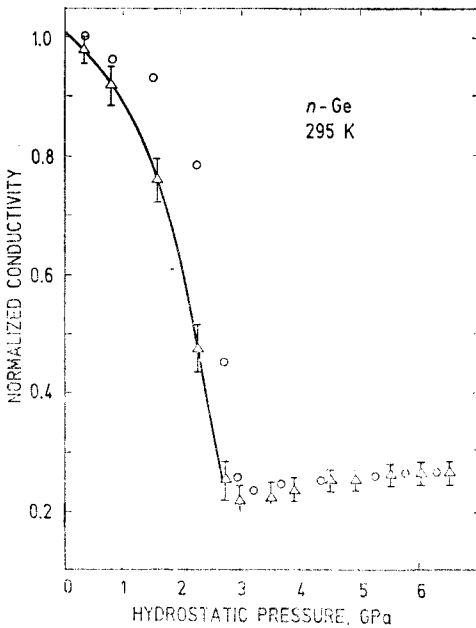


Fig. 1.52. Normalized conductivity,  $\sigma/\sigma_0$ , vs. hydrostatic pressure for *n*-Ge at 295 K. Triangles correspond to  $\langle 100 \rangle$  and circles to  $\langle 111 \rangle$  current direction [1.32]. Solid curve [1.36].

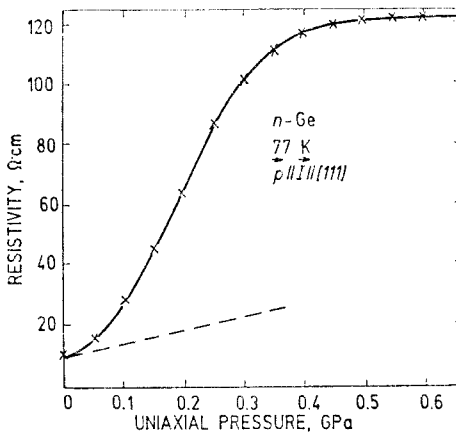


Fig. 1.53. Longitudinal resistivity vs. uniaxial pressure  $p$  in the direction of the largest resistivity increase ( $p \parallel I \parallel [111]$ ) for *n*-Ge sample with electron concentration  $1.59 \cdot 10^{13} \text{ cm}^{-3}$  [1.42]. The dashed line corresponds to linear piezoresistance  $(\pi_{11} + 2\pi_{12} + 2\pi_{44})/3 = -4.25$ .  $T = 77 \text{ K}$ .



Fig. 1.54. Seebeck coefficient  $S$  times temperature  $T$  vs. temperature for  $n$ -Ge having various excess donor concentrations: 1 -  $8.9 \cdot 10^{13} \text{ cm}^{-3}$ , 2 -  $7.8 \cdot 10^{14} \text{ cm}^{-3}$ , 3 -  $6.4 \cdot 10^{15} \text{ cm}^{-3}$ , 4 -  $1.08 \cdot 10^{17} \text{ cm}^{-3}$ , 5 -  $2.3 \cdot 10^{18} \text{ cm}^{-3}$  [1.88].

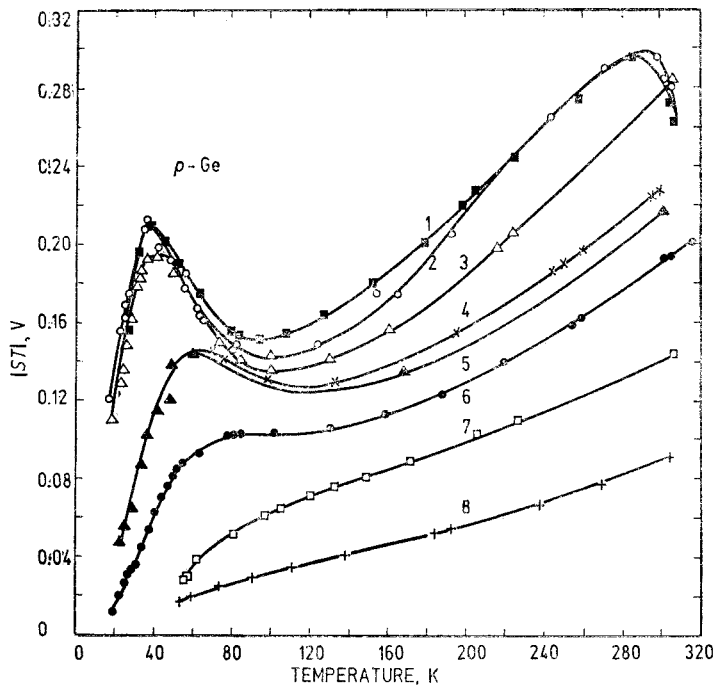
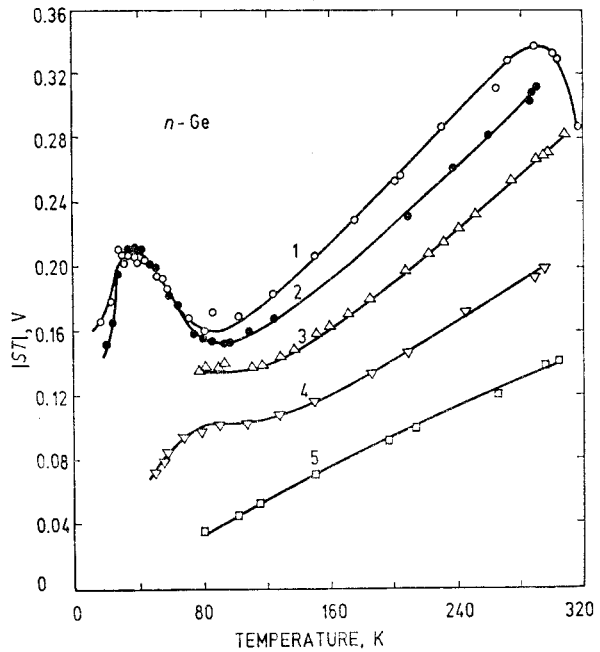


Fig. 1.55. Seebeck coefficient  $S$  times temperature  $T$  vs. temperature for  $p$ -Ge having various excess acceptor concentrations: 1 -  $1.9 \cdot 10^{14} \text{ cm}^{-3}$ , 2 -  $1.6 \cdot 10^{14} \text{ cm}^{-3}$ , 3 -  $1.5 \cdot 10^{15} \text{ cm}^{-3}$ , 4 -  $1.5 \cdot 10^{16} \text{ cm}^{-3}$ , 5 -  $2.1 \cdot 10^{16} \text{ cm}^{-3}$ , 6 -  $8 \cdot 10^{16} \text{ cm}^{-3}$ , 7 -  $6 \cdot 10^{17} \text{ cm}^{-3}$ , 8 -  $7.1 \cdot 10^{18} \text{ cm}^{-3}$  [1.88].

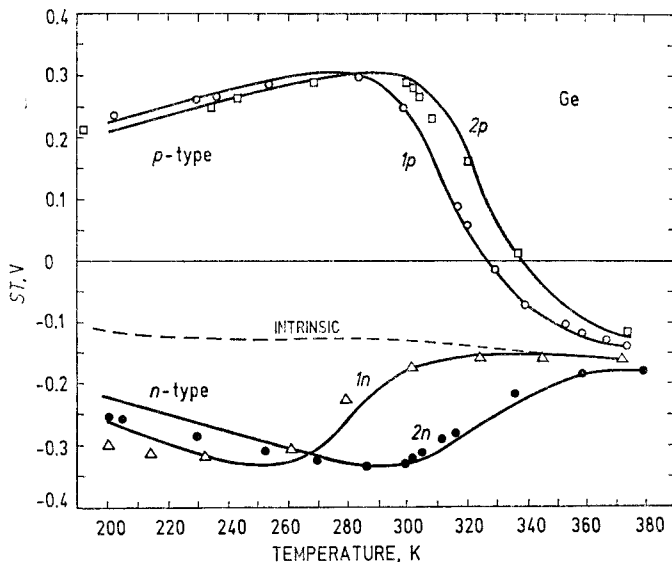


Fig. 1.56. Seebeck coefficient  $S$  times temperature  $T$  vs. temperature for Ge in high temperature region where transition to intrinsic conductivity occurs. Excess donor concentration for  $n$ -type samples:  $1n - 8 \cdot 10^{12} \text{ cm}^{-3}$ ,  $2n - 8.9 \cdot 10^{13} \text{ cm}^{-3}$ ; excess acceptor concentration for  $p$ -type samples:  $1p - 8 \cdot 10^{13} \text{ cm}^{-3}$ ,  $2p - 1.6 \cdot 10^{14} \text{ cm}^{-3}$  [1.88].

**Magnetic susceptibility.** Ge lattice contribution to the magnetic susceptibility  $\chi_m$  at room temperature and respective temperature coefficient [1.89]:

$$\chi_m = (-7.23 \pm 0.25) \cdot 10^{-6},$$

$$d\chi_m/dT = (1.66 \pm 0.05) \cdot 10^{-9} \text{ K}^{-1}.$$

The free carrier contribution to the susceptibility does not exceed 5 % of the lattice susceptibility at free carrier concentration smaller than  $10^{18} \text{ cm}^{-3}$  [1.90].

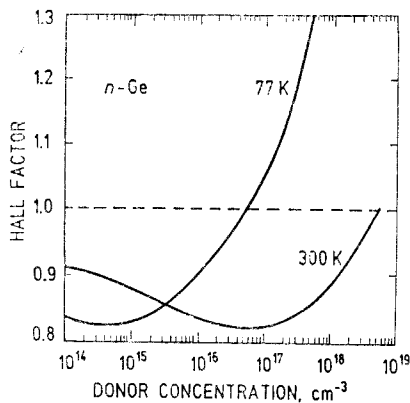


Fig. 1.57. Electron Hall factor vs. ionized donor concentration at room and liquid nitrogen temperatures in  $n$ -Ge [1.91].

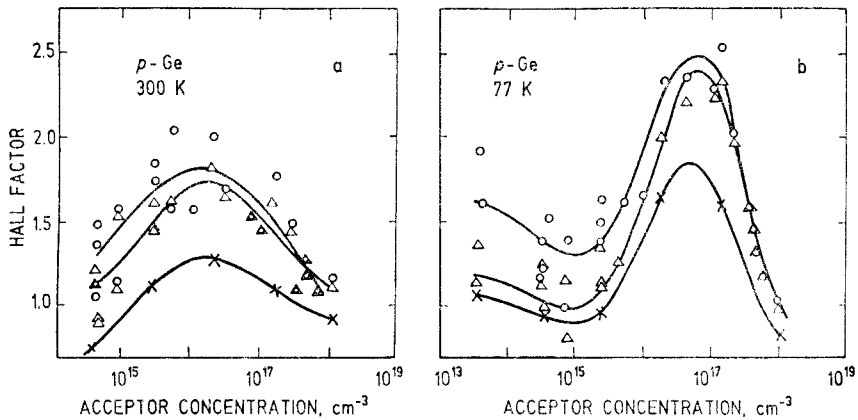


Fig. 1.58. Hole Hall factor vs. acceptor concentration at room (a) and liquid nitrogen (b) temperatures in  $p$ -Ge. Circles:  $B \rightarrow 0$ , triangles:  $B = 0.52 \text{ T}$ , crosses:  $B = 2.86 \text{ T}$  [1.92]. Solid lines are average values drawn through experimental points.

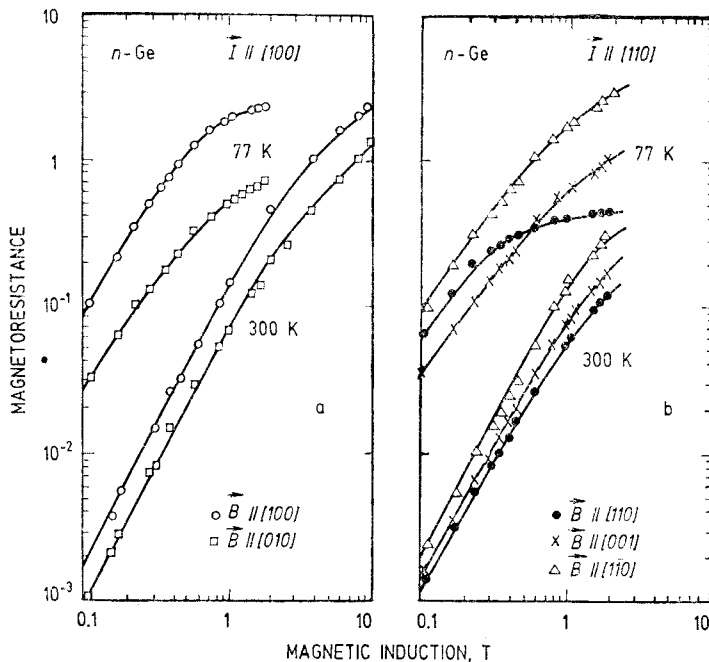


Fig. 1.59. Magnetoresistance  $[\rho(B) - \rho_0]/\rho_0$  of  $n$ -Ge vs. magnetic induction at room and liquid nitrogen temperatures for two directions of the current  $I$  flowing through a long sample,  $a - I \parallel [100]$  and  $b - I \parallel [110]$ , and various directions of the magnetic field.  $\rho_0(300 \text{ K}) = 11.5 \Omega \cdot \text{cm}$ ,  $R_H = 4.4 \cdot 10^4 \text{ cm}^3/\text{C}$  [1.93].

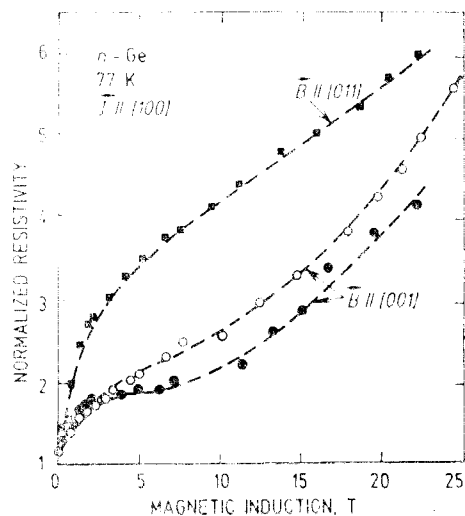


Fig. 1.60. Normalized transverse resistivity  $\rho(B)/\rho_0$  vs. magnetic induction for  $n$ -Ge doped with Sb having electron concentration: full squares and circles —  $n = 1.59 \cdot 10^{13} \text{ cm}^{-3}$ , open circles —  $n = 6 \cdot 10^{13} \text{ cm}^{-3}$ ,  $T = 77 \text{ K}$  [1.94].

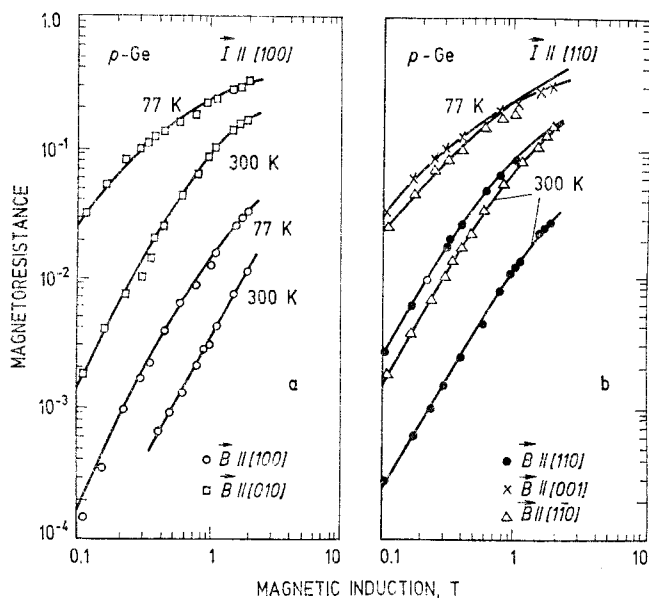


Fig. 1.61. Magnetoresistance  $[\rho(B) - \rho_0]/\rho_0$  of  $p$ -Ge vs. magnetic induction at room and liquid nitrogen temperatures for two directions of the current  $I$  flowing through a long sample,  $a - I \parallel [100]$  and  $b - I \parallel [110]$ , and various directions of the magnetic field.  $\rho_0(300 \text{ K}) = 0.385 \Omega \cdot \text{cm}$ ,  $R_H = 8.4 \cdot 10^2 \text{ cm}^3/\text{C}$  [1.93].

## 1.6. Ge impurity properties

**TABLE 1.17 Optical ionization energies and absorption cross sections** for transitions from the impurity ground state into the conduction or valence bands of Ge. The energies are referred relative to the conduction  $E_c$  or valence  $E_v$  band edges. For shallow impurities the cross section at the corresponding photon energy  $h\nu$  has been deduced from  $\sigma = \alpha_{\max}/N$ , where  $\alpha_{\max}$  is the maximum absorption coefficient and  $N$  is the impurity concentration

Impurity	Ionization energy, meV	Absorption cross section, $\text{cm}^2$	Photon energy, meV	Reference
<b>Donors</b>				
As	$E_c - 14.18^*$	$1.1 \cdot 10^{-14}$	14	[1.95]
Bi	$E_c - 12.75^*$	$1.4 \cdot 10^{-14}$	12.6	[1.95]
Li	$E_c - 10^*$	$2.5 \cdot 10^{-14}$	10	[1.96]
P	$E_c - 12.87^*$	$1.4 \cdot 10^{-14}$	12.8	[1.95]
S	$E_c - 280$			[1.97]
S <sup>+</sup>	$E_c - 590$			[1.97]
Sb	$E_c - 10.32^*$	$1.5 \cdot 10^{-14}$	10.3	[1.95]
Se	$E_c - 268$			[1.97]
Se <sup>+</sup>	$E_c - 512$			[1.97]
Te	$E_c - 93$			[1.97]
Te <sup>+</sup>	$E_c - 332$			[1.97]
<b>Acceptors</b>				
Al	$E_v + 11.15^{**}$	$\sim 2 \cdot 10^{-14}$	11	[1.98]
B	$E_v + 10.82^{**}$	$10^{-14}$	11	[1.98, 1.99]
Be	$E_v + 24.87$	$\sim 2.5 \cdot 10^{-14}$	25	[1.100]
Be <sup>-</sup>	$E_v + 58.02$			[1.100]
Cu	$E_v + 43.25$	$\sim 10^{-15}$	43	[1.101]
Cd	$E_v + 54.96$			[1.100]
Cd <sup>-</sup>	$E_v + 160$			[1.102]
Ga	$E_v + 11.32^{**}$	$10^{-14}$	11	[1.98]
Hg	$E_v + 91.2$	$4 \cdot 10^{-16}$	150	[1.103, 1.104]
Hg <sup>-</sup>	$E_v + 230$			[1.105]
In	$E_v + 11.96^{**}$	$10^{-14}$	12	[1.98]
Mg	$E_v + 35.83$			[1.100]
Tl	$E_v + 13.43^{**}$	$\sim 10^{-14}$	13.5	[1.98, 1.99]
Zn	$E_v + 32.98$			[1.100]
Zn <sup>-</sup>	$E_v + 86.514$			[1.100]

TABLE 1.17 (Continued)

Impurity	Ionization energy, meV	Absorption cross section, $\text{cm}^2$	Photon energy, meV	Reference
<b>Amphoteric impurities</b>				
Au				
acceptor state	$E_v + 150$	$2 \cdot 10^{-16}$	690	[1.106]
	$E_c - 200$			[1.107]
	$E_c - 41$			[1.107]
donor state	$E_v + 41$			[1.107]

\* — Deduced assuming that the binding energy of the  $3p_{\pm}$  state is 1.03 meV.

\*\* — Deduced assuming that the binding energy of the  $(8-1)$  state is 2.88 meV.

**TABLE 1.18** Binding energies of the energy levels of **shallow donors** (phosphorus, arsenic, antimony, bismuth and lithium) in Ge found by optical methods. The energies in meV are measured relative to the conduction band edge [1.110]

Level	Level energy, meV					Effective mass theory
	P	As	Sb	Bi	Li	
$1s(A_1) \equiv E_I$ (ionization energy)	12.88	14.18	10.45	12.75	8.1	9.81
$1s(T_2)$	10.06	9.94	9.99	9.90	10	9.81
$2p_0$	4.72	4.74	4.74	4.75		4.74
$2s$						3.52
$3p_0$	2.54	2.57	2.57	2.55		2.56
$3s$						2.01
$2p_{\pm}$	1.72	1.74	1.71	1.67	1.72	1.73
$4p_0$						1.67
$4s$						1.17
$3p_{\pm}$	1.03	1.03	1.03	1.03	1.03	1.03
$5p_0$						0.84
$4p_{\pm}$	0.75		0.75		0.74	0.73
$5s$						0.72
$4f_{\pm}$	0.62		0.59			0.61
$5p_{\pm}$	0.47		0.46			0.53
$5f_{\pm}$	0.39		0.39			0.41
$6p_{\pm}$	0.32		0.32			0.38
$6f_{\pm}$			0.30			0.32

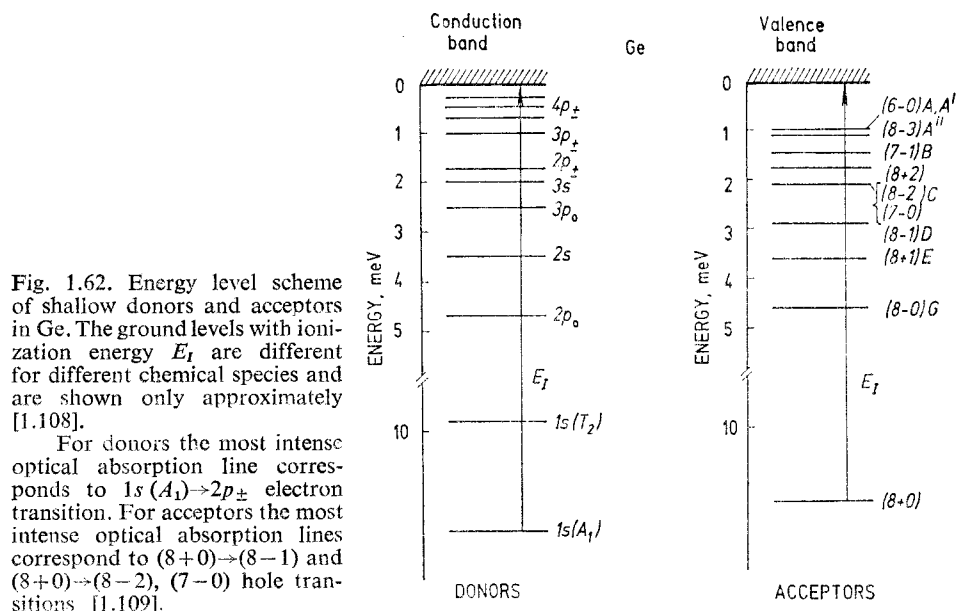


**TABLE 1.19** Binding energies of the energy levels of **shallow acceptors** (boron, aluminium, gallium, indium and thallium) in Ge found by optical methods. The energies in meV are measured relative to the valence band edge [1.110]

Level	Level energy, meV					Effective mass theory
	B	Al	Ga	In	Tl	
$(8+0) \equiv E_I$ (ionization energy)	10.82	11.15	11.32	11.96	13.43	
$(8-0)$	4.61	4.56	4.58	4.57	4.52	4.58 ( $1\Gamma_8^-$ )
$(8+1)$	3.27		3.30	3.54	3.57	
$(8-1)$	2.88	2.88	2.88	2.88	2.88	2.88 ( $2\Gamma_8^-$ )
$(7-0)$	2.14	2.13	2.13	2.10	2.13	2.13 ( $1\Gamma_7^-$ )
$(8-2)$						2.11 ( $3\Gamma_8^-$ )
$(8+2)$	1.76			1.76	1.78	
$(7-1)$	1.49	1.48	1.48	1.48	1.50	1.48 ( $4\Gamma_8^-$ )
						1.22 ( $5\Gamma_8^-$ )
$(8-3)$	1.16	1.13	1.15	1.15	1.14	1.14 ( $2\Gamma_7^-$ )
						1.14 ( $2\Gamma_6^-$ )
						1.13 ( $6\Gamma_8^-$ )
$(6-0)$	1.03	1.00	1.01	1.00	1.01	

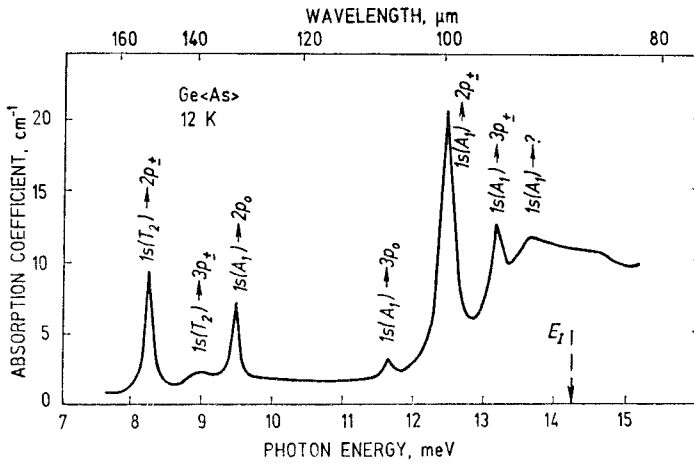


Fig. 1.63. Optical absorption coefficient vs. photon energy for arsenic doped Ge with  $N_{As} \approx 1 \cdot 10^{15} \text{ cm}^{-3}$  at  $T=12 \text{ K}$ . Initial and final states of the transitions are marked in the spectrum.  $E_I$  is the ionization energy of arsenic [1.96].

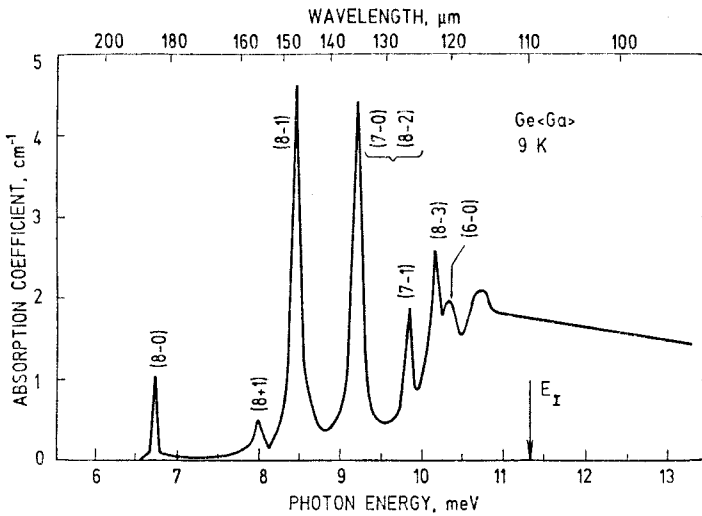


Fig. 1.64. Optical absorption coefficient due to hole transitions from  $(8+0)$  ground level to excited levels of gallium in Ge vs. photon energy at  $T=9 \text{ K}$ .  $N_{Ga} \approx 2 \cdot 10^{14} \text{ cm}^{-3}$ .  $E_I$  is ionization energy of gallium [1.98].



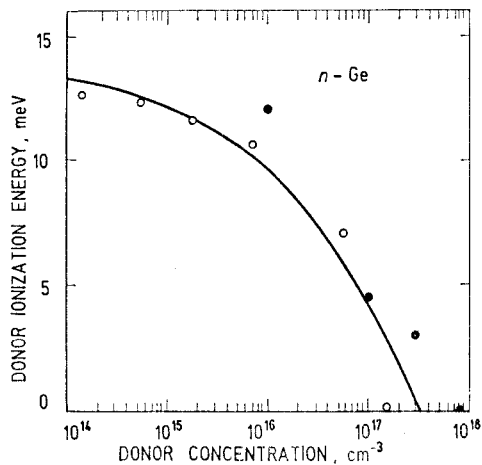


Fig. 1.65. Dependence of shallow donor (arsenic) ionization energy  $E_I$  on electrically active donor concentration  $N_D^*$  in  $n$ -Ge. Full circles — optical measurements [1.49], open circles — thermal measurements [1.69]. Solid line is an empirical formula  $E_I = 14.2 - 2.12 \cdot 10^{-5} N_D^{*1/8}$ ,  $E_I$  is in meV and  $N_D^*$  is in  $\text{cm}^{-3}$ .

**TABLE 1.20** Energies of the energy levels of **double acceptors** (magnesium, cadmium, mercury, beryllium and zinc) in Ge found by optical methods. The energies in meV are measured relative to the valence band edge [1.100]

Level	Level energy, meV							Theory for neutral acceptor
	Mg	Cd	Hg	Be	Be <sup>-</sup>	Zn	Zn <sup>-</sup>	
Ionization energy, $E_I$	35.83	54.96	91.88 ( $\Gamma_3 + \Gamma_5$ ) 91.18 ( $\Gamma_1$ )	24.87 ( $\Gamma_3 + \Gamma_5$ ) 24.77 ( $\Gamma_1$ )	58.02	32.98	86.514	
<i>G</i>	4.62	4.56	4.68	4.90		4.66	18.72	4.58 ( $1\Gamma_8^-$ )
<i>D</i>	2.88	2.88	2.88	2.88	11.52	2.88	11.52	2.88 ( $2\Gamma_8^-$ )
<i>C</i>	2.12	2.13	2.18	2.10	8.24	2.12	8.32 8.188 7.72	2.13 ( $1\Gamma_7^-$ ) 2.13 ( $1\Gamma_7^-$ ) 2.11 ( $3\Gamma_8^-$ )
<i>B</i>	1.49	1.55	1.58	1.47	5.84	1.50	5.816	1.48 ( $4\Gamma_8^-$ )
<i>A''</i>	1.15			1.11		1.15	4.32	1.22 ( $5\Gamma_8^-$ )
<i>A'</i>	0.95		1.08	0.91	4.32	0.98	3.724	1.14 ( $2\Gamma_7^-$ ) 1.14 ( $1\Gamma_6^-$ )
<i>A</i>	0.69			0.61		0.8		1.13 ( $6\Gamma_8^-$ )

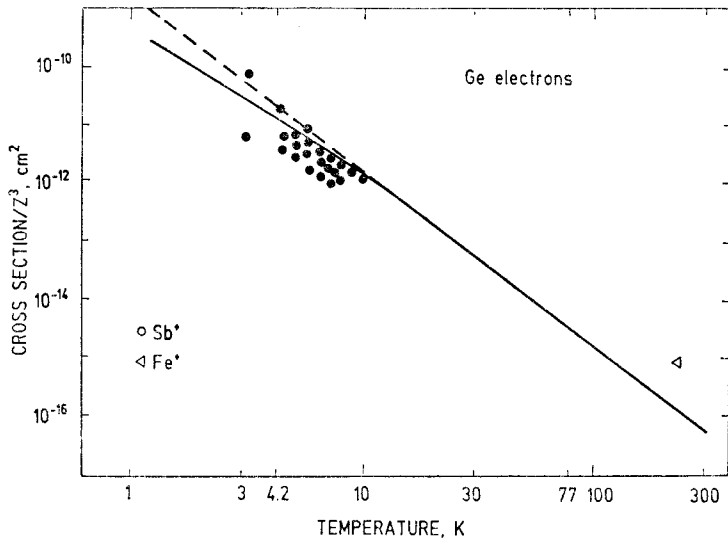


Fig. 1.66. Electron capture cross section on the positively single-charged ( $Z=1$ ) centers in Ge. Solid and dashed lines are theoretical calculations [1.111].

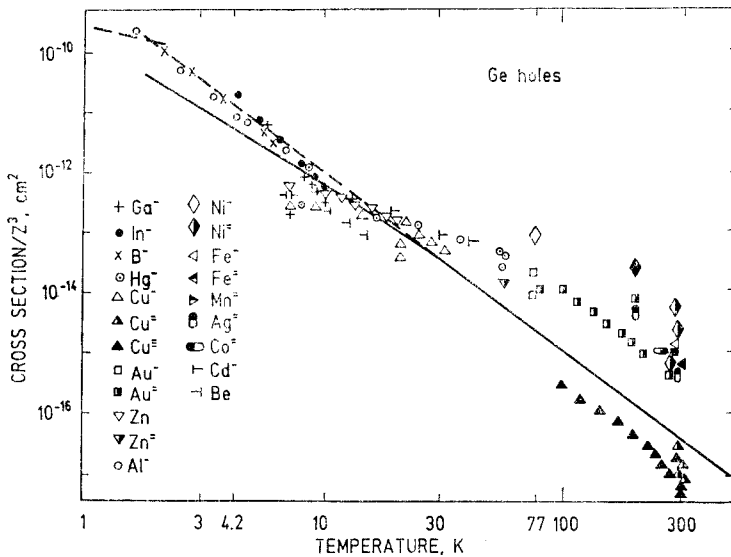


Fig. 1.67. Hole capture cross section on the negatively single-charged ( $Z=1$ ), double-charged ( $Z=2$ ) and triple-charged ( $Z=3$ ) centers in Ge. Solid and dashed lines are theoretical calculations [1.111].

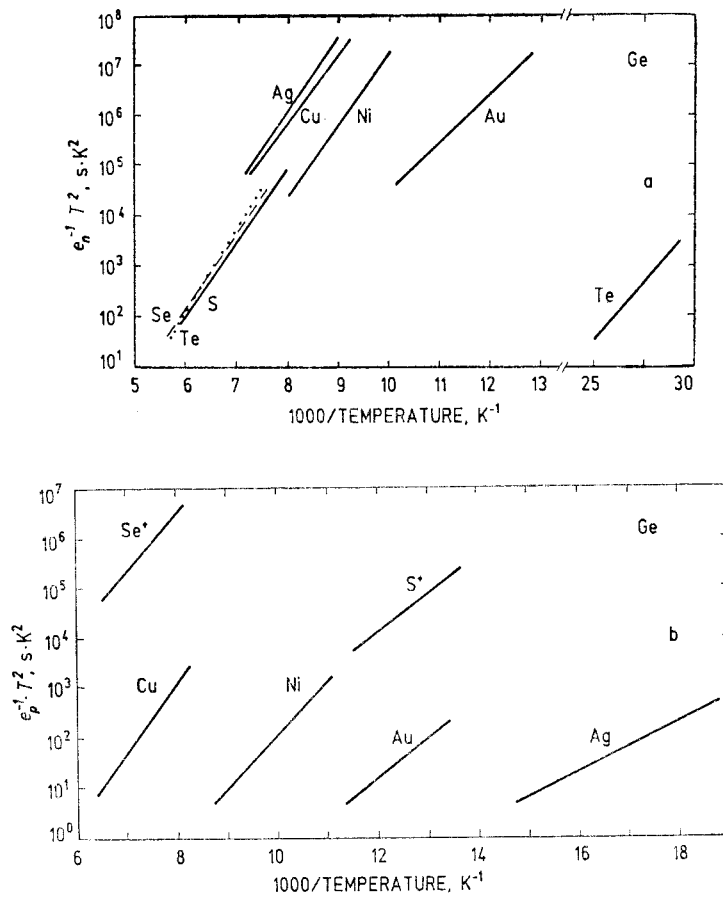


Fig. 1.68. Inverse emission rate multiplied by  $T^2$  for electron (a) and hole (b) emission from deep impurities indicated on curves as obtained with DLTS (deep level transient spectroscopy) on Ge.  $T$  is the lattice temperature. For details see Table 1.21.

**TABLE 1.21** Thermal ionization energy measured relative to the conduction  $E_c$  or valence  $E_v$  band edges and capture cross sections associated with **deep impurities** in Ge as determined by Deep Level Transient Spectroscopy (DLTS)

Impurity	Depth from conduction or valence band edge, meV	Temperature, K	Capture cross section, $\text{cm}^2$	Reference
<b>Donors</b>				
S	$E_c - 296$	135–165	$\sigma_n = (1.86 - 1.56) \cdot 10^{-16}$	[1.97]
S <sup>+</sup>	$E_v + 149$	73–85		
Se	$E_c - 284$	135–165	$\sigma_n = (1.82 - 1.67) \cdot 10^{-16}$	
Se <sup>+</sup>	$E_v + 245$	120–150		
Te	$E_c - 92$	35–42		
Te <sup>+</sup>	$E_v - 332$	135–165	$\sigma_n = (1.67 - 1.02) \cdot 10^{-16}$	
<b>Acceptors</b>				
Cu	$E_v + 320$	125–150	$\sigma_p = (2.5 - 1.4) \cdot 10^{-12}$	[1.112]
Cu	$E_c - 260$	115–130	$\sigma_n = (1.6 - 1.8) \cdot 10^{-17}$	
Ag	$E_v + 130$	55–70	$\sigma_p = (1.5 - 0.68) \cdot 10^{-13}$	
Ag	$E_c - 280$	120–140	$\sigma_n = (4.6 - 5.2) \cdot 10^{-17}$	
Au	$E_v + 150$	77–95	$\sigma_p = 6.2 \cdot 10^{-14}$	
Au	$E_c - 200$	77–90	$\sigma_n = 1.5 \cdot 10^{-16}$	
Ni	$E_v + 230$	95–110	$\sigma_p = 8.8 \cdot 10^{-13}$	
Ni	$E_c - 300$	105–125	$\sigma_n = 1.8 \cdot 10^{-14}$	

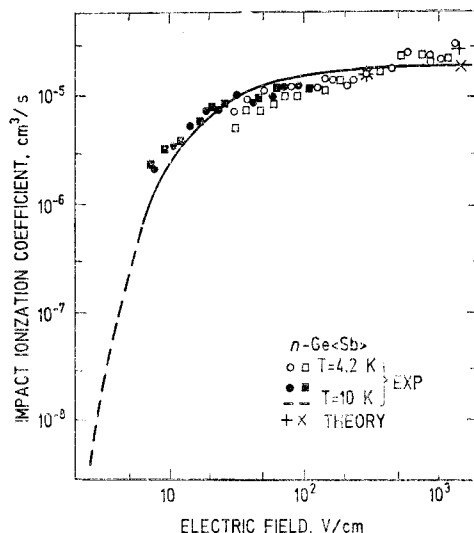


Fig. 1.69. Experimental dependence (dashed line, circles and squares) of the impact ionization coefficient for antimony impurity in Ge on the electric field strength [1.113, 1.114]. Theoretical points (crosses) were calculated with the impact ionization cross section  $\sigma_0 = 8.6 \cdot 10^{-13}$   $\text{cm}^2$ . Solid line: empirical formula  $A_I = 2 \cdot 10^{-5} \exp(-20.7/E)$ ,  $A_I$  is in  $\text{cm}^2/\text{s}$  and  $E$  is in  $\text{V/cm}$ .

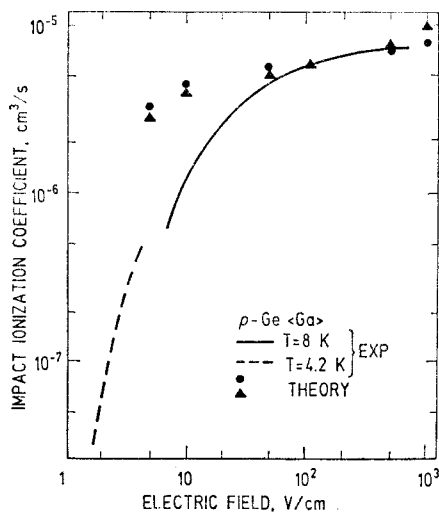
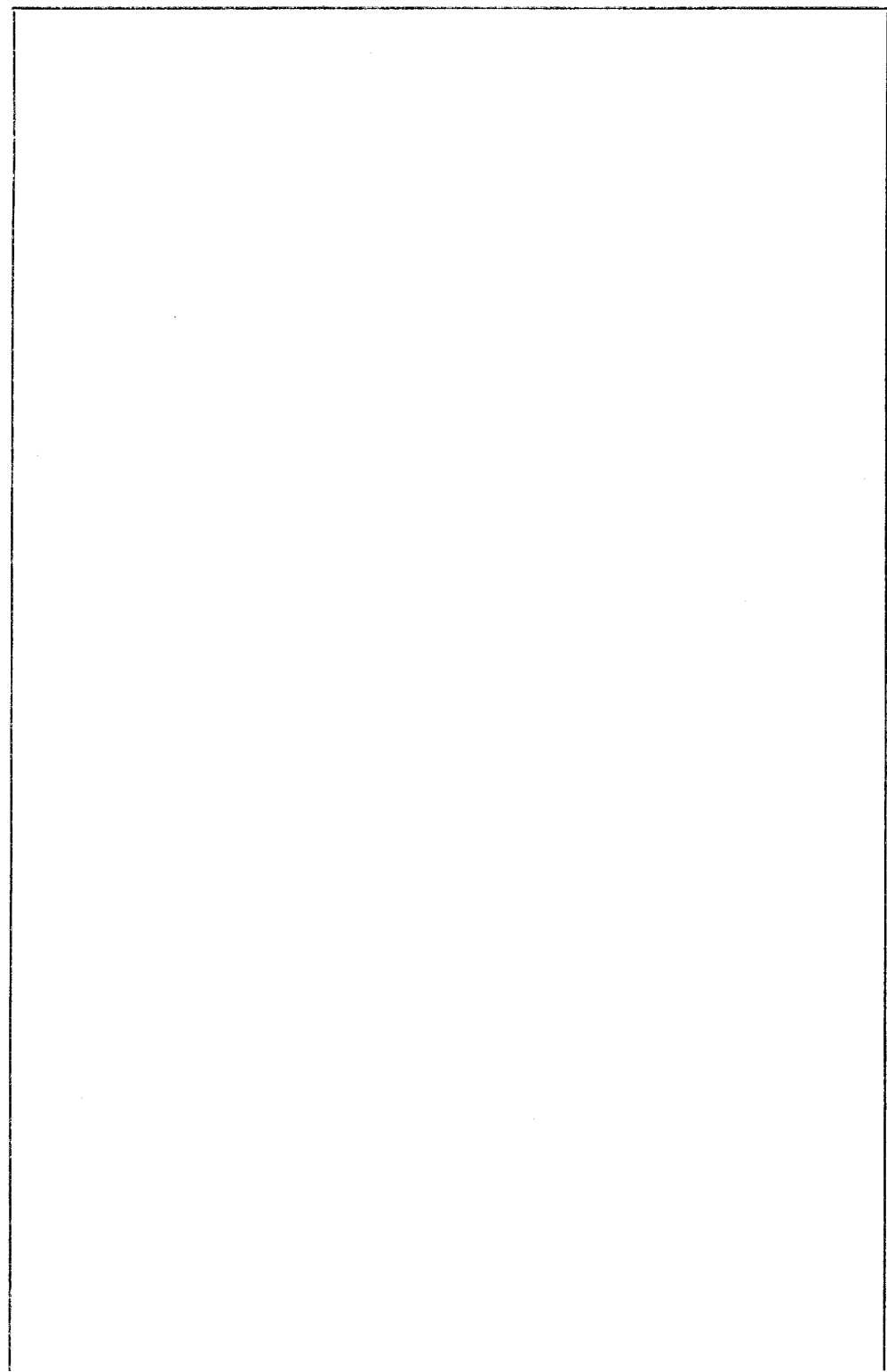


Fig. 1.70. Experimental dependence (solid and dashed lines) of the impact ionization coefficient of gallium impurity in Ge on the electric field strength [1.114, 1.115]. Theoretical points (circles and triangles) were calculated with the impact ionization cross section  $\sigma_0 = 6.7 \cdot 10^{-13}$   $\text{cm}^2$ .



## 2. Physical data for silicon

### 2.1. Si lattice properties

1. Si consists of the following isotopes (as a result the translational symmetry of Si lattice is not exact) [1.1]
  - $^{28}\text{Si}$  ..... 92.2 %
  - $^{29}\text{Si}$  ..... 4.7 %
  - $^{30}\text{Si}$  ..... 3.1 %
2. Average atomic weight: 28.08 [1.2]
3. Si has a diamond-type lattice. Space group is  $Fd\bar{3}m (O_h^h)$ . Lattice symmetry formula is  $3L^44L^36L^29PC$ , which means that there are 3 symmetry axes of the fourth-order, 4 symmetry axes of the third-order, 6 symmetry axes of the second-order, 9 symmetry planes and inversion center.
4. Lattice constant in vacuum:  $a=0.543\ 101\ 96\ \text{nm}$  at 295.6 K [28]
 

Temperature dependence of the lattice parameter in high purity material in the range 293–1073 K can be approximated by formula

$$a=5.4304+1.8138\cdot 10^{-5}(T-273.15)+1.542\cdot 10^{-9}(T-273.15)^2, T \text{ is in K.} \quad [2.1]$$
5. Density:  $2.329\ 02\ \text{g/cm}^3$  at  $298\pm 0.01\ \text{K}$  [1.4]
6. Number of atoms in  $1\ \text{cm}^3$  is  $5\cdot 10^{23}$
7. Melting temperature: 1685 K [2.2]
8. Transition to metallic phase occurs at the pressure  $12.5\pm 0.5\ \text{GPa}$  at 300 K [2.3]
9. Si cleaves most readily on  $\{111\}$  family planes [1.7]

**TABLE 2.1** Elastic parameters of Si at the lattice temperature 77 K and 298 K [2.4]

Parameter	Value	
	77 K	298 K
Elastic constants:		
$c_{11}$ , GPa	167.7	165.8
$c_{12}$ , GPa	64.98	63.9
$c_{44}$ , GPa	80.35	79.6
Sound velocity in the direction [100]:		
longitudinal $v_L$ , cm/s	$8.48 \cdot 10^5$	$8.43 \cdot 10^5$
transverse $v_T$ , cm/s	$5.87 \cdot 10^5$	$5.84 \cdot 10^5$
Sound velocity in the direction [111]:		
longitudinal $v_L$ , cm/s	$9.4 \cdot 10^5$	$9.35 \cdot 10^5$
transverse $v_T$ , cm/s	$5.11 \cdot 10^5$	$5.09 \cdot 10^5$
Elastic anisotropy factor $a$	0.639	0.640
Poisson ratio $\nu$	0.279	0.278
Young's modulus $E$ , GPa:		
direction [100]	131.4	130.2
direction [110]	170.8	169.2
direction [111]	189.8	187.8
Bulk modulus $B_0$ , GPa	99.2	98
$B'_0 = dB_0/dp$		4.16*

\* — [110].



**TABLE 2.2** Si phonon energies for high symmetry points  $\Gamma$ ,  $X$  and  $L$  in the Brillouin zone at 300 K [2.5, 1.11, 2.6]

Phonon branch	Phonon energy, meV		
	$\Gamma$	$X$	$L$
$LO$	$64.35 \pm 0.12$	$51.44 \pm 0.12$	$52.1 \pm 1.3$
$TO$	$64.35 \pm 0.12$	$57.03 \pm 0.25$	$60.75 \pm 0.25$
$LA$	0	$51.44 \pm 0.12$	$46.9 \pm 1.2$
$TA$	0	$18.65 \pm 0.08$	$14.10 \pm 0.08$

**TABLE 2.3** Types and energies of intervalley  $g$ - and  $f$ -phonons for electron-phonon intervalley interaction in  $n$ -Si [2.7]

Phonon type	Energy, meV	Frequency, THz
$g^* LO$	63.2	15.3
$g TO$	62	15
$g LA$	18.8	4.53
$g TA$	11.4	2.76
$f^* TO$	59.1	14.3
$f LO$	48.8	11.8
$f^* LA$	46.3	11.2
$f TA$	25.4	6.15
$f TA$	18.4	4.45

\*—Allowed by group-theoretical analysis of electron-phonon interaction [2.8], therefore, in  $n$ -Si the electron-phonon interaction mediated by these phonons is the strongest.

**Temperature variation of phonon energies.** In Si the optical phonon energy at  $\Gamma$  point is 65.1 meV at 0 K, 64.5 meV at 300 K and 63.1 meV at 800 K [2.9].

**Optical phonon lifetime.** At the symmetry point  $\Gamma$  the half-width of the first-order Raman line is  $1.45 \pm 0.05 \text{ cm}^{-1}$  at 17 K and  $3.5 \pm 0.05 \text{ cm}^{-1}$  at 305 K. These half-widths yield phonon lifetime 3.6 ps and 1.5 ps, respectively [2.5].

**Raman activity.** Silicon possesses the diamond structure  $O_h^7 (Fd3m)$ , therefore, it has only one first-order Raman-active phonon of symmetry  $\Gamma_{25'}$  located at the Brillouin zone center with energy 64.35 meV at  $T=305 \text{ K}$  [2.5].

**TABLE 2.4** Grüneisen parameters for different phonon branches in Si at X, K,  $\Gamma$  and L critical points.  $T=300 \text{ K}$  [3, 2.10]

Phonon branch	Grüneisen parameter			
	X	K	$\Gamma$	L
LO	0.9	0.9	$0.98 \pm 0.06$	0.9
TO	$1.5 \pm 0.1$	1.5	$0.98 \pm 0.06$	$1.3 \pm 0.2$
LA	0.9	0.9	1.11* [q00]	0.9
LA			1.11* [qq0]	
LA			1.08* [qqq]	
TA	$-1.4 \pm 0.3$		0.324* [q00]	$-1.3 \pm 0.3$
TA			0.113* [qqq]	
TA <sub>1</sub>		-0.3	0.324* [qq0]	
TA <sub>2</sub>		-1.0	-0.05* [qq0]	

\*—Calculated from lattice elastic parameters [4]. The direction of wave vector is given in parentheses;  $q \ll 2\pi/a$ , where  $a$  is the lattice constant.

### Lattice dielectric permittivity.

Relative static [2.11]:

$$\begin{aligned}\varepsilon/\varepsilon_0 &= 11.9 \text{ at } 300 \text{ K,} \\ &12.1 \text{ at } 4.2 \text{ K.}\end{aligned}$$

Dependence on hydrostatic pressure [2.12]:

$$(1/\varepsilon)(d\varepsilon/dp) = -2.8 \cdot 10^{-3} \text{ 1/GPa.}$$

Dependence on temperature [1.18]:

$$(1/\varepsilon)(d\varepsilon/dT) = 9.4 \cdot 10^{-5} \text{ K}^{-1}.$$

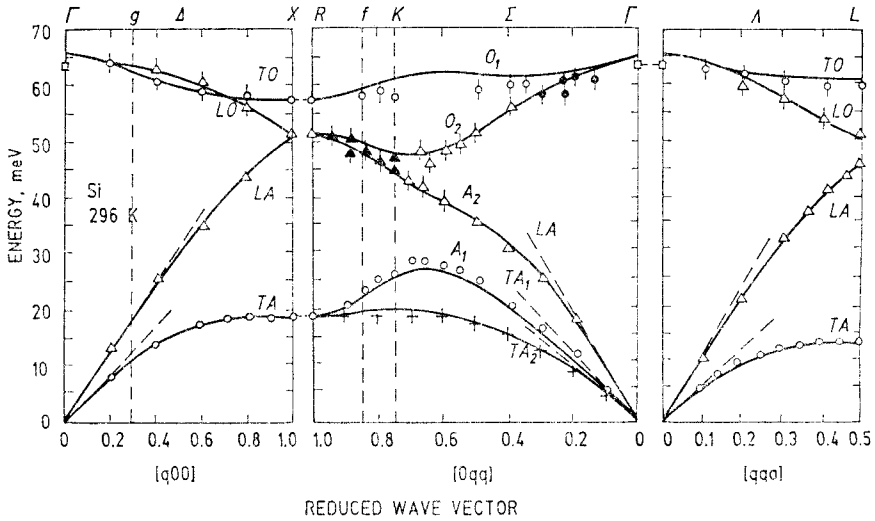


Fig. 2.1. Phonon dispersion curves for Si in the main crystallographic directions at 296 K [2.6].  $TA_2$  branch is replotted from [1.11]. The dashed lines show the slopes for sound velocity in various directions. Intervalley  $g$ -phonons lie in  $\langle 100 \rangle$  while  $f$ -phonons lie in  $\langle 110 \rangle$  directions and correspond to wave vectors:  $\mathbf{q}_g = [0.29, 0, 0]2\pi/a$ ,  $\mathbf{q}_f = [0.855, 0.855, 0]2\pi/a$ . The path from  $K$  to  $R$  is equivalent to the path from  $U$  to  $K$  on the Brillouin zone boundary.

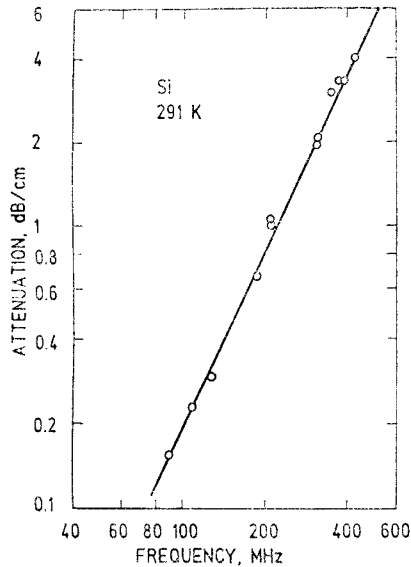


Fig. 2.2. Frequency dependence of ultrasound attenuation coefficient by Si lattice in [111] direction at room temperature [2.13].

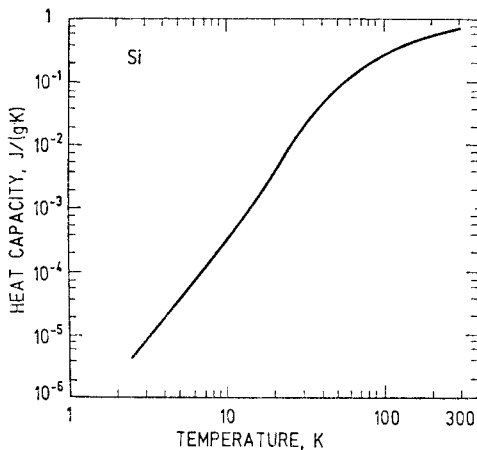


Fig. 2.3. Heat capacity  $C_p$  of pure Si as a function of temperature [1.21].

Selected values:

$$C_p = 3.3 \cdot 10^{-5} \text{ J/(g} \cdot \text{K)} \text{ at } 5 \text{ K,}$$

$$0.178 \text{ J/(g} \cdot \text{K)} \text{ at } 77.4 \text{ K,}$$

$$0.71 \text{ J/(g} \cdot \text{K)} \text{ at } 295 \text{ K.}$$

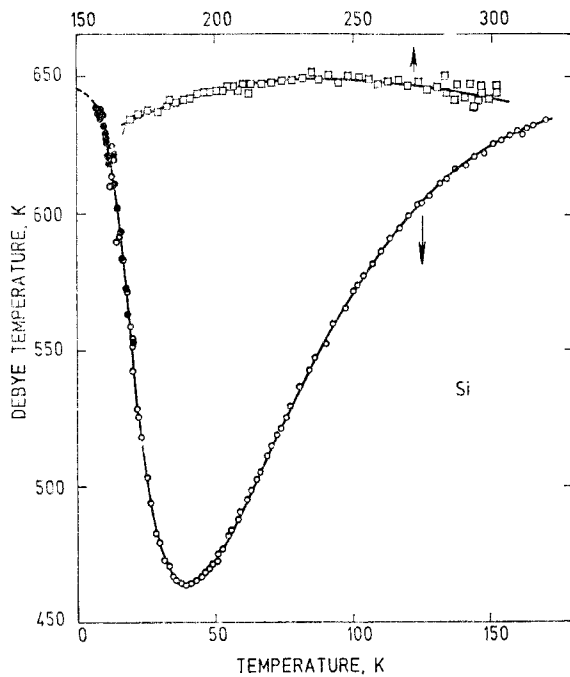


Fig. 2.4. Si Debye temperature vs. lattice temperature [1.21].

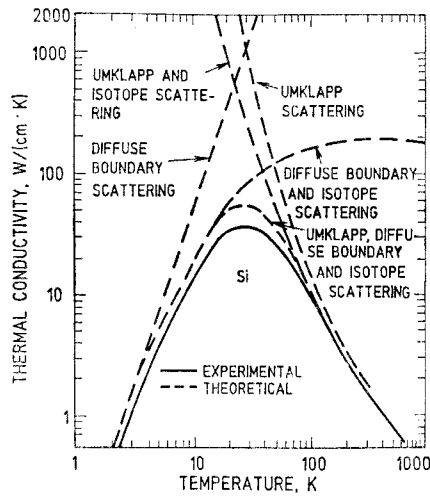


Fig. 2.5. Thermal conductivity  $\chi$  of Si [1.22].

Selected values:

$\chi = 26 \text{ W/(cm} \cdot \text{K)}$  at 50 K,  
 $14.7 \text{ W/(cm} \cdot \text{K)}$  at 77.4 K,  
 $1.56 \text{ W/(cm} \cdot \text{K)}$  at 300 K.

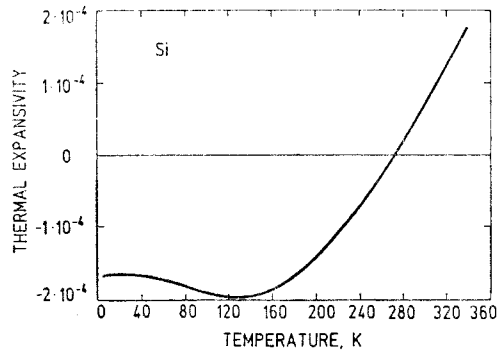


Fig. 2.6. Thermal expansivity  $(l_T - l_{273.2})/l_{273.2}$  as a function of temperature for Si [2.14].  $l_{273.2}$  is a length at 273.2 K.

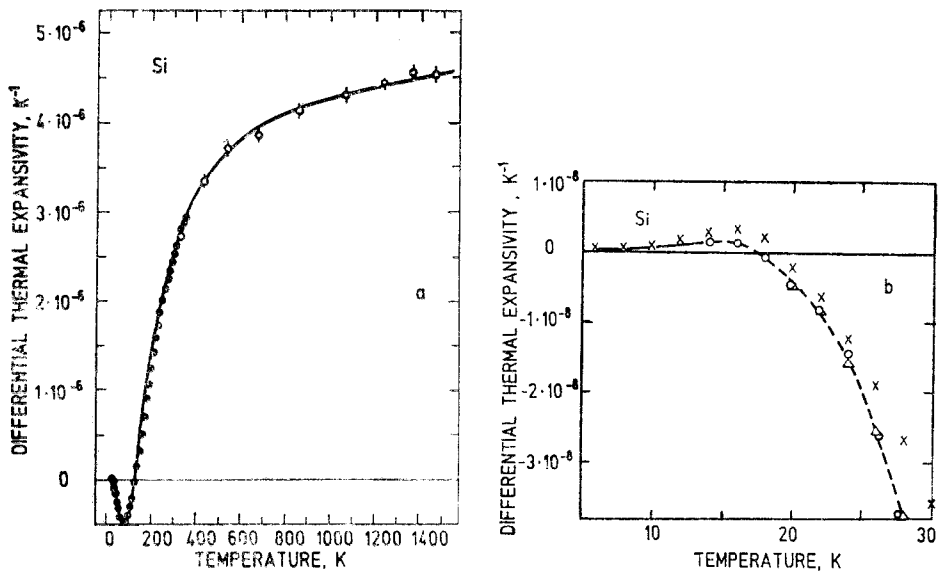


Fig. 2.7. Differential thermal expansivity  $\alpha = (1/l_{273.2})(dl/dT)$  as a function of temperature for Si: a - full circles [2.14], open circles [2.15], solid line in the range  $T = 120 - 1500 \text{ K}$  is an empirical curve  $\alpha = [3.725 \{1 - \exp[-5.88 \cdot 10^{-3}(T - 124)]\} + 5.548 \cdot 10^{-4} T] \cdot 10^{-6}$ ,  $\alpha$  is in  $\text{K}^{-1}$ ,  $T$  is in Kelvins; b - [1.24].

Selected values:

- $\alpha = 5.6 \cdot 10^{-11} \text{ K}^{-1}$  at 4 K [2.16],
- $-0.474 \cdot 10^{-6} \text{ K}^{-1}$  at 77.4 K [2.14],
- $2.57 \cdot 10^{-6} \text{ K}^{-1}$  at 295 K [2.14].

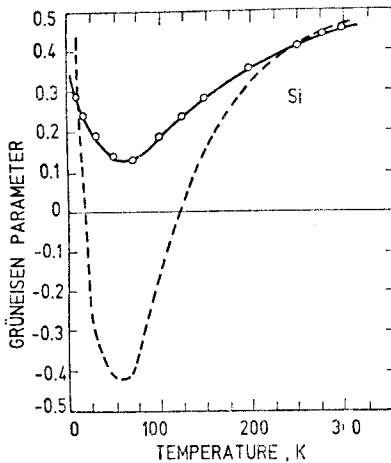


Fig. 2.8. Averaged Grüneisen parameter for Si as a function of the lattice temperature [1.27]. Solid line: from third-order elastic constants; dashed line: from thermal expansion.

## 2.2. Si band properties

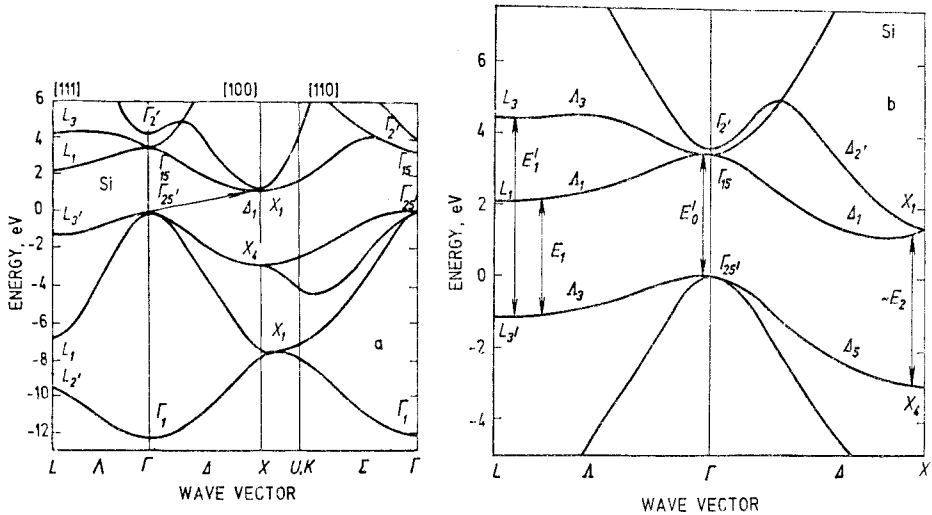


Fig. 2.9. Band structure of Si with spin-orbit interaction neglected. *a* – General view. Indirect gap between points  $\Gamma_{25'}$  and  $\Delta_1$  is shown by an arrow [1.28]. *b* – Enlarged portion with main interband optical transitions indicated by vertical arrows [2.17].

**TABLE 2.5** Critical points associated with band-band transitions in Si which are important in optical measurements. Spin-orbit interaction neglected (see also Fig. 2.9)

Critical point	Corresponding band-band transition	$\mathbf{k}$ -space location (units of $2\pi/a$ )
$E_0$	$\Gamma_{25'}^v \rightarrow \Gamma_2^c$	Weak transition in the center of Brillouin zone
$E'_0$	$\Gamma_{25'}^v \rightarrow \Gamma_{15}^c$	Dominated by small region around (0,0,0)
$E_1$	$\Delta_3^v \rightarrow \Delta_1^c$	Transition to the first conduction band along $\Delta$ line
$E'_1$	$\Delta_3^v \rightarrow \Delta_3^c$	Transition to the second band near $L$ point. This transition is nearly degenerate with $E'_0$
$E_2$	$\Sigma_2^v \rightarrow \Sigma_3^c$ $\Delta_5^v \rightarrow \Delta_1^c$	Attributed to transitions in a large region near the $X$ point centered at (0.9, 0.1, 0.1). Because of large phase space and matrix element this transition dominates

**TABLE 2.6** Energetic distances between important critical points in the energy band of Si at room temperature and respective hydrostatic pressure coefficients. For transition and critical point nomenclature see Fig. 2.9 and Table 2.5

Energy separation and pressure coefficient	Value	Comment	Reference
$E_g = E(\Delta_1^c) - E(\Gamma_{25'}^g)$ , eV	1.124	Indirect forbidden energy gap	[2.18]
$E_{XL} = E(L_1^c) - E(\Delta_1^c)$ , eV	0.74		[1.41]
$E_{XR} = E(\Gamma_{15}^c) - E(\Delta_1^c)$ , eV	2.2	$E_{XR} = E'_0 - E_g$	[2.17]
$\Delta_0$ , meV	42.6	Spin-orbit splitting in the valence band at $\mathbf{k}=0$	[2.19]
$\Delta_1$ , meV	29	Spin-orbit splitting along $\Lambda$ line (apparent value)	[2.20]
$E'_0$ , eV	3.32		[2.17]
$E_1$ , eV	3.4		[2.17]
$E_2$ , eV	4.27		[2.17]
$dE_g/dp$ , eV/GPa	-0.0141	Minus sign indicates that the gap decreases with hydrostatic pressure	[2.21]
$dE'_0/dp$ , eV/GPa	$0.01 \pm 0.01$		[2.22]
$dE_1/dp$ , eV/GPa	0.062		[2.22]
$dE_2/dp$ , eV/GPa	0.029		[1.38]



**TABLE 2.7** Si conduction band principal valley parameters

Parameter	X valley*	L valley	$\Gamma$ valley	Reference
Valley location in the Brillouin zone	$\Delta_1$ , on $\langle 100 \rangle$ axis at the distance $k_0/k_{\max} = 0.85 \pm 0.005$	$L_1$ , on the boundary of the zone in $\langle 111 \rangle$ direction	$\Gamma_{15}$ , in the center of the zone	
Number of valleys	6	4	1	
Valley separation relative to the lowest X valley, eV	0	0.74	2.2	[1.41]
Electron masses:				
scalar $m_n/m_0$			0.156**	[2.23]
longitudinal $m_l/m_0$	0.916	1.42		[2.24, 2.23]
transverse $m_t/m_0$	0.19	0.13		[2.24, 2.23]
conductivity $m_c/m_0$	0.259	0.19	0.156	
density-of-states $m_d/m_0$	0.321	0.288	0.156	
Uniaxial deformation				
potential $\Xi_u$ , eV	8.77			[2.25]
$g_c$ -factor	1.998 75			[2.26]

\* — It is the most important valley in transport property analysis.

\*\* — Calculated.

**TABLE 2.8** Si valence band parameters

Parameter	Value	Reference
<b>Light and heavy mass bands at <math>\Gamma_{8v}^+</math></b>		
Luttinger parameters:		
$\gamma_1$	4.22	[2.27]
$\gamma_2$	0.53	[2.27]
$\gamma_3$	1.38	[2.27]
$g_v$ -factor: $2k$	-0.84	[2.28]
$q$	0.01	[2.28]
Valence band nonsphericity $\delta$	0.2	
Average heavy hole mass for "spherical" bands $m_h/m_0$	0.467	
Average light hole mass for "spherical" bands $m_l/m_0$	0.159	
Density-of-states mass $m_a/m_0$	0.527	
Uniaxial deformation potentials, eV		
$D_u$	2.88	[2.29]
$D'_u$	4.19	[2.29]
<b>Spin-orbit split-off valence band at <math>\Gamma_{7v}^+</math></b>		
$\Delta_0 = E(\Gamma_{8v}^+) - E(\Gamma_{7v}^+)$ , meV	42.6	[2.19]
Average mass for "spherical" bands $m_{so}/m_0$	0.29	[2.30]

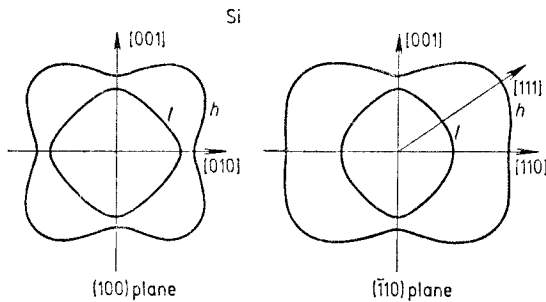


Fig. 2.10. Si valence band warping. The contours are the constant energy surfaces of heavy ( $h$ ) and light ( $l$ ) mass bands in (100) and  $(\bar{1}10)$  planes. The band nonparabolicity is not included (cf. Fig. 2).

Fig. 2.11. Location of the lowest energies in the conduction band indicated by dots and constant energy surfaces (spheroids) in the Brillouin zone of Si. The crosses on the axes show the edges of the Brillouin zone where wave vector is  $k_{\max}$ . Arrows indicate the intervalley scattering:  $g$ -type (on the same axis) and  $f$ -type (between perpendicular axes).  $k_0 = 0.85 k_{\max}$ .

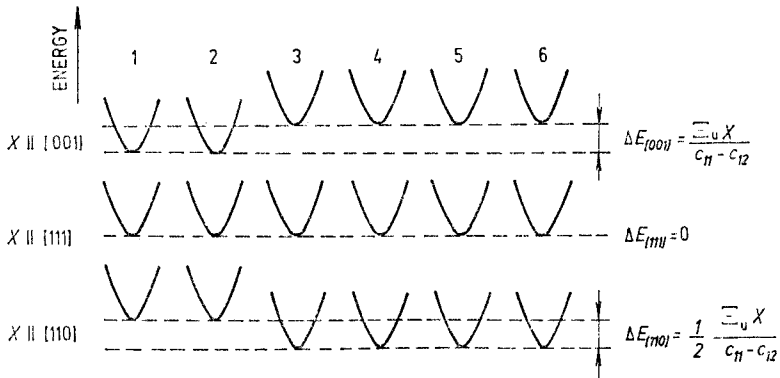
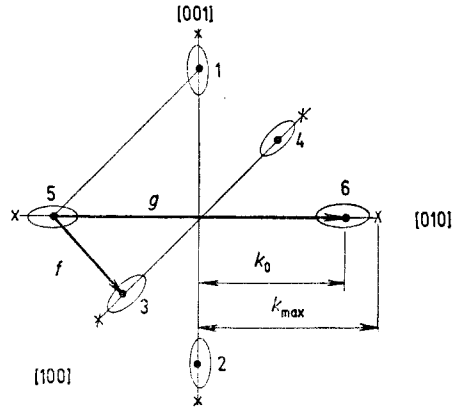


Fig. 2.12.  $X$  valley splitting under uniaxial compressive stress  $X$  (cf. Fig. 2.11 for valley numbering). The stress removes sixfold degeneracy and, as a result, the energy difference  $\Delta E$  appears between different groups of valleys.  $\Xi_u$  is uniaxial deformation potential.  $\Xi_u = 8.77$  eV for  $n$ -Si [2.25].

**Si valence band splitting under uniaxial compressive stress** is similar to that of Ge (see Table 1.8). For Si the valence band uniaxial deformation potential and elastic constant values can be found in Tables 2.1 and 2.8.

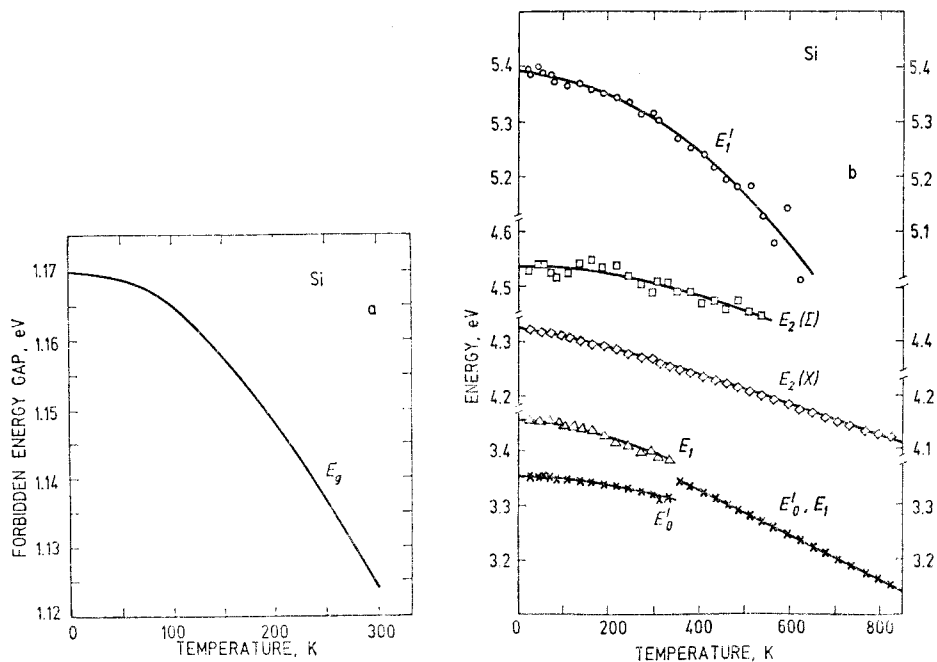


Fig. 2.13. Temperature dependence of  $a$  – indirect forbidden energy gap  $E_g$  [2.18] and  $b$  – interband critical-point energies  $E'_1$ ,  $E_2$ ,  $E_1$  and  $E'_0$  in Si (see Fig. 2.9,  $b$  for corresponding optical transitions). The solid lines are the best fits with empirical formulas and parameter values listed in Table 2.9 [2.17].

**TABLE 2.9** Values of the parameters  $a$ ,  $b$  and  $\Theta$  in equation  $E(T) = a - b[1 + 2/(e^{\Theta/T} - 1)]$ , which have been obtained by fitting the critical point energies vs. temperature  $T$  in Fig. 2.13

Critical point	$a$ , eV	$b$ , eV	$\Theta$ , K
$E'_0$	3.38	0.025	267
$E_1$ at $T < 350$ K	3.49	0.039	245
$E_1$ at $T > 350$ K	$E_1 [\text{eV}] = 3.486 - 4.07 \cdot 10^{-4} T [\text{K}]$		
$E_2(X)$	4.35	0.027	199
$E_2(\Sigma)$	4.63	0.098	624
$E'_1$	5.72	0.336	703

**Indirect energy gap**, Fig. 2.13,  $a$ , can be fitted by equations [2.18]:

$$E_g(T) = 1.17 + 1.059 \cdot 10^{-5} T - 6.05 \cdot 10^{-7} T^2, \quad 0 < T \leq 190 \text{ K},$$

$$E_g(T) = 1.1785 - 9.025 \cdot 10^{-5} T - 3.05 \cdot 10^{-7} T^2, \quad 150 \leq T \leq 300 \text{ K}.$$

$E_g$  is in eV and  $T$  is in K.

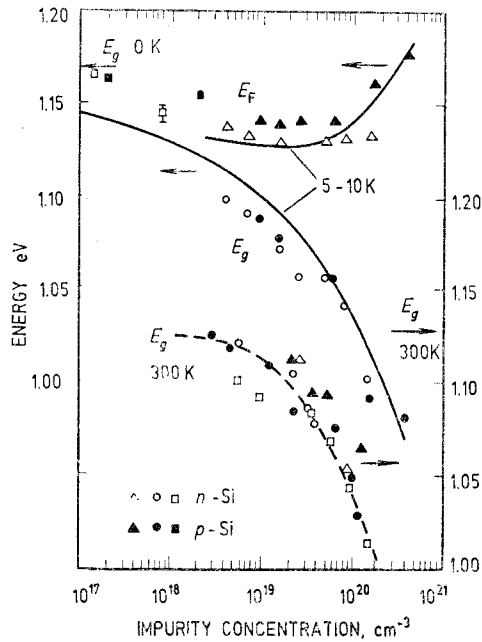


Fig. 2.14. Forbidden energy gap  $E_g$  and Fermi energy  $E_F$  relative to the valence band edge for  $n$ -Si or conduction band edge for  $p$ -Si as a function of impurity concentration: 5-10 K [2.31]; 300 K, squares - [2.32], triangles - [2.33], circles - [2.34]. Arrows on the energy scale indicate  $E_g$  of pure silicon at  $T=0$  K and  $T=300$  K.

### 2.3. Si optical properties

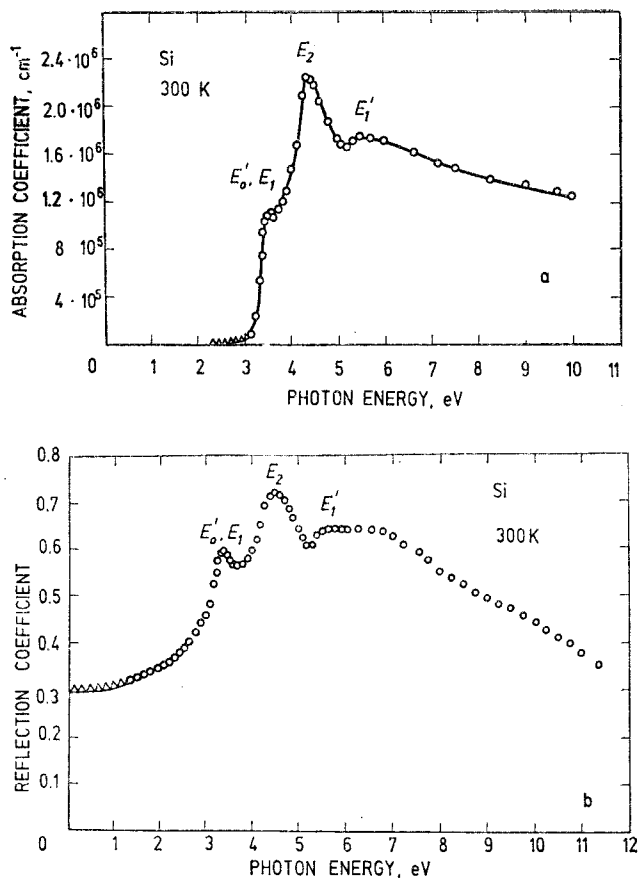


Fig. 2.15. Dependence of absorption (a) and reflection (b) coefficients of Si on photon energy [2.35].

**Refractive index** of Si in the range  $\lambda = 2.4 - 25 \mu\text{m}$  can be approximated by the dispersion formula [2.36]:

$$n = A + BL + CL^2 + D\lambda^2 + E\lambda^4,$$

where  $A = 3.419\ 83$ ,  $B = 0.159\ 906$ ,  $L = 1/(\lambda^2 - 0.028)$ ,  $C = -0.123\ 109$ ,  $D = 1.268\ 78 \cdot 10^{-6}$ ,  $E = -1.951\ 04 \cdot 10^{-9}$ .  $\lambda$  is in micrometers.

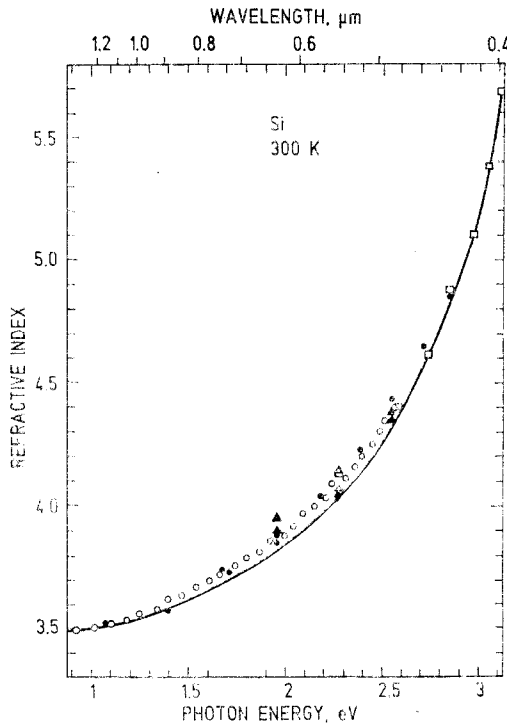


Fig. 2.16. Refractive index of Si at room temperature. Different symbols and a line correspond to different sources [2.37].

**Absorption coefficient** of Si in the photon energy range  $\hbar\omega = 1.05 - 2.7$  eV at temperature 298 K can be approximated by the empirical dispersion formula [2.38]:

$$\alpha = (\hbar\omega)^{-1} \left[ \sum_{i=1}^2 \sum_{j=-1}^1 \{ c_{ij} [f(\hbar\omega - \varepsilon_1 + j d\varepsilon_i)]^2 \} + c_3 [2f(\hbar\omega - \varepsilon_3)]^{(N+dN\hbar\omega)} \right],$$

where  $j=0$  is not used in the second sum and

$$f(x) = (x + |x|)/2.$$

The values of parameters are given below

Parameter	Value	Parameter	Value
$\varepsilon_1$ , eV	1.099 69	$c_{2, -1}$ , eV/cm	1 634.30
$d\varepsilon_1$ , eV	0.058 314 8	$\varepsilon_3$ , eV	1.409 85
$c_{1, +1}$ , eV/cm	483.916	$c_3$ , eV/cm	1 046.08
$c_{1, -1}$ , eV/cm	5 030.02	$dN$ , eV <sup>-1</sup>	1.230 84
$d\varepsilon_2$ , eV	0.022 016 1	$N$	0.394 122
$c_{2, +1}$ , eV/cm	79.407 9		

The units of parameters give  $\alpha$  in cm<sup>-1</sup>.

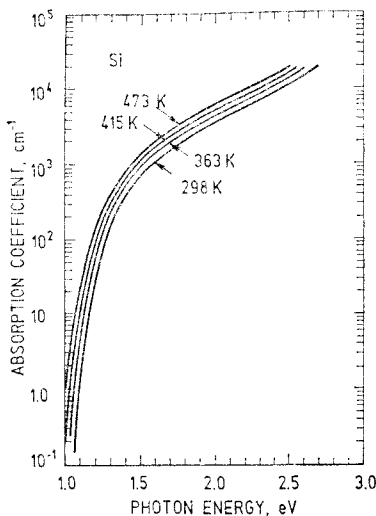


Fig. 2.17. Optical absorption coefficient of Si at lattice temperature  $T=298$ , 363, 415 and 473 K [2.39].

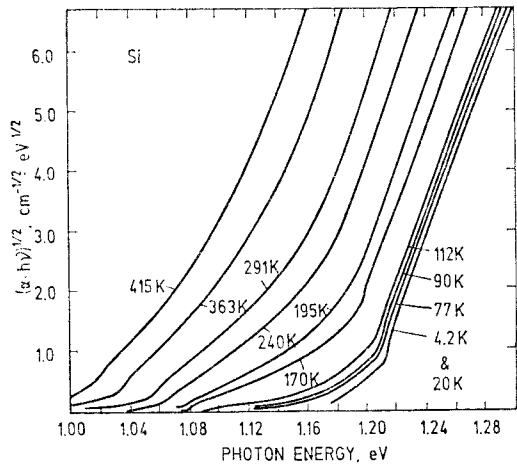


Fig. 2.18. Optical low-intensity absorption spectrum of high-purity Si (square root of absorption coefficient multiplied by photon energy vs. photon energy) near band gap energy at various temperatures [2.40].



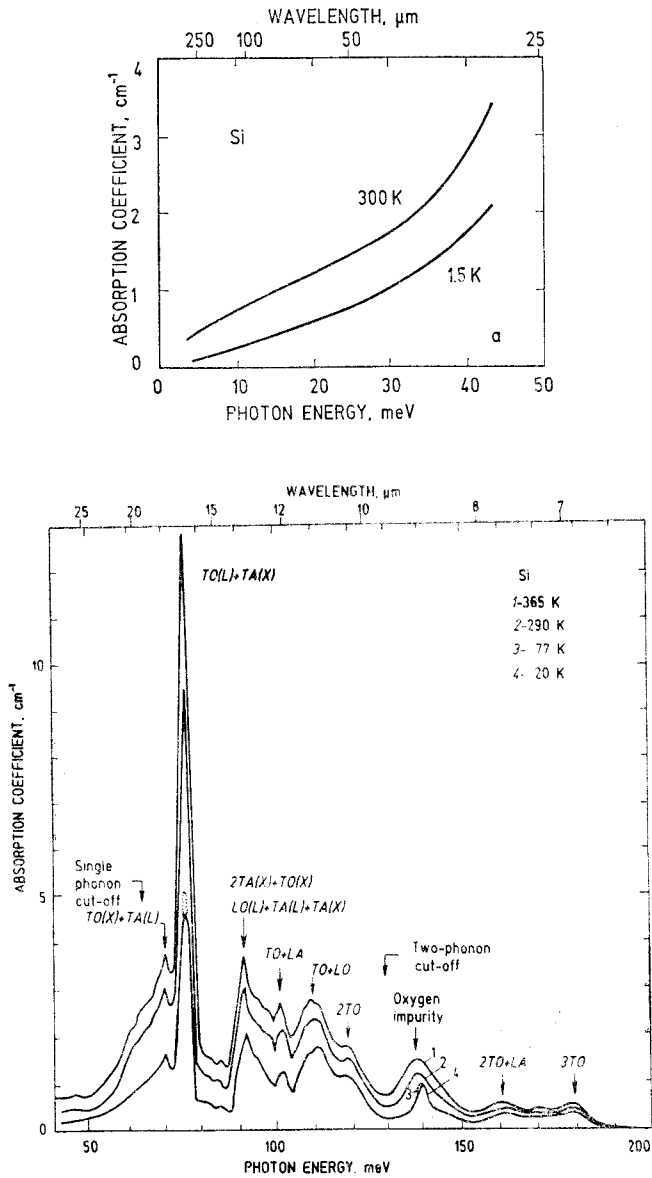


Fig. 2.19. Lattice optical absorption of Si at different temperatures: *a* – in the single-phonon region [1.55], *b* – in the multiphonon region [2.41]. For phonon assignment see Table 2.2.

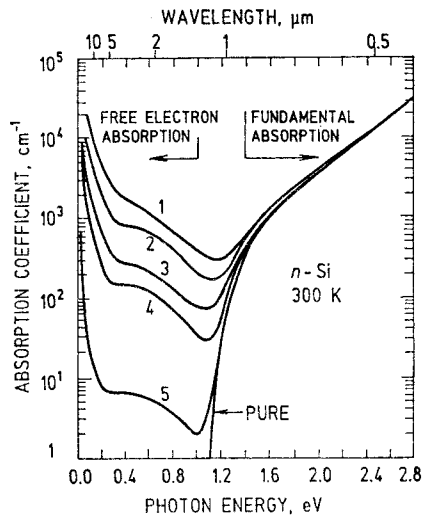


Fig. 2.20. Optical absorption spectra of *n*-Si at room temperature showing the influence of various concentrations of free electrons: 1 —  $n = 4 \cdot 10^{19} \text{ cm}^{-3}$ , 2 —  $2.4 \cdot 10^{19} \text{ cm}^{-3}$ , 3 —  $1 \cdot 10^{19} \text{ cm}^{-3}$ , 4 —  $6 \cdot 10^{18} \text{ cm}^{-3}$ , 5 —  $3.2 \cdot 10^{17} \text{ cm}^{-3}$  [2.42].

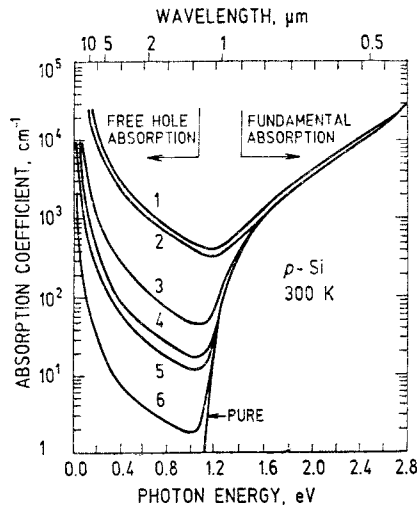


Fig. 2.21. Optical absorption spectra of *p*-Si at room temperature showing the influence of various concentrations of free holes: 1 —  $p = 1 \cdot 10^{20} \text{ cm}^{-3}$ , 2 —  $7 \cdot 10^{19} \text{ cm}^{-3}$ , 3 —  $1.2 \cdot 10^{19} \text{ cm}^{-3}$ , 4 —  $5 \cdot 10^{18} \text{ cm}^{-3}$ , 5 —  $2.8 \cdot 10^{18} \text{ cm}^{-3}$ , 6 —  $5 \cdot 10^{17} \text{ cm}^{-3}$  [2.42].

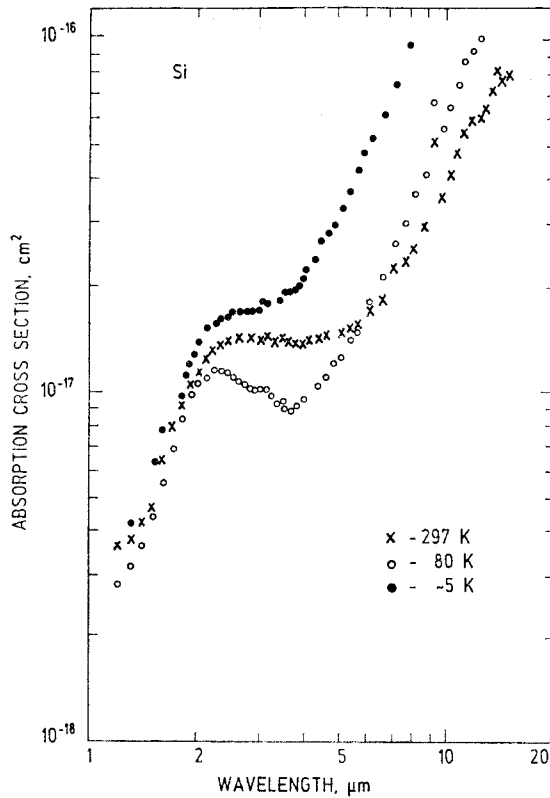


Fig. 2.22. Free electron absorption cross section vs. photon wavelength at three lattice temperatures for  $n$ -Si. Full circles — 5 K, open circles — 80 K, crosses — 297 K. The measurements have been performed for a sample with electron concentration  $1.7 \cdot 10^{17} \text{ cm}^{-3}$  [2.43].

**TABLE 2.10** Properties of free excitons and excitons bound to impurities in Si as observed in luminescence experiments (see also Fig. 2.23)

Particle	Dissociation channel	Particle lifetime, $\mu\text{s}$	Luminescence energy, meV	Comments, reference
<b>Free exciton, <math>X</math></b>				
$X_{TA}$	$h\nu + TA$		1135.8	1.8–4.2 K, $\rho(300\text{ K}) = 4 \cdot 10^4 \Omega \cdot \text{cm}$ [2.44]
$X_2$	$h\nu + X + TA$		1134.6	1.8–4.2 K, $\rho(300\text{ K}) = 4 \cdot 10^4 \Omega \cdot \text{cm}$ , biexciton [2.44]
$X_{LO}$	$h\nu + LO$		1098.2	4.5–10 K [2.45]
$X_{TO}$	$h\nu + TO$		1096.3	4.5–10 K [2.45]
$X$		1–100		2–10 K, free exciton lifetime increases with temperature [2.46, 2.47]
<b>Exciton(s) bound to donor, <math>[DX_n]</math></b>				
$[PX]$	$P + h\nu$	0.245	1150.1	4.2 K, $N_P = 1.5 \cdot 10^{14} \text{ cm}^{-3}$ , intense line [2.48]
$[PX_2]$	$[PX] + h\nu$	0.134	1146.4	4.2 K, $N_P = 1.5 \cdot 10^{14} \text{ cm}^{-3}$ [2.48]
$[PX_3]$	$[PX_2] + h\nu$	0.095	1143.7	4.2 K, $N_P = 1.5 \cdot 10^{14} \text{ cm}^{-3}$ [2.48]
$[PX]_{TA}$	$P + h\nu + TA$		1131.04	4.5 K, $N_P = 1.4 \cdot 10^{14} \text{ cm}^{-3}$ [2.45]
$[PX]_{LO}$	$P + h\nu + LO$		1094.03	4.5 K, $N_P = 1.4 \cdot 10^{14} \text{ cm}^{-3}$ [2.45]
$[PX]_{TO}$	$P + h\nu + TO$		1091.83	4.2 K, $N_P = 1.5 \cdot 10^{14} \text{ cm}^{-3}$ , intense line [2.48]
$[PX_2]_{TO}$	$[PX] + h\nu + TO$		1088.2	4.2 K, $N_P = 1.5 \cdot 10^{14} \text{ cm}^{-3}$ [2.48]
$[\text{Li}X]$	$\text{Li} + h\nu$		1151.2	Unobserved [2.45]
$[\text{Li}X]_{TA}$	$\text{Li} + h\nu + TA$		1132.62	6 K, $N_{\text{Li}} = 8 \cdot 10^{14} \text{ cm}^{-3}$ [2.45]
$[\text{Li}X]_{LO}$	$\text{Li} + h\nu + LO$		1095.07	6 K, $N_{\text{Li}} = 8 \cdot 10^{14} \text{ cm}^{-3}$ [2.45]
$[\text{Li}X]_{TO}$	$\text{Li} + h\nu + TO$	1.1	1093.21	6 K, $N_{\text{Li}} = 8 \cdot 10^{14} \text{ cm}^{-3}$ , intense line [2.45]
$[\text{Sb}X]$	$\text{Sb} + h\nu$		1150.1	4.2 K, $N_{\text{Sb}} = 1.7 \cdot 10^{15} \text{ cm}^{-3}$ [2.49]
$[\text{Sb}X]_{LO}$	$\text{Sb} + h\nu + LO$		1094.1	4.2 K, $N_{\text{Sb}} = 1.7 \cdot 10^{15} \text{ cm}^{-3}$ [2.49]
$[\text{Sb}X]_{TO}$	$\text{Sb} + h\nu + TO$		1092.1	4.2 K, $N_{\text{Sb}} = 1.7 \cdot 10^{15} \text{ cm}^{-3}$ [2.48]
$[\text{As}X]$	$\text{As} + h\nu$		1149.2	4.2 K, $N_{\text{As}} = 4 \cdot 10^{15} \text{ cm}^{-3}$ [2.50]
$[\text{As}X]_{TA}$	$\text{As} + h\nu + TA$		1130.5	20 K, $N_{\text{As}} = 4 \cdot 10^{15} \text{ cm}^{-3}$ [2.50]
$[\text{As}X]_{TO}$	$\text{As} + h\nu + TO$		1090.7	15 K, $N_{\text{As}} = 2 \cdot 10^{17} \text{ cm}^{-3}$ [2.51]
$[\text{As}X]$		0.183*		4.2 K [2.52]
$[\text{Bi}X]$	$\text{Bi} + h\nu$		1146.9	15 K, $N_{\text{Bi}} = 3 \cdot 10^{16} \text{ cm}^{-3}$ [2.51]
$[\text{Bi}X]_{TO}$	$\text{Bi} + h\nu + TO$		1088.8	15 K, $N_{\text{Bi}} = 3 \cdot 10^{16} \text{ cm}^{-3}$ [2.51]

TABLE 2.10 (Continued)

Particle	Dissociation channel	Particle lifetime, $\mu$ s	Luminescence energy, meV	Comments, reference
<b>Exciton(s) bound to acceptor, <math>[AX_n]</math></b>				
[BX]	$B + h\nu$		1150.7	Boron complex spectra [2.53]
[BX] <sub>TA</sub>	$B + h\nu + TA$		1131.6	were obtained with [2.53]
[BX <sub>2</sub> ] <sub>TA</sub>	$[BX] + h\nu + TA$		1129.2	samples having $N_B =$ [2.53]
[BX] <sub>LO</sub>	$B + h\nu + LO$		1094.3	$1.6 \cdot 10^{16} - 7.5 \cdot 10^{17} \text{ cm}^{-3}$ in the temperature range 10–15 K [2.53]
[BX] <sub>TO</sub>	$B + h\nu + TO$		1092.5	Intense line [2.53]
[BX <sub>2</sub> ] <sub>TO</sub>	$[BX] + h\nu + TO$		1090.3	[2.53]
[BX]		1.055*		4.2 K, $\rho(300 \text{ K}) = 100 \Omega \cdot \text{cm}$ [2.52]
[AlX]	$Al + h\nu$	0.104	1149.5	4.2 K, $N_{Al} =$ [2.54, $5 \cdot 10^{14} \text{ cm}^{-3}$ 2.55]
[AlX] <sub>TA</sub>	$Al + h\nu + TA$		1131	9 K, $N_{Al} = 2.2 \cdot 10^{16} \text{ cm}^{-3}$ [2.53]
[AlX] <sub>TO</sub>	$Al + h\nu + TO$		1092	9 K, $N_{Al} = 2.2 \cdot 10^{16} \text{ cm}^{-3}$ [2.53]
[AlX]		0.076*		4.2 K [2.52]
[GaX]	$Ga + h\nu$		1149	4.2 K, $N_{Ga} = 2 \cdot 10^{15} \text{ cm}^{-3}$ [2.55]
[GaX] <sub>TA</sub>	$Ga + h\nu + TA$		1131	9.5 K, $N_{Ga} = 10^{17} \text{ cm}^{-3}$ [2.53]
[GaX] <sub>TO</sub>	$Ga + h\nu + TO$		1091	9.5 K, $N_{Ga} = 10^{17} \text{ cm}^{-3}$ [2.53]
[GaX]		0.077*		4.2 K [2.53]
[InX]	$In + h\nu$		1140.8	7 K, $N_{In} = 3.2 \cdot 10^{15} \text{ cm}^{-3}$ [2.55]
[InX] <sub>TA</sub>	$In + h\nu + TA$		1121.6	11.3 K, $N_{In} = 1.3 \cdot 10^{17} \text{ cm}^{-3}$ [2.53]
[InX] <sub>TO</sub>	$In + h\nu + TO$		1082.6	11.3 K, $N_{In} = 1.3 \cdot 10^{17} \text{ cm}^{-3}$ [2.53]
[InX]		0.0027*		4.2 K [2.52]
[TlX]	$Tl + h\nu$		1110.5	11.1 K, $N_{Tl} = 3 \cdot 10^{15} \text{ cm}^{-3}$ [2.53]
[BeX]	$Be + h\nu$	4.6	1078.27	15–40 K, intense line [2.56]
[BeX]	$Be + h\nu'$	180	1076.34	1.2–15 K [2.56]
[BeX]	$Be + h\nu''$	480	1075.74	1.2 K [2.56]

*LO, TO, TA* are longitudinal optical, transverse optical and transverse acoustical phonon energies.  $h\nu$  is photon energy.

Excitonic energy gap  $E_{gX} = 1154.59 \pm 0.1 \text{ meV}$  [2.57].

Exciton binding energy  $E_X = 14.2 \text{ meV}$  [2.57a].

\* – The time dependence is similar for all phonon replicas and nonphonon lines.

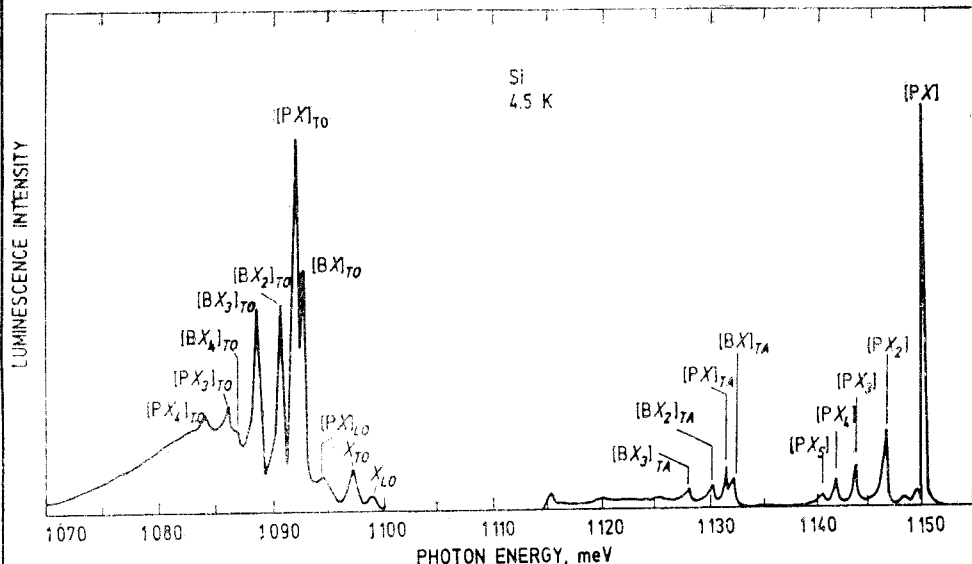


Fig. 2.23. Typical photoluminescence spectrum due to radiative decay of free excitons and excitonic complexes in Si doped with  $1.4 \cdot 10^{14} \text{ cm}^{-3}$  phosphorus atoms and compensated by  $1.6 \cdot 10^{13} \text{ cm}^{-3}$  boron atoms [2.45]. Dissociation channels and peak energies are given in Table 2.10.

**Relative change of the refractive index with the hydrostatic pressure  $p$  [2.12]:**

$$(1/n)(dn/dp) = -1.4 \cdot 10^{-3} \text{ 1/GPa at } 1-2 \text{ } \mu\text{m and } 294 \text{ K.}$$

$$n = 3.55 - 3.45 \text{ at } 1-2 \text{ } \mu\text{m [2.37, 1.54].}$$

**Temperature dependence of the refractive index in the wavelength range from 1.2 to 12  $\mu\text{m}$  at room temperature [1.18]:**

$$(1/n)(dn/dT) = 4.7 \cdot 10^{-5} \text{ K}^{-1}.$$

**TABLE 2.11** Elastooptic and piezooptic coefficients of Si at lattice temperature  $T=300 \text{ K}$  and different laser wavelengths [2.58, 2.59, 2.60]

Coefficient	0.4579 $\mu\text{m}$	0.6471 $\mu\text{m}$	3.39 $\mu\text{m}$
<b>Elastooptic, dimensionless</b>			
$p_{11}$	-0.145	-0.152	-0.094
$p_{12}$	-0.092	-0.05	0.017
$p_{44}$	-0.057	-0.058	-0.051
<b>Piezooptic, 1/GPa</b>			
$\pi_{11} - \pi_{12}$	$5.9 \cdot 10^{-4}$	$9.3 \cdot 10^{-4}$	
$\pi_{44}$	$1.05 \cdot 10^{-3}$	$6.9 \cdot 10^{-4}$	
$\frac{1}{2}(\pi_{11} - \pi_{12} + \pi_{44})$		$8.8 \cdot 10^{-4}$	
<b>Refractive index</b>			
$n$	4.51	3.83	3.43

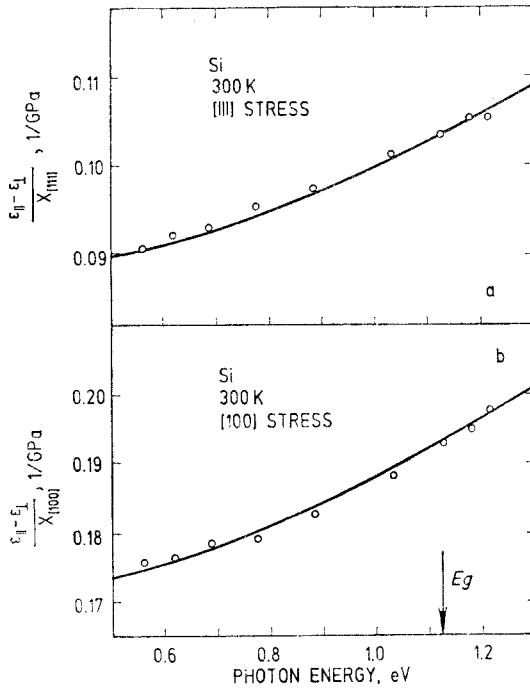


Fig. 2.24. Piezoelectric effect. Measured values (points) and fitted curves of  $(\epsilon_{\parallel} - \epsilon_{\perp})/X_{[111]} = -n^4 \pi_{44}$  and  $(\epsilon_{\parallel} - \epsilon_{\perp})/X_{[100]} = -n^4 (\pi_{11} - \pi_{12})$  for Si as a function of photon energy, where  $\epsilon_{\parallel}$  and  $\epsilon_{\perp}$  are the relative dielectric permittivities for light polarized parallel and perpendicular to the uniaxial stress  $X$  applied in [111] and [100] directions.  $n$  is the refractive index and  $\pi_{ij}$  are the piezoelectric constants.  $T=300$  K [1.66].

**Electrooptic coefficients.** All linear electrooptic coefficients (Pockels coefficients) of Si are equal to zero:  $r_{ijk}=0$ .

**Nonlinear susceptibility.** Second-order nonlinear susceptibility of Si is equal to zero because silicon is centrosymmetric.

Valence electron contribution to the third-order nonlinear susceptibility  $c_{ijkl}(\omega_2 - 2\omega_1, \omega_1, \omega_1, -\omega_2)$  of Si measured by mixing  $\lambda_1 = 10.6 \mu\text{m}$  and  $\lambda_2 = 9.5 \mu\text{m}$  radiation [1.67]:

$$|c_{1111}| = 8.4 \cdot 10^{-20} \text{ m}^2/\text{V}^2, \text{ 10 \% accuracy,}$$

$$c_{1122}/c_{1111} = 0.48 \pm 0.03.$$

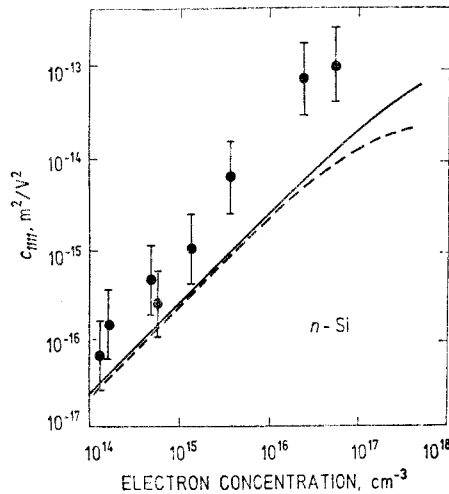


Fig. 2.25. Absolute values of third-order nonlinear susceptibility  $c_{1111}(3\omega, \omega, \omega, \omega)$  measured by frequency tripling of 0.5 mm radiation, vs. free electron concentration, for  $n$ -Si at room temperature. The anisotropy of susceptibility is  $\sigma = (1 + 3c_{1122}/c_{1111})/2 = 0.86 \pm 0.02$ . The curves are theoretical predictions for the nonparabolicity (solid line) and relaxation (dashed line) contributions, respectively [1.68].

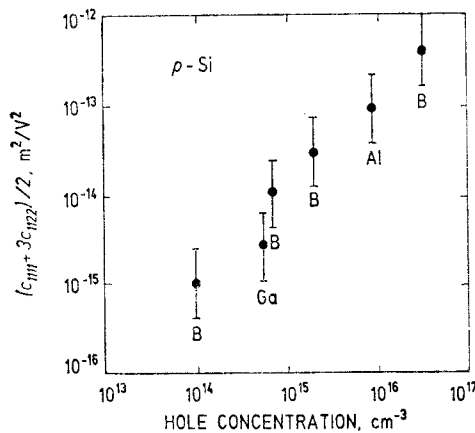


Fig. 2.26. Absolute values of third-order effective nonlinear susceptibility  $(c_{1111} + 3c_{1122})/2$  measured by frequency tripling of 0.5 mm radiation, vs. free hole concentration of boron, gallium and aluminium, for  $p$ -Si at room temperature. The anisotropy of susceptibility is  $\sigma = (1 + 3c_{1122}/c_{1111})/2 = 1.61 \pm 0.06$  [1.68].



## 2.4. Si electrical properties

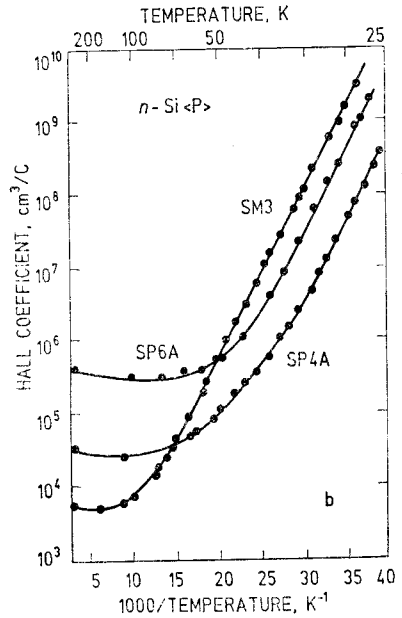
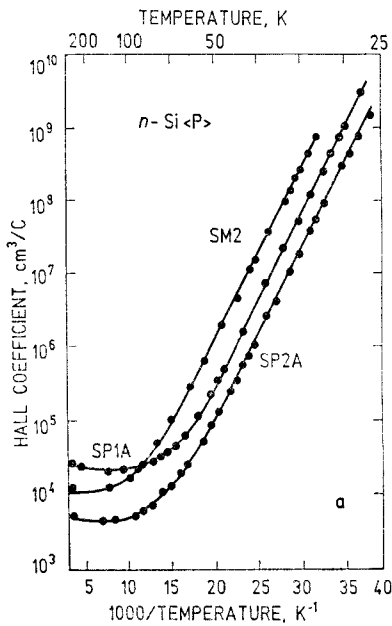


Fig. 2.27. Hall coefficient of two sets of phosphorus doped  $n$ -Si samples as a function of inverse temperature. For parameter values of set  $a$  and  $b$  see Table 2.12 [2.61].

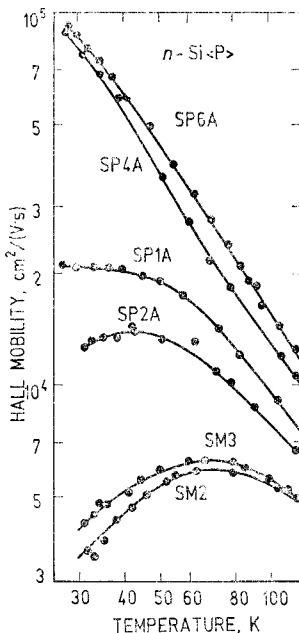


TABLE 2.12 Concentrations of phosphorus  $N_D$  (donor) and of compensating acceptor  $N_A$  for silicon samples in Fig. 2.27 and Fig. 2.28

Sample	$N_D, \text{cm}^{-3}$	$N_A, \text{cm}^{-3}$
SP6A	$2.8 \cdot 10^{13}$	$0.75 \cdot 10^{13}$
SP4A	$2.35 \cdot 10^{14}$	$0.1 \cdot 10^{14}$
SP1A	$6.7 \cdot 10^{14}$	$3.8 \cdot 10^{14}$
SP2A	$2.3 \cdot 10^{15}$	$0.83 \cdot 10^{15}$
SM2	$3.9 \cdot 10^{15}$	$3.3 \cdot 10^{15}$
SM3	$4.5 \cdot 10^{15}$	$3.3 \cdot 10^{15}$

Fig. 2.28. Hall mobility of two sets of phosphorus doped  $n$ -Si samples as a function of temperature. For parameter values see Table 2.12 [2.61].

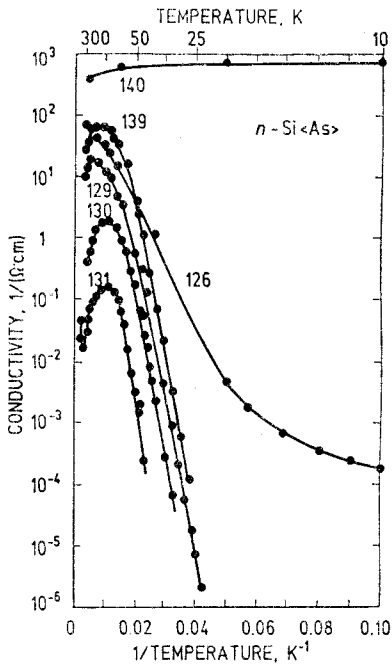


Fig. 2.29. Conductivity of *n*-Si doped with arsenic vs. reciprocal temperature. Sample parameters are given in Table 2.13 [2.62].

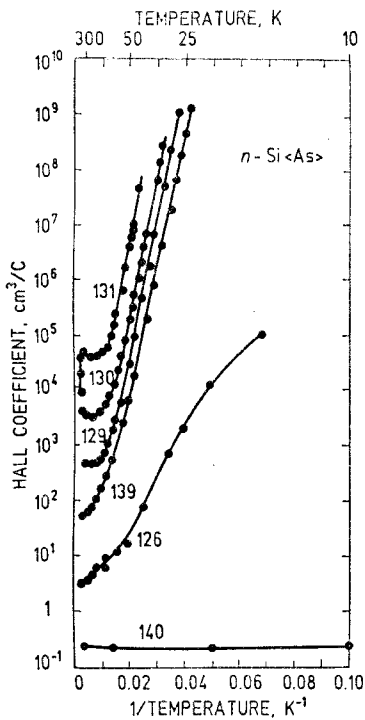


Fig. 2.30. Hall coefficient of *n*-Si doped with arsenic vs. reciprocal temperature. Sample parameters are given in Table 2.13 [2.62].

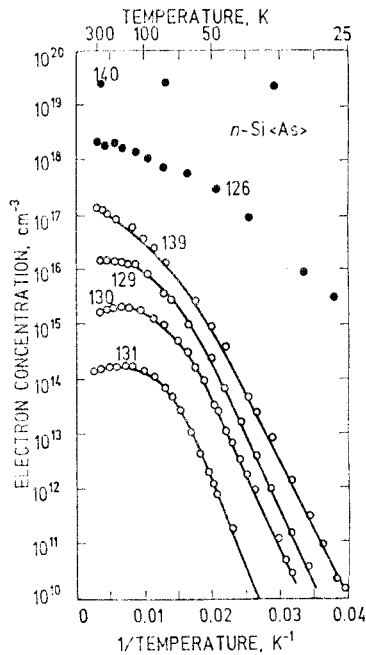


Fig. 2.31. Electron concentration of  $n$ -Si doped with arsenic as a function of reciprocal temperature. Sample parameters are given in Table 2.13 [2.62].

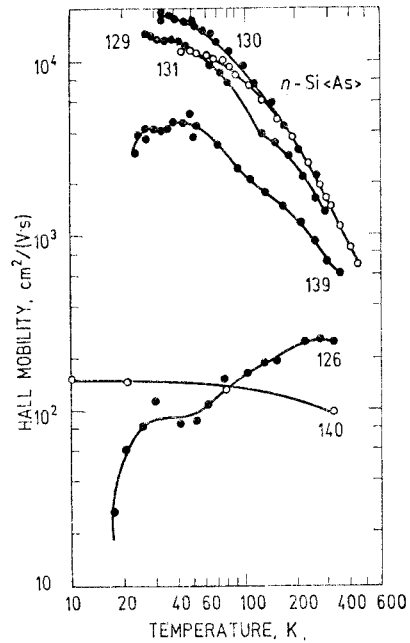


Fig. 2.32. Hall mobility of electrons in  $n$ -Si doped with arsenic as a function of temperature. Sample parameters are given in Table 2.13 [2.62].

**TABLE 2.13** Concentrations of arsenic  $N_D$  (donor) and of compensating acceptor  $N_A$  for silicon samples in Figs. 2.29–2.32

Sample	$N_D$ , $\text{cm}^{-3}$	$N_A$ , $\text{cm}^{-3}$
131	$1.75 \cdot 10^{14}$	$1.0 \cdot 10^{14}$
130	$2.1 \cdot 10^{15}$	$5.25 \cdot 10^{14}$
129	$1.75 \cdot 10^{16}$	$1.48 \cdot 10^{15}$
139	$1.3 \cdot 10^{17}$	$2.2 \cdot 10^{15}$
126	$2.2 \cdot 10^{18}$	
140	$2.7 \cdot 10^{19}$ (degenerate)	

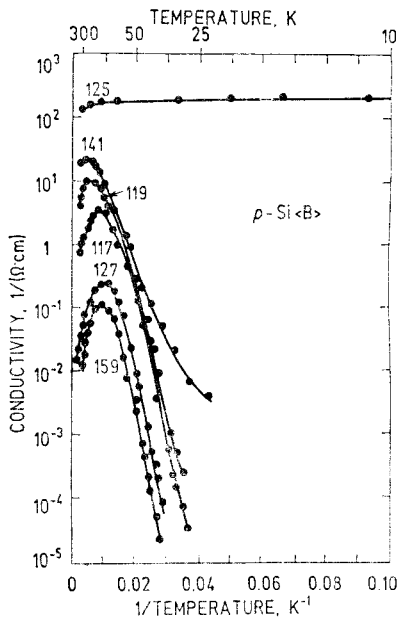


Fig. 2.33. Conductivity of  $p$ -Si doped with boron, as a function of reciprocal temperature. Sample parameters are given in Table 2.14 [2.62].

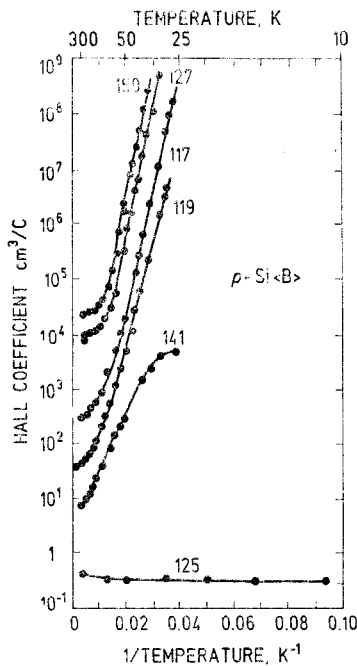


Fig. 2.34. Hall coefficient of  $p$ -Si doped with boron as a function of reciprocal temperature. Sample parameters are given in Table 2.14 [2.62].

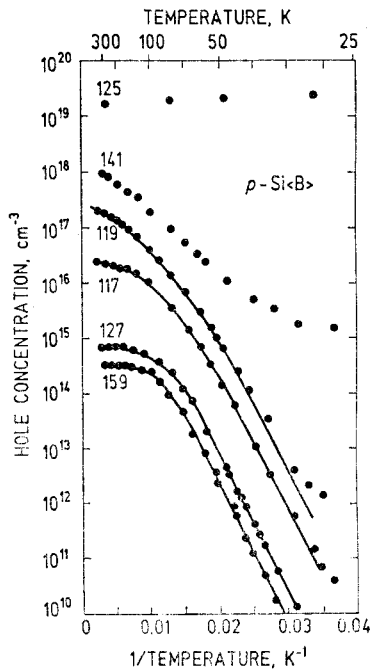


Fig. 2.35. Hole concentration of  $p$ -Si doped with boron as a function of reciprocal temperature. Sample parameters are given in Table 2.14 [2.62].

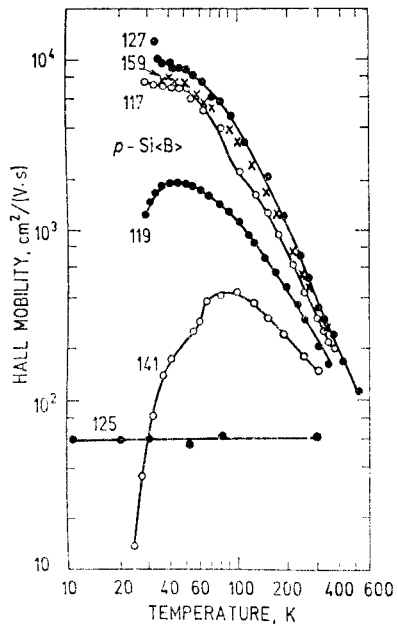


Fig. 2.36. Hall mobility of holes in  $p$ -Si doped with boron as a function of temperature. Sample parameters are given in Table 2.14 [2.62].

**TABLE 2.14** Concentrations of boron  $N_A$  (acceptor) and of compensating donor  $N_D$  for silicon samples in Figs. 2.33–2.36

Sample	$N_A$ , $\text{cm}^{-3}$	$N_D$ , $\text{cm}^{-3}$
159	$3.1 \cdot 10^{14}$	$4.1 \cdot 10^{14}$
127	$7.0 \cdot 10^{14}$	$2.2 \cdot 10^{14}$
117	$2.4 \cdot 10^{16}$	$2.3 \cdot 10^{15}$
119	$2.0 \cdot 10^{17}$	$4.9 \cdot 10^{15}$
141	$1.0 \cdot 10^{18}$	
125	$1.5 \cdot 10^{19}$ (degenerate)	

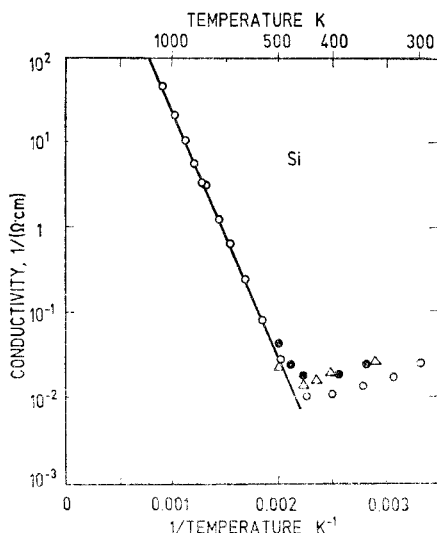


Fig. 2.37. Conductivity of Si vs. inverse temperature in the intrinsic region [2.62]. The intrinsic conductivity (solid line) can be approximated by empirical expression:  $\log_{10} \sigma_i = 4.247 - 2.924 \cdot 10^3/T$ , here,  $\sigma_i$  is in  $1/(\Omega \cdot \text{cm})$  and  $T$  is in K. At  $T = 300 \text{ K}$   $\sigma_i = 3.16 \cdot 10^{-6} \text{ } 1/(\Omega \cdot \text{cm})$  [2.63].

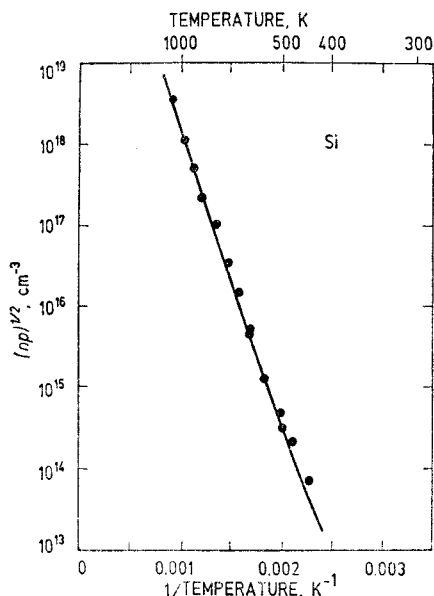


Fig. 2.38. Square root of the product of electron and hole concentration in the intrinsic region of Si as a function of reciprocal temperature [2.62].

Empirical expressions for intrinsic concentration: in the temperature range  $200 \text{ K} < T < 500 \text{ K}$  [2.64]  $n_i = \sqrt{np} = 5.71 \cdot 10^{19} (T/300)^{2.365} \exp(-6733/T)$ ; in the temperature range  $450 \text{ K} < T < 700 \text{ K}$  [2.62]  $n_i = \sqrt{np} = 3.87 \cdot 10^{16} T^{1.5} \exp(-7021/T)$ . Here,  $n_i$  is in  $\text{cm}^{-3}$  and  $T$  is in K. At  $T = 300 \text{ K}$   $n_i = 1.02 \cdot 10^{10} \text{ cm}^{-3}$ .

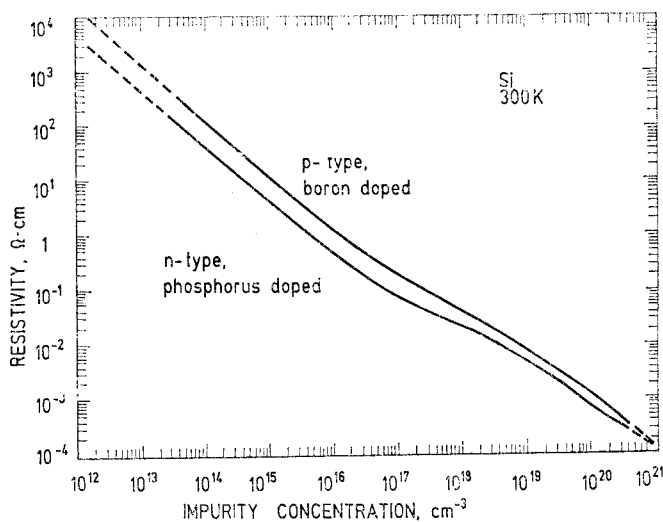


Fig. 2.39. Relation between resistivity and shallow impurity concentration for Si at 300 K [2.65]

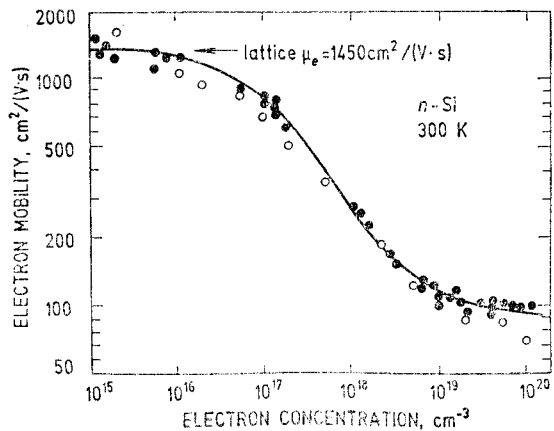


Fig. 2.40. Electron Hall mobility in  $n$ -Si at 300 K as a function of electron concentration. Solid line is the best fit with equation:  $\mu_e = 92 + 1268/[1 + (n/1.3 \cdot 10^{17})^{0.91}]$ ,  $\mu_e$  is in  $\text{cm}^2/(\text{V}\cdot\text{s})$  and  $n$  is in  $\text{cm}^{-3}$  [2.66].

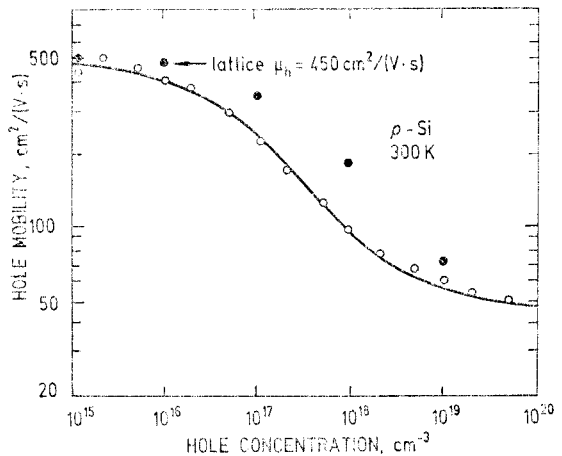


Fig. 2.41. Hole Hall mobility in  $p$ -Si at 300 K as a function of hole concentration. Solid line is the best fit with equation:  $\mu_h = 47.7 + 447.3/[1 + (p/6.3 \cdot 10^{16})^{0.76}]$ ,  $\mu_h$  is in  $\text{cm}^2/(\text{V}\cdot\text{s})$  and  $p$  is in  $\text{cm}^{-3}$  [2.66].

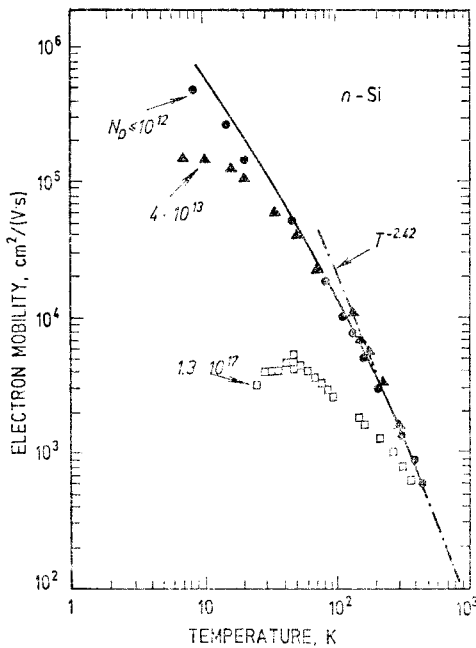


Fig. 2.42. Mobility of electrons in Si as a function of temperature for various donor concentrations: circles —  $N_D \leq 10^{12} \text{ cm}^{-3}$ , triangles —  $N_D = 4 \cdot 10^{13} \text{ cm}^{-3}$ , squares —  $N_D = 1.3 \cdot 10^{17} \text{ cm}^{-3}$ . The solid line indicates the theoretical results for pure lattice mobility [2.66]. The dot-dashed line gives  $\mu_e = 1.43 \cdot 10^9 T^{-2.42}$ ,  $\mu_e$  is in  $\text{cm}^2/(\text{V} \cdot \text{s})$  and  $T$  is in K.

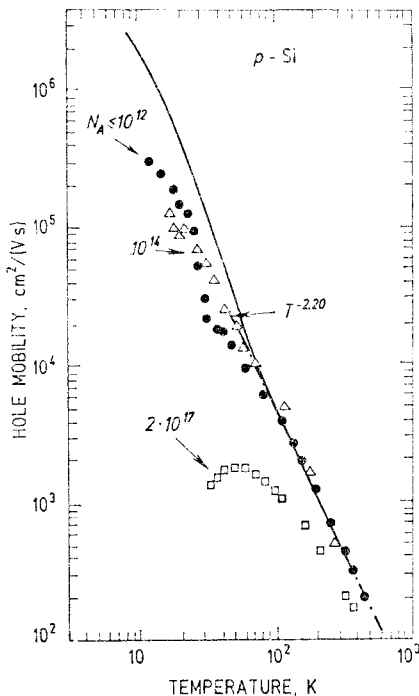


Fig. 2.43. Mobility of holes in Si as a function of temperature at various acceptor concentrations: circles —  $N_A \leq 10^{12} \text{ cm}^{-3}$ , triangles —  $N_A = 10^{14} \text{ cm}^{-3}$ , squares —  $N_A = 2 \cdot 10^{17} \text{ cm}^{-3}$ . The solid line indicates the theoretical results for pure lattice mobility [2.66]. The dot-dashed line gives  $\mu_h = 1.35 \cdot 10^8 T^{-2.2}$ ,  $\mu_h$  is in  $\text{cm}^2/(\text{V} \cdot \text{s})$  and  $T$  is in K.



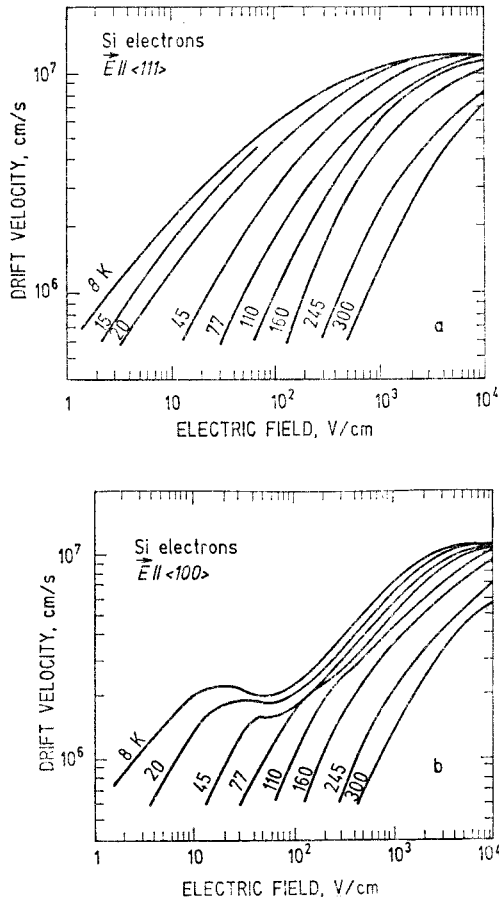


Fig. 2.44. Electron drift velocity in pure Si as a function of electric field at different lattice temperatures for two directions of electric field:  $a - E \parallel \langle 111 \rangle$ ,  $b - E \parallel \langle 100 \rangle$  [2.67].

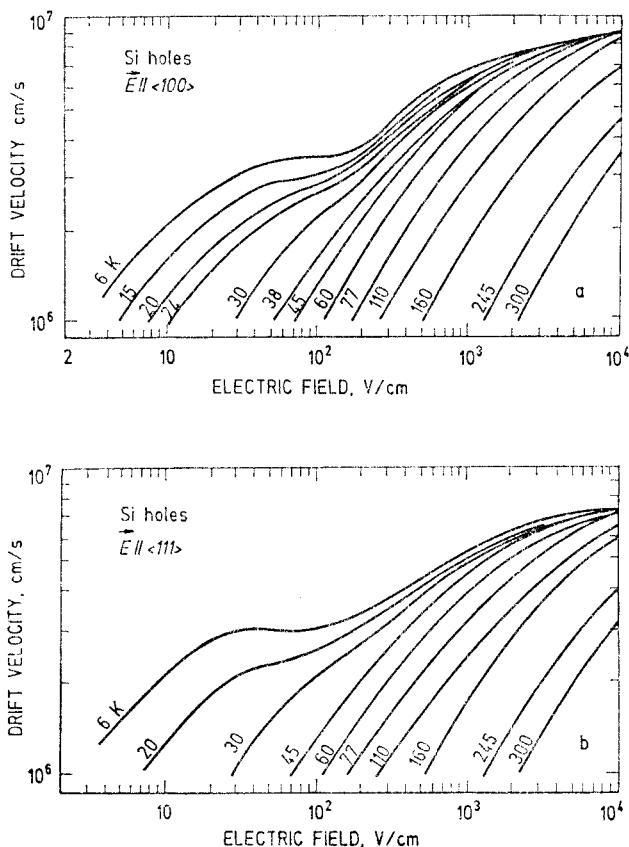


Fig. 2.45. Hole drift velocity in pure Si as a function of electric field at different temperatures for two directions of electric field: *a* –  $E \parallel \langle 100 \rangle$ , *b* –  $E \parallel \langle 111 \rangle$  [2.68].

Electron and hole drift velocities as functions of the electric field applied along  $\langle 111 \rangle$  direction can be fitted by equation [2.66]:

$$v_d = v_m \frac{E/E_c}{[1 + (E/E_c)^\beta]^{1/\beta}}.$$

The values and temperature dependences of parameters  $v_m$ ,  $E_c$  and  $\beta$  for  $T > 250$  K are given in Table 2.15.

**TABLE 2.15** Parameters for drift velocity in  $\langle 111 \rangle$  direction.  $T$  is temperature in Kelvins

Parameter	Electrons	Holes
$v_m$ , cm/s	$1.53 \cdot 10^9 T^{-0.87}$	$1.62 \cdot 10^8 T^{-0.52}$
$E_c$ , V/cm	$1.01 \cdot T^{1.55}$	$1.24 \cdot T^{1.68}$
$\beta$	$2.57 \cdot 10^{-2} T^{0.66}$	$0.46 \cdot T^{0.17}$

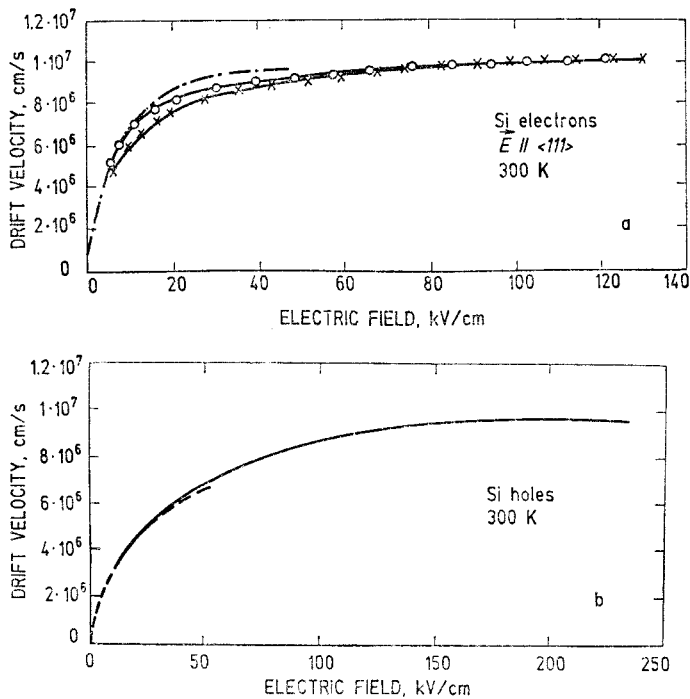


Fig. 2.46. Drift velocity of  $a$  — electrons and  $b$  — holes in pure Si at very high electric fields and at 300 K [2.69, 2.70].

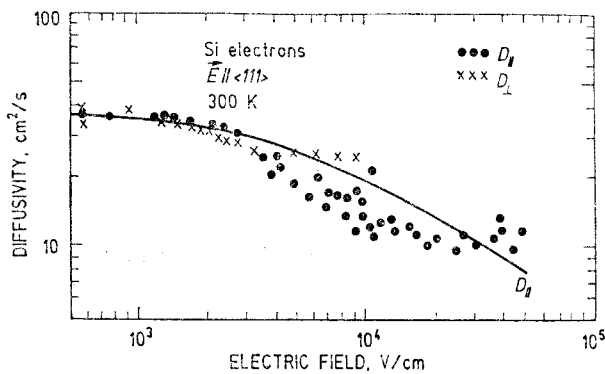


Fig. 2.47. Parallel  $D_{\parallel}$  (circles) and perpendicular  $D_{\perp}$  (crosses) to electric field diffusion coefficient (diffusivity) of electrons in Si at room temperature as functions of electric field applied parallel to  $\langle 111 \rangle$  crystallographic direction. Continuous line shows theoretical computation of  $D_{\parallel}$  [2.66].

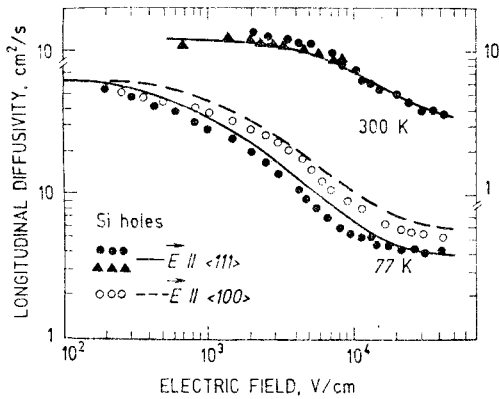


Fig. 2.48. Parallel to electric field diffusion coefficient of holes in Si as a function of electric field strength at lattice temperatures 300 K and 77 K. Points refer to experiments and curves to theoretical calculations [1.41].

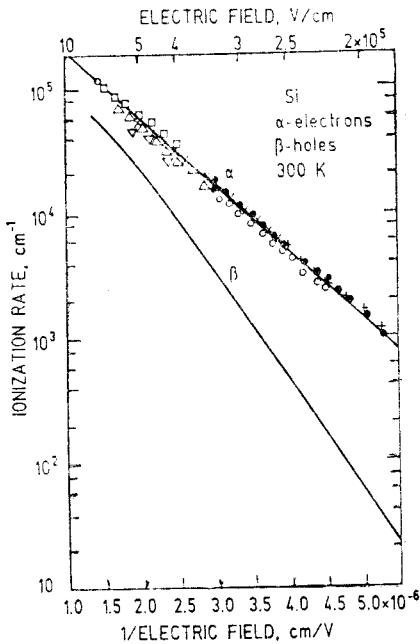


Fig. 2.49. Band-band impact ionization rates for electrons  $\alpha$  and holes  $\beta$  in Si as functions of reciprocal electric field at room temperature [2.71].

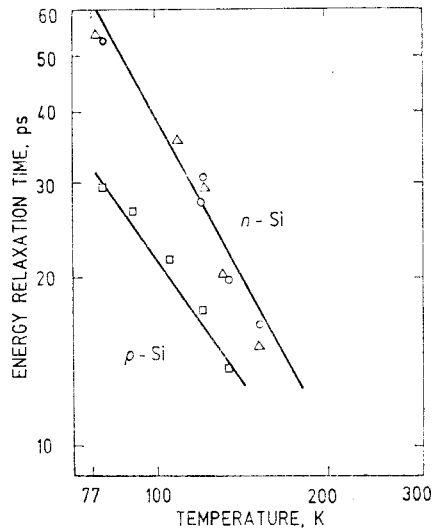


Fig. 2.50. Warm electron and hole energy relaxation times as functions of the lattice temperature in Si. Room temperature resistivity: triangles —  $70 \Omega \cdot \text{cm}$ , squares —  $190 \Omega \cdot \text{cm}$ , circles —  $700 \Omega \cdot \text{cm}$  [1.79].

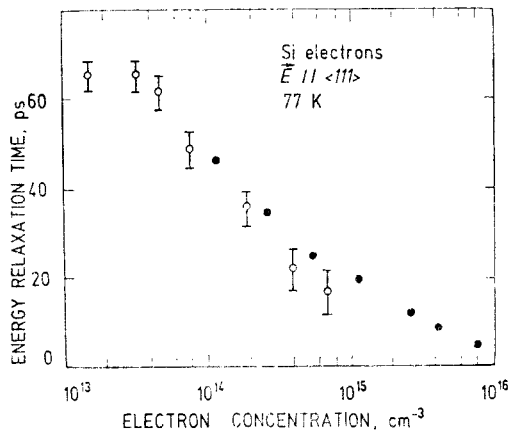


Fig. 2.51. Warm electron energy relaxation time in *n*-Si at 77 K and electric field parallel to  $\langle 111 \rangle$  crystallographic direction [1.81, 2.72].

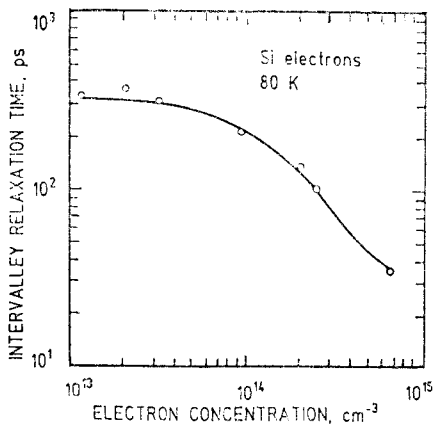


Fig. 2.52. Dependence of warm electron intervalley relaxation time on the electron concentration in Si at  $T=80$  K [2.73].

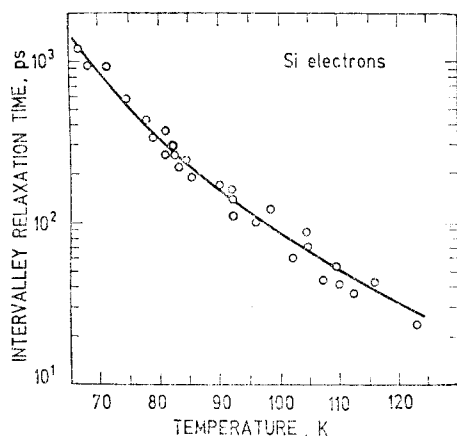


Fig. 2.53. Dependence of warm electron intervalley relaxation time on lattice temperature for pure Si,  $n < 2 \cdot 10^{13} \text{ cm}^{-3}$  [2.73].

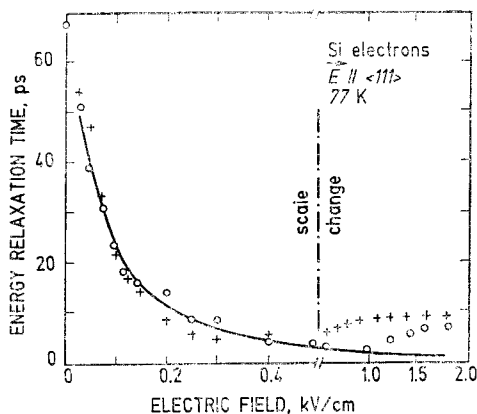


Fig. 2.54. Electron energy relaxation time in pure Si as a function of electric field applied along  $\langle 111 \rangle$  crystallographic direction at 77 K. Points are experimental data [1.83] and line is theoretical calculation [1.41].

**TABLE 2.16** Parameters for high electric field transport calculation in *n*-Si [1.41]

Parameter	Value			
	Lattice	$\Gamma$ valley	<i>L</i> valley	<i>X</i> valley
Density, g/cm <sup>3</sup>	2.33			
Dielectric permittivity $\epsilon/\epsilon_0$	11.7			
<b>Intravalley properties</b>				
Number of valleys		1	4	6
Effective masses:				
$m_l/m_0$				0.91
$m_t/m_0$				0.19
Nonparabolicity parameter, eV <sup>-1</sup>				0.27*
Valley separation relative to <i>X</i> valley, eV		2.95	0.74	0
<b>Acoustic scattering parameters</b>				
Sound velocity, cm/s	9 · 10 <sup>5</sup>			
Deformation potential, eV				9
Optical intravalley scattering is negligible				
<b>Intervalley properties</b>				
Transition	Coupling constant		Phonon energy	Type**
<i>X</i> – <i>X</i>	0.5 · 10 <sup>8</sup> eV/cm		12.1 meV	<i>TA</i> <i>g</i> -type
	0.8 · 10 <sup>8</sup> eV/cm		18.5 meV	<i>LA</i> <i>g</i> -type
	11 · 10 <sup>8</sup> eV/cm		62.0 meV	<i>LO</i> <i>g</i> -type
	0.3 · 10 <sup>8</sup> eV/cm		19.0 meV	<i>TA</i> <i>f</i> -type
	2.0 · 10 <sup>8</sup> eV/cm		47.4 meV	<i>LA</i> <i>f</i> -type
	2.0 · 10 <sup>8</sup> eV/cm		59.0 meV	<i>TO</i> <i>f</i> -type
$\left. \begin{array}{l} \Gamma - L \\ \Gamma - X \\ L - L \\ L - X \end{array} \right\}$	Negligible			

\* – [2.74].

\*\* – *g*- and *f*-type intervalley phonon energies given in Table 2.16 differ slightly from those in Table 2.3.

## 2.5. Si piezoelectric, thermoelectric and magnetic properties

**Piezoelectric tensor.** For silicon, which possesses the center of symmetry, all piezoelectric tensor components are equal to zero.

**TABLE 2.17** Piezoresistance coefficients of Si in 1/GPa. For physical

Experimental conditions	$\pi_{11}$	$\pi_{12}$
<b><i>n</i>-type</b>		
$n = (1.3-9.9) \cdot 10^{14} \text{ cm}^{-3}$ , 78 K	-3	
$n = (7.8-130) \cdot 10^{14} \text{ cm}^{-3}$ , 77 K	-3.5	
300 K	-1.05	
$n = 4 \cdot 10^{16} \text{ cm}^{-3}$ , 300 K	-0.773	0.401
$n = 9.4 \cdot 10^{16} \text{ cm}^{-3}$ , 77 K	-2.8	
300 K	-0.98	
$n = 1 \cdot 10^{17} \text{ cm}^{-3}$ , 300 K	-0.715	0.373
$n = 9.4 \cdot 10^{17} \text{ cm}^{-3}$ , 77 K	-2.2	
300 K	-0.83	
$n = 2 \cdot 10^{18} \text{ cm}^{-3}$ , 300 K	-0.619	0.31
$n = 9 \cdot 10^{18} \text{ cm}^{-3}$ , 77 K	-1.4	
300 K	-0.7	
$\rho = 11.7 \Omega \cdot \text{cm}$ , 300 K	-1.022	
<b><i>p</i>-type</b>		
$\rho = 7.8 \Omega \cdot \text{cm}$ , 300 K	0.066	-0.011
$p = 3 \cdot 10^{14} \text{ cm}^{-3}$ , 78 K		
$p = 1.3 \cdot 10^{16} \text{ cm}^{-3}$ , 78 K	-0.25	0.1

\* - Calculated values for  $\pi_{44} = -0.125$  1/GPa.  $\pi_{44}$  is constant up to



interpretation refer Table 5

$\frac{\pi_{11} + \pi_{12} + \pi_{14}}{2}$	$\frac{\pi_{11} + 2\pi_{13} + 2\pi_{44}}{3}$	$\pi_{11} + 2\pi_{12}$	Reference
			[1.85]
-0.26	-0.076*	0.021	[2.75] [2.76]
-0.2185	-0.08*	0.01	[2.75] [2.76]
-0.198	-0.079*	0.012	[2.75] [2.76]
-0.312	-0.077*	0.019 0.057	[2.75] [14]
0.718		0.06	[14]
1.25			[1.85]
1.5	1.9		[2.77]

$5 \cdot 10^{19} \text{ cm}^{-3}$  impurity concentration at room temperature [2.75].

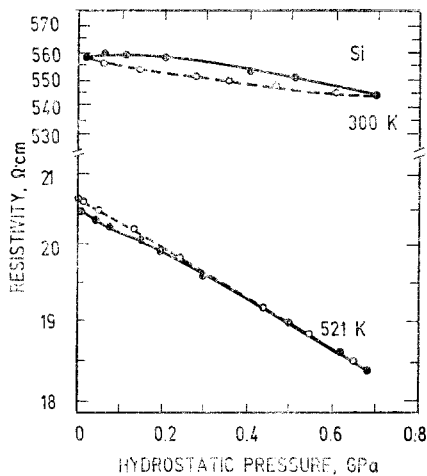


Fig. 2.55. Resistivity of *n*-Si vs. hydrostatic pressure at lattice temperatures 300 K and 521 K [2.78].

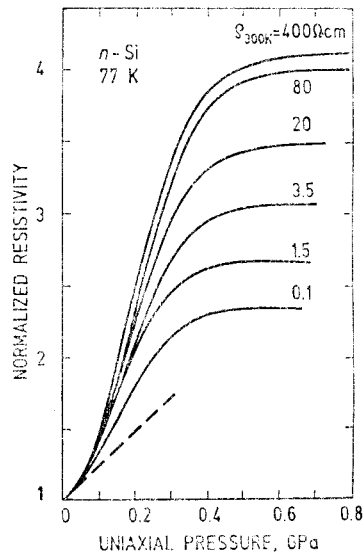


Fig. 2.56. Normalized longitudinal resistivity  $\rho_{\parallel 100}/\rho_0$  of *n*-Si vs. uniaxial pressure  $p$  at 77 K for arrangement when stress and current are parallel to [100] crystallographic direction. Different curves correspond to different room temperature resistivities [2.7]. Dashed line:  $\rho_{\parallel 100}/\rho_0 = 1 - \pi_{\parallel 1}p$ ,  $\pi_{\parallel 1} = -3.5 \text{ (GPa)}^{-1}$ .

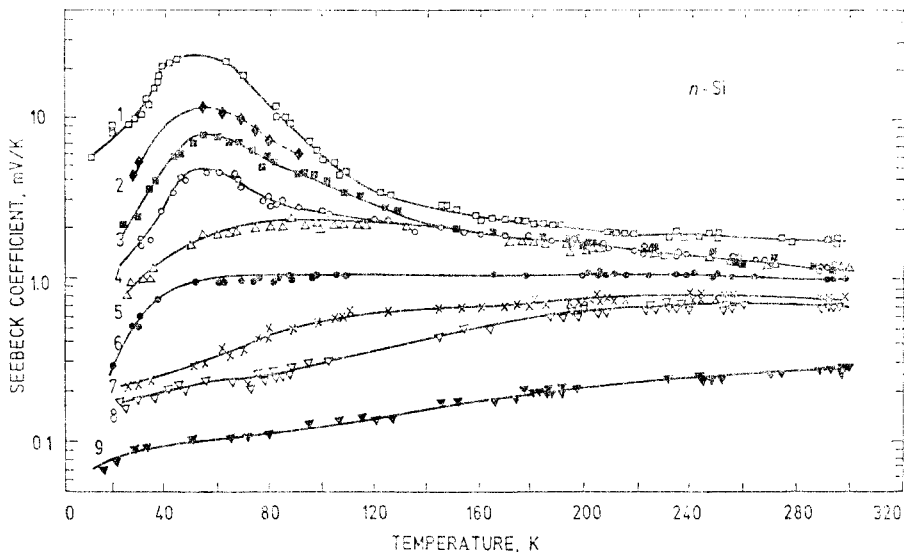


Fig. 2.57. Seebeck coefficient vs. temperature for *n*-Si at various donor concentrations: 1 —  $3.67 \cdot 10^{14} \text{ cm}^{-3}$ , 2 —  $2.71 \cdot 10^{15} \text{ cm}^{-3}$ , 3 —  $4.8 \cdot 10^{16} \text{ cm}^{-3}$ , 4 —  $1.04 \cdot 10^{17} \text{ cm}^{-3}$ , 5 —  $3.47 \cdot 10^{17} \text{ cm}^{-3}$ , 6 —  $7.8 \cdot 10^{17} \text{ cm}^{-3}$ , 7 —  $4.46 \cdot 10^{18} \text{ cm}^{-3}$ , 8 —  $2.71 \cdot 10^{18} \text{ cm}^{-3}$ , 9 —  $5.67 \cdot 10^{19} \text{ cm}^{-3}$  [2.79].

Fig. 2.58. Seebeck coefficient  $S$  times temperature  $T$  vs. temperature for  $p$ -Si having various acceptor and compensating donor concentrations: 1 -  $N_A = 1 \cdot 10^{15} \text{ cm}^{-3}$ ,  $N_D = 1.9 \cdot 10^{14} \text{ cm}^{-3}$ ; 2 -  $N_A = 9.2 \cdot 10^{14} \text{ cm}^{-3}$ ,  $N_D = 2.2 \cdot 10^{14} \text{ cm}^{-3}$ ; 3 -  $N_A = 2.6 \cdot 10^{16} \text{ cm}^{-3}$ ,  $N_D = 2.3 \cdot 10^{15} \text{ cm}^{-3}$ ; 4 -  $N_A = 2 \cdot 10^{17} \text{ cm}^{-3}$ ,  $N_D = 4.9 \cdot 10^{15} \text{ cm}^{-3}$ ; 5 -  $N_A = 1 \cdot 10^{18} \text{ cm}^{-3}$ ; 6 -  $N_A = 1.5 \cdot 10^{19} \text{ cm}^{-3}$  [2.80].

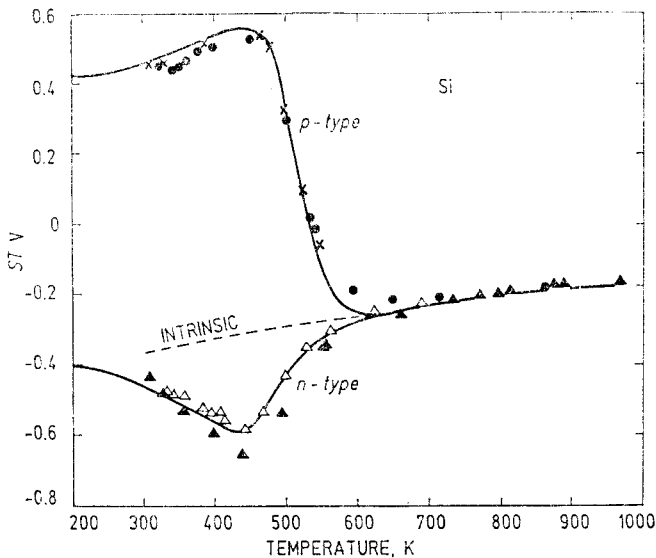
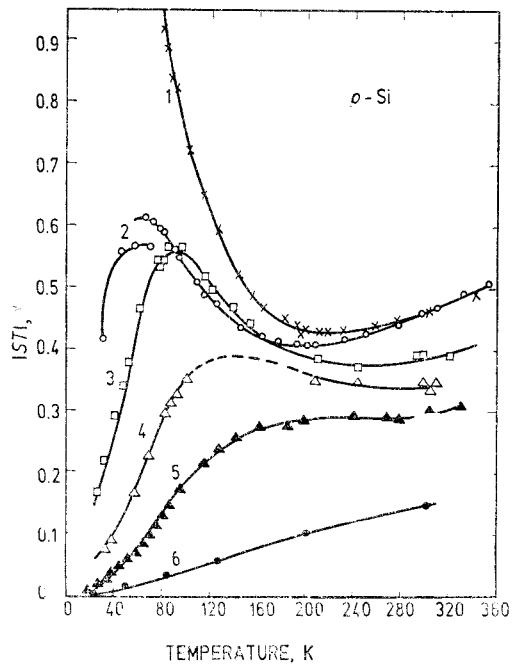


Fig. 2.59. Seebeck coefficient  $S$  times temperature  $T$  vs. temperature for Si in high temperature region where transition to intrinsic conductivity occurs. Excess donor and acceptor concentration:  $n$ -type -  $N_D = 3.7 \cdot 10^{14} \text{ cm}^{-3}$ ,  $N_A = 9 \cdot 10^{13} \text{ cm}^{-3}$  and  $p$ -type -  $N_A = 1 \cdot 10^{15} \text{ cm}^{-3}$ ,  $N_D = 1.9 \cdot 10^{14} \text{ cm}^{-3}$  [2.80].

**Magnetic susceptibility.** Si lattice contribution to the magnetic susceptibility  $\chi_m$  at room temperature and respective temperature coefficient [1.89]:

$$\chi_m = (-3.33 \pm 0.1) \cdot 10^{-6},$$

$$d\chi_m/dT = (0.78 \pm 0.03) \cdot 10^{-9} \text{ K}^{-1}.$$

Free carrier contribution to the susceptibility does not exceed 5% of the lattice susceptibility at free carrier concentration smaller than  $10^{18} \text{ cm}^{-3}$  [2.81].

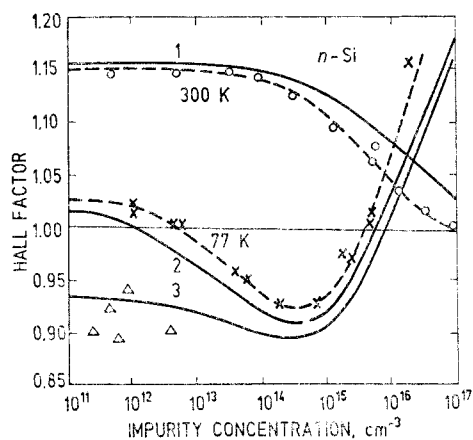


Fig. 2.60. Hall factor vs. impurity concentration in *n*-Si. Experimental data: crosses and triangles — 77 K, open circles — 300 K. Theory: curves 1 and 2 — calculated without taking into account of scattering by neutral impurities at 300 K and 77 K; curve 3 — calculated by taking into account the scattering by neutral impurities of concentration  $6 \cdot 10^{16} \text{ cm}^{-3}$  at 77 K [2.82].

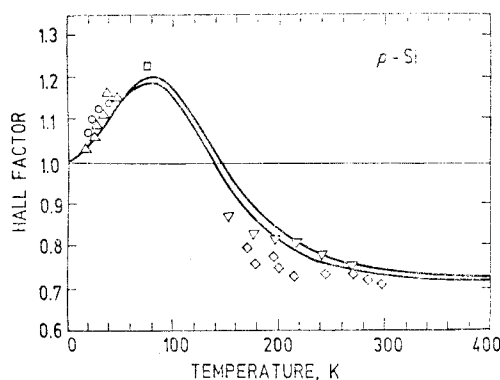


Fig. 2.61. Experimental (points) and calculated (lines) Hall factor vs. temperature for pure *p*-Si. The acceptor concentration is in the range  $N_A \approx 10^{11} - 10^{16} \text{ cm}^{-3}$  [2.83].

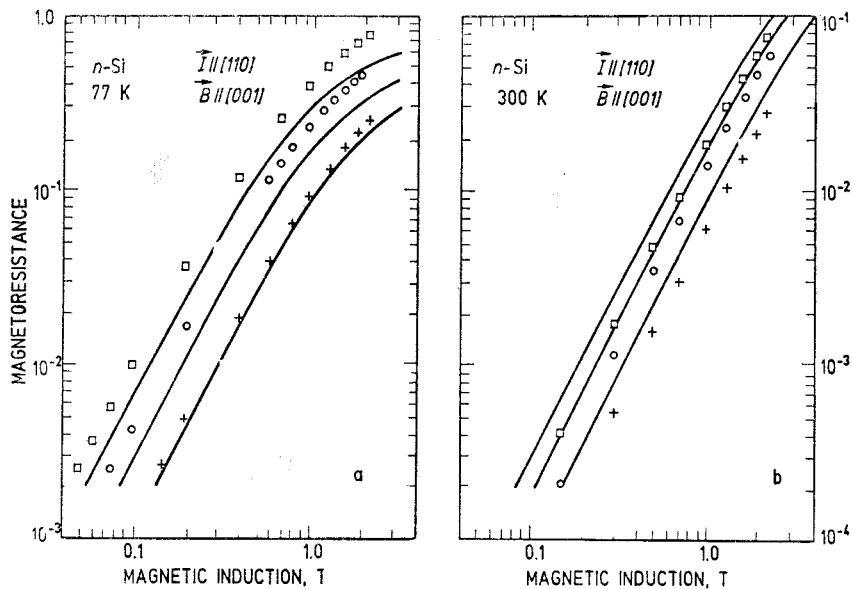


Fig. 2.62. Magnetic field dependence of transverse magnetoresistance  $[\rho(B) - \rho_0]/\rho_0$  in  $n$ -Si for current flowing in [110] and magnetic field pointing in [001] direction. *a* - 77 K, *b* - 300 K. Sample parameters at 300 K: squares -  $\rho = 27 \Omega \cdot \text{cm}$ ,  $N_D \approx 1.3 \cdot 10^{14} \text{ cm}^{-3}$ , circles -  $\rho = 1.9 \Omega \cdot \text{cm}$ ,  $N_D \approx 1.9 \cdot 10^{15} \text{ cm}^{-3}$ , crosses -  $\rho = 0.22 \Omega \cdot \text{cm}$ ,  $N_D \approx 2 \cdot 10^{16} \text{ cm}^{-3}$ . Solid lines are calculated [2.84].

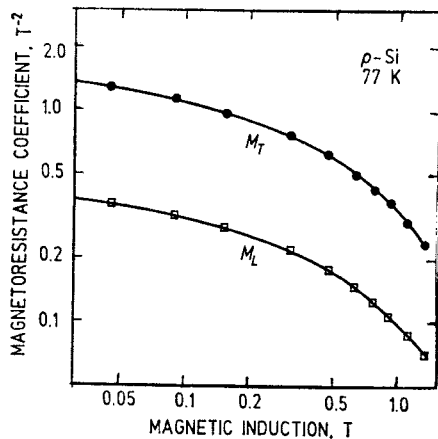


Fig. 2.63. Magnetoresistance coefficient  $M = [\rho(B) - \rho_0]/(\rho_0 B^2)$  vs. magnetic induction  $B$  at 77 K for  $p$ -Si with  $\rho_0 = 85 \Omega \cdot \text{cm}$  at room temperature.  $M_T$  corresponds to transverse magnetoresistance:  $B \parallel [001]$ ,  $I \parallel [100]$ .  $M_L$  corresponds to longitudinal magnetoresistance  $B \parallel I \parallel [100]$  [2.85].

## 2.6. Si impurity properties

**TABLE 2.18. Optical ionization energies and absorption cross sections** for transitions from the impurity ground state into the conduction or valence bands of Si. The energies are measured relative to the conduction  $E_c$  or valence  $E_v$  band edges. For shallow impurities the cross section at the corresponding photon energy has been deduced from  $\sigma = \alpha_{\max}/N$ , where  $\alpha_{\max}$  is the maximum absorption coefficient and  $N$  is the impurity concentration

Impurity	Ionization energy, meV	Absorption cross section, $\text{cm}^2$	Photon energy, meV	Reference
<b>Donors</b>				
As	$E_c - 53.76$	$1.6 \cdot 10^{-15}$	56	[2.86, 2.87, 2.88]
Bi	$E_c - 70.6$	$7 \cdot 10^{-16}$	71	[2.89]
Fe	$E_c - 795.7$		1000—1200	[2.90]
Li	$E_c - 31.24$	$\sim 3 \cdot 10^{-15}$	33	[2.86]
Mg	$E_c - 107.5$	$1.7 \cdot 10^{-15}$		[2.91]
Mg <sup>+</sup>	$E_c - 256.47$			[2.91]
P	$E_c - 45.59$	$2.5 \cdot 10^{-15}$	46	[2.86, 2.87, 2.88, 2.92]
S	$E_c - 318$	$(2-7) \cdot 10^{-16}$	$\sim 500$	[2.93, 2.94, 2.95, 2.96]
S <sup>+</sup>	$E_c - 612$	$1 \cdot 10^{-15}$	$\sim 800^*$	[2.93, 2.96]
S <sup>+</sup>	$E_c - 612$	$1 \cdot 10^{-16}$	$\sim 1000^{**}$	[2.93, 2.96]
Sb	$E_c - 42.74$	$8.1 \cdot 10^{-15}$	42	[2.86, 2.87, 2.88]
Se	$E_c - 307$	$2 \cdot 10^{-16}$	400	[2.96, 2.97]
Se <sup>+</sup>	$E_c - 593$	$1.10^{-16}$	700*	[2.96, 2.97]
Se <sup>+</sup>	$E_c - 593$	$4 \cdot 10^{-18}$	$\sim 1000^{**}$	[2.96, 2.97]
Te	$E_c - 199$		200	[2.93]
Te <sup>+</sup>	$E_c - 411$	$5 \cdot 10^{-16}$	600*	[2.93]
Te <sup>+</sup>	$E_c - 411$	$3 \cdot 10^{-18}$	$\sim 1100^{**}$	[2.93]

TABLE 2.18 (Continued)

Impurity	Ionization energy, meV	Absorption cross section, $\text{cm}^2$	Photon energy, meV	Reference
<b>Acceptors</b>				
Al	$E_v + 67$	$8.5 \cdot 10^{-16}$	82	[2.98, 2.99]
Ag		$2 \cdot 10^{-16}$	620	[2.100]
B	$E_v + 46$	$1.4 \cdot 10^{-15}$	50	[2.98, 2.99]
Be	$E_v + 191$	$5 \cdot 10^{-18}$	200	[2.101]
Cu		$5 \cdot 10^{-18}$	330	[2.102]
In	$E_v + 156.9$	$3.3 \cdot 10^{-17}$	300	[2.103, 2.104]
Ga	$E_v + 71$	$5 \cdot 10^{-16}$	110	[2.98, 2.99]
Tl	$E_v + 246$	$2.6 \cdot 10^{-17}$	446	[2.105]
Zn	$E_v + 320$	$1.5 \cdot 10^{-16}$	500	[2.106]
Zn <sup>-</sup>	$E_v + 620$	$4.8 \cdot 10^{-17}$	900	[2.106]
<b>Amphoteric impurities</b>				
Au <sup>0</sup> →Au <sup>-</sup>				
acceptor state	$E_c - 530$	$8 \cdot 10^{-18}$	750*	[2.107, 2.108]
	$E_c - 530$	$8 \cdot 10^{-17}$	900**	[2.107, 2.108]
Au <sup>0</sup> →Au <sup>+</sup>				
donor state	$E_v + 350$	$1.8 \cdot 10^{-16}$	480 – 750**	[2.108]
Mn <sup>-</sup> →Mn <sup>0</sup>	$E_c - 130$			[2.109]
Mn <sup>0</sup> →Mn <sup>+</sup>	$E_c - 450$			[2.109]
Pt <sup>0</sup> →Pt <sup>-</sup>				
acceptor state	$E_c - 230$	$(0.6 - 3.5) \cdot 10^{-17}$	300 – 600*	[2.110, 2.111]
	$E_c - 230$	$(0.25 - 1.3) \cdot 10^{-16}$	1000 – 1200**	[2.110, 2.111]
Pt <sup>0</sup> →Pt <sup>+</sup>				
donor state	$E_v + 320$	$(1.8 - 4) \cdot 10^{-18}$	900 – 1000*	[2.110, 2.111]
	$E_v + 320$	$(0.1 - 3) \cdot 10^{-16}$	420 – 1000**	[2.110, 2.111]

\* – For electron emission.

\*\* – For hole emission.

**TABLE 2.19** Binding energies of the energy levels of **shallow donors** (phosphorus, arsenic, antimony, bismuth and lithium) in Si found by optical methods. The energies in meV are measured relative to the conduction band edge [1.110]

Level	Level energy, meV					Effective mass theory
	P	As	Sb	Bi	Li	
$1s(A_1) \equiv E_I$ (ionization energy)	45.59	53.76	42.74	70.98	31.24	31.27
$1s(E)$	32.58	31.26	30.47			
$1s(T_2)$	33.89	32.67	32.89	32.89		31.27
			32.91	31.89		
$1s(E+T_2)$					33.02	31.27
$2p_0$	11.48	11.50	11.51	11.44	11.51	11.51
$2s$		9.11		8.78		8.83
$2p_{\pm}$	6.40	6.40	6.38	6.37	6.40	6.40
$3p_0$	5.47	5.49	5.50	5.48	5.49	5.48
$3s$				4.7		4.75
$3d_0$	3.83	3.8		3.8		3.75
	3.73					
$4p_0$	3.31	3.31	3.33	3.30	3.32	3.33
$3p_{\pm}$	3.12	3.12	3.12	3.12	3.12	3.12
$4s$				2.89		2.85
$4f_0$	2.33			2.36		2.33
$4p_{\pm}, 5p_0$	2.19	2.19	2.20	2.18	2.20	2.19; 2.23
$4f_{\pm}$	1.90	1.90	1.94	1.91	1.90	1.89
$5f_0$	1.65		1.71	1.67	1.64	1.62
$5p_{\pm}$	1.46	1.46	1.48	1.46	1.47	1.44
$5f_{\pm}$	1.26				1.25	1.27
$6p_{\pm}$	1.09	1.07	1.10	1.08	1.07	1.04



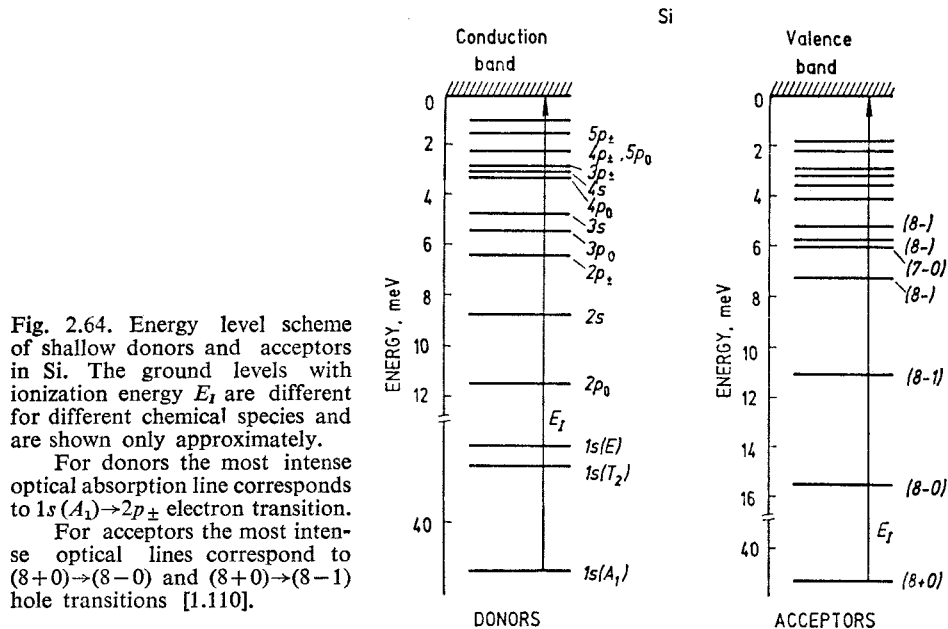


**TABLE 2.20** Binding energies of the energy levels of **shallow acceptors** (boron, aluminium, gallium, indium) in Si found by optical methods. The energies in meV are measured relative to the valence band edge [1.110]

Level	Level energy, meV				Effective mass theory
	B	Al	Ga	In	
$(8+0) \equiv E_I$ (ionization energy)	45.71	70.18	74.05	156.90	
(8-0)	15.33	15.30	15.82	14.91	15.5 ( $1\Gamma_8^-$ )
(8-1)	11.18	11.69		11.11	11.4 ( $2\Gamma_8^-$ )
(8-)	7.36		6.93	7.16	7.3 ( $3\Gamma_8^-$ )
(7-0)	6.1	6.1	6.1	6.1	6.1 ( $1\Gamma_7^-$ )
(8-)	5.79	5.22	5.80	5.82	5.8 ( $1\Gamma_6^-$ )
(8-)	6.03	5.02	5.62		5.8 ( $4\Gamma_8^-$ )
5	4.19	3.9	4.20	4.1	4.1 ( $5\Gamma_8^-$ )
6	3.52	3.43	3.56	3.63	3.6; 3.5 ( $2\Gamma_6^-$ , $6\Gamma_8^-$ )
7	2.92	3.08	3.25		
8	2.44	2.79	2.94	2.93	
9	1.85	2.28			
10	1.39	1.78			

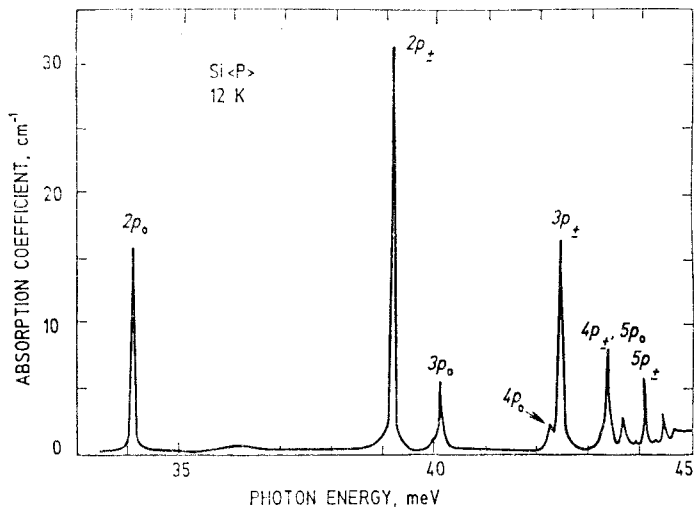


Fig. 2.65.  $1s (A_1) \rightarrow 2p_0, 2p_{\pm}, 3p_0, 4p_{\pm}, 5p_0$  and  $5p_{\pm}$  lines of the absorption spectrum of phosphorus atoms in Si. Phosphorus concentration:  $7.5 \cdot 10^{14} \text{ cm}^{-3}$ .  $T = 12 \text{ K}$ . The optical transitions  $1s (A_1) \rightarrow 2s, 3s, \dots$  are forbidden [2.91].

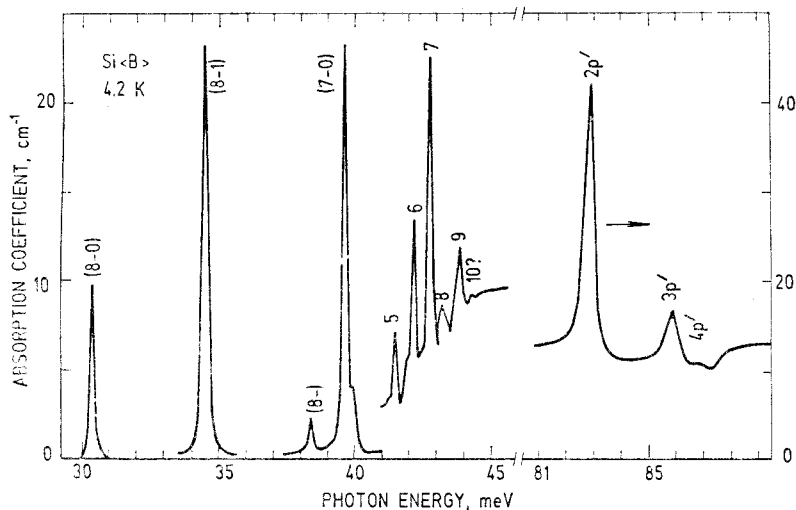


Fig. 2.66. Absorption coefficient due to hole transitions from  $(8+0)$  ground level of boron atom in Si vs. photon energy (cf. Table 2.20).

Lines  $(8-0) - (7-)$  have been measured for a sample with boron concentration  $1.5 \cdot 10^{15} \text{ cm}^{-3}$ . Lines  $5-10$  and  $2p', 3p', 4p'$  have been measured for a sample with boron concentration  $2.2 \cdot 10^{16} \text{ cm}^{-3}$ . The lines  $2p', 3p', 4p'$  correspond to transitions from boron ground state to the valence band continuum [1.110, 2.103].

Fig. 2.67. Dependence of shallow donor thermal ionization energy  $E_I$  on electrically active donor concentration  $N_D^*$  in  $n$ -Si. Circles — arsenic doped Si [2.62], closed points — phosphorus doped Si [2.112], triangles — arsenic doped Si [2.113]. Solid line is an empirical formula:  $E_I = 54 - 3.5 \cdot 10^{-5} N_D^{*1/3}$ ,  $E_I$  is in meV,  $N_D^*$  is in  $\text{cm}^{-3}$ .

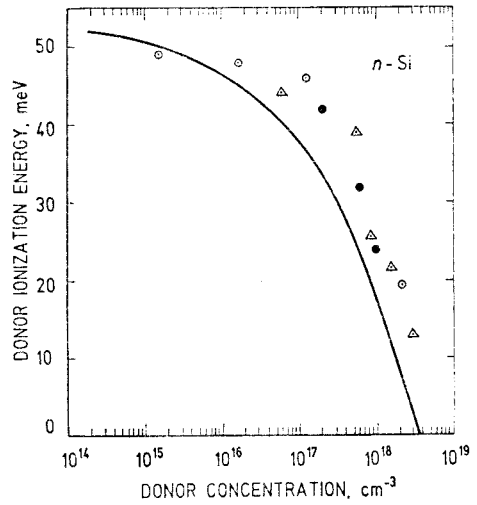
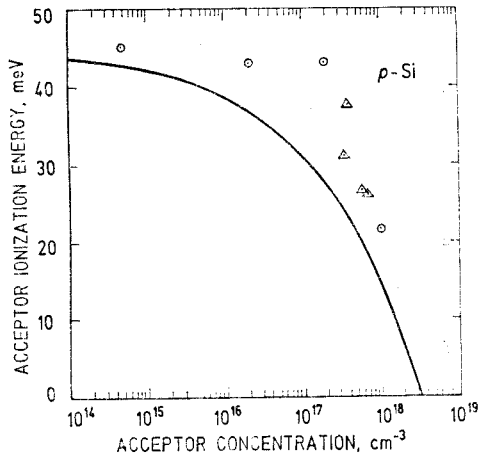


Fig. 2.68. Dependence of shallow acceptor (boron) thermal ionization energy  $E_I$  on electrically active acceptor concentration  $N_A^*$  in  $p$ -Si. Circles — [2.62], Triangles — [2.113]. Solid line is an empirical formula:  $E_I = 45 - 3 \cdot 10^{-5} N_A^{*1/3}$ ,  $E_I$  is in meV and  $N_A^*$  is in  $\text{cm}^{-3}$ .



**TABLE 2.21** Binding energies of the energy levels of **double donors** in Si. The energies in meV are measured relative to the conduction band edge. Sulphur, selenium and tellurium [2.93] are substitutional donors, while magnesium [2.91] is interstitial

Level	Level energy, meV							
	S	Se	Te	Mg	S <sup>+</sup>	Se <sup>+</sup>	Te <sup>+</sup>	Mg <sup>+</sup>
1s( <i>A</i> <sub>1</sub> )≡ <i>E</i> <sub>I</sub> (ionization energy)	318	307	199	107.5	612	589	411	256.47
1s( <i>T</i> <sub>2</sub> )	35	35	39		184	161	177	
2 <i>p</i> <sub>0</sub>	11	12	12	11.7	45	45	47	47.84
2 <i>p</i> <sub>±</sub>	6	7	7	6.38	26	25	26	26.25

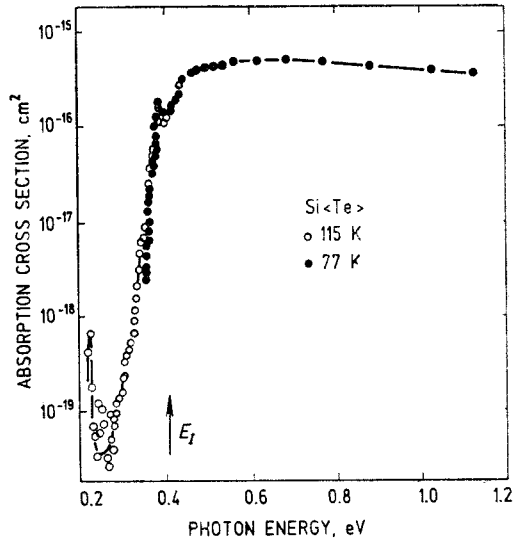


Fig. 2.69. Optical absorption cross section for transition  $\text{Te}^{2+} + h\nu \rightarrow \text{Te}^{2+} + e$  vs. photon energy for Si at two temperatures. The onset of photoionization of electrons from the ground state into the conduction band is marked with an arrow. The sharp peak at about 0.23 eV in the 115 K spectrum is caused by the internal transition  $1s(A_1) \rightarrow 1s(T_2)$  of  $\text{Te}^+$  (see Table 2.21) [2.93].

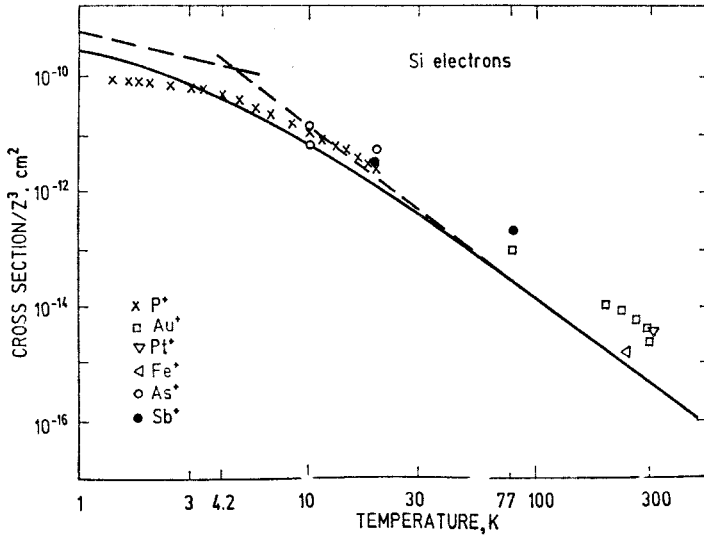


Fig. 2.70. Electron capture cross section on the positively single-charged ( $Z=1$ ) centers in Si. Solid and dashed lines are theoretical calculations [1.111].

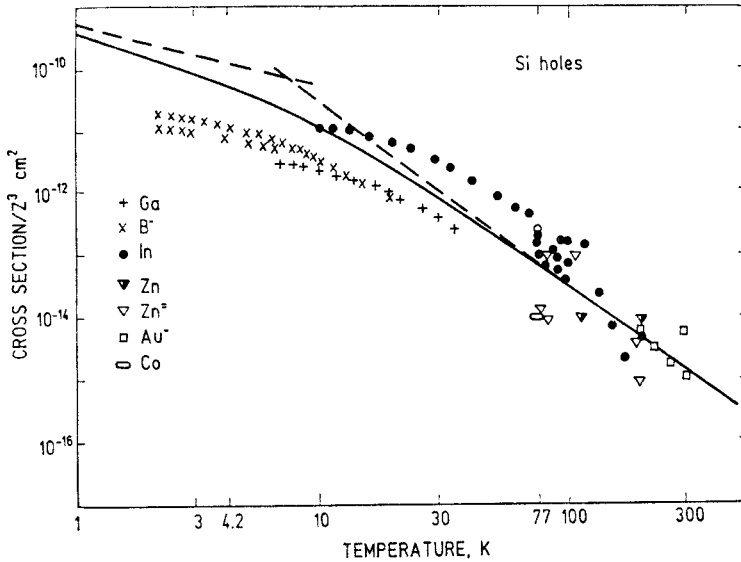


Fig. 2.71. Hole capture cross section on the negatively single-charged ( $Z=1$ ) and double-charged ( $Z=2$ ) centers in Si. Solid and dashed lines are theoretical calculations [1.111].

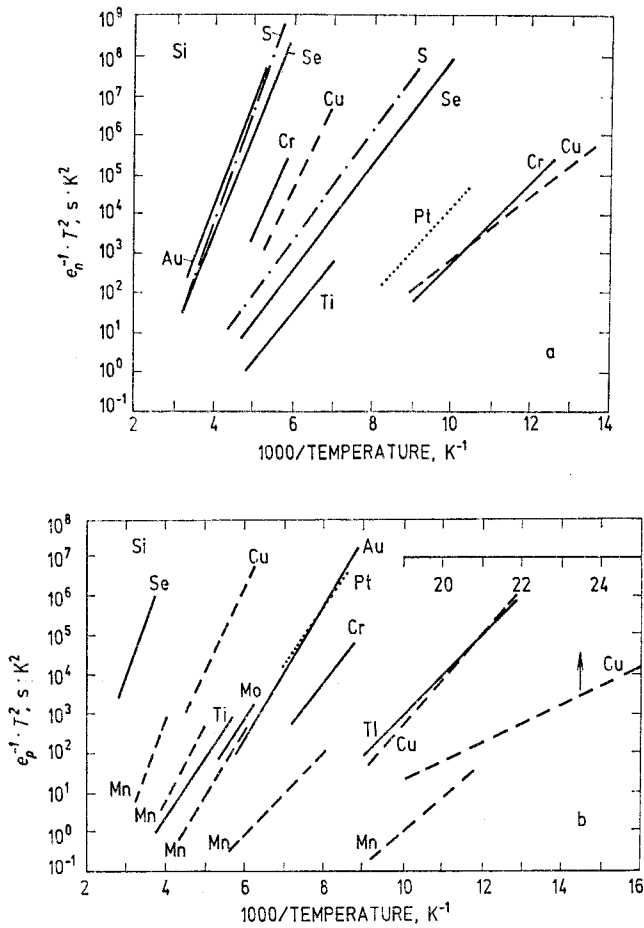


Fig. 2.72. Inverse emission rate multiplied by  $T^2$  for electron (a) and hole (b) emission from deep impurities indicated on curves as obtained with DLTS (deep level transient spectroscopy).  $T$  is a lattice temperature. For details see Table 2.22.

**TABLE 2.22** Thermal ionization energy measured relative to the conduction  $E_c$  or valence  $E_v$  band edges and capture cross sections associated with **deep impurities** in Si as determined by Deep Level Transient Spectroscopy (DLTS)

Impurity	Donor or acceptor level	Depth from conduction or valence band edge, meV	Temperature, K	Capture cross section, $\text{cm}^2$	Reference
Au	$D$	$E_c - 800$	158	$\sigma_n = 1.1 \cdot 10^{-15}$	[2.114]
Au		$E_v + 350$	70–190	$\sigma_p = 3.5 \cdot 10^{-15}$	
Au	$A$	$E_c - 550$	80–200	$\sigma_n = 8.5 \cdot 10^{-17}$	
Au		$E_v + 580$	300	$\sigma_p = 9 \cdot 10^{-15}$	
Cr	$D_1$	$E_c - 200$	88	$\sigma_n = 4.1 \cdot 10^{-15}$	[2.115]
Cr	$D_2$	$E_v + 250$	94	$\sigma_p = 9 \cdot 10^{-18}$	
Cr	$A$	$E_c - 430$	175	$\sigma_n = 2 \cdot 10^{-16}$	
Cu	$D_1$	$E_v + 93$	45	$\sigma_p > 10^{-14}$	[2.116]
Cu	$D_2$	$E_v + 233$	76–108	$\sigma_p \geq 1.4 \cdot 10^{-14}$	
Cu	$A_1$	$E_c - 161$	80–106	$\sigma_n = (1.8 - 3.3) \cdot 10^{-17}$	
Cu	$A_2?$	$E_c - 402$	130–190	$\sigma_n = 3 \cdot 10^{-15}$	
Cu	$A_3$	$E_v + 425$	183–227	$\sigma_p \geq 7.4 \cdot 10^{-15}$	
Mn	?	$E_v + 170$			[2.117]
Mn	?	$E_v + 220$	140	$\sigma_p = 3.9 \cdot 10^{-16}$	
Mn	?	$E_v + 330$	185	$\sigma_p = 1.7 \cdot 10^{-16}$	
Mn	?	$E_v + 440$	220	$\sigma_p = 3.5 \cdot 10^{-16}$	
Mn	?	$E_v + 510$	276	$\sigma_p = 3.7 \cdot 10^{-16}$	
Mn		$E_c - 200$	125	$\sigma_n = 7 \cdot 10^{-17}$	[2.118]
Mn		$E_c - 420$	190	$\sigma_n = 8 \cdot 10^{-15}$	
Mn		$E_c - 540$	240	$\sigma_n = 2 \cdot 10^{-14}$	
Mo	?	$E_v + 300$	177.5	$\sigma_p = 4.3 \cdot 10^{-16}$	[2.119]
Ni	$D$	$E_v + (160 - 190)$			[2.120]
Ni	$A$	$E_c - (430 - 460)$			
Pt	?	$E_c - 231$	100–130	$\sigma_n = 7 \cdot 10^{-15}$	[2.121,
Pt	?	$E_v + 321$	135–240	$\sigma_p = (7.8 - 10) \cdot 10^{-16}$	2.122]
S	$D_1$	$E_c - 320$	100	$\sigma_n = 2 \cdot 10^{-15}$	[2.123]
S	$D_2$	$E_c - 590$	250	$\sigma_n \geq 10^{-14}$	
Se	$D_1$	$E_c - 520$	250	$\sigma_n > 10^{-14}$	[2.124]
Se	$D_2$	$E_c - 300$	100	$\sigma_n = 3 \cdot 10^{-15}$	
Ti	$D_1$	$E_c - 260$	300	$\sigma_n = 3 \cdot 10^{-15}$	[2.125]
Ti	$D_2$	$E_v + 290$	300	$\sigma_p = 1.7 \cdot 10^{-17}$	
Tl	$A$	$E_v + 240$	77–110	$\sigma_p = 2.4 \cdot 10^{-14}$	[2.126]
W	$D$	$E_c - 220$			[2.127]
W	$D$	$E_v + 410$			

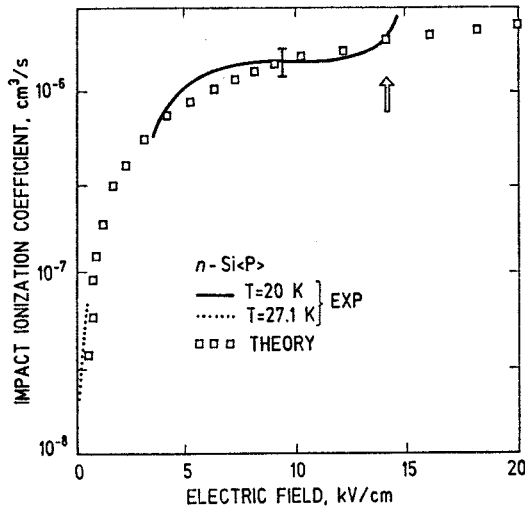
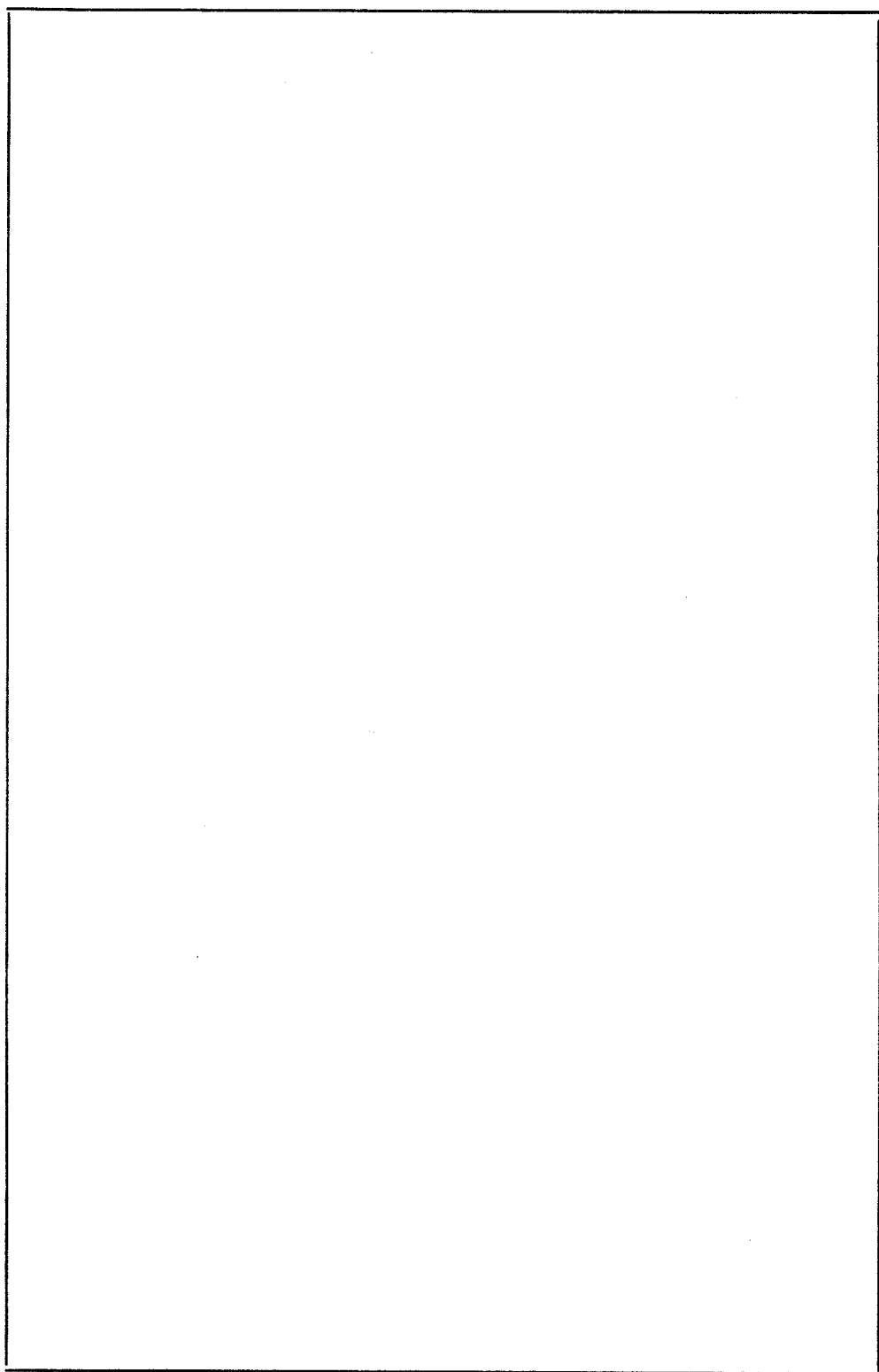
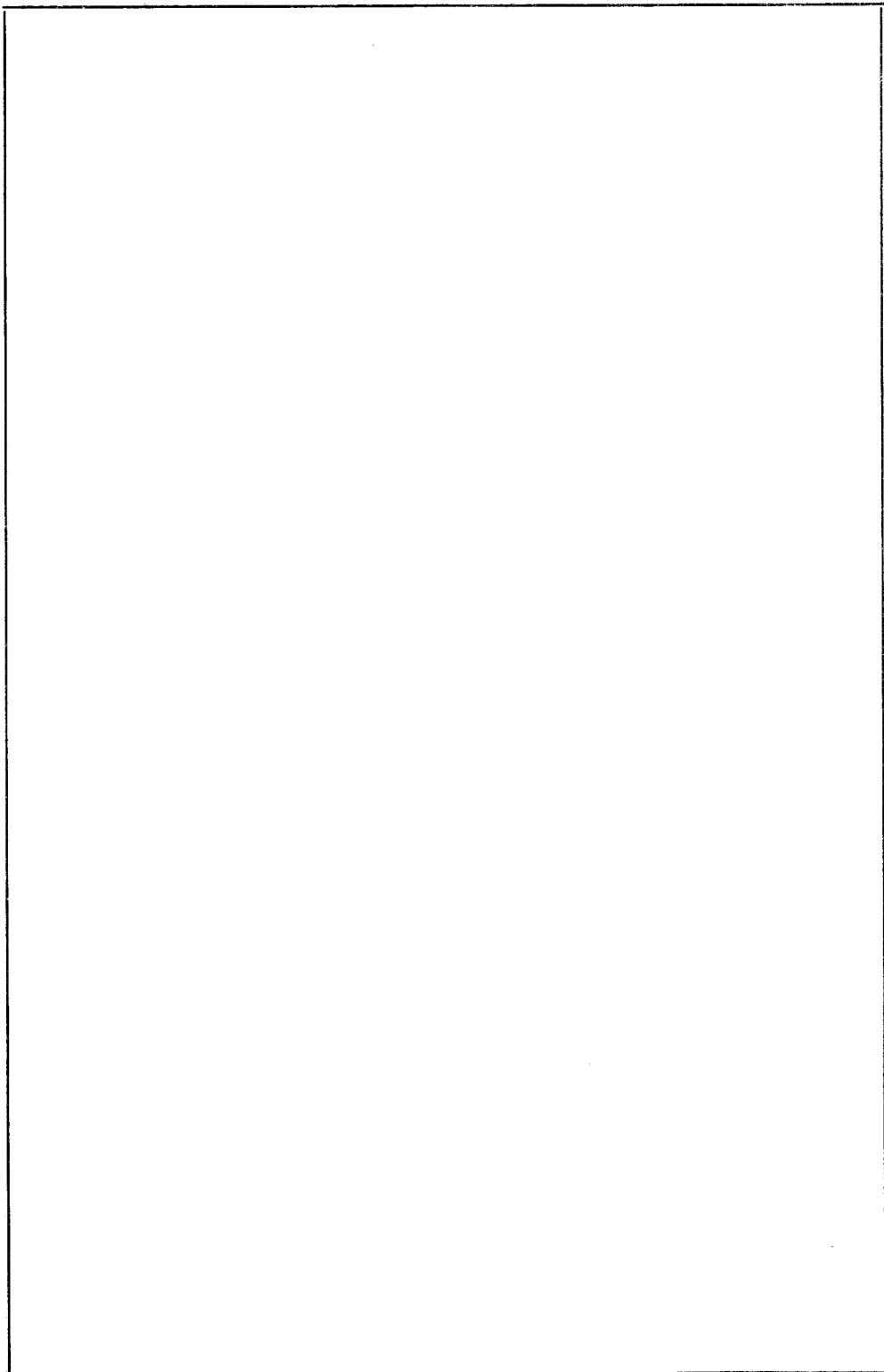


Fig. 2.73. The dependence of the impact ionization coefficient of phosphorus impurity in Si on the electric field strength. The lines are measurements at the lattice temperature  $T$ : dotted line —  $T=27.1\text{ K}$  [2.128], solid line —  $T=20\text{ K}$  [2.129]. The squares are Monte Carlo calculations with the impact ionization cross section  $\sigma_0 = 1 \cdot 10^{-13}\text{ cm}^2$ . The arrow indicates the sudden increase of ionization coefficient due to impurity tunnel ionization.







### 3. Physical data for gallium arsenide

#### 3.1. GaAs lattice properties

1. GaAs consists of the following isotopes (as a result the translational symmetry of GaAs lattice is not exact) [1.1]  
 $^{69}\text{Ga}$ ..... 60.1 %  
 $^{71}\text{Ga}$ ..... 39.9 %  
 $^{75}\text{As}$ ..... 100 %
2. Average molecular weight: 144.63 [3.1]
3. GaAs has cubic sphalerite (zincblende) lattice. Space group is  $\bar{F}43m (T_d^2)$ .  
Lattice symmetry formula is  $3L^24L^36P$ , which means that there are 3 symmetry axes of the second-order, 4 symmetry axes of the third-order and 6 symmetry planes. The inversion symmetry is absent, and by this reason the directions  $[111]$  and  $[\bar{1}\bar{1}\bar{1}]$  are not equivalent
4. Lattice constant:  $a=0.565\ 368\ \text{nm}$  at 298 K [3.2]
5. Density:  $5.316\ 5 \pm 0.0003\ \text{g/cm}^3$  at 298 K [3.2]
6. Number of Ga or As atoms in  $1\ \text{cm}^3$  is  $2.2 \cdot 10^{22}$
7. Melting temperature for stoichiometric GaAs: 1511 K [3.3]
8. Transition to metallic phase occurs at the pressure  $17.2 \pm 0.7\ \text{GPa}$  [3.4]
9. GaAs cleaves most readily on  $\{110\}$  family planes [1.7]

**TABLE 3.1** Elastic parameters of GaAs at the lattice temperature close to absolute zero, 78 K and 298 K [3.5]

Parameter	Value		
	$\sim 0$ K	78 K	298 K
Elastic constants:			
$c_{11}$ , GPa	121.07	120.85	118.41
$c_{12}$ , GPa	54.77	54.69	53.72
$c_{44}$ , GPa	60.36	60.29	59.12
Sound velocity in the direction [100]:			
longitudinal $v_L$ , cm/s	$4.770 \cdot 10^5$	$4.766 \cdot 10^5$	$4.719 \cdot 10^5$
transverse $v_T$ , cm/s	$3.368 \cdot 10^5$	$3.366 \cdot 10^5$	$3.334 \cdot 10^5$
Sound velocity in the direction [111]:			
longitudinal $v_L$ , cm/s	$5.446 \cdot 10^5$	$5.442 \cdot 10^5$	$5.384 \cdot 10^5$
transverse $v_T$ , cm/s	$2.821 \cdot 10^5$	$2.819 \cdot 10^5$	$2.786 \cdot 10^5$
Elastic anisotropy factor $a$	0.549	0.548	0.547
Poisson ratio $\nu$	0.311	0.311	0.312
Young's modulus $E$ , GPa:			
direction [100]	87	86.7	84.9
direction [110]	123.4	123.2	120.7
direction [111]	143.5	143.3	140.5
Bulk modulus $B$ , GPa	76.9	76.7	75.3
$B'_0 = dB_0/dp$			4.67*

\* — [3.6].

**TABLE 3.2** GaAs phonon energies for high symmetry points  $\Gamma$ ,  $X$  and  $L$  in the Brillouin zone at 296 K [3.7]

Phonon branch	Phonon energy, meV		
	$\Gamma$	$X$	$L$
$LO$	$35.4 \pm 0.8$	$29.9 \pm 0.6$	$29.6 \pm 0.3$
$TO$	$33.2 \pm 0.3$	$31.3 \pm 0.3$	$32.4 \pm 0.5$
$LA$	0	$28.1 \pm 0.25$	$25.9 \pm 0.4$
$TA$	0	$9.76 \pm 0.06$	$7.69 \pm 0.08$

**Optical phonon lifetime.** The lifetime of nonthermal  $LO$  phonon in GaAs is  $7 \pm 1$  ps at 77 K [3.8].

**Raman activity.** GaAs has two first-order Raman-active phonons,  $LO(\Gamma)$  and  $TO(\Gamma)$ , which are located at the Brillouin zone center and have energies [3.9]:

$$LO(\Gamma) \ E = 36.19 \text{ meV at } 300 \text{ K,}$$

$$36.75 \text{ meV at } 4 \text{ K,}$$

$$TO(\Gamma) \ E = 33.30 \text{ meV at } 300 \text{ K,}$$

$$33.86 \text{ meV at } 4 \text{ K.}$$

**TABLE 3.3** Grüneisen parameters for different phonon branches in GaAs at  $X$ ,  $K$ ,  $\Gamma$  and  $L$  critical points.  $T = 300$  K [3]

Phonon branch	Grüneisen parameter			
	$X$	$K$	$\Gamma$	$L$
$LO$			1.23	
$TO$	1.73		1.39	1.5
$LA$			1.3* $[q00]$	
$LA$			1.29* $[qq0]$	
$LA$			1.29* $[qqq]$	
$TA$	-1.62		0.53* $[q00]$	-1.7
$TA$			0.23* $[qqq]$	
$TA_1$		-0.4	0.53* $[qq0]$	
$TA_2$		-1.62	-0.05* $[qq0]$	

\* — Calculated from lattice elastic parameters [3.10]. The direction of wave vector is given in parentheses;  $q \ll 2\pi/a$ , where  $a$  is the lattice constant.

#### Lattice dielectric permittivity.

Relative static [3.11]:

$$\varepsilon/\varepsilon_0 = 12.8 \text{ at } 300 \text{ K,}$$

$$12.5 \text{ at } 77 \text{ K.}$$

Relative high frequency [1.17]:

$$\varepsilon_\infty/\varepsilon_0 = 10.92 \text{ at } 300 \text{ K.}$$

Relative change of the static [3.12] and high frequency [1.17] dielectric permittivities with hydrostatic pressure  $p$  in GPa at  $T = 300$  K:

$$(1/\varepsilon)(d\varepsilon/dp) = -1.73 \cdot 10^{-2} \text{ 1/GPa,}$$

$$\varepsilon_\infty/\varepsilon_0 = 10.92 - 0.088p.$$

Dependence of the static [3.12] and high frequency [1.18, 3.12] dielectric permittivities on temperature:

$$(1/\varepsilon)(d\varepsilon/dT) = 2.04 \cdot 10^{-4} \text{ K}^{-1} \text{ at } 300 \text{ K,}$$

$$9.4 \cdot 10^{-5} \text{ K}^{-1} \text{ at } 75.6 \text{ K,}$$

$$(1/\varepsilon_\infty)(d\varepsilon_\infty/dT) = 1.2 \cdot 10^{-4} \text{ K}^{-1} \text{ at } 300 \text{ K.}$$

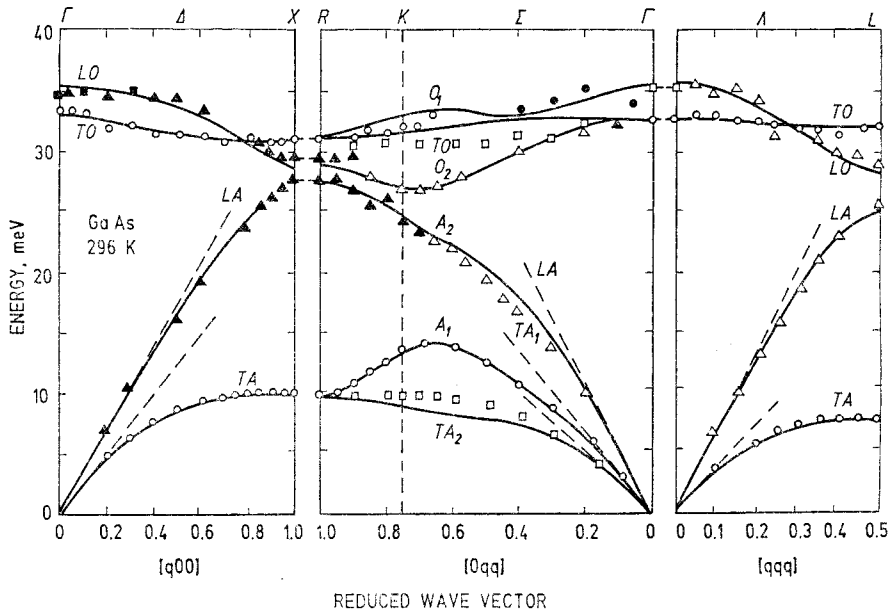


Fig. 3.1. Phonon dispersion curves for GaAs at 296 K [3.7]. The dashed lines show the slopes for sound velocity in various directions. For  $A_1$ ,  $A_2$ ,  $O_1$  and  $O_2$  branches the polarization is elliptical. Other modes are either strictly longitudinal (L) or transverse (T).

For  $[0qq]$  direction the data extend beyond the Brillouin zone boundary shown by vertical dashed line. The path from K to R is equivalent to the path from U to X on the Brillouin zone boundary (see Fig. 1).

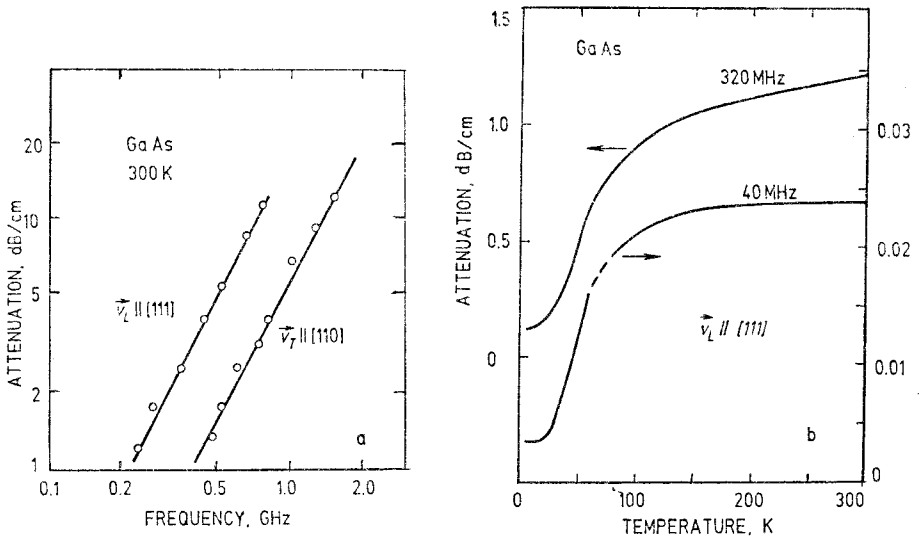


Fig. 3.2. Ultrasound attenuation. *a* — Frequency dependence of ultrasound attenuation coefficient for longitudinal (L) and transverse (T) waves propagating in GaAs lattice in the direction  $[111]$  and  $[110]$ , respectively.  $T=300$  K [3.13]. *b* — Temperature dependence of the attenuation of longitudinal ultrasonic waves propagating in the  $[111]$  direction of GaAs at ultrasonic frequencies 40 and 320 MHz [3.14].

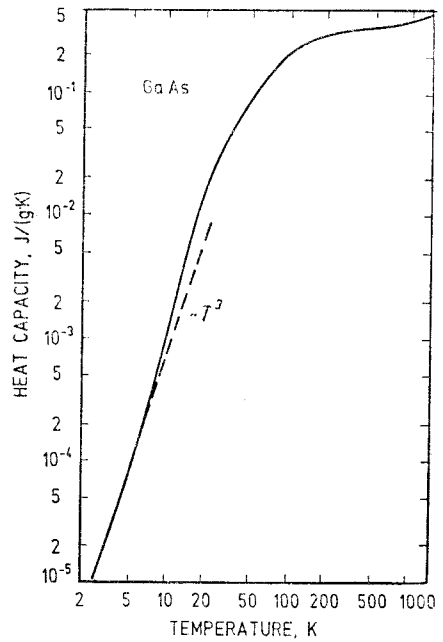


Fig. 3.3. Heat capacity  $C_p(T)$  of pure GaAs as a function of temperature [3.15].

Selected values:

$$C_p = 5 \cdot 10^{-5} \text{ J/(g·K) at 4.2 K [3.16],}$$

$$0.147 \text{ J/(g·K) at 77.4 K [3.1],}$$

$$0.327 \text{ J/(g·K) at 300 K [3.17].}$$

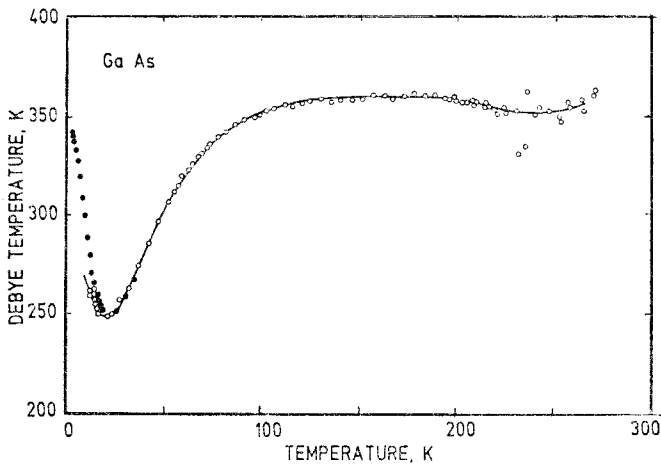


Fig. 3.4. GaAs Debye temperature vs. lattice temperature [3.1, 3.16].

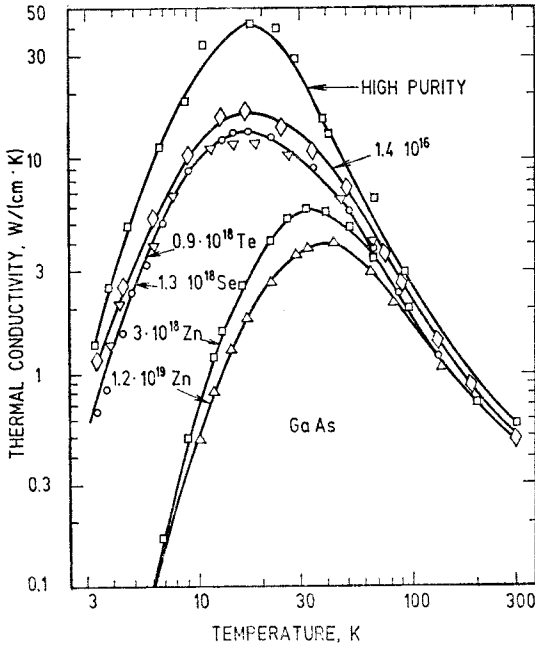


Fig. 3.5. Thermal conductivity  $\chi$  of GaAs with indicated impurity concentrations and dopants [3.18].

Selected values:

$\chi = 24.6 \text{ W/(cm} \cdot \text{K)}$  at 30 K,  
 $4.3 \text{ W/(cm} \cdot \text{K)}$  at 77.4 K,  
 $0.58 \text{ W/(cm} \cdot \text{K)}$  at 295 K.

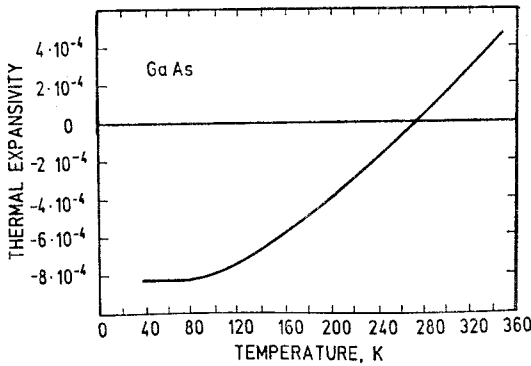


Fig. 3.6. Thermal expansivity  $(l_T - l_{273.2})/l_{273.2}$  as a function of the lattice temperature for GaAs [3.19].  $l_{273.2}$  is a length at  $T = 273.2 \text{ K}$ .



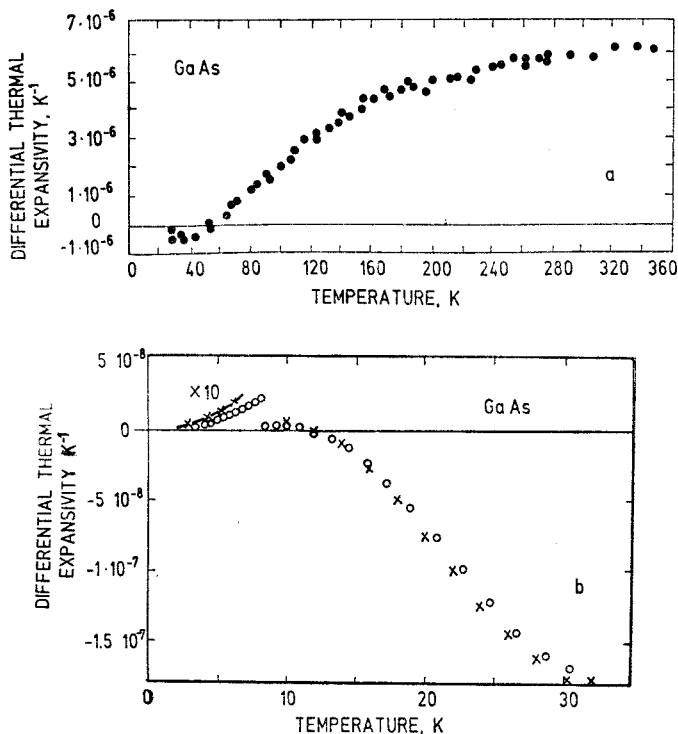


Fig. 3.7. Differential thermal expansivity  $\alpha = (1/l_{273.2}) (dl/dT)$  as a function of temperature  $T$  for GaAs. *a* –  $T > 30$  K [3.19], *b* –  $T < 30$  K [1.24]. Note, that below 8 K the values are multiplied by the factor 10.

Empirical formula valid in the range  $200 < T < 1000$  K [3.15]:

$$\alpha = (4.24 + 5.82 \cdot 10^{-8} T - 2.82 \cdot 10^{-6} T^2) \cdot 10^{-6}, \alpha \text{ is in } K^{-1} \text{ and } T \text{ is in } K.$$

Selected values:

$$\begin{aligned} \alpha &= 4.4 \cdot 10^{-10} K^{-1} \text{ at } 4.2 \text{ K [1.24]}, \\ &1.0 \cdot 10^{-6} K^{-1} \text{ at } 78 \text{ K [3.19]}, \\ &5.6 \cdot 10^{-6} K^{-1} \text{ at } 298 \text{ K [3.20]}. \end{aligned}$$

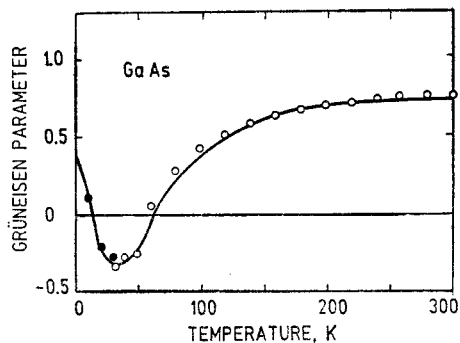


Fig. 3.8. Averaged Grüneisen parameter for GaAs as a function of the lattice temperature. Solid curve: theoretical calculations. Points: obtained from experimental linear expansion coefficient and heat capacity [3.10].

### 3.2. GaAs band properties

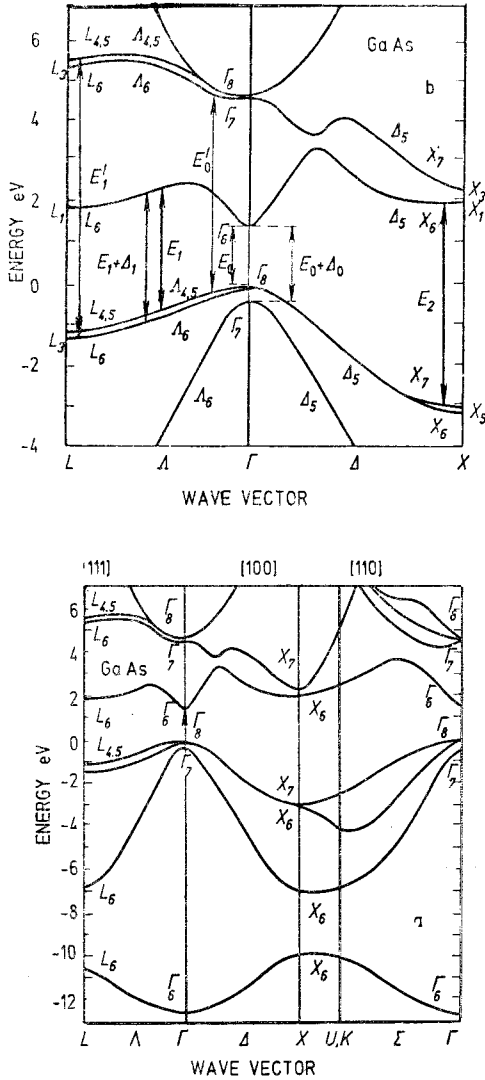


Fig. 3.9. Band structure of GaAs with spin-orbit interaction included. *a* – General view [1.28]. *b* – Enlarged portion with main interband optical transitions near  $\Gamma$  point ( $E_0$ ,  $E_0 + \Delta_0$ ,  $E'_0$ ), along  $\Delta$  direction ( $E_1$ ,  $E_1 + \Delta_1$ ) and near  $X$  point ( $E_2$ ) shown by vertical lines. The forbidden energy gap  $E_g$  is equal to  $E_0$  [3.21].

GaAs does not possess inversion symmetry, as a result the bands in the general point of the Brillouin zone are not degenerate. The exceptions are  $[100]$  axes,  $L$  and  $\Gamma$  points.

**TABLE 3.4** Critical points associated with band-band transitions in GaAs which are important in optical measurements (see also Fig. 3.9)

Critical point	Corresponding band-band transition with spin-orbit interaction		<b>k</b> -space location (units of $2\pi/a$ )
	included	neglected	
$E_0 \equiv E_g$ $E_0 + \Delta_0$	$\Gamma_{8v} \rightarrow \Gamma_{6c}$ $\Gamma_{7v} \rightarrow \Gamma_{6c}$	$\Gamma_{15}^v \rightarrow \Gamma_1^c$	Arises from transitions at fundamental absorption edge, dominated by small region around (0,0,0); the transition is weak
$E'_0$ $E'_0 + \Delta'_0$	$\Gamma_{8v} \rightarrow \Gamma_{7c}$ $\Delta_{5v} \rightarrow \Delta_{5c}$ $\Gamma_{8v} \rightarrow \Gamma_{8c}$	$\Gamma_{15}^v \rightarrow \Gamma_{15}^c$	Arises from transitions to the second conduction band near (0, 0, 0) and along $\Delta$ direction near (0.1, 0, 0)
$E_1$ $E_1 + \Delta_1$	$(\Lambda_4, \Lambda_5)_v \rightarrow \Lambda_{6c}$ $\Lambda_{6v} \rightarrow \Lambda_{6c}$	$\Lambda_3^v \rightarrow \Lambda_1^c$	Originates from transitions to the first conduction band along $\Lambda$ direction near $L$
$E_2$ $E_2 + \Delta_2$	$X_{7v} \rightarrow X_{6c}$ $X_{6v} \rightarrow X_{6c}$ $X_{6v} \rightarrow X_{7c}$ $X_{7v} \rightarrow X_{7c}$	$X_3^v \rightarrow X_1^c$	Arises from a well defined interband plateau region near the point (0.75, 0.25, 0.25); the transitions in this region dominate the spectra because of the large phase space and strong matrix elements

Additional energies  $\Delta_0$ ,  $\Delta'_0$  etc. are associated with splitting caused by spin-orbit interaction.

**TABLE 3.5** Energetic distances between experimentally important critical points in the energy band of GaAs at room temperature and respective hydrostatic pressure coefficients. For transition and critical point nomenclature see Fig. 3.9 and Table 3.4

Energy separation and pressure coefficient	Value	Comment	Reference
$E_g \equiv E_0 = E(\Gamma_{6c}) - E(\Gamma_{8v}), \text{ eV}$	1.429	Direct forbidden energy gap	[3.21]
$E_{\Gamma X} = E(\Delta_{5c}) - E(\Gamma_{6c}), \text{ eV}$	0.46		[3.22]
$E_{\Gamma L} = E(L_{6c}) - E(\Gamma_{6c}), \text{ eV}$	0.3		[3.22]
$E_{XL} = E(\Delta_{5c}) - E(L_{6c}), \text{ eV}$	0.17		[3.23]
$\Delta_0 = E(\Gamma_{8v}) - E(\Gamma_{7v}), \text{ eV}$	0.34	Spin-orbit splitting in the valence band	[3.24]
$E_1, \text{ eV}$	2.91		[3.21]
$E_2, \text{ eV}$	4.96		[3.21]
$\Delta_1, \text{ eV}$	0.22		[3.21]
$d E_g/dp, \text{ eV/GPa}$	0.108	Gap increases with pressure	[3.25, 3.26]
$d E_X/dp, \text{ eV/GPa}$	-0.0135	X valley relative to the valence band edge	[3.25, 3.27]
$d E_{\Gamma X}/dp, \text{ eV/GPa}$	-0.12	Due to $\Gamma$ and X valley crossover GaAs becomes an indirect gap semiconductor at hydrostatic pressure $p \gtrsim 4.2 \pm 0.3 \text{ GPa}$ (cf. Fig. 3.46)	[3.25, 3.27]
$d E_L/dp, \text{ eV/GPa}$	0.062	L valley relative to the valence band edge	[3.28]
$d E_{\Gamma L}/dp, \text{ eV/GPa}$	-0.045		[3.28]
$d E_1/dp, \text{ eV/GPa}$	0.072		[3.29]

**TABLE 3.6** GaAs conduction band principal valley parameters

Parameter	$\Gamma$ valley	$L$ valley	$X$ valley	Reference
Valley location in the Brillouin zone	$\Gamma_{6c}$ , the lowest valley in the center of the zone	$L_{6c}$ , in $\langle 111 \rangle$ direction on the zone boundary	$\Delta_{5c}$ , in $\langle 100 \rangle$ direction about 10% away from the zone boundary	
Number of valleys	1	4	6	[3.15]
Valley separation relative to $\Gamma$ valley, eV	0	0.3	0.46	[3.22]
Electron masses*:				
scalar $m_n/m_0$				
at 290 K	0.0636			[3.30]
at 1.46 K	0.0665			[3.31]
longitudinal $m_l/m_0$		1.9	1.9**	[3.15]
transverse $m_t/m_0$		0.075	0.19**	[3.15]
density-of-states $m_d/m_0$	0.0636	0.22	0.41	
Nonparabolicity parameter $\alpha$ , eV $^{-1}$	0.69			[3.32]
Uniaxial deformation potential $\Xi_u$ , eV		14.5	6.5	[3.28]
$g_c$ -factor	-0.44			[3.33]

\* - In  $A^3B^5$  semiconductors the polaronic corrections to conduction and valence band effective masses are small and often are neglected [3.30, 3.34].

\*\* - Deduced from the transport measurements assuming 3-valley model.

**TABLE 3.7** GaAs valence band parameters

Parameter	Value	Reference
<b>Light and heavy mass band at <math>\Gamma_{8v}</math></b>		
Luttinger parameters:		
$\gamma_1$	6.85	[3.35]
$\gamma_2$	2.1	[3.35]
$\gamma_3$	2.9	[3.35]
$g_v$ -factor: $2k$	2.4	[3.35]
$q$	0.04	[3.35]
Valence band nonsphericity $\delta$	0.12	
Average heavy hole mass for "spherical" bands $m_h/m_0$	0.59	
Average light hole mass for "spherical" bands $m_l/m_0$	0.083	
Density-of-states mass $m_d/m_0$	0.61	
Uniaxial deformation potentials at $\Gamma_{8v}$ , eV		
$D_u$	2.55	[3.36]
$D'_u$	3.94	[3.36]
<b>Spin-orbit split-off valence band at <math>\Gamma_{7v}</math></b>		
$\Delta_0 = E(\Gamma_{8v}) - E(\Gamma_{7v})$ , meV	0.341	[3.24, 3.37]
Mass $m_{so}/m_0$	0.154	[3.38]
$g_{so}$ -factor	-4.9	[3.38]

Fig. 3.10. Valence band warping in GaAs. The contours are constant energy surfaces of heavy ( $h$ ) and light ( $l$ ) mass bands in (100) and  $(\bar{1}\bar{1}0)$  planes. The band nonparabolicity is not included (cf. Fig. 2).

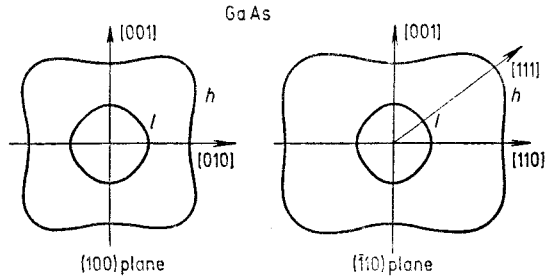
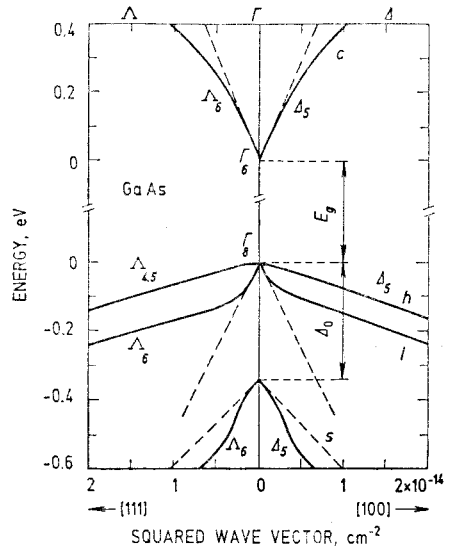


Fig. 3.11. Energies of electron in the conduction band ( $c$ ) and of hole in heavy ( $h$ ), light ( $l$ ) and split-off ( $s$ ) valence bands of GaAs in [100] and [111] crystallographic directions as functions of squared wave vector. The dashed lines show the parabolic bands [3.15].

The wave vector range covered here is equivalent to about one tenth of the Brillouin zone radius



**GaAs valence band splitting under uniaxial compressive stress** is similar to that of Ge (see Table 1.8). For GaAs the valence band uniaxial deformation potential and elastic constant values can be found in Tables 3.1 and 3.7.

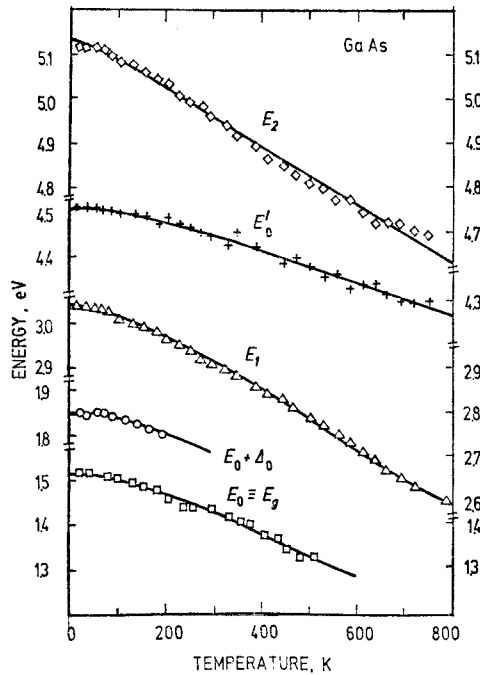


Fig. 3.12. Temperature dependence of the energy gap  $E_0 \equiv E_g$  and interband critical point energies of GaAs. The corresponding vertical transitions are shown in Fig. 3.9, *b*. The solid lines represent the best fits with empirical formulas and parameter values listed in Table 3.8 [3.21].

**TABLE 3.8** Values of the parameters  $a$ ,  $b$  and  $\Theta$  in equation  $E(T) = a - b [1 + 2/(e^{\Theta/T} - 1)]$ , which have been obtained by fitting the critical point energies vs. temperature  $T$  by solid lines in Fig. 3.12

Critical point	$a$ , eV	$b$ , eV	$\Theta$ , K
$E_0 \equiv E_g$ (energy gap)	1.57	0.057	240
$E_0 + \Delta_0$	1.91	0.058	240
$E_1$	3.12	0.091	274
$E_0'$	4.56	0.059	323
$E_2$	5.16	0.038	114



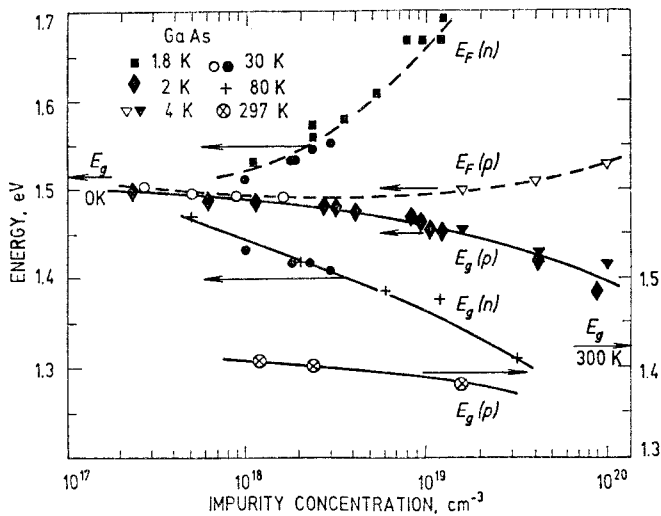


Fig. 3.13. The energy band gap  $E_g$  and Fermi energy  $E_F$  relative to: ( $n$ ) — the valence band edge in case of  $n$ -GaAs, and ( $p$ ) — conduction band edge in case of  $p$ -GaAs, as a function of impurity concentration at various lattice temperatures. Arrows on the energy scale indicate  $E_g$  of pure gallium arsenide at 0 and 300 K. The lines serve as a guide to the eye. Triangles —  $T=4$  K [3.39]. Rhombs —  $T=2$  K [3.40]. Circles —  $T=30$  K [3.41]. Squares —  $T=1.8$  K [3.42]. Crossed circles —  $T=297$  K [3.43]. Crosses —  $T=80$  K [3.44].

### 3.3. GaAs optical properties

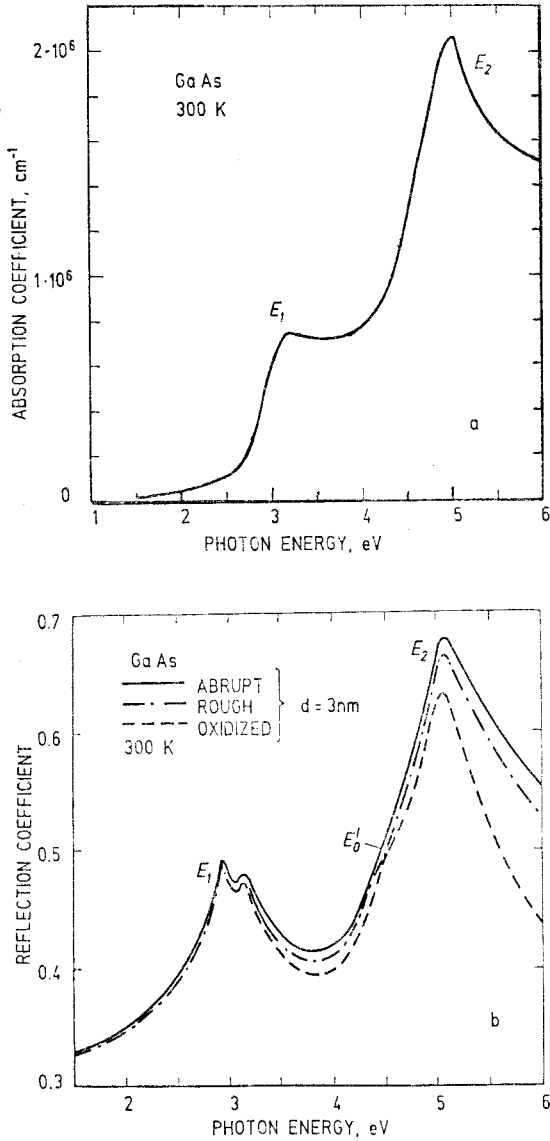


Fig. 3.14. Dependence of absorption (a) and reflection (b) coefficients of GaAs on photon energy at 300 K [1.53]. In (b) the influence of sample surface quality (rough, oxidized) is shown;  $d$  is the interface thickness.

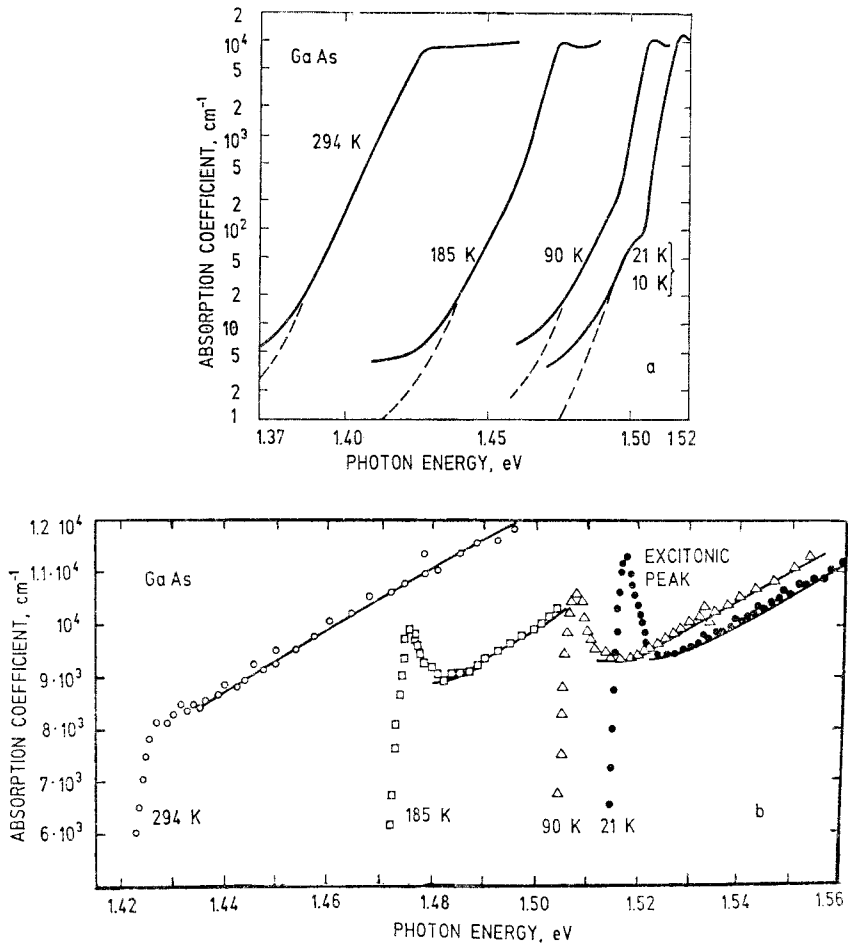


Fig. 3.15. Optical absorption near the band gap edge of GaAs. *a* – Optical low-intensity absorption. Dashed line: corrected for impurity absorption. *b* – The enlarged portion of the edge at the excitonic peak [3.45].

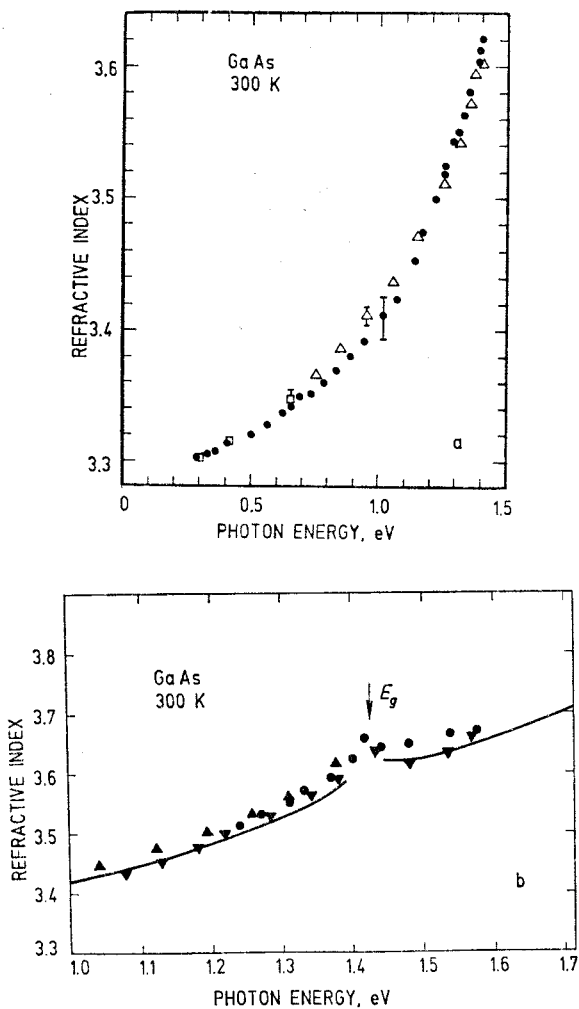


Fig. 3.16. Refractive index vs. photon energy in GaAs: *a* — for energies below the band gap [3.15], *b* — in the vicinity of the band gap energy  $E_g$  [3.46]. Solid line: calculated values. Symbols: experimental data.

Empirical formula of the square of refractive index on photon energy in the range  $\hbar\omega=0.3\text{--}1.4$  eV [3.15]:  $n^2=7.1+\frac{3.78}{1-0.18\hbar\omega}$ ,  $\hbar\omega$  is in eV.

Fig. 3.17. Absorption coefficient vs. photon energy in *n*-GaAs near the forbidden energy gap. Electron concentration: 1 -  $n = 5.9 \cdot 10^{17} \text{ cm}^{-3}$ , 2 -  $2 \cdot 10^{18} \text{ cm}^{-3}$ , 3 -  $3.3 \cdot 10^{18} \text{ cm}^{-3}$ , 4 -  $6.7 \cdot 10^{18} \text{ cm}^{-3}$ .  $T = 297 \text{ K}$  [3.47].

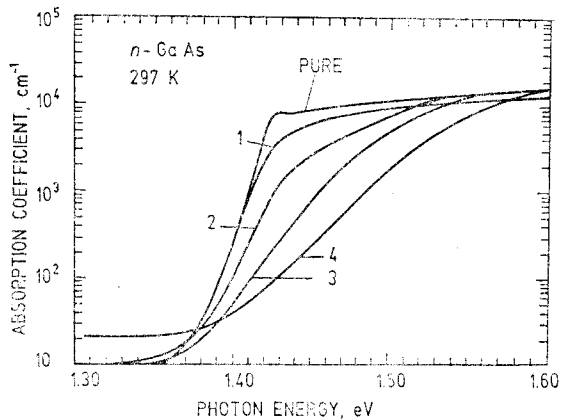


Fig. 3.18. Absorption coefficient vs. photon energy in *p*-GaAs near the forbidden energy gap. Hole concentration: 1 -  $p = 1.6 \cdot 10^{16} \text{ cm}^{-3}$ , 2 -  $2.2 \cdot 10^{17} \text{ cm}^{-3}$ , 3 -  $4.9 \cdot 10^{17} \text{ cm}^{-3}$ , 4 -  $1.2 \cdot 10^{18} \text{ cm}^{-3}$ , 5 -  $2.4 \cdot 10^{18} \text{ cm}^{-3}$ , 6 -  $1.6 \cdot 10^{19} \text{ cm}^{-3}$ .  $T = 297 \text{ K}$  [3.47].

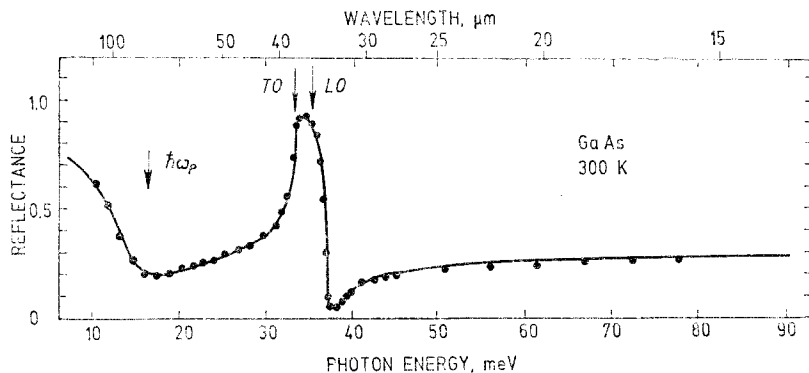
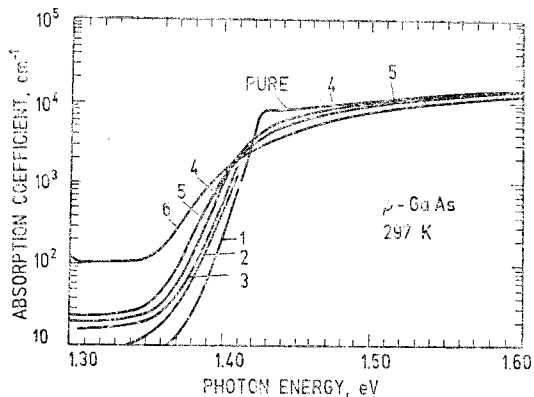
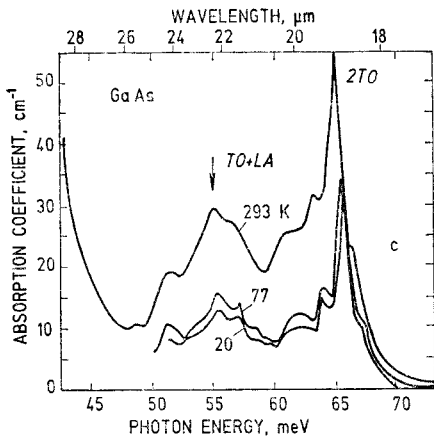
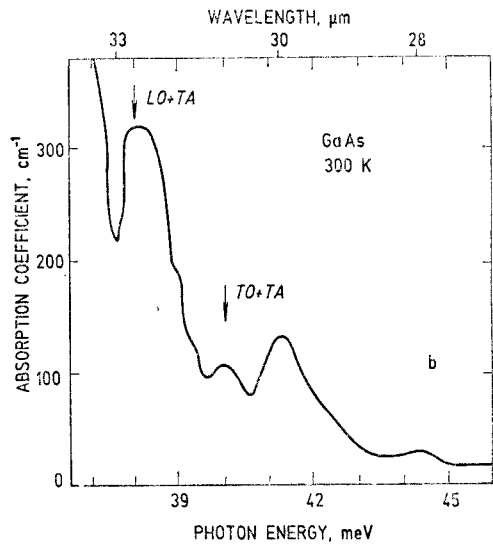
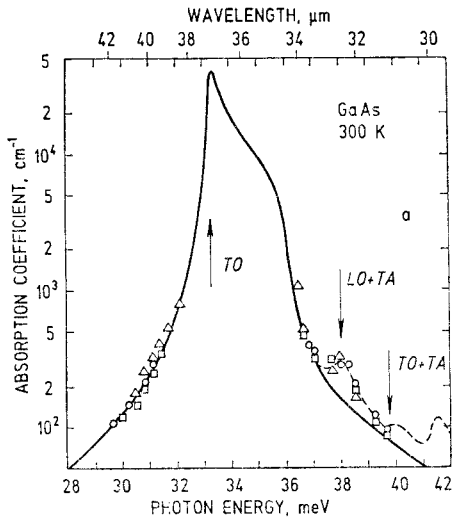


Fig. 3.19. Reflectance of GaAs lattice at 300 K. The increase of the reflectance at photon energies smaller than the plasma energy  $\hbar\omega_p$  is due to free carrier plasma effects, while in the reststrahlen region, 33–35 meV, due to TO and LO phonons [3.48].



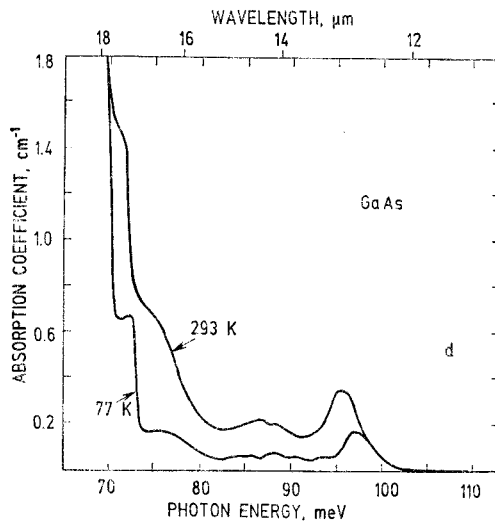


Fig. 3.20. Lattice absorption coefficient of high resistivity GaAs at different temperatures. *a* — In the reststrahlen region. Solid line is theoretical calculation, while dashed curve and points are results of transmission measurements [3.15]. *b, c, d* — In the multiphonon region [3.49]. Note widely differing ordinate scales for different parts.

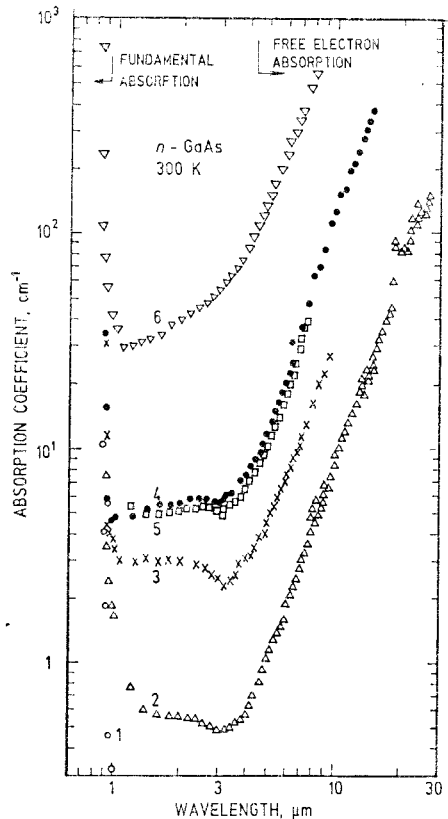


Fig. 3.21. Absorption coefficient vs. photon wavelength in *n*-GaAs at room temperature. Free electron concentration: 1 —  $n \lesssim 5 \cdot 10^{14} \text{ cm}^{-3}$ , 2 —  $1.3 \cdot 10^{17} \text{ cm}^{-3}$ , 3 —  $4.9 \cdot 10^{17} \text{ cm}^{-3}$ , 4 —  $1.09 \cdot 10^{18} \text{ cm}^{-3}$ , 5 —  $1.12 \cdot 10^{18} \text{ cm}^{-3}$ , 6 —  $5.4 \cdot 10^{18} \text{ cm}^{-3}$  [3.50].

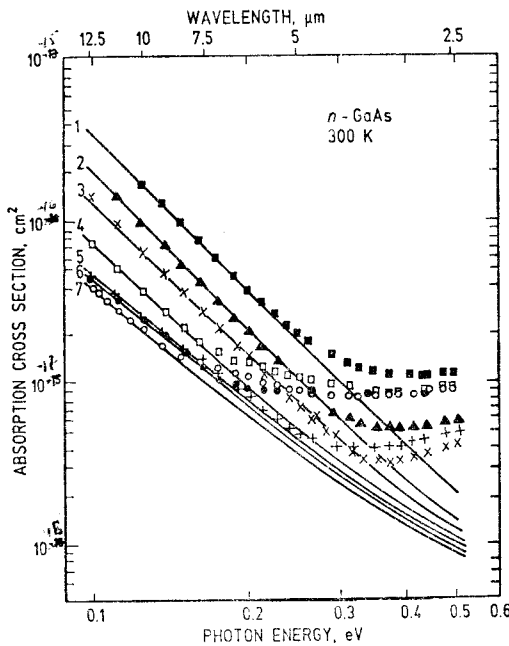


Fig. 3.22. Absorption cross section of  $n$ -GaAs defined as  $\alpha/n$ , where  $\alpha$  is the absorption coefficient and  $n$  is the electron concentration, vs. photon energy at  $T = 300$  K. Dots are experimental results, while lines are theoretical calculations due to free electron absorption when acoustic phonon, optical phonon and impurity scattering are included [3.51]. 1 -  $n = 10^{18}$  cm<sup>-3</sup>, 2 -  $7.4 \cdot 10^{17}$  cm<sup>-3</sup>, 3 -  $2.7 \cdot 10^{17}$  cm<sup>-3</sup>, 4 -  $1.7 \cdot 10^{17}$  cm<sup>-3</sup>, 5 -  $10^{17}$  cm<sup>-3</sup>, 6 -  $4.5 \cdot 10^{16}$  cm<sup>-3</sup>, 7 -  $10^{16}$  cm<sup>-3</sup>.

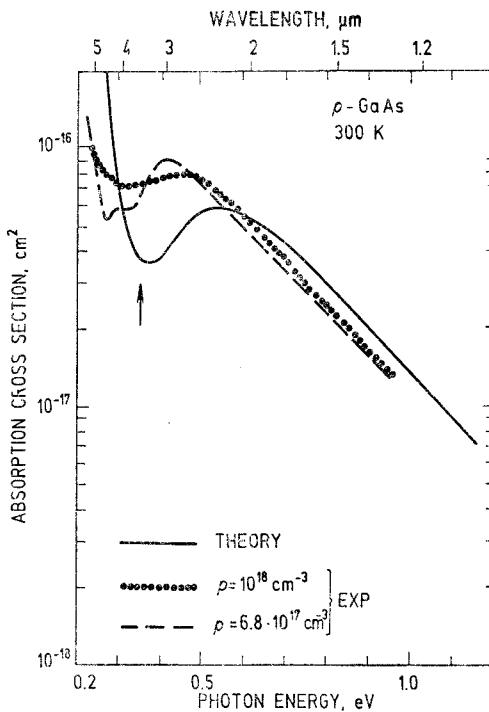


Fig. 3.23. Free hole absorption cross section in  $p$ -GaAs defined as  $\alpha/p$ , where  $\alpha$  is the absorption coefficient and  $p$  is the hole concentration, vs. photon energy. The arrow indicates the onset of transitions to split-off valence band. Dotted and dashed lines: experiments with  $p \leq 10^{18}$  cm<sup>-3</sup> and  $p = 6.8 \cdot 10^{17}$  cm<sup>-3</sup> [3.52, 3.53]. Solid line: theory [3.54].



**TABLE 3.9** Luminescence and related properties of some quasiparticles in GaAs

Property	Value	Comment	Reference
<b>Free exciton, <math>X</math></b>			
Luminescence energy:			
ground state	1515.3 meV		[3.55]
1st excited state	1518.5 meV	1.2–2.1 K	[3.55]
Binding energy	$4.2 \pm 0.3$ meV		[3.55]
Lifetime	3.3–10 ns	1.7–10 K, $2 \cdot 10^{14} \text{ cm}^{-3}$	[3.56]
<b>Exciton bound to shallow donor, <math>[DX]</math></b>			
Average luminescence energy	1514.1 meV	2 K	[3.57]
Dissociation energy:			
$[DX] \rightarrow D + e + h$	5.3 meV	1.8 K	[3.58]
$[DX] \rightarrow [D^+X] + e$	5.1 meV		[3.58]
$[DX] \rightarrow D + X$	1.2 meV		[3.58]
Lifetime	1.07–0.7 ns	1.6 K	[3.59]
<b>Exciton bound to acceptor, <math>[AX]</math></b>			
Average luminescence energy of $[ZnX]$ , $[CX]$ , $[GeX]$ :			
ground state	1512.25–1512.73 meV		[3.57]
2s-excited state			
$[ZnX](2s)$	1490.49–1490.67 meV		[3.57]
$[CX](2s)$	1493.85–1494.00 meV		[3.57]
Ground state of $[SnX]$	1507.4 meV	4.2 K, deep acceptor	[3.60]
Dissociation energy:			
$[AX] \rightarrow A + e + h$	7 meV		[3.58]
$[AX] \rightarrow [A^+X] + e$	7 meV		[3.58]
$[AX] \rightarrow A + X$	2.9 meV		[3.58]
Lifetime	1.2–1.6 ns	1.6 K	[3.59]

TABLE 3.9 (Continued)

Property	Value	Comment	Reference
----------	-------	---------	-----------

Free electron-acceptor transitions, *e-A*

Luminescence energy:

<i>e</i> -Sn	1349.0 meV	5 K	[3.61]
<i>e</i> -Mn	1405 meV	2 K	[3.62]
<i>e</i> -Ge	1479.0 meV	5 K	[3.61]
<i>e</i> -Cd	1484.8 meV	5 K	[3.61]
<i>e</i> -Si	1485.0 meV	5 K	[3.61]
<i>e</i> -Zn	1488.8 meV	5 K	[3.61]
<i>e</i> -Mg	1491.1 meV	5 K	[3.61]
<i>e</i> -Be	1491.5 meV	5 K	[3.61]
<i>e</i> -C	1493.5 meV	5 K	[3.61]

Donor-acceptor transitions, *D-A*

Luminescence energy:

<i>D</i> -Ge	1472.2 meV	$\leq 4$ K, $\sim 10^{14}$ cm $^{-3}$	[3.63]
<i>D</i> -Si	1479.5 meV	$\leq 4$ K, $\sim 10^{14}$ cm $^{-3}$	[3.63]
<i>D</i> -Si	1489 meV	$\leq 4$ K, $1.2 \cdot 10^{17}$ cm $^{-3}$	[3.63]
<i>D</i> -Zn	1484.0 meV	$\leq 4$ K, $\sim 10^{14}$ cm $^{-3}$	[3.63]
<i>D</i> -C	1487.5 meV	$\leq 4$ K, $\sim 10^{14}$ cm $^{-3}$	[3.63]
<i>D</i> -C	1497 meV	$\leq 4$ K, $1.2 \cdot 10^{17}$ cm $^{-3}$	[3.63]
<i>D</i> -Sn	1349 meV	deep acceptor	[3.60]

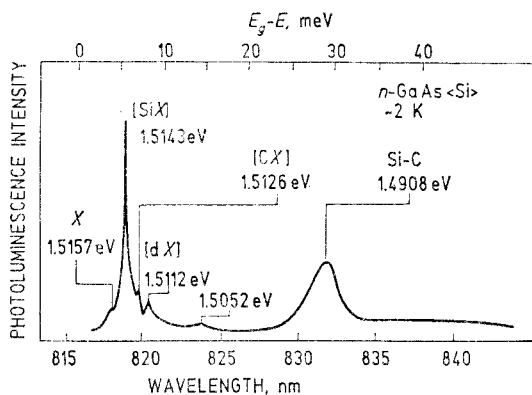


Fig. 3.24. Typical photoluminescence spectra of GaAs measured at 2K.  $n(300\text{ K}) = 1.2 \cdot 10^{15} \text{ cm}^{-3}$ . The following luminescence lines in order of increasing energies are shown: X — free exciton, [SiX] — exciton bound to neutral donor silicon, [CX] — exciton bound to neutral acceptor carbon, [dX] — exciton bound to defect, Si-C — silicon-carbon pair recombination [3.64].

**Relative change of the refractive index** with the hydrostatic pressure  $p$  at 300 K [1.17]:

$$(1/n)(dn/dp) = -5 \cdot 10^{-3} \text{ 1/GPa} \quad \text{at } h\nu = 0.7 \text{ eV, } n = 3.36;$$

$$(1/n)(dn/dp) = -5.7 \cdot 10^{-3} \text{ 1/GPa} \quad \text{at } h\nu = 1 \text{ eV, } n = 3.42;$$

$$(1/n)(dn/dp) = -8.3 \cdot 10^{-3} \text{ 1/GPa} \quad \text{at } h\nu = 1.3 \text{ eV, } n = 3.54.$$

Temperature dependence of the refractive index in the wavelength range from 1 to 12  $\mu\text{m}$  at room temperature [1.18]:

$$(1/n)(dn/dT) = 6 \cdot 10^{-5} \text{ K}^{-1}.$$

**TABLE 3.10** Elastooptic coefficients (dimensionless)  $p_{ij}$  and refractive index  $n$  of GaAs at wavelength  $\lambda = 1.15 \mu\text{m}$  [3.65]

Parameter	Value
$p_{11}$	-0.165
$p_{12}$	-0.140
$p_{44}$	-0.072
$n$	3.37

**TABLE 3.11** Electrooptic (Pockels) coefficient  $r_{14}$  and refractive index of GaAs at some electromagnetic radiation wavelengths [3.66, 3.67]

Radiation wavelength, $\mu\text{m}$	$r_{14}$ , m/V	Refractive index
0.9	$1.10 \cdot 10^{-12}$	3.6
1.15	$1.43 \cdot 10^{-12}$	3.43
3.39	$1.24 \cdot 10^{-12}$	3.3
10.6	$1.51 \cdot 10^{-12}$	3.3

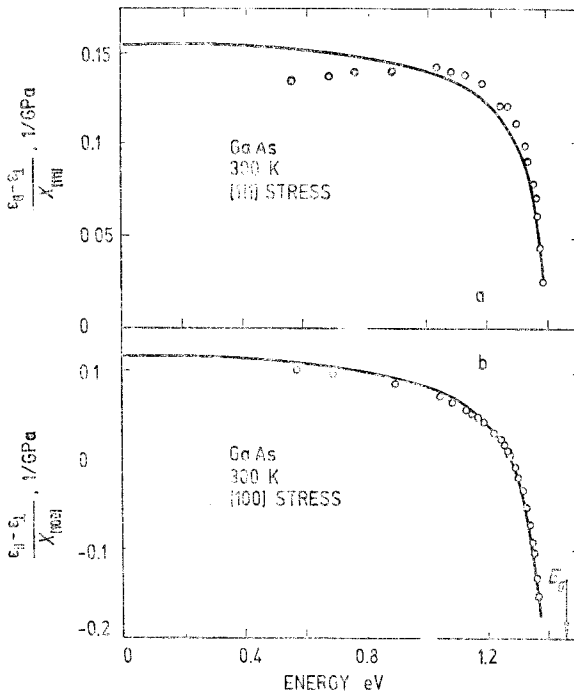


Fig. 3.25. Piezooptic effect. Measured values (points) and fitted curves of  $(\epsilon_{\parallel} - \epsilon_{\perp}) / X_{[111]} = -n^4 \pi_{44}$  and  $(\epsilon_{\parallel} - \epsilon_{\perp}) / X_{[100]} = -n^4 (\pi_{11} - \pi_{12})$  for GaAs as a function of photon energy, where  $\epsilon_{\parallel}$  and  $\epsilon_{\perp}$  are the relative dielectric permittivities for light polarized parallel and perpendicular to the uniaxial stress  $X$  applied in  $[111]$  and  $[100]$  directions.  $n$  is the refractive index and  $\pi_{ij}$  are the piezooptic coefficients.  $T=300$  K [1.66]

#### Nonlinear susceptibilities of GaAs. Second-order nonlinear susceptibility:

$$d_{14} = (1.34 \pm 0.4) \cdot 10^{-10} \text{ m/V at } 10.6 \mu\text{m} [3.68],$$

$$d_{14} = 5 \cdot 10^{-11} \text{ m/V at } 500 - 175 \mu\text{m} [3.69].$$

Valence electron contribution to the third-order nonlinear susceptibility  $c(\omega_2 - 2\omega_1, \omega_1, \omega_1, -\omega_2)$  of GaAs measured by mixing  $\lambda_1 = 10.6 \mu\text{m}$  and  $\lambda_2 = 9.5 \mu\text{m}$  radiation [1.67]:

$$c_{1111} = 1.7 \cdot 10^{-19} \text{ m}^2/\text{V}^2, 10 \% \text{ accuracy},$$

$$c_{1122}/c_{1111} = 0.25 \pm 0.01.$$

For free electron contribution see Fig. 3.26.

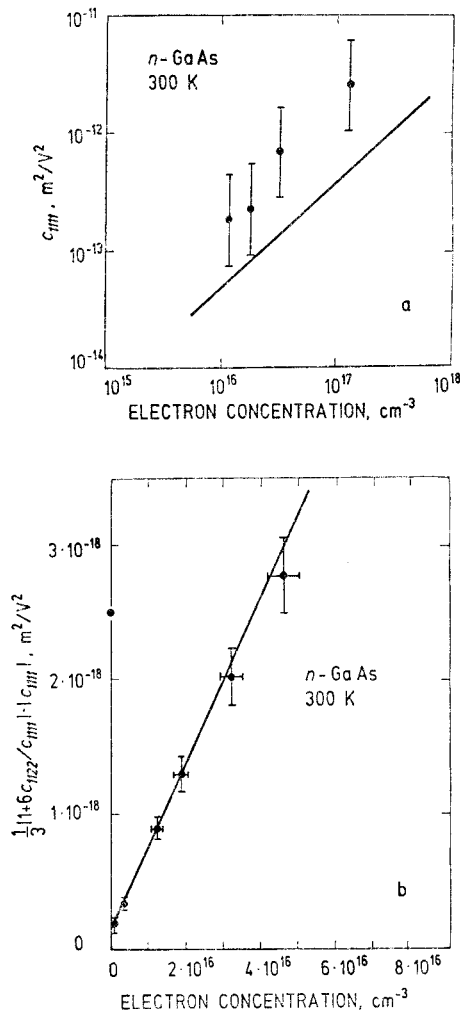


Fig. 3.26. Free electron contribution to third-order nonlinear susceptibilities. *a* — Absolute values of third-order nonlinear susceptibility  $c_{III}(3\omega, \omega, \omega, \omega)$  measured by frequency tripling of 0.5 mm radiation, vs. free electron concentration, for *n*-GaAs at room temperature. The anisotropy of susceptibility is  $\sigma = (1 + 3c_{1122}/c_{1111})/2 = 1.11 \pm 0.02$ . The solid curve is theoretical prediction for the nonparabolicity contribution [1.68]. *b* — Variation of nonlinear third-order susceptibility  $c(\omega_3 - 2\omega_1, \omega_1, \omega_1, -\omega_2) = \frac{1}{3} |1 + 6c_{1122}/c_{1111}| \cdot |c_{1111}|$  with carrier concentration in *n*-GaAs at room temperature obtained by measuring the difference frequency  $\omega_3 = 2\omega_1 - \omega_2$ , where  $\omega_1, \omega_2$  and  $\omega_3$  correspond to wavelengths 10.6, 9.5 and 11.8  $\mu\text{m}$ , respectively. The straight line is the fit which minimizes the fractional mean deviation from each point [1.67].

### 3.4. GaAs electrical properties

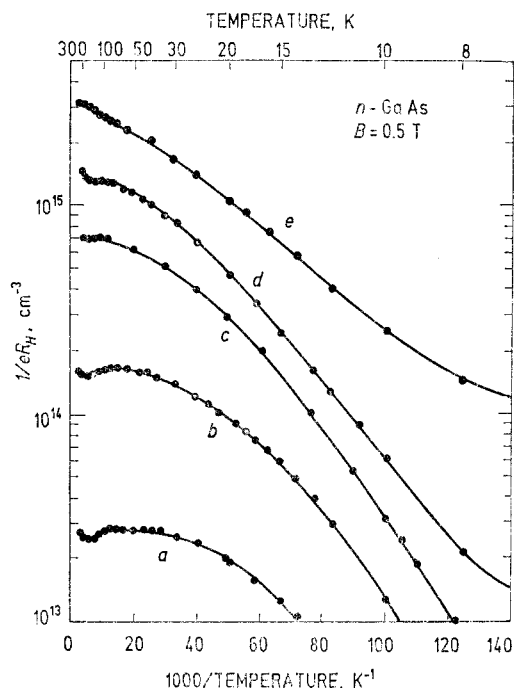


Fig. 3.27. Reciprocal of the Hall coefficient times the elementary charge,  $1/eR_H$ , measured at 0.5 T for  $n\text{-GaAs}$  samples whose parameters are given, in Table 3.12. At low temperatures  $1/eR_H$  decreases due to electron freeze-out to shallow donors. At high temperatures the temperature variation of  $1/eR_H$  is due to variation of Hall factor [3.70].

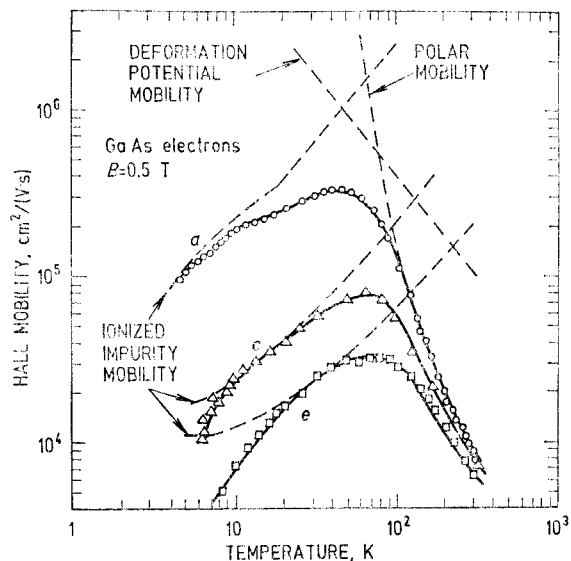
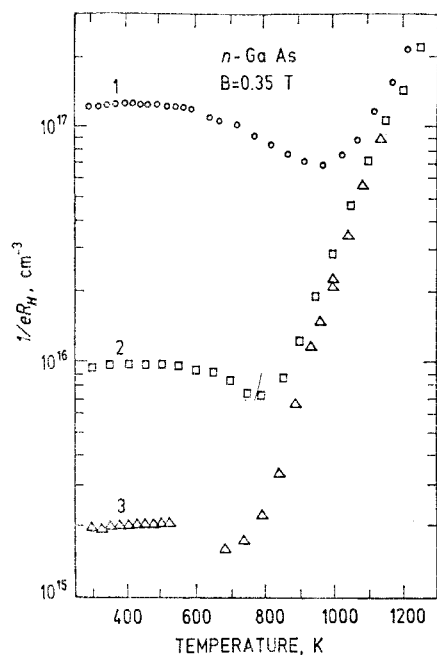
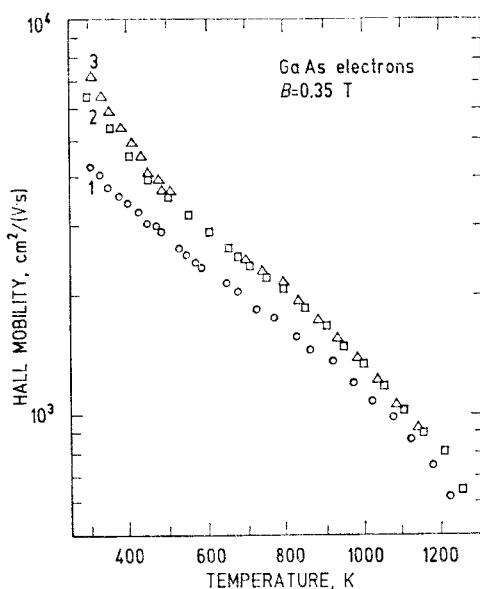


Fig. 3.28. Temperature variation of electron Hall mobility at 0.5 T for three  $n\text{-GaAs}$  samples with parameters shown in Table 3.12 [3.70].

**TABLE 3.12** Donor concentration  $N_D$ , acceptor concentration  $N_A$  and apparent impurity activation energy  $E_D$  at  $B=0.5$  T of samples in Figs. 3.27 and 3.28

Sample	$N_D$ , $\text{cm}^{-3}$	$N_A$ , $\text{cm}^{-3}$	$E_D$ , meV
<i>a</i>	$4.8 \cdot 10^{13}$	$2.1 \cdot 10^{13}$	5.52
<i>b</i>	$2.0 \cdot 10^{14}$	$4.1 \cdot 10^{13}$	5.09
<i>c</i>	$1.1 \cdot 10^{15}$	$3.3 \cdot 10^{14}$	3.88
<i>d</i>	$2.1 \cdot 10^{15}$	$6.0 \cdot 10^{14}$	3.29
<i>e</i>	$4.7 \cdot 10^{15}$	$1.6 \cdot 10^{15}$	1.89

**Fig. 3.29.** High temperature reciprocal of the Hall coefficient times the elementary charge,  $1/eR_H$ , as a function of temperature for  $n$ -GaAs. Sample parameters are shown in Table 3.13 [3.71].**Fig. 3.30.** High temperature electron Hall mobility in  $n$ -GaAs vs. temperature. Sample parameters are shown in Table 3.13 [3.71].**TABLE 3.13** Electron  $n$ , total donor  $N_D$  and acceptor  $N_A$  concentrations of samples in Figs. 3.29 and 3.30

Sample	$n(300\text{ K})$ , $\text{cm}^{-3}$	$N_D + N_A$ , $\text{cm}^{-3}$	$N_A/N_D$
1	$1.2 \cdot 10^{17}$	$2.0 \cdot 10^{17}$	0.25
2	$9.7 \cdot 10^{15}$	$1.6 \cdot 10^{16}$	0.23
3	$1.9 \cdot 10^{15}$	$4.2 \cdot 10^{15}$	0.38

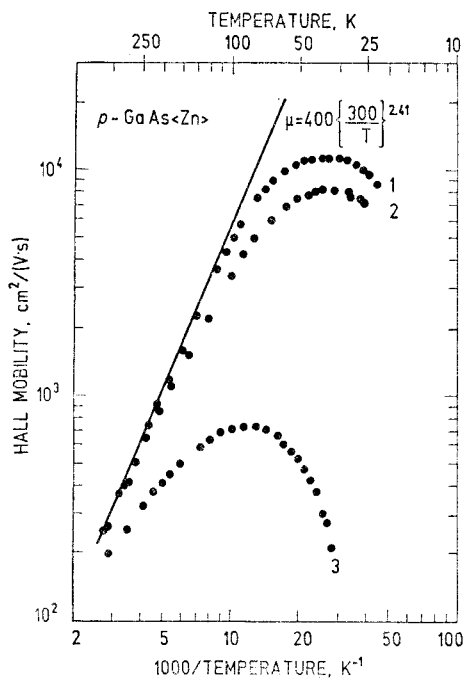


Fig. 3.31. Hole Hall mobility in Zn-doped  $p$ -GaAs as a function of inverse temperature: 1 -  $N_A = 1.12 \cdot 10^{15} \text{ cm}^{-3}$ ,  $K = N_D/N_A = 0.86$ ; 2 -  $N_A = 4.13 \cdot 10^{15} \text{ cm}^{-3}$ ,  $K = 0.94$ ; 3 -  $N_A = 3.08 \cdot 10^{17} \text{ cm}^{-3}$ ,  $K = 0.75$  [3.72].

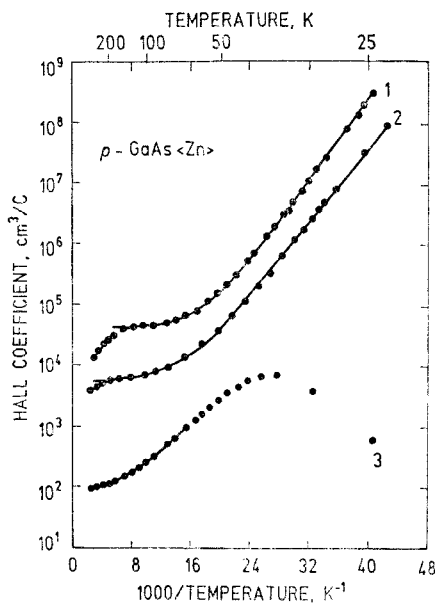


Fig. 3.32. Hole Hall coefficient in Zn-doped  $p$ -GaAs as a function of inverse temperature [3.72]. For sample parameters see Fig. 3.31.



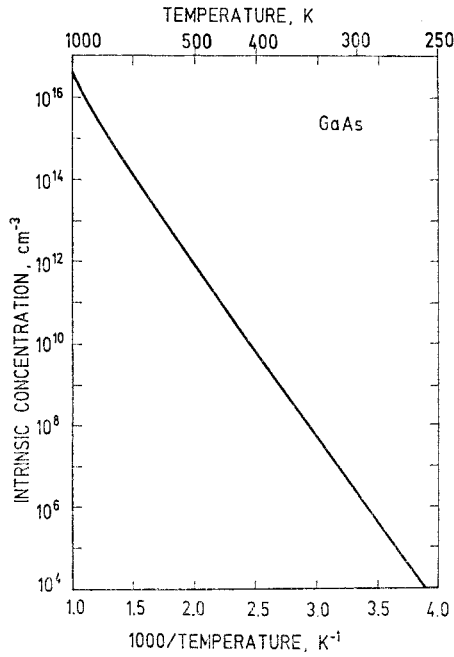


Fig. 3.33. The intrinsic carrier concentration vs. inverse temperature for GaAs [3.73]. The empirical expression:  $n_i = 1.05 \cdot 10^{16} T^{3/2} \exp(-9307/T)$  for  $300 < T < 475$  K.  $n_i$  is in  $\text{cm}^{-3}$  and  $T$  is in K. At 300 K  $n_i = 1.8 \cdot 10^6 \text{ cm}^{-3}$ .

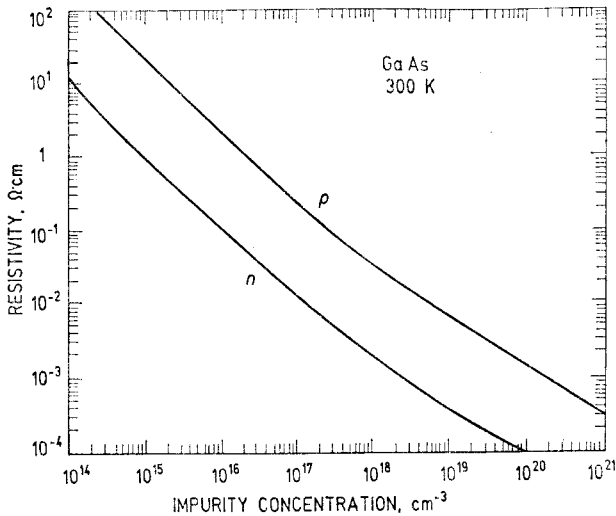


Fig. 3.34. Resistivity vs. shallow impurity concentration for GaAs at 300 K [1.73].

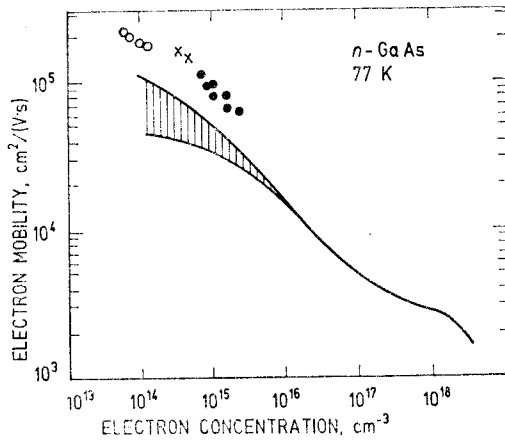


Fig. 3.35. Variation of electron Hall mobility at 77 K with electron concentration in  $n$ -GaAs. Points are experimental data on high purity samples. The solid lines show typical spread of the experimental data obtained by [3.74, 3.75, 3.76].

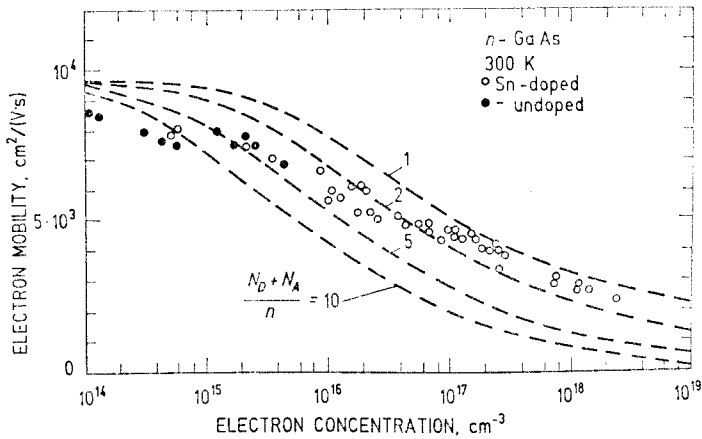


Fig. 3.36. Electron Hall mobility vs. electron concentration,  $n = N_D - N_A$ , in  $n$ -GaAs at 300 K. The dashed lines show the theoretical Hall mobility for different compensation ratios  $(N_D + N_A)/n$  [3.76].

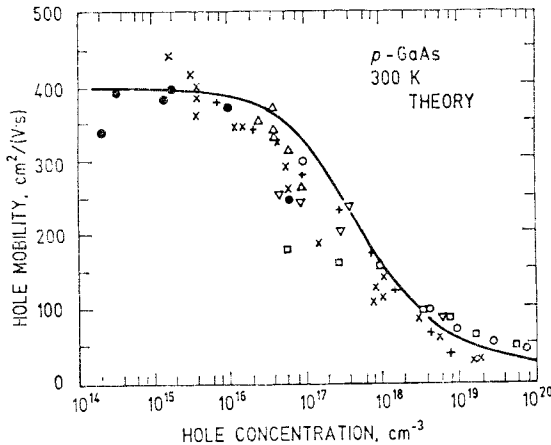


Fig. 3.37. The concentration dependence of the hole Hall mobility in  $p$ -GaAs at 300 K [3.77].

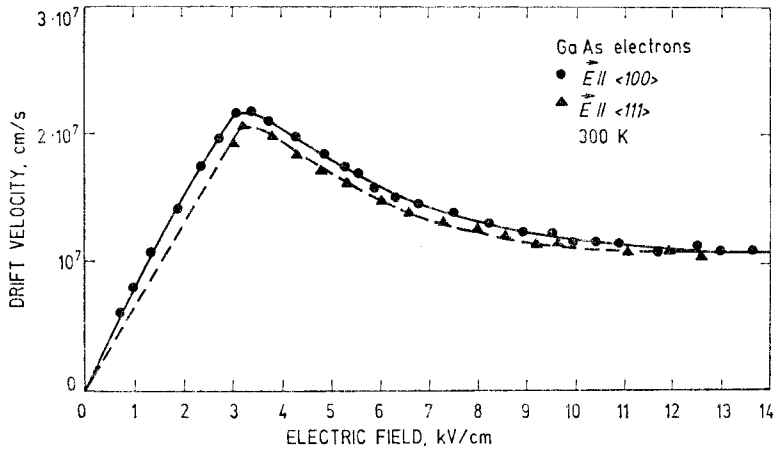


Fig. 3.38. Electron drift velocity in  $\langle 100 \rangle$  and  $\langle 111 \rangle$  directions vs. electric field in GaAs at 300 K [3.78]. The lines are meant as a guide for the eye.

Empirical formula for the electron drift velocity vs. electrical field in GaAs is  $v = \mu E$  if  $E < E_0$ ,  $v = \mu E / \sqrt{1 + (E - E_0)^2 / E_c^2}$  if  $E > E_0$ .  $E$  is the electric field,  $\mu$  is the low field mobility,  $E_c$  and  $E_0$  are critical fields. For high-purity GaAs typical parameters:  $\mu = 7500 \text{ cm}^2/(\text{V} \cdot \text{s})$ ,  $E_c = 1.07 \text{ kV/cm}$  and  $E_0 = 2.8 \text{ kV/cm}$  [3.79].

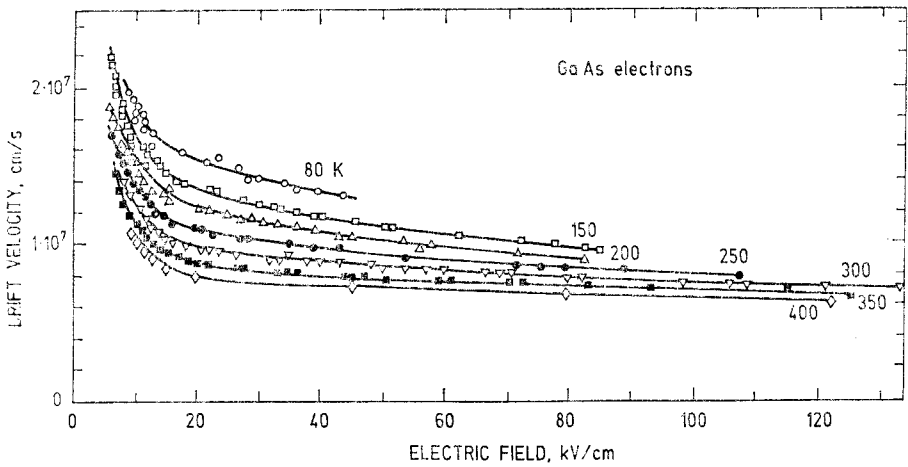


Fig. 3.39. Electron drift velocity vs. electric field in GaAs at different lattice temperatures in the region of negative differential mobility [3.80].

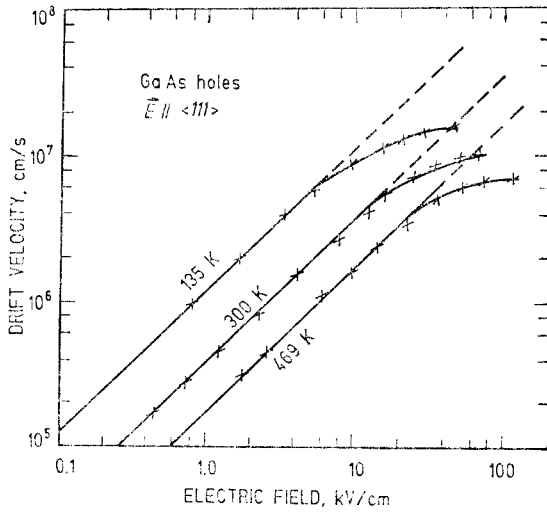


Fig. 3.40. Hole drift velocity vs. electric field in GaAs at different lattice temperatures in  $\langle 111 \rangle$  direction. The dashed line describes Ohm's law [3.81].

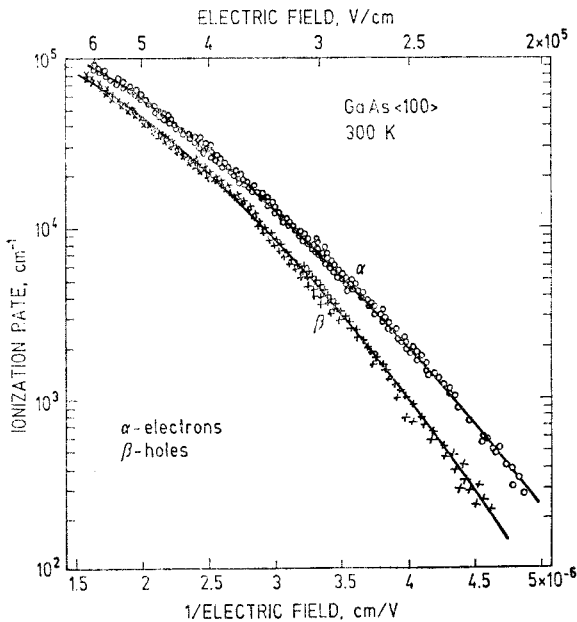


Fig. 3.41. Band-band impact ionization rates for electrons  $\alpha$  and holes  $\beta$  in GaAs as a function of inverse electric field at 300 K [3.82].

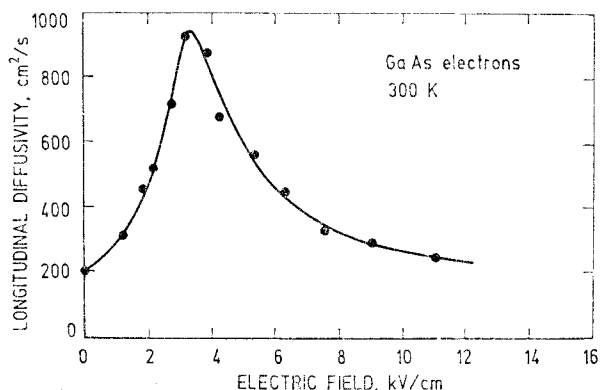


Fig. 3.42. Electron diffusion coefficient (diffusivity) in GaAs as a function of electric field at 300 K [3.78].

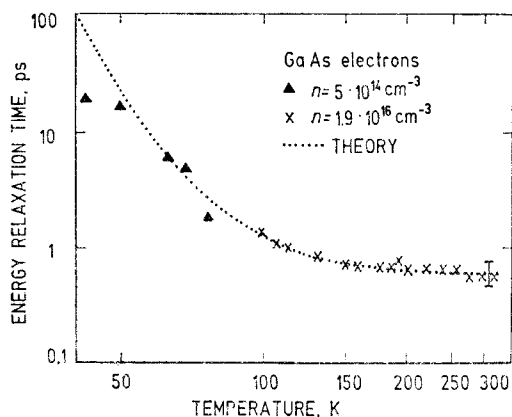


Fig. 3.43. Warm electron energy relaxation time in n-GaAs vs. lattice temperature. Free electron concentration: triangles —  $n = 5 \cdot 10^{14} \text{ cm}^{-3}$ , crosses —  $n = 1.9 \cdot 10^{16} \text{ cm}^{-3}$ . Curve: theory [3.83].

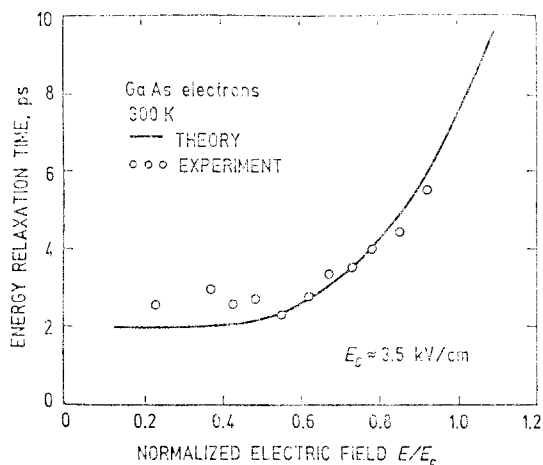


Fig. 3.44. Hot electron energy relaxation time in pure GaAs as a function of normalized electric field at 300 K,  $E_c \approx 3.5 \text{ kV/cm}$ . Dots: experiment. Curve: theory [3.84].

**Intervalley scattering times.** Hot electron scattering times from  $\Gamma$  valley to L and X valleys in GaAs are [3.85]:

$$\tau_{\Gamma L} = 0.54 \pm 0.12 \text{ ps for } 0.48 \text{ eV and } \tau_{\Gamma X} = 0.18 \pm 0.04 \text{ ps for } 0.58 \text{ eV electrons.}$$

**TABLE 3.14** Parameters for high electric field transport calculation in *n*-GaAs [3.32]

Parameter	Value			
	Lattice	$\Gamma$ valley	$L$ valley	$X$ valley
Density, g/cm <sup>3</sup>	5.32			
Intravalley properties				
Number of valleys		1	4	3
Effective mass $m_n/m_0$		0.063	0.23	0.43
Nonparabolicity parameter, eV <sup>-1</sup>		0.69	0.65	0.36
Valley separation, eV		0	0.33	0.52
Acoustic scattering parameters				
Sound velocity, cm/s	5.24 · 10 <sup>5</sup>			
Deformation potential, eV		8		
Optical scattering parameters				
Static dielectric permittivity $\epsilon/\epsilon_0$	12.8			
High frequency dielectric permittivity $\epsilon_\infty/\epsilon_0$	10.9			
Polar optical phonon energy, meV		35	34.3	34.3
Intervalley properties				
Transition	Coupling constant		Phonon energy	
$\Gamma-L^*$	1.0 · 10 <sup>9</sup> eV/cm		26 meV	
$\Gamma-X$	1.0 · 10 <sup>9</sup> eV/cm		26 meV	
$L-L$	1.0 · 10 <sup>9</sup> eV/cm		26 meV	
$L-X$	0.9 · 10 <sup>9</sup> eV/cm		26 meV	
$X-X$	0.9 · 10 <sup>9</sup> eV/cm		26 meV	

\*—There is no universal acceptance of the value for  $\Gamma-L$  coupling constant. Different experiments and their interpretations yield  $(0.15-1) \cdot 10^9$  eV/cm [3.86].

### 3.5. GaAs piezoelectric, thermoelectric and magnetic properties

**Piezoelectric coefficients of GaAs** at room temperature are [3.87]:

$$|e_{14}| = 0.16 \text{ C/m}^2, |d_{14}| = 2.7 \cdot 10^{-12} \text{ m/V}, |g_{14}| = 2.4 \cdot 10^{-2} \text{ m}^2/\text{C}, \\ |h_{14}| = 1.45 \cdot 10^9 \text{ V/m}, \text{ accuracy is } \pm 10 \%.$$

**TABLE 3.15** Piezoresistance coefficients of GaAs in 1/GPa. For physical interpretation refer Table 5

Experimental conditions	$\pi_{11}$	$\frac{\pi_{11} + \pi_{12} + \pi_{44}}{2}$	$\frac{\pi_{11} + 2\pi_{12} + 2\pi_{44}}{3}$	$\pi_{11} + 2\pi_{12}$	Reference
<i>n</i> -type					
$n = 8 \cdot 10^{16} \text{ cm}^{-3}$					
300 K	-0.022	-0.042		-0.098	[3.88]
<i>p</i> -type					
$p \lesssim 10^{18} \text{ cm}^{-3}$					
295 K	0.05		0.38—0.45		
100 K	0.13		0.6—0.74		[3.89]

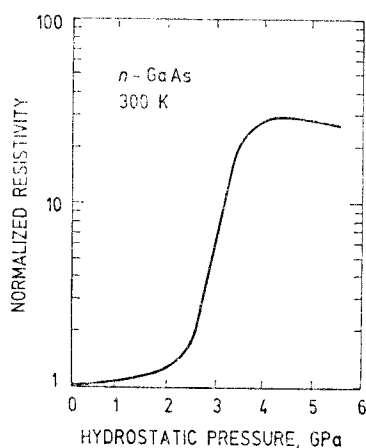


Fig. 3.45. Normalized resistivity,  $\rho/\rho_0$  vs. hydrostatic pressure for *n*-GaAs at room temperature [3.90].

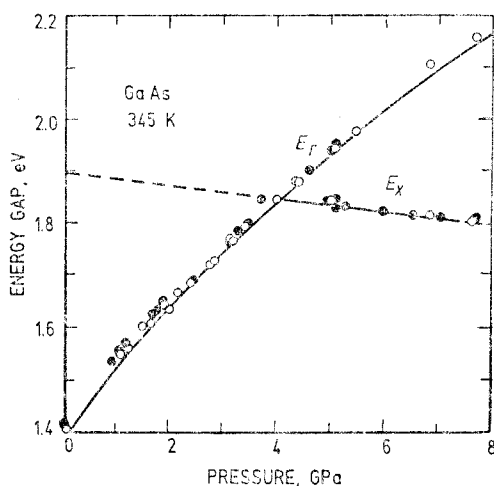


Fig. 3.46. Pressure dependence of direct  $E_{\Gamma}(\Gamma_{6c} - \Gamma_{8v})$  and indirect  $E_{\chi}(X_{6c} - \Gamma_{8v})$  gap. Full circles: *n*-type sample. Open circles: *p*-type sample. Data were obtained from the luminescence band maxima at 345 K [3.91].

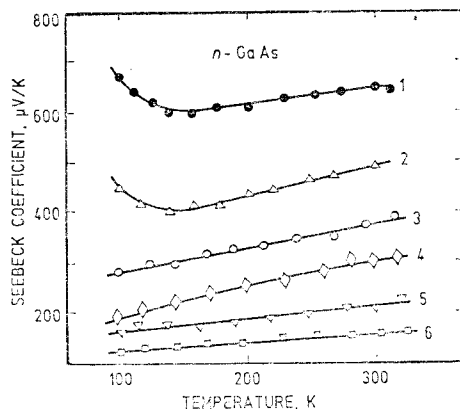


Fig. 3.47. Seebeck coefficient vs. temperature for *n*-GaAs having different excess donor concentrations: 1 —  $N_D = 3.7 \cdot 10^{15} \text{ cm}^{-3}$ , 2 —  $2.4 \cdot 10^{16} \text{ cm}^{-3}$ , 3 —  $7.0 \cdot 10^{16} \text{ cm}^{-3}$ , 4 —  $1.8 \cdot 10^{17} \text{ cm}^{-3}$ , 5 —  $3 \cdot 10^{18} \text{ cm}^{-3}$ , 6 —  $9.1 \cdot 10^{18} \text{ cm}^{-3}$  [3.92].

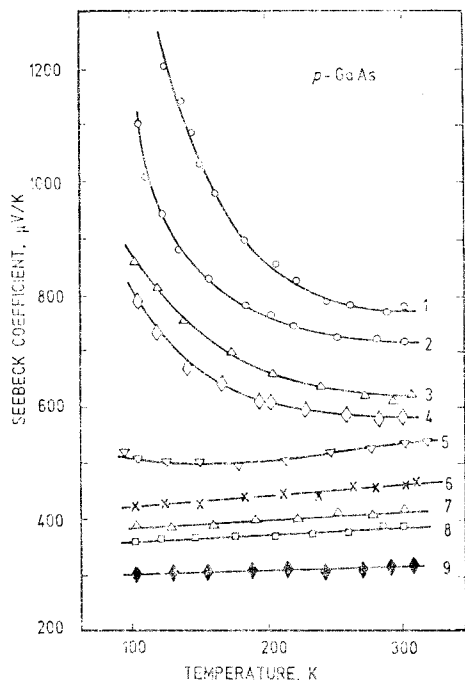


Fig. 3.48. Seebeck coefficient vs. temperature for *p*-GaAs having various excess acceptor concentrations: 1 —  $N_A = 3 \cdot 10^{16} \text{ cm}^{-3}$ , 2 —  $7.5 \cdot 10^{16} \text{ cm}^{-3}$ , 3 —  $2.7 \cdot 10^{17} \text{ cm}^{-3}$ , 4 —  $5.1 \cdot 10^{17} \text{ cm}^{-3}$ , 5 —  $8.3 \cdot 10^{18} \text{ cm}^{-3}$ , 6 —  $2.1 \cdot 10^{19} \text{ cm}^{-3}$ , 7 —  $3.3 \cdot 10^{19} \text{ cm}^{-3}$ , 8 —  $6.2 \cdot 10^{19} \text{ cm}^{-3}$ , 9 —  $1.34 \cdot 10^{20} \text{ cm}^{-3}$  [3.92].

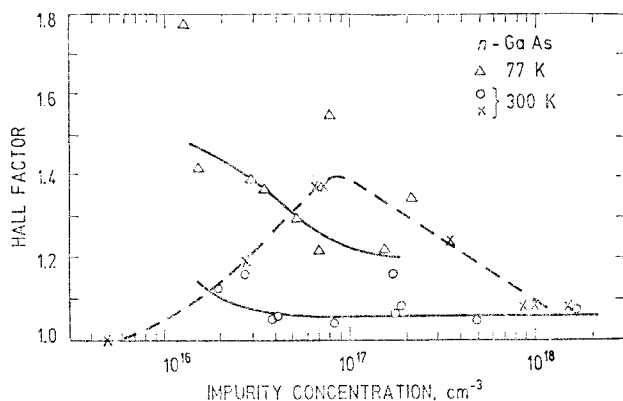
**Magnetic susceptibility.** GaAs lattice contribution to the magnetic susceptibility  $\chi_m$  at room temperature and respective temperature coefficient [1.89]:

$$\chi_m = (-15.4 \pm 0.25) \cdot 10^{-6},$$

$$d\chi_m/dT = (0.42 \pm 0.02) \cdot 10^{-9} \text{ K}^{-1}.$$



Fig. 3.49. Hall factor vs. impurity concentration in  $n$ -GaAs at room (circles, crosses) and liquid nitrogen (triangles) temperatures. Solid lines: theory. Ratio of donor to acceptor concentrations: triangles, circles —  $N_D/N_A=0.5-0.8$  [3.93], crosses —  $N_D/N_A=0.7$  [3.94].



In  $p$ -GaAs the Hall factor is in the range 1.7–2.2 for hole concentration  $p=3.9 \cdot 10^{14}-8.6 \cdot 10^{15} \text{ cm}^{-3}$  and the lattice temperature  $T=78 \text{ K}$  [3.94].

Fig. 3.50. Hall factor vs. magnetic field induction in pure  $n$ -GaAs at 300 K. Triangles:  $N_D=4.8 \cdot 10^{13} \text{ cm}^{-3}$ ,  $N_D+N_A=7 \cdot 10^{13} \text{ cm}^{-3}$  [3.70]. Circles:  $N_D-N_A=6.1 \cdot 10^{13} \text{ cm}^{-3}$ ,  $N_D+N_A=2.6 \cdot 10^{14} \text{ cm}^{-3}$ . Solid line: theory [3.95].

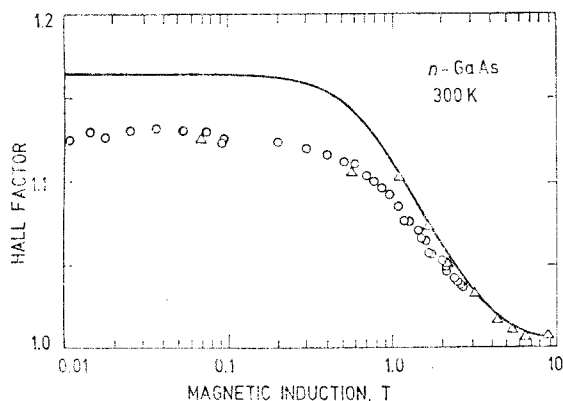
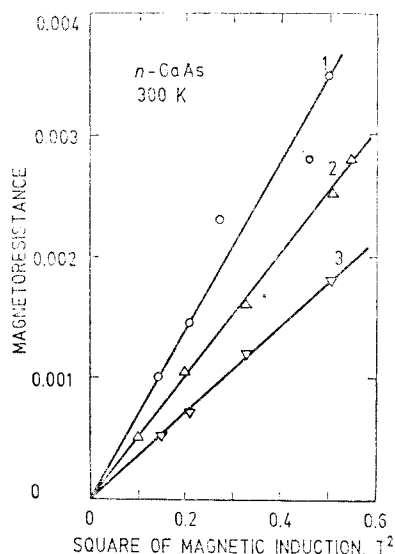


Fig. 3.51. Transverse magnetoresistance  $[\rho(B)-\rho_0]/\rho_0$  of  $n$ -GaAs at room temperature vs. square of the magnetic induction. 1 —  $n=8.1 \cdot 10^{16} \text{ cm}^{-3}$ , 2 —  $n=3.7 \cdot 10^{17} \text{ cm}^{-3}$ , 3 —  $n=1.6 \cdot 10^{18} \text{ cm}^{-3}$  [3.93].



### 3.6. GaAs impurity properties

**TABLE 3.16** Donor and acceptor ionization energies associated with various impurities in GaAs. Donor ionization energy is referenced relative to the conduction band edge  $E_c$  while acceptor ionization energy is referenced relative to the valence band edge  $E_v$

Impurity	Donor or acceptor	Ionization energy, meV	Reference
Au	A	$E_v + 90$	[3.96]
Ag	$A_{Ga}$	$E_v + 238$	[3.97]
Be	$A_{Ga}$	$E_v + 28$	[3.61]
C	$D_{Ga}$	$E_c - 5.91$	[3.98]
C	$A_{As}$	$E_v + 26$	[3.99]
Cd	$A_{Ga}$	$E_v + 34.7$	[3.61]
Co	A	$E_v + 160$	[3.100]
Cr	$A_{Ga}$	$E_v + 790$	[3.100]
Cu	A	$E_v + 150$	[3.101]
Cu	A	$E_v + 470$	[3.102]
Fe	$A_{Ga}$	$E_v + 520$	[3.100]
Ge	$D_{Ga}$	$E_c - 5.88$	[3.98]
Ge	$A_{As}$	$E_v + 40.4$	[3.99]
Mg	$A_{Ga}$	$E_v + 28.7$	[3.103]
Mn	$A_{Ga}$	$E_v + 113$	[3.104, 3.105]
Ni	A	$E_v + 220$	[3.100]
O	$D_{As}$	$E_c - 750$	[3.106]
S	$D_{As}$	$E_c - 5.87$	[3.98]
Se	$D_{As}$	$E_c - 5.79$	[3.98]
Si	$D_{Ga}$	$E_c - 5.84$	[3.98]
Si	$A_{As}$	$E_v + 34.5$	[3.99]
Sn	$D_{Ga}$	$E_c - 5.82$	[3.107]
Sn	$A_{As}$	$E_v + 167$	[3.60]
Ti	D	$E_c - 1000$	[3.108]
Ti	A	$E_v + 1250$	[3.108]
Zn	$A_{Ga}$	$E_v + 30.7$	[3.99]

$D_{Ga}$ ,  $A_{Ga}$ —Ga-site donor or acceptor,

$D_{As}$ ,  $A_{As}$ —As-site donor or acceptor.

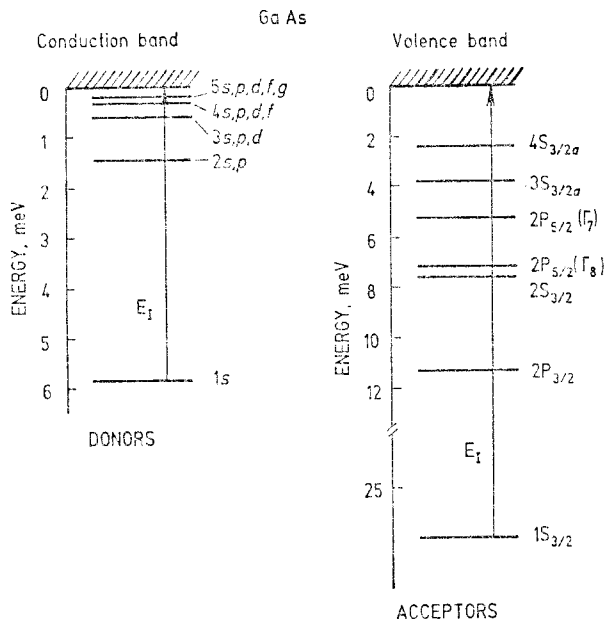


Fig. 3.52. Energy level scheme of shallow donors and acceptors in GaAs within effective mass approximation. Ionization energy  $E_I$  is different for different chemical species (see Table 3.17 and 3.18).

**TABLE 3.17** Binding energies of the energy levels of **shallow donors** (silicon, germanium, selenium, sulphur) in GaAs [3.109, 3.110]

Level	Level energy, meV				
	Si <sub>Ga</sub>	Ge <sub>Ga</sub>	Se <sub>As</sub>	S <sub>As</sub>	Hydrogenic model
1s state ionization energy $E_I$	5.76	5.95	5.83	6.1	5.79
2s, p	1.4	1.31	1.37	1.45	1.45
3s, p, d					0.64
4s, p, d, f					0.36
5s, p, d, f, g					0.23

**Electron capture cross section** by shallow single-charged donors in GaAs at the lattice temperature  $T=10$  K is  $\sigma \approx (2-4) \cdot 10^{-14} \text{ cm}^2$  [3.111].

**TABLE 3.18** Binding energies of the energy levels of **shallow acceptors** (carbon, zinc, silicon, germanium) in GaAs. Experiment – [3.99]. Effective mass theory – [3.112]

Level	Level energy, meV				
	C <sub>As</sub>	Zn <sub>Ga</sub>	Si <sub>As</sub>	Ge <sub>As</sub>	Theory
1S <sub>3/2</sub> , ionization energy $E_I$	26	30.7	34.5	40.4	26
2P <sub>3/2</sub>	10.8	11.5	11.0	14.3	11.3
2S <sub>3/2</sub>	7.6	9.0	9.4	12.1	7.6
2P <sub>5/2</sub> ( $\Gamma_8$ )	6.6	7.6	7.2	10.3	7.2
2P <sub>5/2</sub> ( $\Gamma_7$ )	4.7	5.5	4.9	8.8	5.3
3S <sub>2/2a</sub>	3.6	4.5	3.7	6.4	3.9
4S <sub>3/2a</sub>					2.4

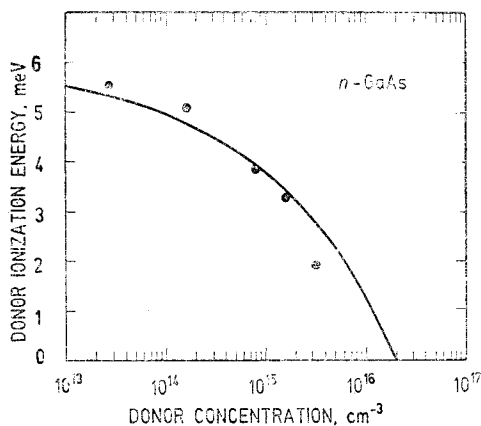


Fig. 3.53. Dependence of shallow donor thermal ionization energy  $E_I$  on electrically active donor concentration  $N_D^*$  in GaAs at  $B=0.5$  T [3.70]. Solid line is an empirical formula  $E_I = 6 - 2.2 \cdot 10^{-5} N_D^{*1/3}$ ,  $E_I$  is in meV and  $N_D^*$  is in cm<sup>-3</sup>.

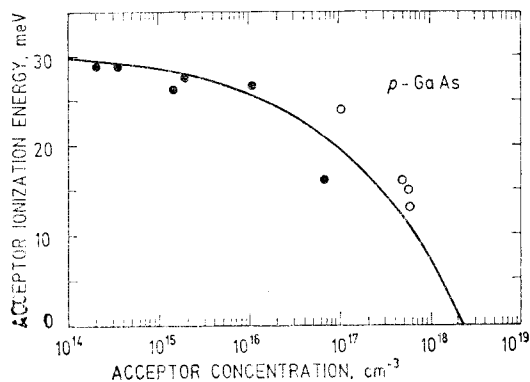


Fig. 3.54. Dependence of shallow acceptor thermal ionization energy  $E_I$  on electrically active acceptor (zinc) concentration  $N_A^*$  in GaAs. Full circles – [3.72], open circles – [3.113]. Solid line is an empirical formula  $E_I = 30.8 - 2.34 \cdot 10^{-5} N_A^{*1/3}$ ,  $E_I$  is in meV and  $N_A^*$  is in cm<sup>-3</sup>.

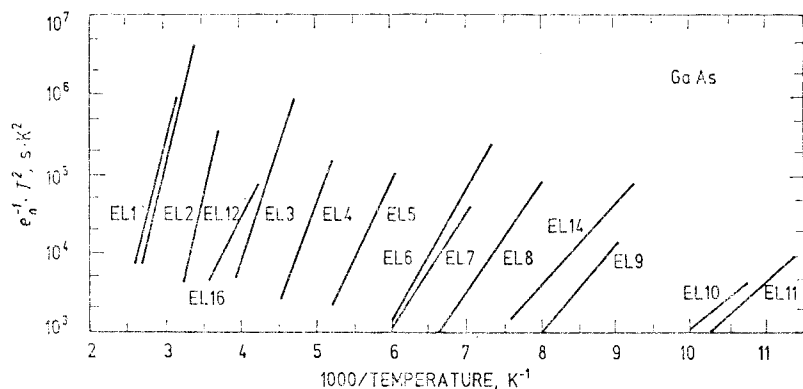


Fig. 3.55. Catalogue of inverse electron thermal emission rates multiplied by  $T^2$  vs. reciprocal temperature,  $1/T$ , for different electron traps in relatively pure vapour-phase epitaxial (VPE), molecular beam epitaxial (MBE) and bulk-grown GaAs measured with deep level transient spectroscopy (DLTS). For details see Table 3.19 [3.114].

**TABLE 3.19** Ionization energy  $E_I$  and thermal capture cross section  $\sigma_n$  of electron traps calculated from Fig. 3.55

Trap level	Ionization energy, meV	Temperature, K	Capture cross section, $\text{cm}^2$	Material
EL1	780	320—380	$1.0 \cdot 10^{-14}$	Cr-doped bulk crystal
EL2	825	300—370	$(0.8—1.7) \cdot 10^{-13}$	VPE
EL3	575	213—255	$(0.8—1.7) \cdot 10^{-13}$	VPE
EL4	510	193—222	$1.0 \cdot 10^{-12}$	as-grown MBE
EL5	420	167—193	$(0.5—2.0) \cdot 10^{-13}$	VPE
EL6	350	136—167	$1.5 \cdot 10^{-13}$	bulk crystal
EL7	300	142—167	$7.2 \cdot 10^{-15}$	as-grown MBE
EL8	275	125—150	$7.7 \cdot 10^{-15}$	VPE
EL9	225	110—125	$6.8 \cdot 10^{-15}$	VPE
EL10	170	93—100	$1.8 \cdot 10^{-15}$	as-grown MBE
EL11	170	88—97	$3.0 \cdot 10^{-16}$	VPE
EL12	780	270—310	$4.9 \cdot 10^{-12}$	VPE
EL14	215	110—130	$5.2 \cdot 10^{-16}$	bulk crystal
EL16	370	240—285	$4.0 \cdot 10^{-18}$	VPE

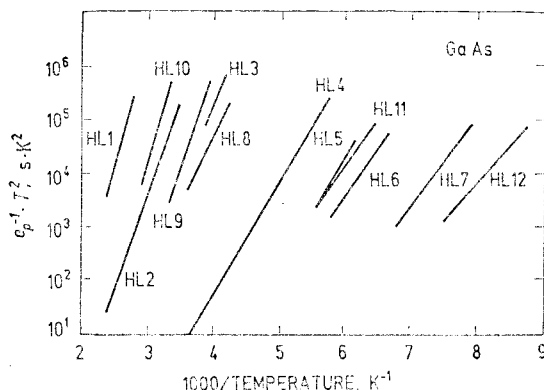


Fig. 3.56. Catalogue of inverse hole thermal emission rates multiplied by  $T^2$  vs. reciprocal temperature for different hole traps in VPE, MBE, liquid-phase epitaxial (LPE) and bulk-grown GaAs measured with DLTS. For details see Table 3.20 [3.115].

**TABLE 3.20** Ionization energy  $E_i$  and thermal capture cross section  $\sigma_p$  of hole traps calculated from Fig. 3.56. VPE – vapour phase epitaxy; LPE – liquid phase epitaxy; MBE – molecular beam epitaxy

Trap level	Ionization energy, meV	Temperature, K	Capture cross section, $\text{cm}^2$	Material	Chemical origin
HL1	940	360—417	$3.7 \cdot 10^{-14}$	Cr-doped VPE	Cr
HL2	730	288—417	$1.9 \cdot 10^{-14}$	as-grown LPE	
HL3	590	240—263	$3.0 \cdot 10^{-15}$	Fe-diffused VPE	Fe
HL4	420	174—275	$3.0 \cdot 10^{-15}$	Cu-diffused VPE	Cu
HL5	410	162—182	$9.0 \cdot 10^{-14}$	as-grown LPE	
HL6	320	150—174	$5.6 \cdot 10^{-14}$	VPE with $p$ -layer	
HL7	350	126—148	$6.4 \cdot 10^{-15}$	as-grown MBE	
HL8	520	236—283	$3.5 \cdot 10^{-16}$	as-grown MBE	
HL9	690	256—300	$1.1 \cdot 10^{-13}$	as-grown VPE	
HL10	830	300—349	$1.7 \cdot 10^{-13}$	as-grown VPE	
HL11	350	155—182	$1.4 \cdot 10^{-15}$	melt grown	
HL12	270	115—134	$1.3 \cdot 10^{-14}$	Zn-contaminated LPE	

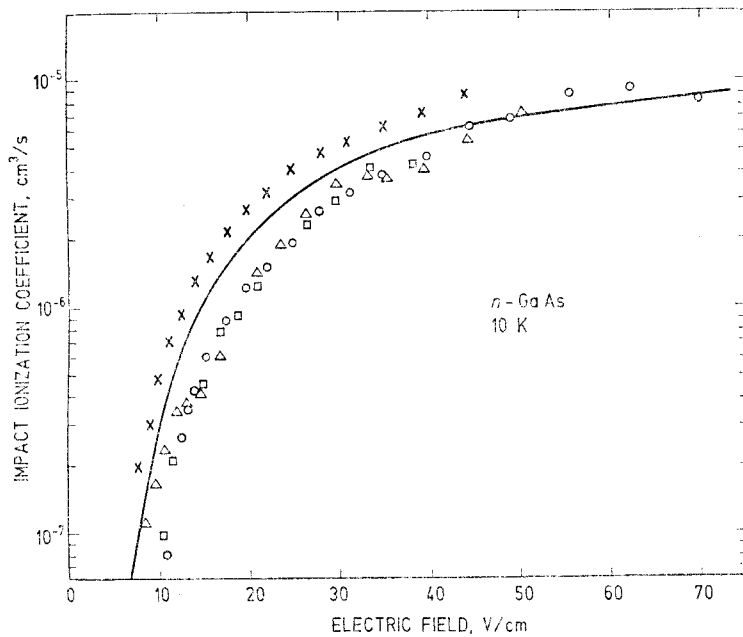
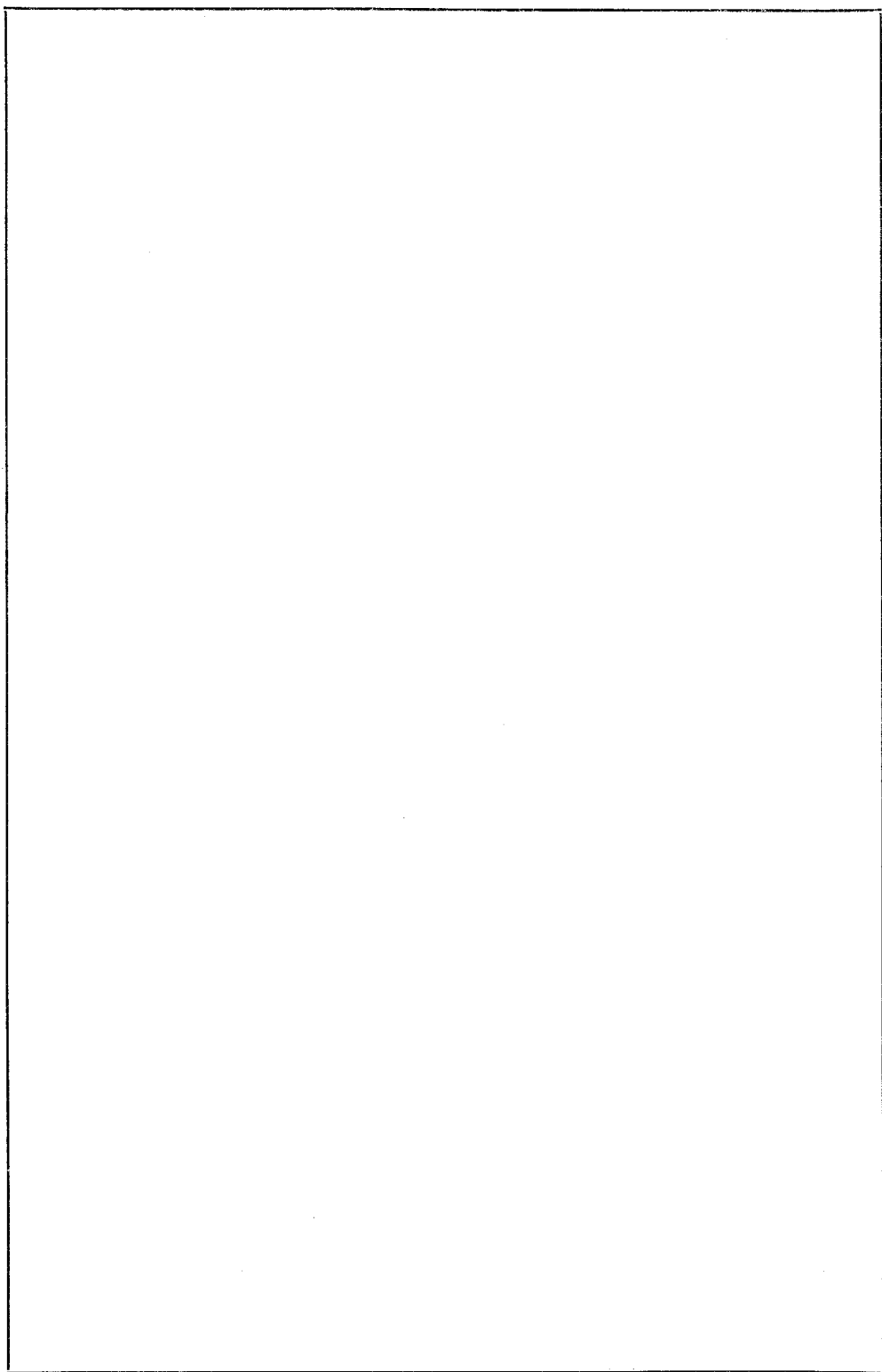


Fig. 3.57. Dependence of the impact ionization coefficient  $A_I$  of shallow donors in  $n$ -GaAs on the electric field strength  $E$ . Dots: experimental data at 10 K. Solid line: empirical formula  $A_I = 1.5 \cdot 10^{-5} \exp(-38/E)$ ,  $A_I$  is in  $\text{cm}^3/\text{s}$  and  $E$  is in  $\text{V}/\text{cm}$  [3.111, 3.116].





## 4. Physical data for indium phosphide

### 4.1. InP lattice properties

1. InP consists of the following isotopes (as a result the translational symmetry of InP lattice is not exact) [1.1]  
 $^{113}\text{In}$  ..... 4.3 %  
 $^{115}\text{In}$  ..... 95.7 %  
 $^{31}\text{P}$  ..... 100 %
2. Average atomic weight: 145.8 [3.1]
3. InP has cubic sphalerite (zincblende) lattice. Space group is  $F\bar{4}3m (T_d^2)$ .  
Lattice symmetry formula is  $3L^24L6P$ , which means that there are 3 symmetry axes of the second-order, 4 symmetry axes of the third-order, and 6 symmetry planes. The inversion symmetry is absent, and by this reason the directions  $\bar{[111]}$  and  $[111]$  are not equivalent
4. Lattice constant:  $a=0.586\ 945\ \text{nm}$  at 300 K [4.1]
5. Density:  $4.81\ \text{g/cm}^3$  [3.1]
6. Number of In or P atoms in  $1\ \text{cm}^3$  is  $1.98 \cdot 10^{22}$
7. Melting temperature for stoichiometric InP at 2.78 MPa is 1335 K [4.2]
8. Transition to metallic phase occurs at the pressure 10.65 GPa [4.3]
9. InP cleaves most readily on  $\{110\}$  family planes [1.7]

**TABLE 4.1** Elastic parameters of InP at the lattice temperature 296 K [4.4]

Parameter	Value
Elastic constants:	
$c_{11}$ , GPa	101.1
$c_{12}$ , GPa	56.1
$c_{44}$ , GPa	45.6
Sound velocity in the direction [100]:	
longitudinal $v_L$ , cm/s	$4.6 \cdot 10^5$
transverse $v_T$ , cm/s	$3.09 \cdot 10^5$
Sound velocity in the direction [111]:	
longitudinal $v_L$ , cm/s	$5.25 \cdot 10^5$
transverse $v_T$ , cm/s	$2.51 \cdot 10^5$
Elastic anisotropy factor $a$	0.493
Poisson ratio $\nu$	0.357
Young's modulus $E$ , GPa:	
direction [100]	61
direction [110]	93
direction [111]	112.7
Bulk modulus $B_0$ , GPa	71.1
$B'_0 = d B_0 / d p$	4.59

**TABLE 4.2** InP phonon energies in meV for high symmetry points  $\Gamma$  [4.5],  $X$  and  $L$  [4.6] in the Brillouin zone at 300 K

Phonon branch	Phonon energy, meV		
	$\Gamma$	$X$	$L$
$LO$	42.82	$41.1 \pm 0.4$	$42.2 \pm 1.2$
$TO$	37.6	$40.1 \pm 0.8$	$39.3 \pm 0.6$
$LA$	0	$24 \pm 1.2$	$20.7 \pm 0.4$
$TA$	0	$8.5 \pm 0.4$	$6.8 \pm 0.08$

**Optical phonon lifetime.** At the symmetry point  $\Gamma$  the half-widths of Raman lines for  $LO$  and  $TO$  phonons at 300 K are  $1.9 \text{ cm}^{-1}$  and  $3.3 \text{ cm}^{-1}$ . These half-widths yield phonon lifetimes 2.8 ps and 1.6 ps, respectively [4.5].

**Raman activity.** InP has two first-order Raman-active phonons,  $LO(\Gamma)$  and  $TO(\Gamma)$ , which are located at the Brillouin zone center and have energies [3.9]:

$$LO(\Gamma) \quad E = 42.77 \text{ meV at 300 K,}$$

$$43.33 \text{ meV at 4 K,}$$

$$TO(\Gamma) \quad E = 37.65 \text{ meV at 300 K,}$$

$$38.21 \text{ meV at 4K.}$$

**TABLE 4.3** Grüneisen parameters for different phonon branches in InP at X, K,  $\Gamma$  and L critical points.  $T=300 \text{ K}$  [3, 4.7]

Phonon branch	Grüneisen parameter			
	X	K	$\Gamma$	L
$LO$			$1.24 \pm 0.02$	
$TO$	$1.42 \pm 0.1$		$1.44 \pm 0.02$	$1.42 \pm 0.1$
$TA$	$-2.08 \pm 0.1$			$-2.0 \pm 0.1$
$TA_1$		$-0.3$		
$TA_2$		$-2.1$		

**Lattice dielectric permittivity.**

Relative static [3.11]:

$$\epsilon/\epsilon_0 = 12.5 \text{ at 300 K,}$$

$$12.2 \text{ at 77 K.}$$

Relative high frequency [4.5]:

$$\epsilon_\infty/\epsilon_0 = 9.52 \text{ at 300 K.}$$

Dependence of the high frequency dielectric permittivity on temperature [1.18]:

$$(1/\epsilon_\infty)(d\epsilon_\infty/dT) = 1.1 \cdot 10^{-4} \text{ K}^{-1} \text{ at 300 K.}$$

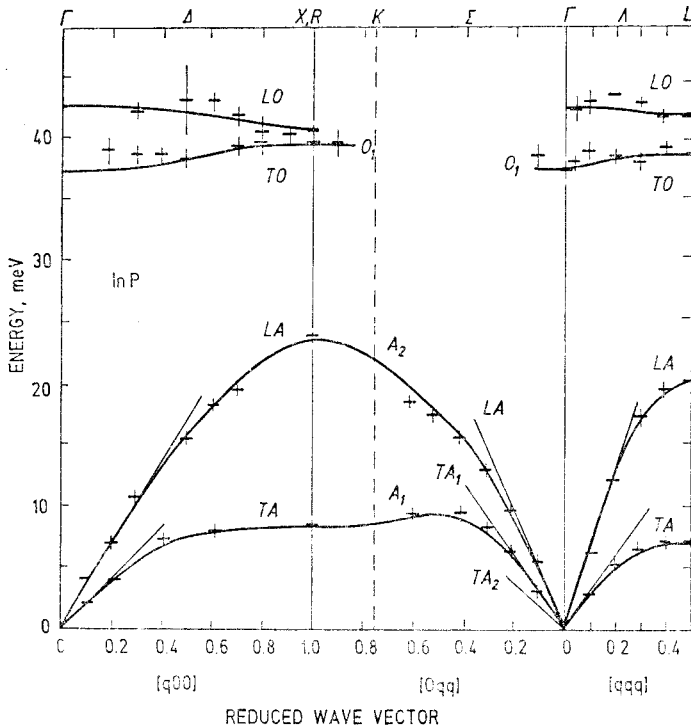


Fig. 4.1. Phonon dispersion curves for InP in the main symmetry directions. The solid straight lines show the slopes for sound velocity in various directions. For  $[qq0]$  direction the data extend beyond the Brillouin zone boundary shown by a vertical dashed line. The path from  $K$  to  $R$  is equivalent to the path from  $U$  to  $X$  on the Brillouin zone boundary (see Fig. 1). For  $A_1$ ,  $A_2$  and  $O_1$  branches the polarization is elliptical. Other modes are either strictly longitudinal ( $L$ ) or transverse ( $T$ ) [4.6].

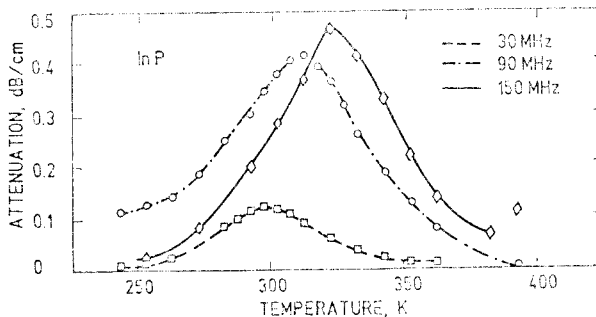


Fig. 4.2. Piezoelectric contribution to ultrasound attenuation of  $\langle 111 \rangle$  longitudinal acoustic waves in chromium doped  $n$ -InP at 30, 90 and 150 MHz as a function of temperature [4.8].

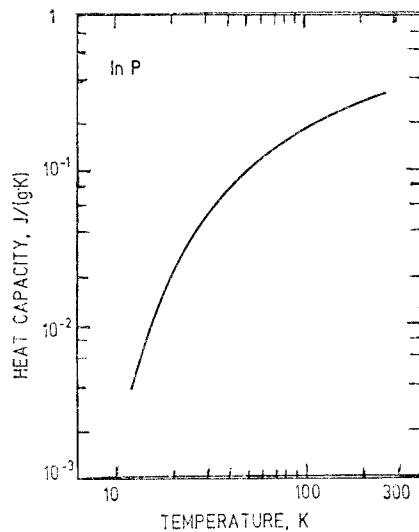


Fig. 4.3. Heat capacity  $C_p$  of InP as a function of temperature [3.1].

Selected values:

$C_p = 3.6 \cdot 10^{-3} \text{ J}/(\text{g} \cdot \text{K})$  at 12 K,  
 0.145  $\text{J}/(\text{g} \cdot \text{K})$  at 77.4 K,  
 0.306  $\text{J}/(\text{g} \cdot \text{K})$  at 273.2 K.

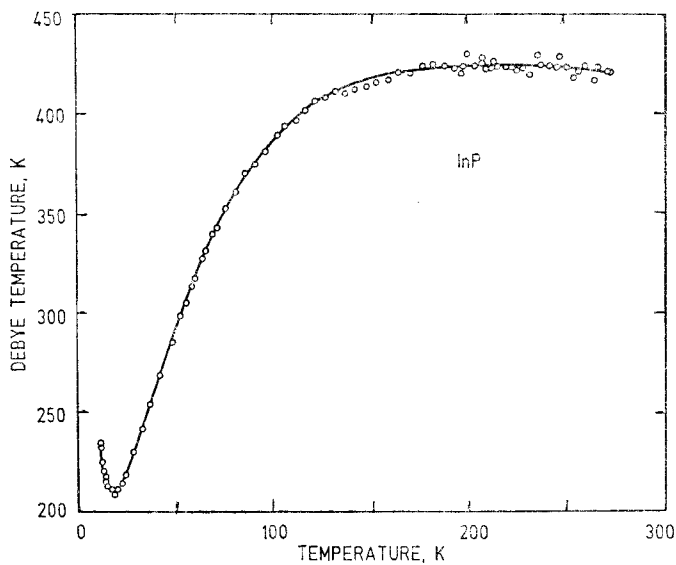


Fig. 4.4. InP Debye temperature vs. lattice temperature [3.1].

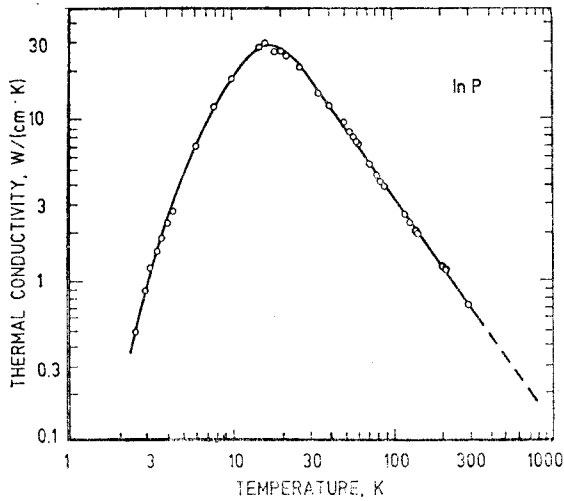


Fig. 4.5. Thermal conductivity  $\chi$  of InP crystal with electron concentration  $n = 2 \cdot 10^{16} \text{ cm}^{-3}$  as a function of temperature [4.9]. The dashed line is from [4.10].

Selected values:

$\chi = 19 \text{ W/(cm} \cdot \text{K)}$  at 30 K,  
 $5.2 \text{ W/(cm} \cdot \text{K)}$  at 77.4 K,  
 $0.70 \text{ W/(cm} \cdot \text{K)}$  at 295 K.

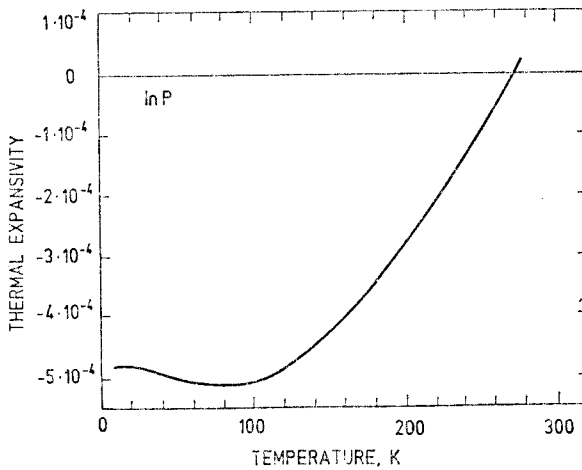


Fig. 4.6. Thermal expansivity  $(l_T - l_{273.2})/l_{273.2}$  as a function of temperature for InP [4.11].  $l_{273.2}$  is a length at  $T = 273.2 \text{ K}$ .

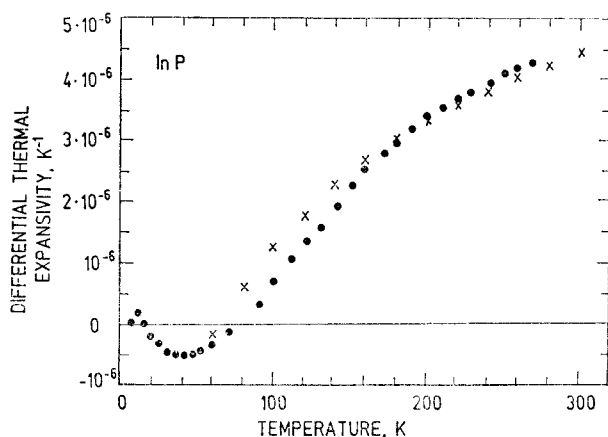


Fig. 4.7. Differential thermal expansivity  $\alpha = (1/L_{273.2})(dL/dT)$  as a function of temperature for InP. Full circles — [4.11], crosses — [4.1].

Selected values:

- $\alpha = 0.2 \cdot 10^{-6} \text{ K}^{-1}$  at 10 K,
- $-0.019 \cdot 10^{-6} \text{ K}^{-1}$  at 77.4 K [4.11],
- $4.48 \cdot 10^{-6} \text{ K}^{-1}$  at 300 K [4.1].

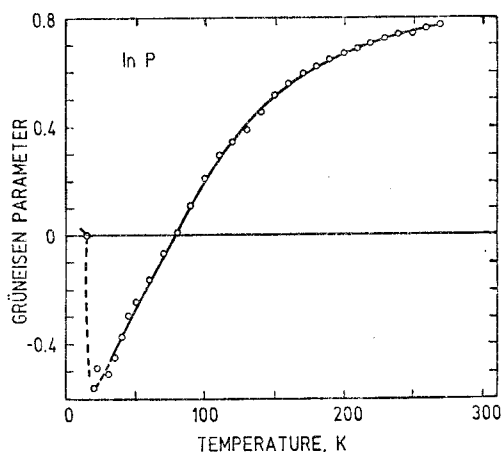


Fig. 4.8. Averaged Grüneisen parameter for InP as a function of lattice temperature [4.11].

## 4.2. InP band properties

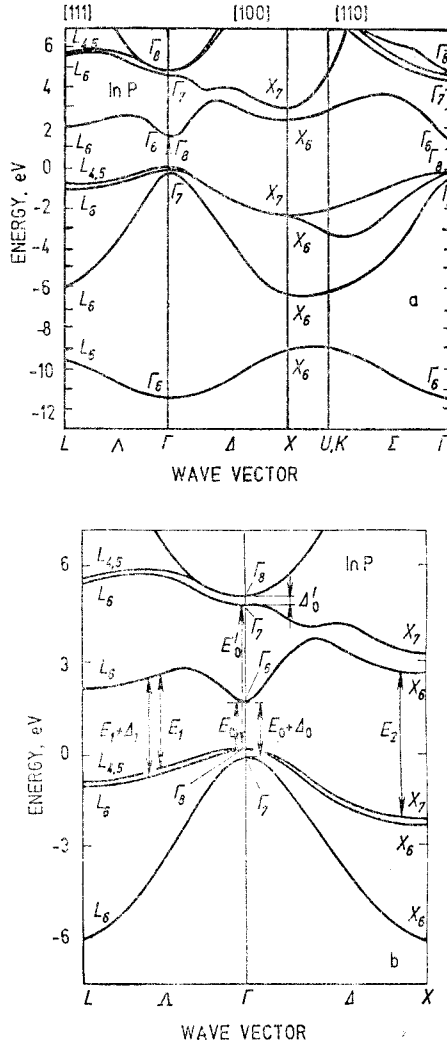


Fig. 4.9. Band structure of InP with spin-orbit interaction included. *a* – General view [1.28]. *b* – Enlarged portion with main interband optical transitions near  $\Gamma$  point ( $E_0$ ,  $E_0 + \Delta_0$ ,  $E'_0$ ,  $E'_0 + \Delta'_0$ ), along  $\Lambda$  direction ( $E_1$ ,  $E_1 + \Delta_1$ ) and near  $X$  point ( $E_2$ ) are shown by vertical lines. The forbidden energy gap  $E_g$  is equal to  $E_0$  [4.12].

InP does not possess inversion symmetry, as a result the bands in the general point of the Brillouin zone are not degenerate. The exceptions are  $\langle 100 \rangle$  axes,  $L$  and  $\Gamma$  points.

**Critical points** associated with band-band transitions in InP which are important in optical measurements coincide with those for GaAs (see Table 3.4).



**TABLE 4.4** Energetic distances between experimentally important critical points in the energy band of InP at room temperature and respective hydrostatic pressure coefficients. For transition and critical point nomenclature see Fig. 4.9,b and Table 3.4

Energy separation and pressure coefficient	Value	Comment	Reference
$E_g \equiv E_0 = E(\Gamma_{6c}) - E(\Gamma_{8v}), \text{ eV}$	1.344	Direct forbidden energy gap	[4.13]
$E_{\Gamma X} = E(X_{6c}) - E(\Gamma_{6c}), \text{ eV}$	0.96		[4.14]
$E_{\Gamma L} = E(L_{6c}) - E(\Gamma_{6c}), \text{ eV}$	0.86		[4.15]
$\Delta_0 = E(\Gamma_{8v}) - E(\Gamma_{7v}), \text{ eV}$	0.108	Spin-orbit splitting in the valence band at 5 K	[4.16]
$E_1, \text{ eV}$	3.16		[4.12]
$E_2, \text{ eV}$	5.04		[4.12]
$\Delta_1, \text{ eV}$	0.16		[4.12]
$d E_g/dp, \text{ eV/GPa}$	0.085	Gap increases with the pressure	[4.17]
$d E_X/dp, \text{ eV/GPa}$	-0.017	X valley relative to the valence band edge, $T = 10 \text{ K}$	[4.3]
$d E_{\Gamma X}/dp, \text{ eV/GPa}$	-0.1	InP becomes an indirect gap semiconductor at hydrostatic pressure $\geq 12 \text{ GPa}$	[4.3]
$d E_L/dp, \text{ eV/GPa}$	0.025	L valley relative to the valence band edge	[3.90]
$d E_{\Gamma L}/dp, \text{ eV/GPa}$	-0.07		[3.90]
$d E_1/dp, \text{ eV/GPa}$	0.07		[4.18]

TABLE 4.5 InP conduction band principal valley parameters

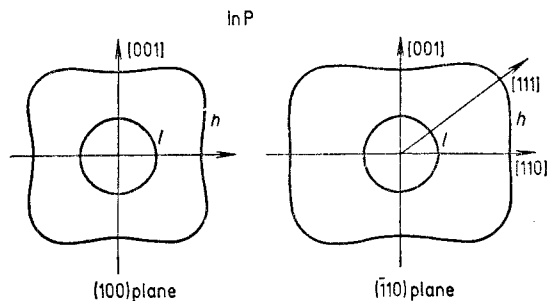
Parameter	$\Gamma$ valley	$L$ valley	$X$ valley	Reference
Valley location in the Brillouin zone	$\Gamma_{6c}$ , the lowest valley in the center of the zone	$L_{6c}$ , in $\langle 111 \rangle$ direction on the zone boundary	$\Delta_{5c}$ , in $\langle 100 \rangle$ direction close to $X_{6c}$	
Number of valleys	1	4	6	
Valley separation relative to $\Gamma$ valley, eV	0	0.5	0.96	[3.90, 4.14]
Electron masses:				
scalar $m_n/m_0$				
at 300 K	0.0781	0.4*	0.56*	[4.19, 3.90]
at 10 K	0.081			[4.20]
density-of-states $m_d/m_0$	0.0781			
Nonparabolicity parameter $\alpha$ , $\text{eV}^{-1}$	0.83			[3.32]
Uniaxial deformation potential $\Xi_u$ , eV	9.5			[4.15]
$g_c$ -factor	1.31			[4.21]

\* — Deduced from the dependence of transport coefficients on hydrostatic pressure and assuming three  $X$  valleys.

**TABLE 4.6** InP valence band parameters

Parameter	Value	Reference
<b>Light and heavy mass band at <math>\Gamma_{8v}</math></b>		
Luttinger parameters:		
$\gamma_1$	5.0	[4.22]
$\gamma_2$	1.6	[4.22]
$\gamma_3$	$2.1 \pm 0.1$	[4.22]
$g_v$ -factor: $2k$	1.94	[4.21]
$q$	$0 - 0.05$	[4.21]
Valence band nonsphericity $\delta$	0.1	
Average heavy hole mass for "spherical" bands $m_h/m_0$	0.83	
Average light hole mass for "spherical" bands $m_l/m_0$	0.11	
Density-of-states mass $m_d/m_0$	0.86	
Uniaxial deformation potentials at $\Gamma_{8v}$ , eV		
$D_u$	2.7	[4.23]
$D'_u$	4.24	[4.23]
<b>Spin-orbit split-off valence band at <math>\Gamma_{7v}</math></b>		
$\Delta_0 = E(\Gamma_{8v}) - E(\Gamma_{7v})$ , meV	0.108	[4.15]
Mass $m_{so}/m_0$	0.21	[4.24]
$g_{so}$ -factor	-1.9	[4.24]

Fig. 4.10. Valence band warping in InP. The contours are constant energy surfaces of heavy ( $h$ ) and light ( $l$ ) mass bands in (100) and (110) planes. The band nonparabolicity is not included (cf. Fig. 2).



InP valence band splitting under uniaxial compressive stress is similar to that of Ge (see Table 1.8). For InP the valence band uniaxial deformation potential and elastic constant values can be found in Tables 4.1 and 4.6.

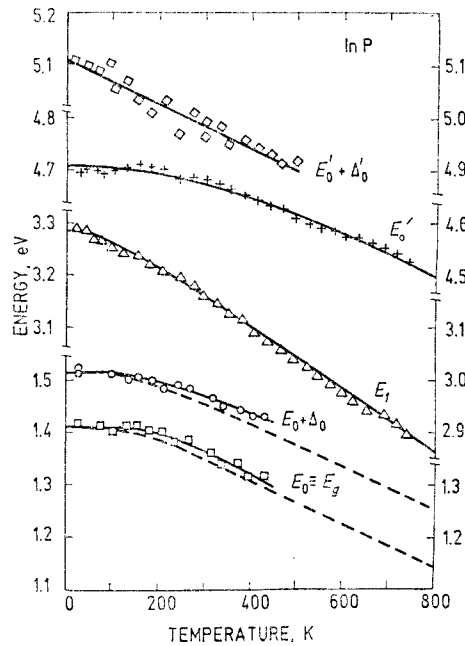


Fig. 4.11. Temperature dependence of the energy gap  $E_0 \equiv E_g$  and interband critical point energies of InP. The corresponding vertical transitions are shown in Fig. 4.9, *b*. The solid lines represent the best fits with empirical formulas and parameter values listed in Table 4.7 [4.12]. The dashed lines are the experimental values from [4.25].

**TABLE 4.7** Values of the parameters  $a$ ,  $b$  and  $\Theta$  in equation  $E(T) = a - b[1 + 2/(e^{\Theta/T} - 1)]$ , which have been obtained by fitting the critical point energies vs. temperature  $T$  by solid lines in Fig. 4.11

Critical point	$a$ , eV	$b$ , eV	$\Theta$ , K
$E_0 \equiv E_g$ (energy gap)	1.63	0.217	697
$E_0 + \Delta_0$	1.58	0.061	370
$E_1$	3.35	0.068	224
$E'_0$	4.87	0.163	775
$E'_0 + \Delta'_0 = 5.112 - 4.25 \cdot 10^{-4} T$			

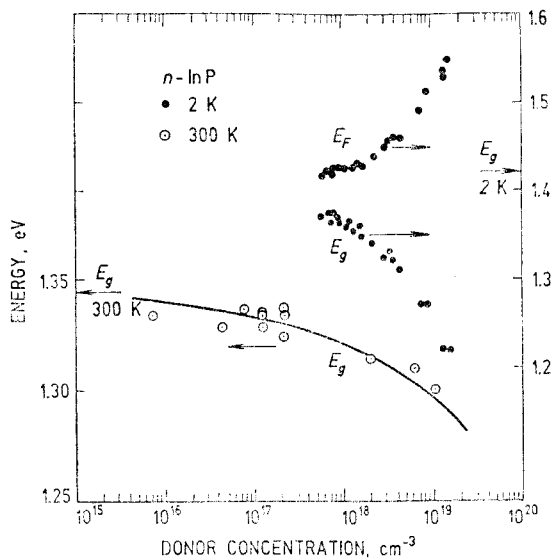


Fig. 4.12. Dependence of the energy gap  $E_g$  and Fermi energy  $E_F$  relative to the valence band gap edge on the donor concentration  $N_D$  for  $n$ -InP. Arrows on the energy scale indicate  $E_g$  at 2 K and 300 K. The solid line is an empirical formula  $E_g = 1.344 - 2.25 \cdot 10^{-8} N_D^{1/3}$ ,  $E_g$  is in eV and  $N_D$  is in  $\text{cm}^{-3}$ . Full circles — [4.26], open circles — [4.13].

### 4.3. InP optical properties

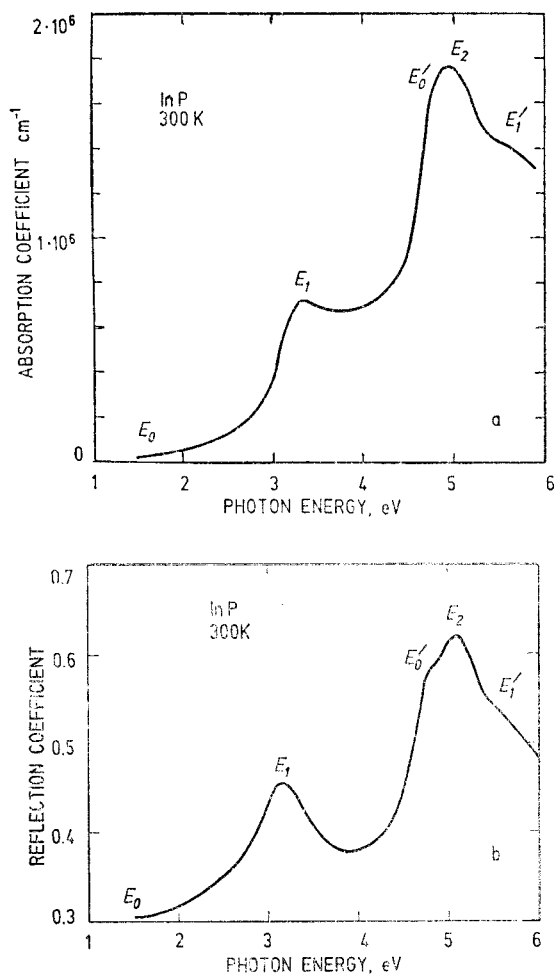


Fig. 4.13. Dependence of absorption (a) and reflection (b) coefficients of InP on photon energy.  $T=300$  K [1.53].

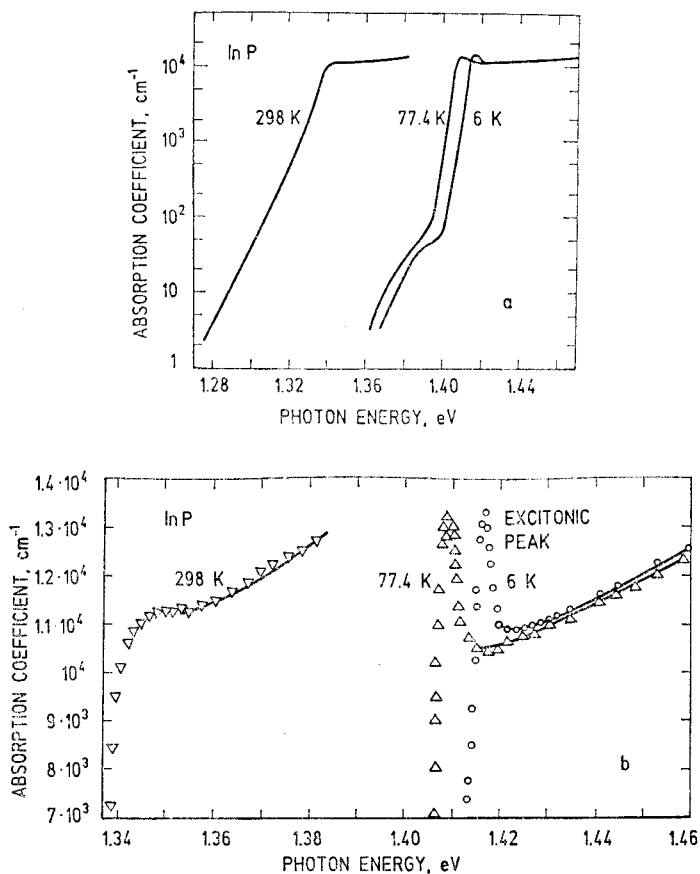


Fig. 4.14. Optical low-intensity absorption near band edge of InP. *a* — General view. *b* — The enlarged portion of the edge at the excitonic peak [4.27].

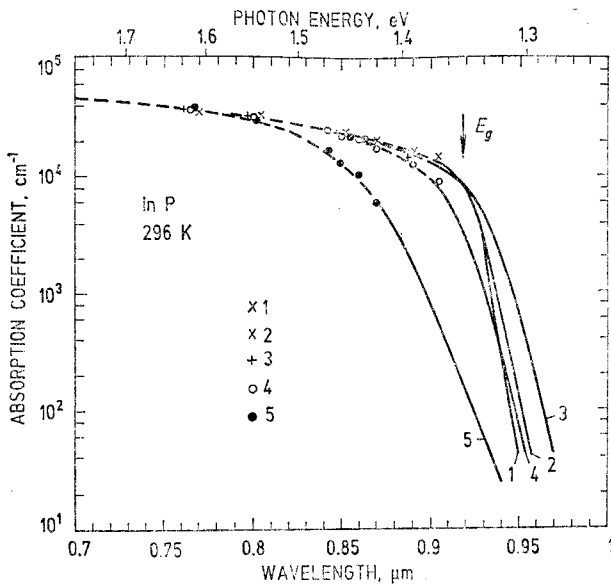
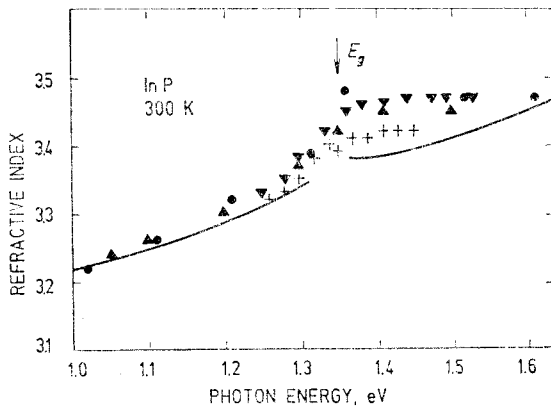


Fig. 4.16. Optical absorption coefficient vs. wavelength of  $n$ - and  $p$ -doped InP in the vicinity of the band gap at 296 K. Solid lines: photoluminescence measurements. Points and dashed lines drawn through them: ellipsometric measurements. 1 -  $n=2.7 \cdot 10^{16} \text{ cm}^{-3}$ , 2 -  $n=7.4 \cdot 10^{16} \text{ cm}^{-3}$ , 3 -  $p=1.1 \cdot 10^{18} \text{ cm}^{-3}$ , 4 -  $n=1.9 \cdot 10^{18} \text{ cm}^{-3}$ , 5 -  $n=7 \cdot 10^{18} \text{ cm}^{-3}$  [4.28].



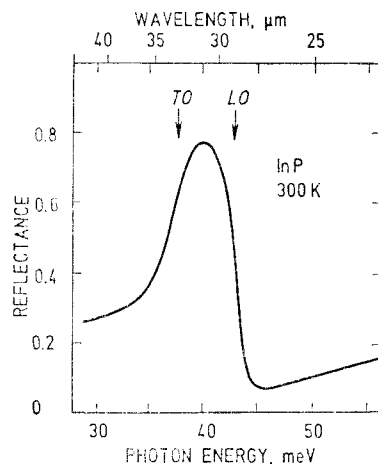


Fig. 4.17. Reflectance of InP lattice in the reststrahlen region due to *LO* and *TO* phonons at room temperature. Arrows indicate *TO* and *LO* phonon energies [4.29].

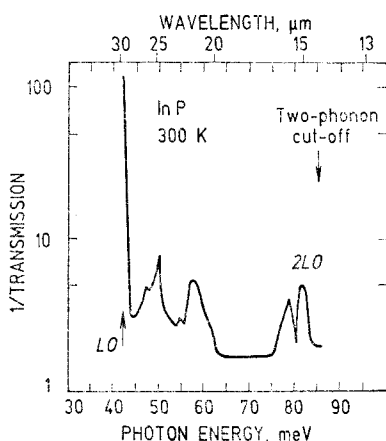


Fig. 4.18. Lattice absorption of 0.01 cm thickness InP sample at 300 K [4.30].

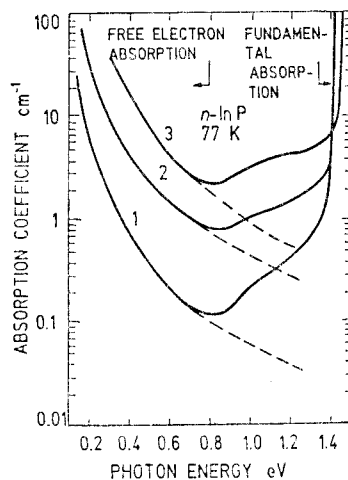


Fig. 4.19. Absorption coefficient vs. photon energy in *n*-InP at nitrogen temperature and for free electron concentration *n*: 1 —  $n = 3.5 \cdot 10^{17} \text{ cm}^{-3}$ , 2 —  $1.65 \cdot 10^{18} \text{ cm}^{-3}$ , 3 —  $5.7 \cdot 10^{18} \text{ cm}^{-3}$  [4.31]. The dashed line is extrapolation of free electron absorption.

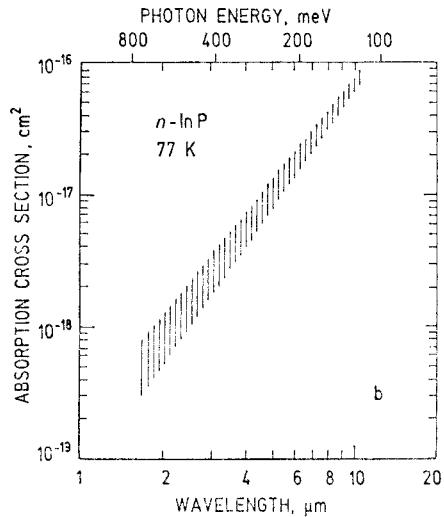
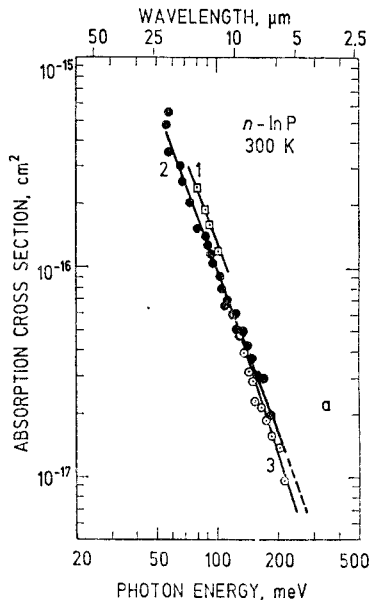


Fig. 4.20. InP free electron absorption cross section defined as  $\sigma = \alpha/n$ , where  $\alpha$  is the absorption coefficient and  $n$  is the free electron concentration, as a function of photon energy (or wavelength) at two lattice temperatures  $T$ :  $a - T = 300$  K,  $1 - n = 4 \cdot 10^{16} \text{ cm}^{-3}$ ,  $2 - 2 \cdot 10^{17} \text{ cm}^{-3}$ ,  $3 - 4 \cdot 10^{17} \text{ cm}^{-3}$  [4.30];  $b - T = 77$  K,  $n = (0.35 - 9.6) \cdot 10^{18} \text{ cm}^{-3}$  [4.31].

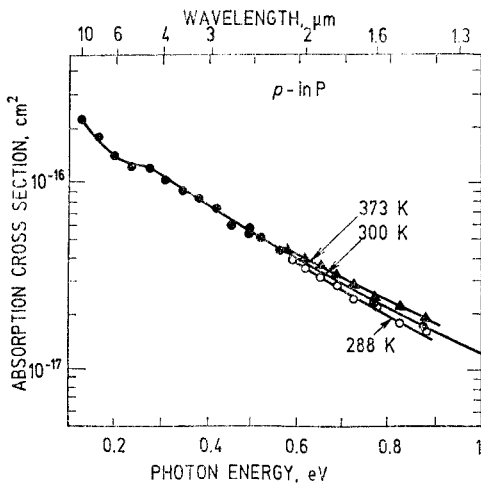


Fig. 4.21. Absorption cross section for free holes in  $p$ -InP vs. photon energy measured on sample with hole concentration  $p = 10^{18} \text{ cm}^{-3}$  at three lattice temperatures [3.53].

**TABLE 4.8** Luminescence and related properties of some quasiparticles in InP

Property	Value	Comment	Reference
<b>Free exciton, <math>X</math></b>			
Ground state luminescence energy	$1418.50 \pm 0.05$ meV		[4.32]
	$1418.67 \pm 0.07$ meV	1.6 K, $(0.28 - 8.6) \cdot 10^{14}$ cm $^{-3}$ , splitting of 0.17 meV is caused by exchange interaction	
Binding energy	$5.1 \pm 0.1$ meV		[4.32]
<b>Exciton bound to shallow donor, <math>[DX]</math></b>			
Luminescence energy:			
ground state	1416.93 meV	2 K, $\sim 3 \cdot 10^{14}$ cm $^{-3}$	[4.33]
1st excited state	1417.18 meV		[4.33]
2nd excited state	1417.38 meV		[4.33]
Dissociation energy:			
$[DX] \rightarrow D + e + \hbar$	6.7 meV		
$[DX] \rightarrow D + X$	1.6 meV		[4.33]
Lifetime	1 ns	2–4 K	[4.34]
<b>Exciton bound to ionized donor, <math>[D^+ X]</math></b>			
Luminescence energy	1416.13 meV	2 K, $\sim 3 \cdot 10^{14}$ cm $^{-3}$	[4.33]
Dissociation energy:			
$[D^+ X] \rightarrow D^+ + X$	2.37 meV		[4.33]
<b>Exciton bound to isoelectronic impurity Bi, <math>[\text{Bi} X]</math></b>			
Luminescence energy	1396.2 meV	1.9 K, $(5 - 500) \cdot 10^{15}$ cm $^{-3}$	[4.35]
Lifetime	200 ns		[4.35]
<b>Exciton bound to acceptor, <math>[AX]</math></b>			
Ground state triplet luminescence energy of $[AX]$			
	1415.4 meV	1.6 K, unidentified ac-	[4.36]
	1415.6 meV	ceptor of concentra-	[4.36]
	1415.8 meV	tion $3 \cdot 10^{13}$ cm $^{-3}$	[4.36]

TABLE 4.8 (Continued)

Property	Value	Comment	Reference
Dissociation energy:			
$[AX] \rightarrow A + X$	3.8 meV		[4.37]
$[MgX]$	1415.5 meV	2 K	[4.38]
	1415.2 meV		[4.38]
$[ZnX]$	1414.3 meV		[4.39]
Free electron-acceptor transitions, $e-A$			
Luminescence energy:			
$e-Mg$	1383 meV	2 K	[4.38]
$e-Be$	1382.7 meV	11.6 – 20.9 K	[4.40]
$e-C$	1379.7 meV	11.6 – 20.9 K	[4.40]
$e-Zn$	1380 meV	77 K	[4.41]
$e-Cd$	1360 meV	77 K	[4.41]
$e-Hg$	1330 meV	77 K	[4.41]
Free hole-donor transition, $h-D$			
Luminescence energy:	1416.27 meV	2 K, $\sim 3 \cdot 10^{14} \text{ cm}^{-3}$	[4.33]
Donor-acceptor transitions, $D-A$			
Luminescence energy:			
$D-A$	1378.8 meV	1.7 – 6.2 K	[4.42]
$D-Mg$	1380.5 meV	4.2 K	[4.43]
$D-Be$	1378.8 meV	1.7 – 11.6 K	[4.40]
$D-C$	1375.1 meV	1.7 – 11.6 K	[4.40]
$D-Zn$	1373.5 meV	1.9 K	[4.44]

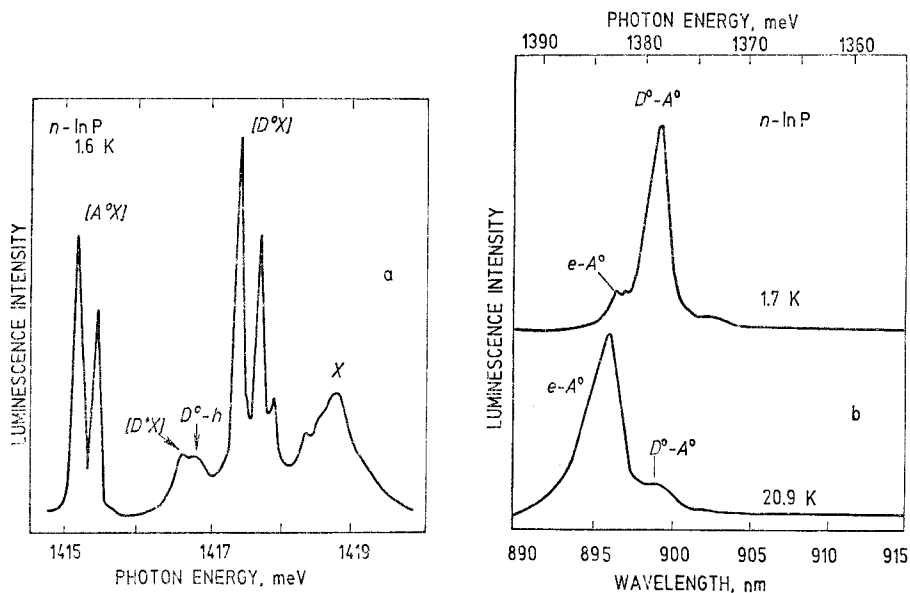


Fig. 4.22. Typical photoluminescence spectra of InP. *a* – Spectrum obtained at 1.6 K with a high-purity epitaxial layer having the residual free electron concentration  $3 \cdot 10^{18} \text{ cm}^{-3}$  at 77 K [4.36]. The following luminescence lines in the order of increasing energies are shown:  $[A^0X]$  – excitons bound to neutral acceptors,  $[D^0X]$  – excitons bound to charged donors,  $D^0-h$  – free hole to neutral donor transition,  $[D^0X]$  – excitons bound to neutral donors,  $X$  – free excitons.  $[A^0X]$  and  $[D^0X]$  consist of triplets. *b* – Photoluminescence spectra associated with acceptors at two lattice temperatures,  $T=1.7$  and 20.9 K.  $e-A^0$  is the free electron to neutral acceptor transition and  $D^0-A^0$  corresponds to donor–acceptor transition.  $n$  (77 K) =  $6.3 \cdot 10^{14} \text{ cm}^{-3}$  [4.42].

**Temperature dependence of the refractive index** in the wavelength range from 1 to 9  $\mu\text{m}$  at the room temperature [1.18]:

$$(1/n)/(dn/dT) = 5.5 \cdot 10^{-5} \text{ K}^{-1}.$$

**TABLE 4.9 Electrooptic (Pockels) coefficient  $r_{14}$  and refractive index of InP at two electromagnetic radiation wavelengths [4.45]**

Radiation wavelength, $\mu\text{m}$	$r_{14}$ , m/V	Refractive index
1.06	$1.45 \cdot 10^{-12}$	3.29
1.35	$1.3 \cdot 10^{-12}$	3.20

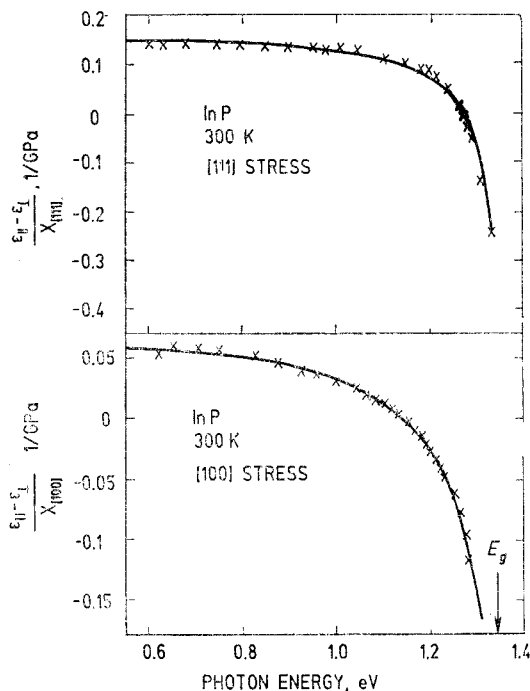


Fig. 4.23. Piezooptic effect. Measured values of  $(\epsilon_{||} - \epsilon_{\perp})/X_{[111]} = -n^4 \pi_{44}$  and  $(\epsilon_{||} - \epsilon_{\perp})/X_{[100]} = -n^4 (\pi_{11} - \pi_{12})$  for InP as a function of photon energy, where  $\epsilon_{||}$  and  $\epsilon_{\perp}$  are the relative dielectric permittivities for light polarized parallel and perpendicular to the uniaxial stress  $X$  applied in [111] and [100] directions.  $n$  is the refractive index and  $\pi_{ij}$  are the piezooptic coefficients.  $T=300$  K [4.46].

**Nonlinear susceptibility of InP.** Second-order nonlinear susceptibility [4.47]:

$$d_{14} = (1.05 \pm 0.33) \cdot 10^{-10} \text{ m/V at } 10.6 \mu\text{m}.$$

#### 4.4. InP electrical properties

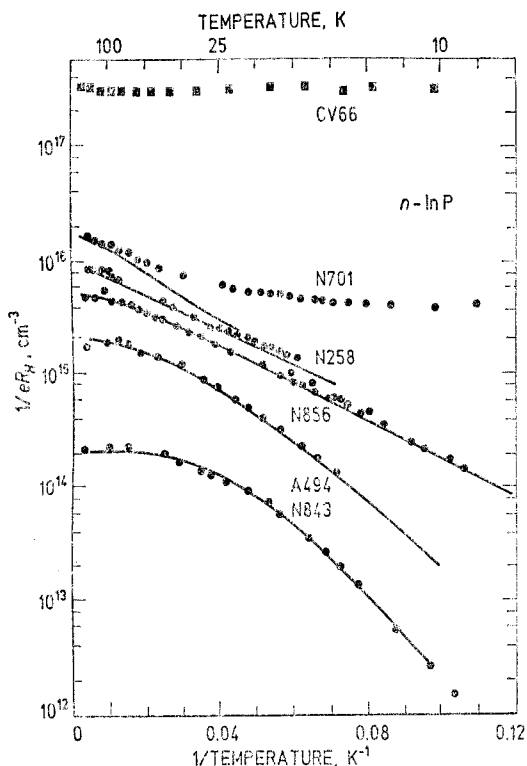


Fig. 4.24. Reciprocal of the  $n$ -InP Hall coefficient times the elementary charge,  $1/eR_H$ , vs. inverse temperature,  $1/T$ . Points are experimental data. Solid curves are theoretical fittings. Sample parameters are listed in Table 4.10. Circles — [3.74], squares — [4.43].

**TABLE 4.10** Sample parameters in Figs. 4.24 and 4.25.  $N_D$  and  $N_A$  are the donor and acceptor concentrations.  $\mu_H$  is the electron Hall mobility.  $E_D$  is the activation energy and  $K$  is the compensation degree found from theoretical fittings

Sample	$N_D - N_A$ (77 K), $\text{cm}^{-3}$	$K = N_A/N_D$	$\mu_H$ (77 K), $\text{cm}^2/(\text{V} \cdot \text{s})$	$E_D$ , meV
CV 66	$3.5 \cdot 10^{17}$		2 490	degenerate
N 701	$1.5 \cdot 10^{16}$	0.15	15 500	3.0
N 258	$9.0 \cdot 10^{15}$	0.2	18 000	2.5
N 856	$5.5 \cdot 10^{15}$	0.13	30 000	3.4
A 494	$2.0 \cdot 10^{15}$	0.15	45 000	5.3
N 843	$2.2 \cdot 10^{14}$	0.35	117 000	6.3

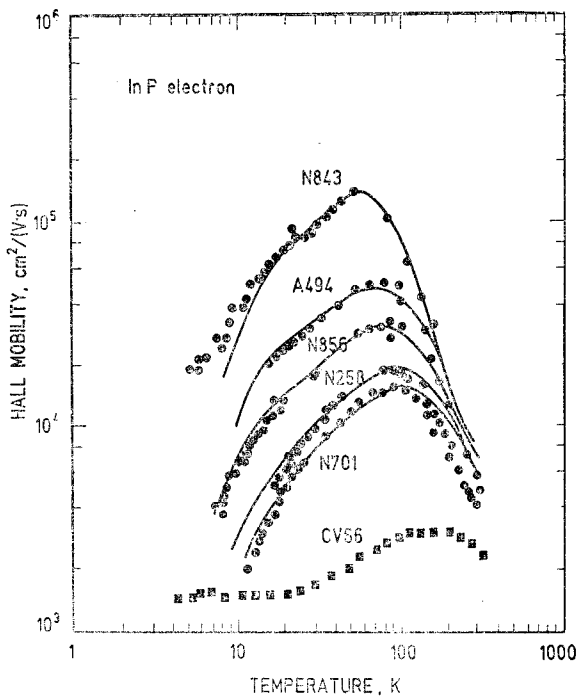


Fig. 4.25. Temperature variations of electron Hall mobility for the same *n*-InP samples as in Fig. 4.24. Solid curves are theoretical fittings. Sample parameters are listed in Table 4.10. Circles — [3.74], squares — [4.48].

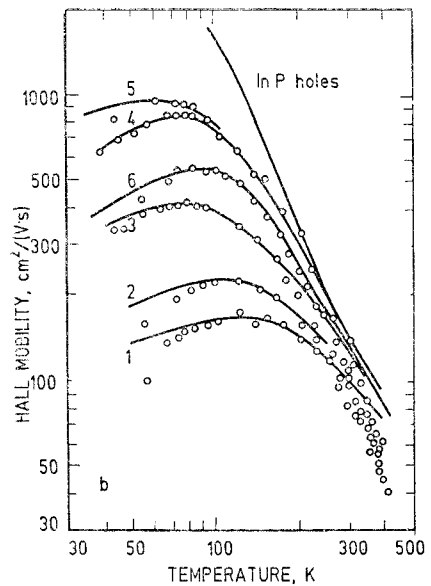
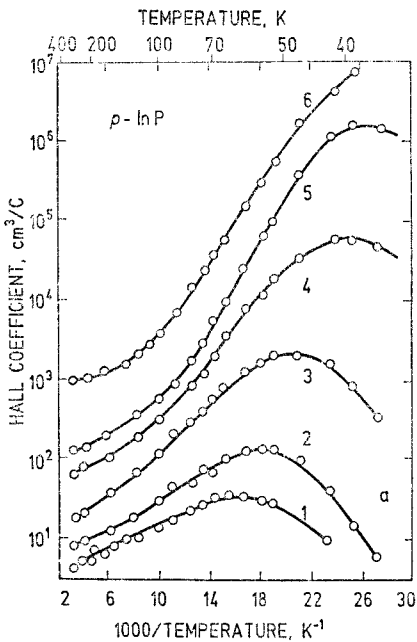


Fig. 4.26. Hole Hall coefficient (a) and mobility (b) for a number of Zn-doped *p*-InP samples as functions of (inverse) temperature. Hole concentration at 300 K: 1 —  $p = 1.75 \cdot 10^{18} \text{ cm}^{-3}$ , 2 —  $1.05 \cdot 10^{18} \text{ cm}^{-3}$ , 3 —  $3.6 \cdot 10^{17} \text{ cm}^{-3}$ , 4 —  $1.21 \cdot 10^{17} \text{ cm}^{-3}$ , 5 —  $4.4 \cdot 10^{18} \text{ cm}^{-3}$ , 6 —  $7.3 \cdot 10^{16} \text{ cm}^{-3}$  [4.49].



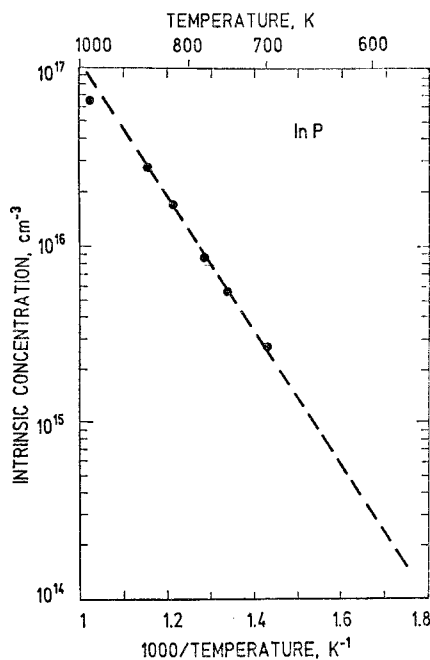


Fig. 4.27. Intrinsic concentration  $n_i$  vs. reciprocal temperature in InP. Dashed line:  $n_i = 8.4 \cdot 10^{15} T^{3/2} \exp(-7775/T)$ ,  $n_i$  is in  $\text{cm}^{-3}$  and  $T$  is in K.  $n_i = 1.2 \cdot 10^3 \text{ cm}^{-3}$  at  $T = 293 \text{ K}$  [4.50].

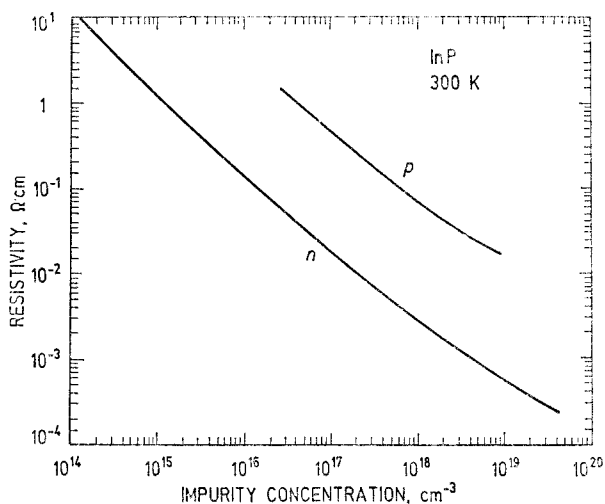


Fig. 4.28. Resistivity vs. shallow impurity concentration for InP at the lattice temperature 300 K. The data were compiled from the following sources: for  $n$ -type - [4.33, 4.37, 4.51-4.58], for  $p$ -type - [4.49, 4.59-4.63].

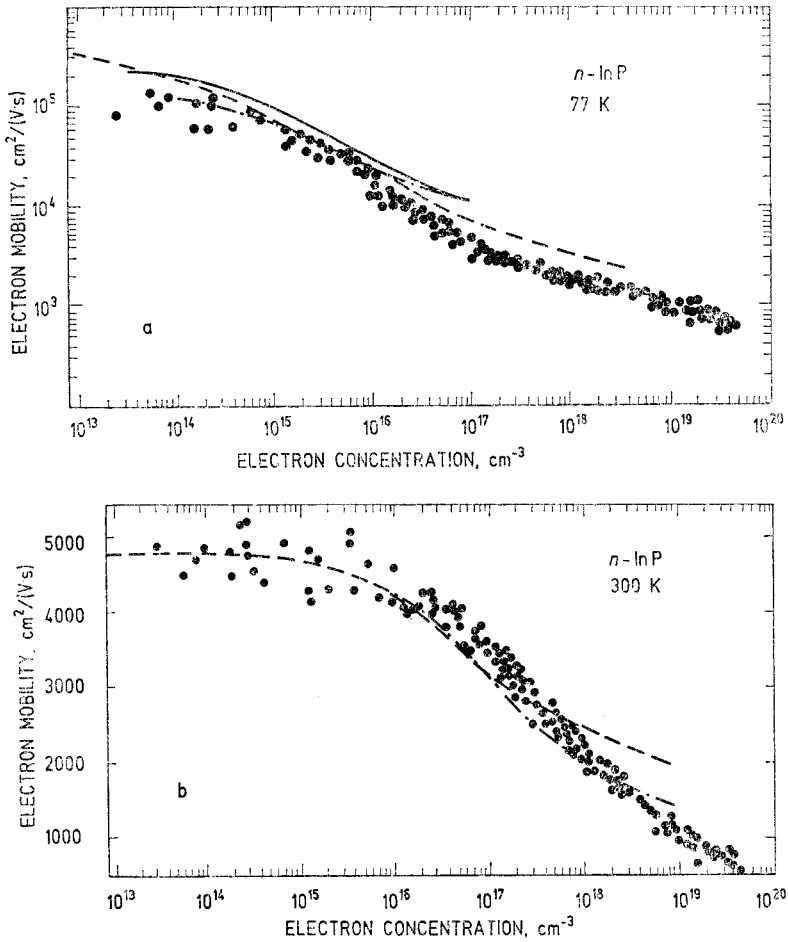


Fig. 4.29. Dependence of the electron Hall mobility on electron concentration,  $n = N_D - N_A$ , in  $n$ -InP at 77 K (a) and 300 K (b). Points are experimental data while lines are theoretical calculations [3.74].

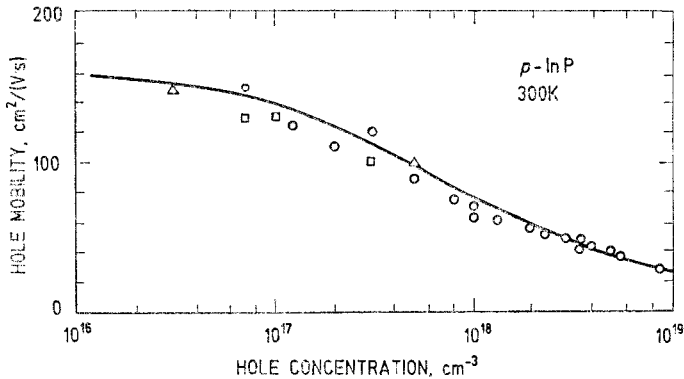


Fig. 4.30. Dependence of the hole Hall mobility on hole concentration,  $p = N_A - N_D$ , in  $p$ -InP at 300 K [3.77].

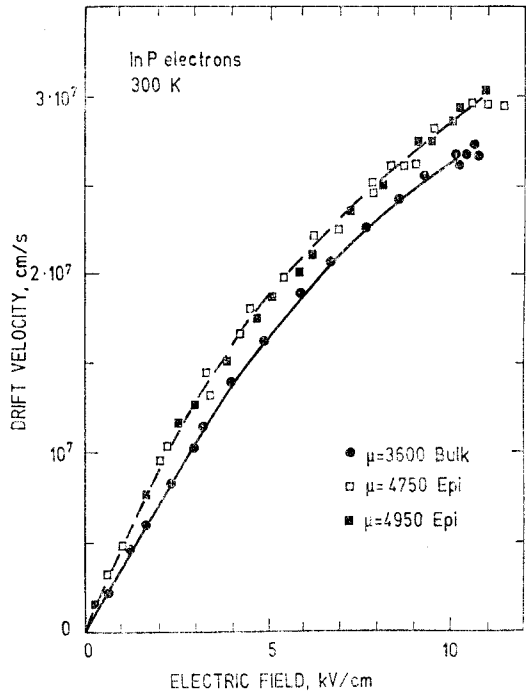


Fig. 4.31. Electron drift velocity at 300 K vs. electric field for *n*-InP having different low electric field mobilities in the region of the positive differential mobility [4.64]. The low-field mobility  $\mu$  is in cm<sup>2</sup>/(V · s).

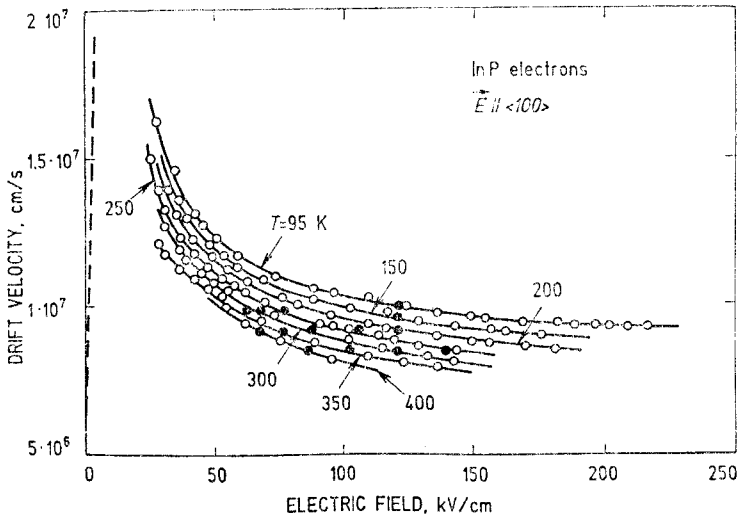


Fig. 4.32. Electron drift velocity vs. electric field in *n*-InP at different lattice temperatures in the region of negative differential mobility [4.65]. The dashed line is velocity replotted from Fig. 4.31.

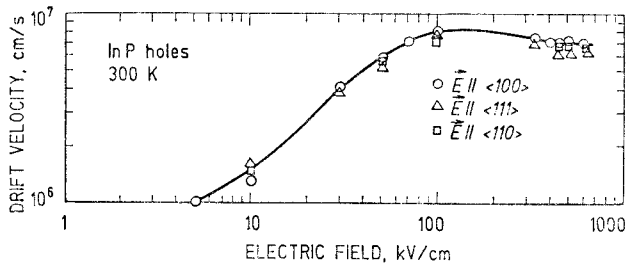


Fig. 4.33. Calculated hole drift velocity by Monte Carlo simulation as a function of electrical field strength at room temperature in InP. Experimental data are not presently available, and solid line is meant as a guide for the eye [4.66].

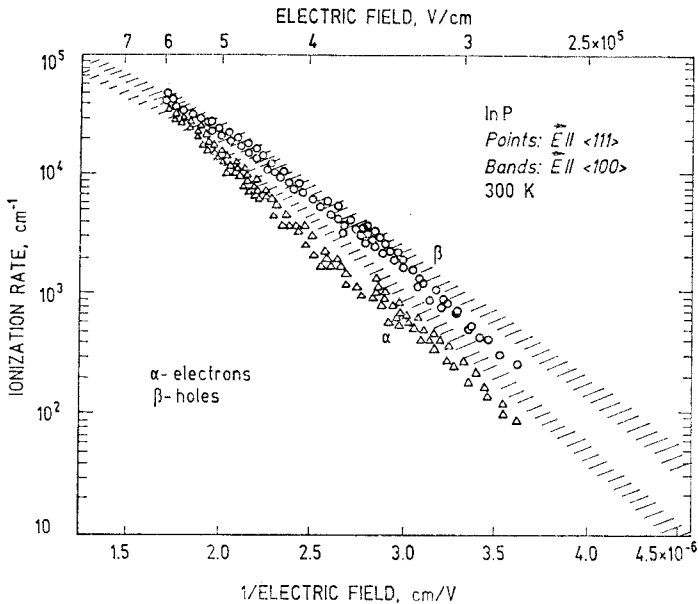


Fig. 4.34. Band-band impact ionization rates for electrons  $\alpha$  and holes  $\beta$  in InP as functions of reciprocal electric field at room temperature. Points: electric field is parallel to  $\langle 111 \rangle$  direction. Hatched bands: electric field is parallel to  $\langle 100 \rangle$  direction [4.67].

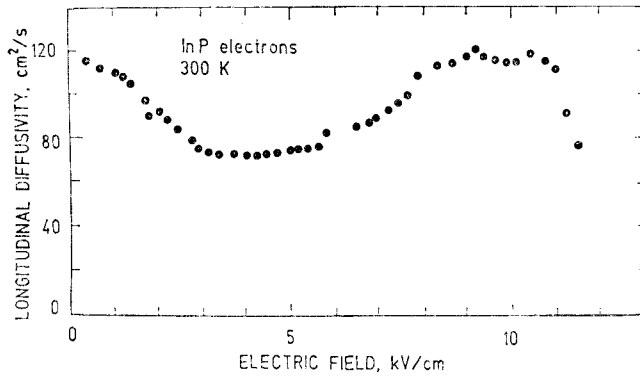


Fig. 4.35. Electron diffusion coefficient (diffusivity) in InP having donor concentration  $N_D = (2.2-5) \cdot 10^{15} \text{ cm}^{-3}$  as a function of electric field at 300 K [4.68].

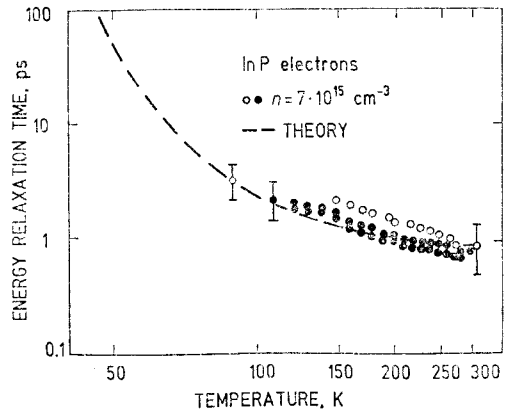


Fig. 4.36. Warm electron energy relaxation time in  $n$ -InP vs. lattice temperature [3.83]. Points: measurement. Line: theory.

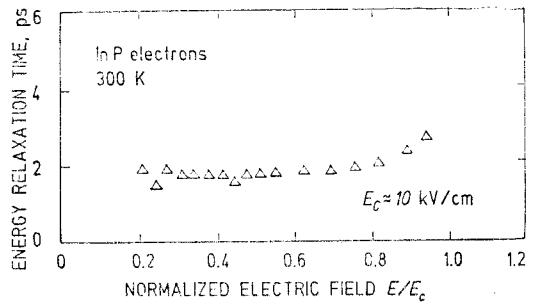


Fig. 4.37. Hot electron energy relaxation time in a lightly doped InP as a function of normalized electric field at 300 K,  $E_c \approx 10 \text{ kV/cm}$  [3.84].

**Intervalley scattering time** of hot electrons from  $\Gamma$  valley to  $L$  valley in InP is  $\tau_{TL} \sim 0.05 \text{ ps}$  for 0.98 eV electrons [4.15].

**TABLE 4.11** Parameters for high electric field transport calculation in *n*-InP [3.32]

Parameter	Value			
	Lattice	$\Gamma$ valley	$L$ valley	$X$ valley
Density, g/cm <sup>3</sup>	4.8			
Intravalley properties				
Number of valleys		1	4	3
Effective mass $m_n/m_0$		0.078	0.26	0.325
Nonparabolicity parameter, eV <sup>-1</sup>		0.83	0.23	0.38
Valley separation, eV		0	0.54	0.77
Acoustic scattering parameters				
Sound velocity, cm/s	5.13 · 10 <sup>5</sup>			
Deformation potential, eV	8			
Optical scattering parameters				
Static dielectric permittivity $\epsilon/\epsilon_0$	12.5			
High frequency dielectric permittivity $\epsilon_\infty/\epsilon_0$	9.52			
Polar optical phonon energy, meV	43		42.3	41.6
Intervalley properties				
Transition	Coupling constant		Phonon energy	
$\Gamma - L$	1.0 · 10 <sup>9</sup> eV/cm		27.8 meV	
$\Gamma - X$	1.0 · 10 <sup>9</sup> eV/cm		29.9 meV	
$L - L$	1.0 · 10 <sup>9</sup> eV/cm		29.0 meV	
$L - X$	0.9 · 10 <sup>9</sup> eV/cm		29.3 meV	
$X - X$	0.9 · 10 <sup>9</sup> eV/cm		29.9 meV	

#### 4.5. InP piezoelectric, thermoelectric and magnetic properties

Piezoelectric coefficient of InP at room temperature [4.69]:

$$|d_{14}| = 1.8 \cdot 10^{-12} \text{ m/V.}$$

**TABLE 4.12** Piezoresistance coefficients of InP in 1/GPa. For physical interpretation refer Table 5

Experimental conditions	$\frac{\pi_{11} + \pi_{12} + \pi_{44}}{2}$	$\pi_{11} + 2\pi_{12}$	Reference
<i>n</i> -type			
$n = 2.5 \cdot 10^{16} \text{ cm}^{-3}$			
77 K, 300 K	-0.013	-0.082	[4.70]

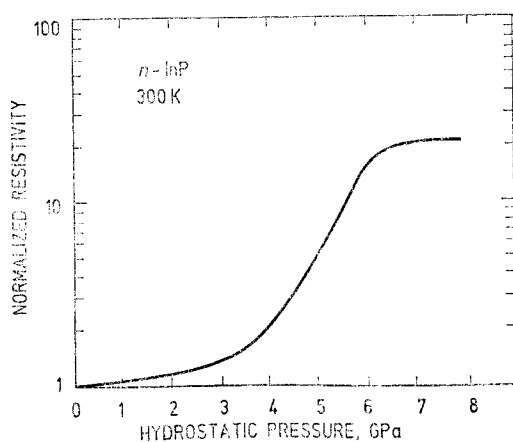


Fig. 4.38. Normalized resistivity  $\rho/\rho_0$  vs. hydrostatic pressure for *n*-InP at room temperature [3.90].

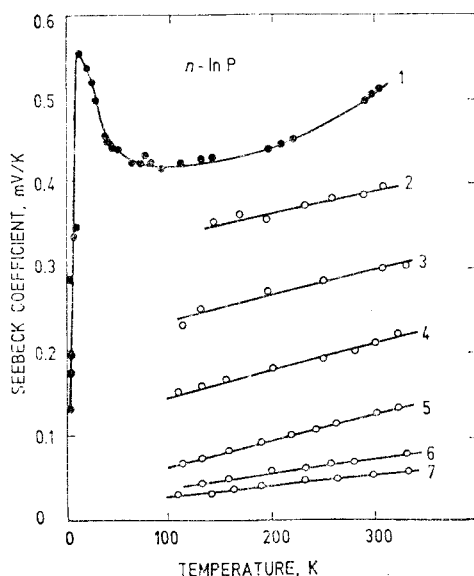


Fig. 4.39. Seebeck coefficient vs. temperature in  $n$ -InP for different electron concentrations: 1 —  $n = 2 \cdot 10^{16} \text{ cm}^{-3}$  [4.9], 2 —  $7.7 \cdot 10^{16} \text{ cm}^{-3}$ , 3 —  $2.2 \cdot 10^{17} \text{ cm}^{-3}$ , 4 —  $9 \cdot 10^{17} \text{ cm}^{-3}$ , 5 —  $3.2 \cdot 10^{18} \text{ cm}^{-3}$ , 6 —  $7.3 \cdot 10^{18} \text{ cm}^{-3}$ , 7 —  $1.8 \cdot 10^{19} \text{ cm}^{-3}$  [4.51].

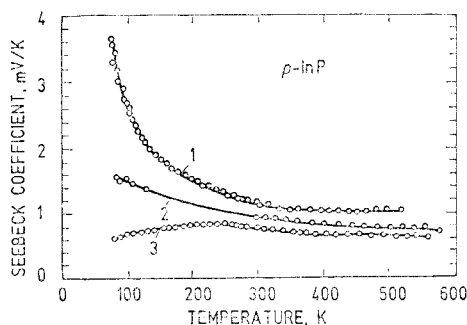


Fig. 4.40. Seebeck coefficient vs. temperature in  $p$ -InP for different hole concentrations: 1 —  $p = 7 \cdot 10^{16} \text{ cm}^{-3}$ , 2 —  $3 \cdot 10^{17} \text{ cm}^{-3}$ , 3 —  $3 \cdot 10^{18} \text{ cm}^{-3}$  [4.62].

**Magnetic susceptibility.** InP lattice contribution to the magnetic susceptibility  $\chi_m$  at room temperature and respective temperature coefficient [4.71]:

$$\chi_m = -1.9 \cdot 10^{-5},$$

$$d\chi_m/dT = 0.74 \cdot 10^{-9} \text{ K}^{-1}.$$



Fig. 4.41. Hall factor for electrons as a function of temperature for samples of  $n$ -InP with different ionized donor concentration  $N_I$ . Open circles:  $N_I = 5 \cdot 10^{14} \text{ cm}^{-3}$ , full circles:  $N_I = 1.4 \cdot 10^{15} \text{ cm}^{-3}$ , lines: theory [4.58].

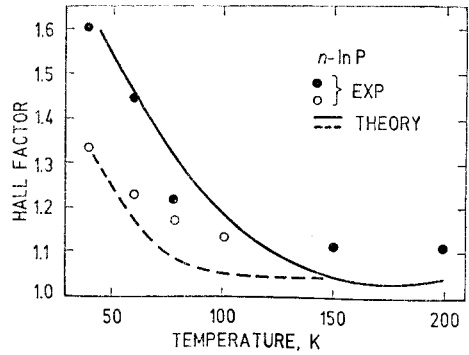


Fig. 4.42. Hall factor vs. magnetic field induction in pure  $n$ -InP at 290 K. Crosses:  $n = 2.4 \cdot 10^{14} \text{ cm}^{-3}$ , points:  $n = 6.7 \cdot 10^{13} \text{ cm}^{-3}$ , dashed line: theory [4.53].

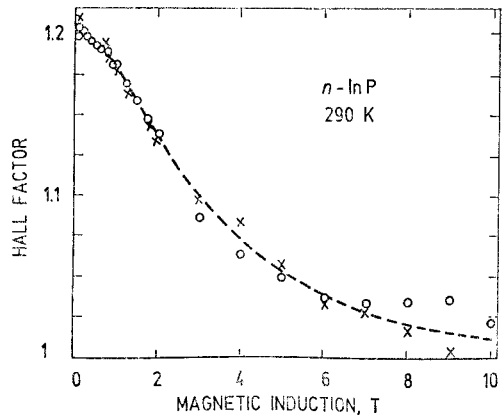
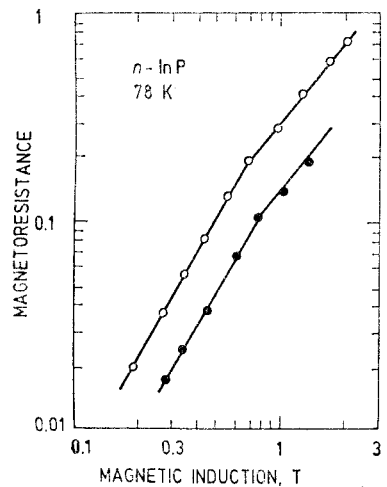


Fig. 4.43. Transverse magnetoresistance  $[\rho(B) - \rho_0]/\rho_0$  of  $n$ -InP at 78 K vs. magnetic induction. Electron concentration: open circles —  $n = 1 \cdot 10^{15} \text{ cm}^{-3}$ , full circles —  $n = 2 \cdot 10^{15} \text{ cm}^{-3}$  [4.72].



#### 4.6. InP impurity properties

**TABLE 4.13** Donor (*D*), acceptor (*A*) and trap (*T*) ionization energy associated with various impurities in InP. Donor (acceptor) energy is referenced relative to the conduction (valence) band edge

Impurity	Type	Energy, meV	Reference
Be	<i>A</i>	$E_v + 41.3$	[4.40]
Bi	<i>T</i>	31	[4.73]
C	<i>A</i>	$E_v + 41.5$	[4.74]
C	<i>A</i>	$E_v + 44.6$	[4.40]
Cd	$A_{In}$	$E_v + 56$	[4.41]
Co	<i>D</i>	$E_v + 240$	[4.75]
Cr	$T_{In}$	$E_v + 940$	[4.76]
Cu <sub>A</sub>	?	$E_v + 260$	[4.77]
Cu <sub>B</sub>	?	$E_v + 640$	[4.77]
Fe <sub>A</sub> ( $^5T_2$ )	$A_{In}$	$E_c - 300$	[4.78]
Fe <sub>B</sub> ( $^5E$ )	$A_{In}$	$E_c - 650$	[4.78]
Ge	<i>D</i>	$E_c - 7^*$	[4.73]
Hg	$A_{In}$	$E_v + 86$	[4.41]
Mg	<i>A</i>	$E_v + 40.6$	[4.38]
Mn	<i>A</i>	$E_v + 230$	[4.78]
O	<i>T</i> , <i>D</i> ?	$E_c - 780$	[4.79]
S	$D_P$	$E_c - 7^*$	[4.73]
Se	$D_P$	$E_c - 7^*$	[4.73]
Si	<i>D</i>	$E_c - 7^*$	[4.73]
Sn	<i>D</i>	$E_c - 7^*$	[4.73]
Te	<i>D</i>	$E_c - 7^*$	[4.73]
Ti	<i>D</i>	$E_c - 630$	[3.107]
V	<i>D</i>	$E_v + 210$	[4.80]
Zn	$A_{In}$	$E_v + 48$	[4.74]

$D_{In}$ ,  $A_{In}$  — In-site donor or acceptor,

$D_P$ ,  $A_P$  — P-site donor or acceptor.

\* — For details see Table 4.14.

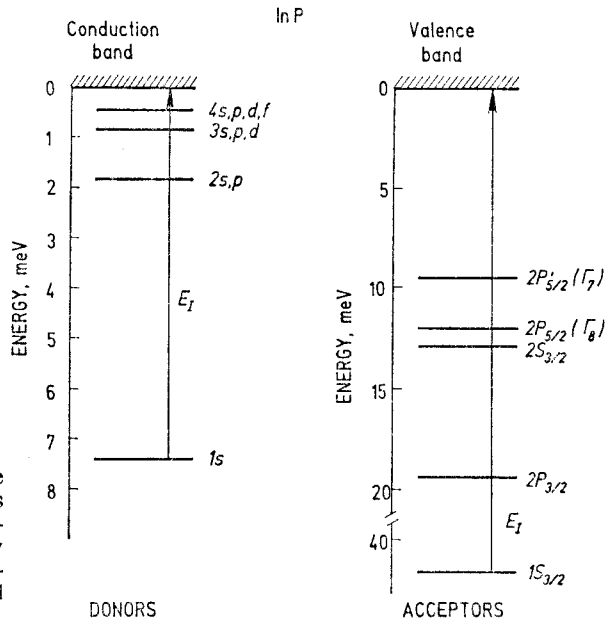


Fig. 4.44. Energy level scheme of shallow donors and acceptors in InP within effective mass approximation. Ionization energy  $E_I$  is different for different chemical species (see Table 4.14 and 4.15).

**TABLE 4.14** Ionization and transition energies from the ground  $1s$  state to excited states for **shallow donors** in InP

$E_I$ or transition	Energy, meV		Reference
	Experiment	Hydrogenic model	
$1s$ state ionization energy $E_I$	7.43	7.4	[4.33]
$1s \rightarrow 2p$	5.6	5.55	[4.81]
$1s \rightarrow 3s, p, d$	6.32	6.58	[4.82]

**Electron capture cross section** by shallow single-charged donors at the lattice temperature  $T=4.2$  K is  $\sigma=(1.3-4.7) \cdot 10^{-14}$  cm<sup>2</sup> [4.83].

**TABLE 4.15** Ionization energy  $E_I$  of the ground state  $1S_{3/2}$  and the transition energies between  $1S_{3/2}$  and excited states  $2P_{3/2}$ ,  $2S_{3/2}$ ,  $2P_{5/2}(\Gamma_8)$ ,  $2P_{5/2}(\Gamma_7)$  for **shallow acceptor** impurities (zinc, carbon [4.74], magnesium [4.38]) in InP. Effective mass theory – [4.84]

$E_I$ or transition	Energy, meV			
	Zn	C	Mg	Theory
Ionization energy $E_I$	48	41.5	40.6	43.1
$1S_{3/2} \rightarrow 2P_{3/2}$	30.5	24.0	25.2	23.7
$1S_{3/2} \rightarrow 2S_{3/2}$	32.8	27.5	27.8	30.2
$1S_{3/2} \rightarrow 2P_{5/2}(\Gamma_8)$	35.2	29.0	29.6	31.1
$1S_{3/2} \rightarrow 2P_{5/2}(\Gamma_7)$	38.2	32.0	31.0	33.6

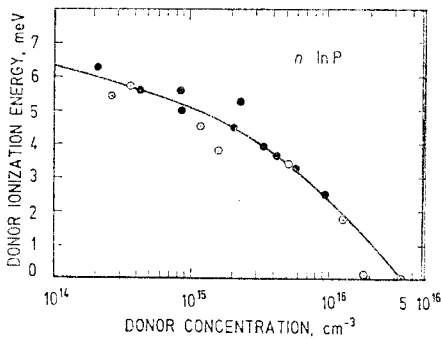


Fig. 4.45. Dependence of shallow donor thermal ionization energy  $E_I$  on electrically active donor concentration  $N_D^*$  in  $n$ -InP. Full circles – [3.74], open circles – [4.85]. Solid line is an empirical formula  $E_I = 7.4 - 2.3 \cdot 10^{-5} N_D^{*1/3}$ ,  $E_I$  is in meV and  $N_D^*$  is in  $\text{cm}^{-3}$ .

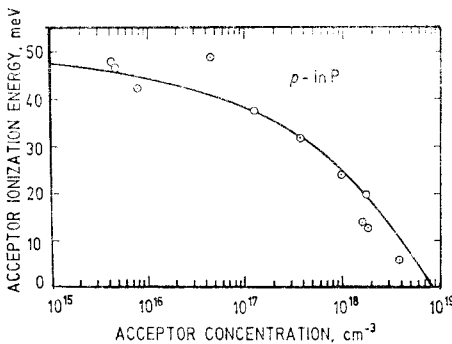


Fig. 4.46. Dependence of shallow acceptor (zinc) thermal ionization energy  $E_I$  on electrically active acceptor concentration  $N_A^*$  in  $p$ -InP. Solid line is an empirical formula  $E_I = 50 - 2.5 \cdot 10^{-5} N_A^{*1/3}$ ,  $E_I$  is in meV and  $N_A^*$  is in  $\text{cm}^{-3}$  [4.49].

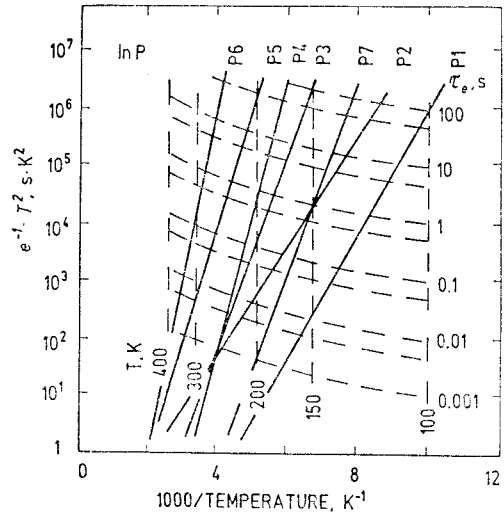


Fig. 4.47. Catalogue of inverse thermal emission rates multiplied by  $T^2$  vs. reciprocal temperature for different traps found by DLTS in relatively pure bulk and vapour phase epitaxial InP. The abacus drawn in dashed lines is composed of vertical isothermal straight lines and curved lines of constant emission times. The parameters of traps are given in Table 4.16 [4.86].

**TABLE 4.16** Ionization energies and thermal capture cross sections calculated from Fig. 4.47

Level label	Ionization energy, meV	Temperature, K	Capture cross section, $\text{cm}^2$
P1	210	95—209	$3 \cdot 10^{-16}$
P2	190	112—380	$7 \cdot 10^{-19}$
P3	330	145—316	$4 \cdot 10^{-16}$
P4	500	169—292	$2 \cdot 10^{-12}$
P5	410	185—420	$1 \cdot 10^{-16}$
P6	630	240—470	$2 \cdot 10^{-14}$
P7	330	123—228	$5 \cdot 10^{-14}$

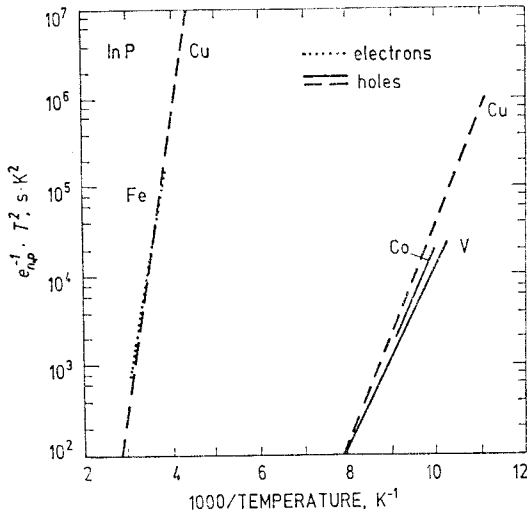


Fig. 4.48. Inverse thermal emission rate multiplied by  $T^2$  vs. reciprocal temperature for deep impurities indicated at the curves as obtained with DLTS on doped InP samples. For details see Table 4.17.

**TABLE 4.17** Ionization energy and capture cross sections of deep impurities in InP as determined by DLTS

Impurity	Donor or acceptor	Depth from the conduction $E_c$ or valence $E_v$ band edge, meV	Temperature, K	Capture cross section, $\text{cm}^2$	Reference
Co	D	$E_v + 240$	102—110	$\sigma_p = 2 \cdot 10^{-14}$	[4.75]
Cu	?	$E_v + 260$	89—128	$\sigma_p = 1.3 \cdot 10^{-13}$	[4.77]
Cu	?	$E_v + 640$	227—330	$\sigma_p = 6 \cdot 10^{-15}$	[4.77]
Fe	A	$E_c - 630$	265—320	$\sigma_n = 3.5 \cdot 10^{-14}$	[4.87]
V	D	$E_v + 210$	100—128	$\sigma_p = 7 \cdot 10^{-16}$	[4.80]

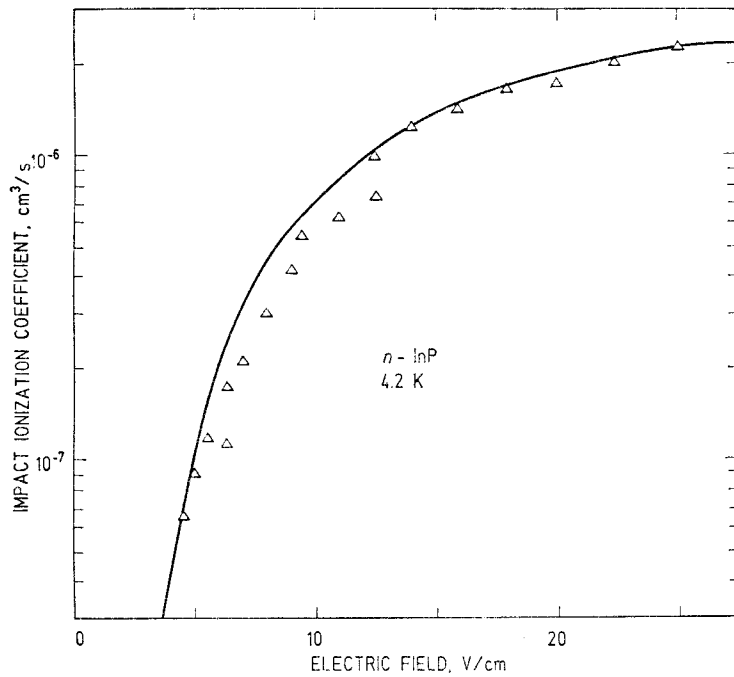
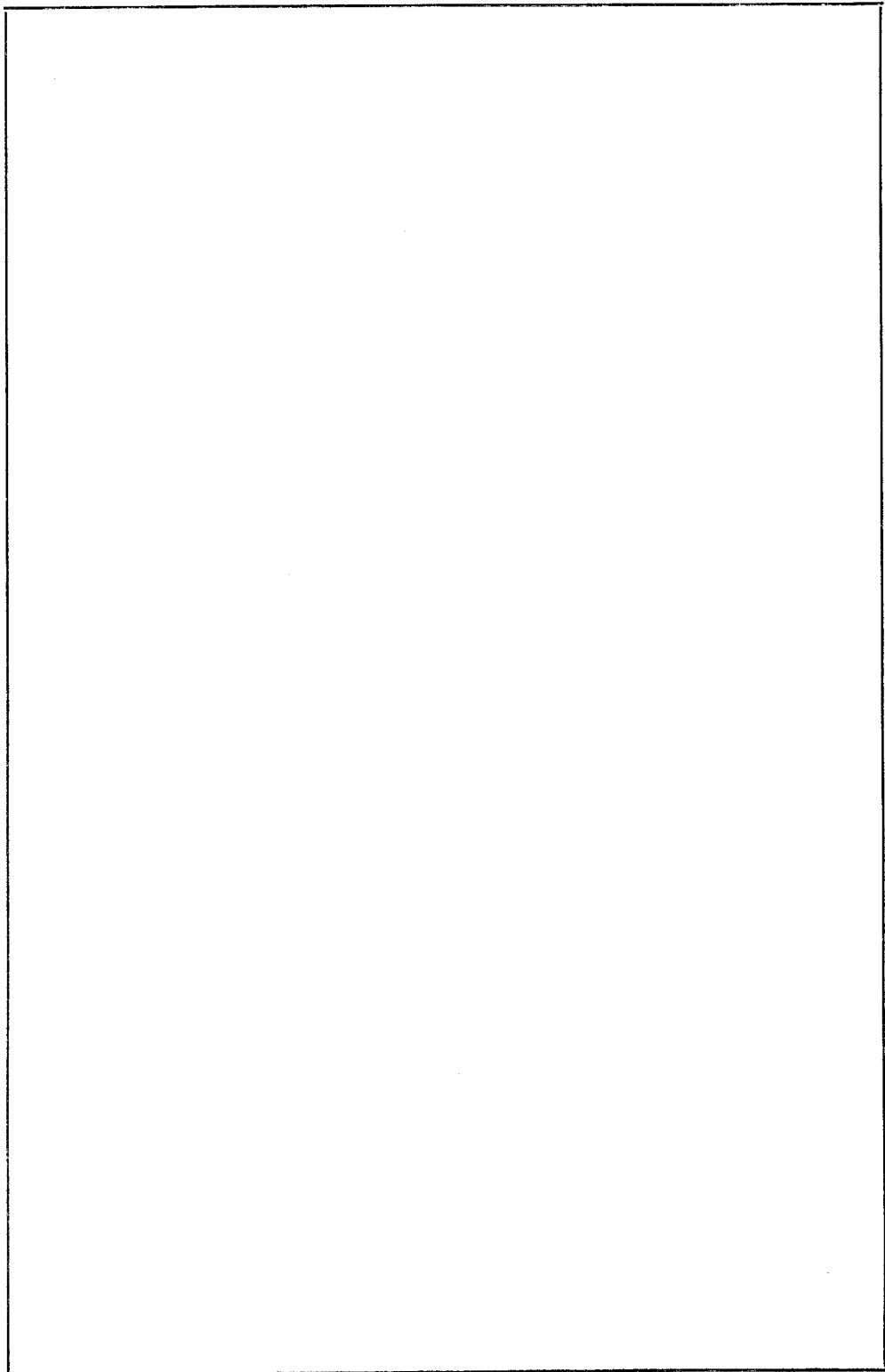


Fig. 4.49. Dependence of the impact ionization coefficient  $A_I$  of shallow donors in  $n\text{-InP}$  on the electric field strength  $E$ . Dots: experimental data at 4.2 K. Solid line: empirical formula  $A_I = 5 \cdot 10^{-6} \exp(-19.5/E)$ ,  $A_I$  is in  $\text{cm}^3/\text{s}$  and  $E$  is in  $\text{V/cm}$  [4.88, 3.116].





## C. References and subject index

### 1. References

1. Kittel C. Quantum Theory of Solids. — New York—London: Wiley, 1963.  
Киттель Ч. Квантовая теория твердых тел. — Москва: Мир, 1967. 491 с.
2. Murnaghan F. D. The compressibility of media under extreme pressures // *Proc. Natl. Acad. Sci. USA*, 1944, v. 30, p. 244—247.
3. *Light Scattering in Solids IV* / Ed. by M. Cardona and G. Güntherodt. — Berlin: Springer-Verlag, 1984.  
Рассеяние света в твердых телах. Выпуск IV / Под ред. М. Кардоны и Г. Гюнтерода. Москва: Мир, 1986. 408 с.
4. Mayer A. P., Wehner R. K. Calculation of Grüneisen constants in Si // *Phys. Stat. Sol. (b)*, 1984, v. 126, No 1, p. 91—103.
5. Piesbergen U. Heat capacity and Debye temperatures // *Semiconductors and Semimetals* / Ed. by R. K. Willardson and A. C. Beer. — New York—London: Academic Press, 1966, p. 49—60.
6. Elliott R. J. Spin-orbit coupling in band theory-character tables for some "double" space groups // *Phys. Rev.*, 1954, v. 96, No 2, p. 280—287.
7. Dresselhaus G. Spin-orbit coupling effects in zinc blende structures // *Phys. Rev.*, 1955, v. 100, No 2, p. 580—586.
8. Baldereschi A., Lipari N. O. Spherical model of shallow acceptor states in semiconductors // *Phys. Rev. B*, 1973, v. 8, No 6, p. 2697—2709.
9. Пикус Г. Е., Марушак В. А., Титков А. Н. Спиновое расщепление зон и спиновая релаксация носителей в кубических кристаллах  $A^{III}B^V$  // *ФТП*, 1988, т. 22, вып. 2, с. 185—200.
10. Christensen N. E., Cardona M. Splitting of the conduction bands of GaAs for  $k$  along [110] // *Solid State Commun.*, 1984, v. 51, No 7, p. 491—493.
11. Hensel J. C. Microwave combined resonances in germanium:  $g$  factor of the free hole // *Phys. Rev. Lett.*, 1968, v. 21, No 14, p. 983—986.
12. Hensel J. C., Suzuki K. Anisotropy of the  $g$  factor of the free hole in Ge and conduction-band spin-orbit splitting // *Phys. Rev. Lett.*, 1969, v. 22, No 16, p. 838—840.
13. Beni G., Capasso F. Effect of carrier drift velocities on measured ionization coefficients in avalanching semiconductors // *Phys. Rev. B*, 1979, v. 19, No 4, p. 2197—2203.
14. Smith C. S. Piezoresistance effect in germanium and silicon // *Phys. Rev.*, 1954, v. 94, No 1, p. 42—49.
15. Fritzsche H. Piezoresistance of  $n$ -type germanium // *Phys. Rev.*, 1959, v. 115, No 2, p. 336—345.
16. Ковтонюк Н. Ф., Концевой Ю. А. Измерения параметров полупроводниковых материалов. — Москва: Металлургия, 1970. 430 с.
17. Runyan W. R. Semiconductor Measurements and Instrumentation. — New York: McGraw-Hill, 1975. 280 p.
18. Greenaway D. L., Harbeke G. Optical Properties and Band Structure of Semiconductors. — Oxford: Pergamon Press, 1968. 159 p.
19. Kingston R. H. Detection of Optical and Infrared Radiation. — Berlin—Heidelberg: Springer-Verlag, 1978. 140 p.
20. Рыбкин С. М. Фотоэлектрические явления в полупроводниках. — Москва: Физматгиз, 1963. 494 с.
21. Blood P., Orton J. W. The electrical characterisation of semiconductors // *Rep. Prog. Phys.*, 1978, v. 41, No 2, p. 157—257.  
Блад П., Ортон Дж. В. Методы измерения электрических свойств полупроводников // *Зарубежная радиоэлектроника*, 1981, № 1, с. 3—50; № 2, с. 3—49.
22. Wieder H. H. Laboratory Notes on Electrical and Galvanomagnetic Measurements. — Amsterdam: Elsevier Scientific Publishing Company, 1979. 277 p.
23. Кучис Е. В. Методы исследования эффекта Холла. — Москва: Сов. радио, 1974. 328 с.

24. Bauer G. Experimental studies of nonlinear transport in semiconductors // *Physics of Nonlinear Transport in Semiconductors* / Ed. by D. K. Ferry, J. R. Barker, C. Jacoboni. — New York: Plenum Press, 1980, p. 175–241.
25. Даргис А. Ю. Измерение дрейфовой скорости в твердых телах. — Вильнюс: Моклас, 1987. 203 с.
26. Lang D. V. Space-charge spectroscopy in semiconductors // *Thermally Stimulated Relaxation in Solids* / Ed. by P. Bräunlich. — Berlin: Springer-Verlag, 1979, p. 93–133.
27. Sell D. D., Stokowski S. E., Dingle R., DiLorenzo J. V. Polariton reflectance and photoluminescence in high-purity GaAs // *Phys. Rev. B*, 1973, v. 7, No 10, p. 4568–4586.
28. Cohen E. R., Taylor B. N. The 1986 adjustment of the fundamental physical constants // *Rev. Mod. Phys.*, 1987, v. 59, No 4, p. 1121–1148.
29. Symbols, units and nomenclature in physics: Document U.I.P.20 (1978). — International Union of Pure and Applied Physics. S.U.N. Commission.  
Обозначения, единицы измерения и терминология в физике. Документ U.I.P.20 (1978) // УФН, 1979, т. 129, вып. 2, с. 290–335.

## Ge

- 1.1. Радциг А. А., Смирнов Б. М. Справочник по атомной и молекулярной физике. — Москва: Атомиздат, 1980. 240 с.
- 1.2. Straumanis M. E., Aka E. Z. Lattice parameters, coefficients of thermal expansion, and atomic weights of purest silicon and germanium // *J. Appl. Phys.*, 1952, v. 23, No 3, p. 330–334.
- 1.3. Baker J. F. C., Hart M. An absolute measurement of the lattice parameter of germanium using multiple-beam X-ray diffractometry // *Acta Cryst.*, 1975, v. A31, p. 364–367.
- 1.4. Smakula A., Sils V. Precision density determination of large single crystals by hydrostatic weighing // *Phys. Rev.*, 1955, v. 99, No 6, p. 1744–1746.
- 1.5. Крестовников А. Н., Евгеньев С. Б., Глазов В. М. Закономерности объемных изменений при плавлении полупроводников различных групп // *ДАН СССР*, 1967, т. 174, № 3, с. 634–637.
- 1.6. Qadri S. B., Skelton E. F., Webb A. W. High pressure studies of Ge using synchrotron radiation // *J. Appl. Phys.*, 1983, v. 54, No 6, p. 3609–3611.
- 1.7. Sze S. M. *Physics of Semiconductor Devices*. — New York: Wiley, 1981.  
Зи С. Физика полупроводниковых приборов: В 2-х кн. Кн. 1. — Москва: Мир, 1984. 455 с.
- 1.8. McSkimin H. J., Andreatch P. Elastic moduli of germanium versus hydrostatic pressure at 25.0 °C and — 195.8 °C // *J. Appl. Phys.*, 1963, v. 34, No 3, p. 651–655.
- 1.9. Буренков Ю. А., Никаноров С. П., Степанов А. В. Упругие свойства германия // *ФТТ*, 1970, т. 12, вып. 8, с. 2428–2430.
- 1.10. Anderson O. L. The use of ultrasonic measurements under modest pressure to estimate compression at high pressure // *J. Phys. Chem. Solids*, 1966, v. 27, No 3, p. 547–565.
- 1.11. Nilsson G., Nelin G. Study of the homology between silicon and germanium by thermal-neutron spectrometry // *Phys. Rev. B*, 1972, v. 6, No 10, p. 3777–3786.
- 1.12. Brockhouse B. N., Dasannacharya B. A. Temperature effects on lattice vibrations in germanium // *Solid State Commun.*, 1963, v. 1, No 4, p. 205–209.
- 1.13. Nelin G., Nilsson G. Phonon anharmonicity of germanium in the temperature range 80–880 K // *Phys. Rev. B*, 1974, v. 10, No 2, p. 612–620.
- 1.14. Ray R. K., Aggarwal R. L., Lax B. Temperature dependence of Raman scattering in germanium // *Light Scattering in Solids* / Ed. by M. Balkanski. Paris: Flammarion, 1971, p. 288–290.
- 1.15. Payne R. T. Shift of [111] phonon energies at the Brillouin zone boundary under uniaxial stress in germanium // *Phys. Rev. Lett.*, 1964, v. 13, No 2, p. 53–55.
- 1.16. Soma T. Thermal expansion coefficient of Si and Ge // *J. Phys. Soc. Jpn.*, 1977, v. 42, No 5, p. 1491–1494.
- 1.17. Goffi A. R., Syassen K., Cardona M. Effect of pressure on the refractive index of Ge and GaAs // *Phys. Rev. B*, 1990, v. 41, No 14, p. 10104–10110.
- 1.18. Bertolotti M., Bogdanov V., Ferrari A., Jascow A., Nazorova N., Pikhlin A., Schirone L. Temperature dependence of the refractive index in semiconductors // *J. Opt. Soc. Am. B*, 1990, v. 7, No 6, p. 918–922.
- 1.19. Nilsson G., Nelin G. Phonon dispersion relations in Ge at 80 K // *Phys. Rev. B*, 1971, v. 3, No 2, p. 364–369.

- 1.20. Dobbs E. R., Chick B. B., Truell R. Attenuation of sound in a germanium crystal at ultrahigh frequencies and low temperatures // *Phys. Rev. Lett.*, 1959, v. 3, No 7, p. 332–334.
- 1.21. Flubacher P., Leadbetter A. J., Morrison J. A. The heat capacity of pure silicon and germanium and properties of their vibrational frequency spectra // *Phil. Mag.*, 1959, v. 4, No 39, p. 273–294.
- 1.22. Glassbrenner C. J., Slack G. A. Thermal conductivity of silicon and germanium from 3 K to the melting point // *Phys. Rev.*, 1964, v. 134, No 4A, p. 1058–1069.
- 1.23. Gibbons D. F. Thermal expansion of some crystals with the diamond structure // *Phys. Rev.*, 1958, v. 112, No 1, p. 136–140.
- 1.23a. Новикова С. И. Тепловое расширение германия при низких температурах // *ФТТ*, 1960, т. 2, вып. 1, с. 43–44.
- 1.24. Smith T. F., White G. K. The low-temperature thermal expansion and Grüneisen parameters of some tetrahedrally bonded solids // *J. Phys. C: Solid State Phys.*, 1975, v. 8, No 13, p. 2031–2042.
- 1.25. Carr R. H., McCammon R. D., White G. K. Thermal expansion of germanium and silicon at low temperatures // *Phil. Mag.*, 1965, v. 12, No 115, p. 157–163.
- 1.26. Slack G. A., Bartram S. F. Thermal expansion of some diamondlike crystals // *J. Appl. Phys.*, 1975, v. 46, No 1, p. 89–98.
- 1.27. Philip J., Breazeale M. A. Third-order elastic constants and Grüneisen parameters of silicon and germanium between 3 and 300 K // *J. Appl. Phys.*, 1983, v. 54, No 2, p. 752–757.
- 1.28. Chelikowsky J. R., Cohen M. L. Nonlocal pseudopotential calculations for the electronic structure of eleven diamond and zinc-blende semiconductors // *Phys. Rev. B*, 1976, v. 14, No 2, p. 556–582.
- 1.29. Cardona M., Shaklee K. L., Pollak F. H. Electorelectance at a semiconductor–electrolyte interface // *Phys. Rev.*, 1967, v. 154, No 3, p. 696–720.
- 1.30. Macfarlane G. G., McLean T. P., Quarrington J. E., Roberts V. Fine structure in the absorption-edge spectrum of Ge // *Phys. Rev.*, 1957, v. 108, No 6, p. 1377–1383.
- 1.31. Zwerdling S., Lax B., Roth L. M., Button K. J. Exciton and magneto-absorption of the direct and indirect transitions in germanium // *Phys. Rev.*, 1959, v. 114, No 1, p. 80–89.
- 1.32. Fletcher K., Pitt G. D. Intervalley scattering in *n* type Ge from a Hall effect experiment to high pressures // *J. Phys. C: Solid State Phys.*, 1971, v. 4, No 13, p. 1822–1834.
- 1.33. Goñi A. R., Syassen K., Cardona M. Direct-band-gap absorption in germanium under pressure // *Phys. Rev. B*, 1989, v. 39, No 17, p. 12921–12924.
- 1.34. Camassel J., Auvergne D. Temperature dependence of the fundamental edge of germanium and zinc-blende-type semiconductors // *Phys. Rev. B*, 1975, v. 12, No 8, p. 3258–3267.
- 1.35. Viña L., Logothetidis S., Cardona M. Temperature dependence of the dielectric function of germanium // *Phys. Rev. B*, 1984, v. 30, No 4, p. 1979–1991.
- 1.36. Nathan M. I., Paul W., Brooks H. Interband scattering in *n*-type germanium // *Phys. Rev.*, 1961, v. 124, No 2, p. 391–407.
- 1.37. Jayaraman A., Kosicki B. B., Irvin J. C.  $\Delta_1$  conduction-band minimum of Ge from high-pressure studies on *p-n* junctions // *Phys. Rev.*, 1968, v. 171, No 3, p. 836–838.
- 1.38. Zallen R., Paul W. Effect of pressure on interband reflectivity spectra of germanium and related semiconductors // *Phys. Rev.*, 1967, v. 155, No 3, p. 703–711.
- 1.39. Aggarwal R. L. Stress-modulated magnetorelectance for the direct transitions  $\Gamma_{25}' \rightarrow \Gamma_{15}'$  and  $\Gamma_{25}' \rightarrow \Gamma_{25}'$  in germanium // *Phys. Rev. B*, 1970, v. 2, No 2, p. 446–458.
- 1.40. Fink D., Braunstein R. Determination of the conduction band effective masses of the germanium-silicon alloy by infrared cyclotron resonance // *Phys. Stat. Sol. (b)*, 1976, v. 73, No 1, p. 361–370.
- 1.41. Jacoboni C., Reggiani L. The Monte Carlo method for the solution of charge transport in semiconductors with applications to covalent materials // *Rev. Mod. Phys.*, 1983, v. 55, No 3, p. 645–705.
- 1.42. Baranskii P. I., Kolomoets V. V. The determination of the deformation potential constants in *n*-germanium // *Phys. Stat. Sol. (b)*, 1971, v. 45, No 1, p. K55–K59.
- 1.43. Ermakov V. N., Kolomoets V. V., Timoshuk V. S. The deformation potentials  $\Xi_X^c, \Xi_X^v$  of the *X*-valleys of the germanium conduction band // *Phys. Stat. Sol. (b)*, 1983, v. 116, No 2, p. K77–K78.
- 1.44. Hensel J. C., Suzuki K. Quantum resonances in the valence bands of germanium. II. Cyclotron resonances in uniaxially stressed crystals // *Phys. Rev. B*, 1974, v. 9, No 10, p. 4219–4257.

- 1.45. Зверев В. Н. Экспериментальное исследование непараболичности зоны легких дырок в германии // ФТТ, 1980, т. 22, вып. 11, с. 3282–3287.
- 1.46. Fawcett W. Valence band structure of germanium // Proc. Phys. Soc., 1965, v. 85, No 547, pt 5, p. 931–944.
- 1.47. Thurmond C. D. The standard thermodynamic functions for the formation of electrons and holes in Ge, Si, GaAs, and GaP // J. Electrochem. Soc., 1975, v. 122, No 8, p. 1133–1141.
- 1.48. Wagner J., Viña L. Radiative recombination in heavily doped *p*-type germanium // Phys. Rev. B, 1984, v. 30, No 12, p. 7030–7036.
- 1.49. Шотов А. П., Мурашов М. С. Рекомбинационное излучение сильно легированного германия // ФТП, 1967, т. 1, вып. 4, с. 573–586.
- 1.50. Haas C. Infrared absorption in heavily doped *n*-type germanium // Phys. Rev., 1962, v. 125, No 6, p. 1965–1971.
- 1.51. Philipp H. R., Taft E. A. Optical constants of germanium in the region 1 to 10 eV // Phys. Rev., 1959, v. 113, No 4, p. 1002–1005.
- 1.52. Dash W. C., Newman R. Intrinsic optical absorption in single-crystal germanium and silicon at 77 K and 300 K // Phys. Rev., 1955, v. 99, No 4, p. 1151–1155.
- 1.53. Aspnes D. E., Studna A. A. Dielectric functions and optical parameters of Si, Ge, GaP, GaAs, GaSb, InP, InAs, and InSb from 1.5 to 6.0 eV // Phys. Rev. B, 1983, v. 27, No 2, p. 985–1009.
- 1.54. Salzberg C. D., Villa J. J. Infrared refractive indexes of silicon, germanium and modified selenium glass // J. Opt. Soc. Am., 1957, v. 47, No 3, p. 244–246.
- 1.55. Loewenstein E. V., Smith D. R., Morgan R. L. Optical constants of far infrared materials. 2: Crystalline solids // Appl. Opt., 1973, v. 12, No 2, p. 398–406.
- 1.56. Fray S. J., Johnson F. A., Quarrington J. E., Williams N. Lattice bands in germanium // Proc. Phys. Soc., 1965, v. 85, No 543, pt 1, p. 153–158.
- 1.57. Fan H. Y., Spitzer W., Collins R. J. Infrared absorption in *n*-type germanium // Phys. Rev., 1956, v. 101, No 2, p. 566–572.
- 1.58. Briggs H. B., Fletcher R. C. Absorption of infrared light by free carriers in germanium // Phys. Rev., 1953, v. 91, No 6, p. 1342–1346.
- 1.59. Mayer A. E., Lightowers E. C. Accurate determination of the exciton energy gap and the *LA* and *LO* momentum-conserving phonon energies in germanium // J. Phys. C: Solid State Phys., 1979, v. 12, No 13, p. L507–L512.
- 1.59a. Labrie D., Timusk T. Direct determination of the equilibrium constant of the exciton-carrier gas in germanium // Solid State Commun., 1989, v. 53, No 4, p. 327–330.
- 1.60. Thomas G. A., Blount E. I., Capizzi M. Indirect recombination mechanisms in germanium // Phys. Rev. B, 1979, v. 19, No 2, p. 702–718.
- 1.61. Mayer A. E., Lightowers E. C. Donor bound exciton luminescence and absorption in germanium // J. Phys. C: Solid State Phys., 1979, v. 12, No 24, p. L945–L950.
- 1.62. Chen M., Smith D. L., McGill T. C. Low-temperature photoluminescence spectra of doped Ge // Phys. Rev. B, 1977, v. 15, No 10, p. 4983–4996.
- 1.63. Mayer A. E., Lightowers E. C. Evidence for an excited hole state of donor bound excitons in germanium and a parity selection rule // J. Phys. C: Solid State Phys., 1980, v. 13, No 27, p. L747–L752.
- 1.64. Гросс Е. Ф., Новиков Б. В., Соколов Н. С. Люминесценция связанных экситонов в кристаллах германия // ФТТ, 1972, т. 14, вып. 2, с. 443–447.
- 1.65. Feldman A., Waxler R. M., Horowitz D. Photoelastic constants of germanium // J. Appl. Phys., 1978, v. 49, No 4, p. 2589–2590.
- 1.66. Higginbotham C. W., Cardona M., Pollak F. H. Intrinsic piezobirefringence of Ge, Si, and GaAs // Phys. Rev., 1969, v. 184, No 3, p. 821–829.
- 1.67. Wynne J. J. Optical third-order mixing in GaAs, Ge, Si, and InAs // Phys. Rev., 1969, v. 178, No 3, p. 1295–1303.
- 1.68. Mayer A., Keilmann F. Far-infrared nonlinear optics. II.  $\chi^{(3)}$  contributions from the dynamics of free carriers in semiconductors // Phys. Rev. B, 1986, v. 33, No 10, p. 6962–6968.
- 1.69. Debye P. P., Conwell E. M. Electrical properties of *n*-type germanium // Phys. Rev., 1954, v. 93, No 4, p. 693–706.
- 1.70. Brown D. M., Bray R. Analysis of lattice and ionized impurity scattering in *p*-type germanium // Phys. Rev., 1962, v. 127, No 5, p. 1593–1602.
- 1.71. Голякова О. А., Мойжес Б. Я., Стильбанс Л. С. Подвижность дырок в германии в зависимости от концентрации и температуры // ФТТ, 1961, т. 3, вып. 10, с. 3105–3114.
- 1.72. Morin F. J., Maita J. P. Conductivity and Hall effect in the intrinsic range of germanium // Phys. Rev., 1954, v. 94, No 6, p. 1525–1529.

- 1.73. Sze S. M., Irvin J. C. Resistivity, mobility and impurity levels in GaAs, Ge, and Si at 300 K // *Solid State Electron.*, 1968, v. 11, No 6, p. 599–602.
- 1.74. Фистуль В. И., Иглицын М. И., Омеляновский Э. М. Подвижность электронов в сильно легированном германии с примесью мышьяка // *ФТТ*, 1962, т. 4, вып. 4, с. 1065–1067.
- 1.75. Jacoboni C., Nava F., Canali C., Ottaviani G. Electron drift velocity and diffusivity in germanium // *Phys. Rev. B*, 1981, v. 24, No 2, p. 1014–1026.
- 1.76. Reggiani L., Canali C., Nava F., Ottaviani G. Hole drift velocity in germanium // *Phys. Rev. B*, 1977, v. 16, No 6, p. 2781–2791.
- 1.77. Reggiani L., Canali C., Nava F., Alberigi Quaranta A. Diffusion coefficient of holes in Ge // *J. Appl. Phys.*, 1978, v. 49, No 8, p. 4446–4452.
- 1.78. Mikawa T., Kagawa S., Kaneda T., Toyama Y., Mikami O. Crystal orientation dependence of ionization rates in germanium // *Appl. Phys. Lett.*, 1980, v. 37, No 4, p. 387–389.
- 1.79. Hess K., Seeger K. Energie-Relaxation warmer Ladungsträger in Germanium und Silizium // *Z. Physik*, 1969, Bd 218, H. 5, S. 431–436.
- 1.80. Dienys V., Kancleris Ž. Influence of  $e$ - $e$  scattering on the phenomenological energy relaxation time in nonpolar semiconductors // *Phys. Stat. Sol. (b)*, 1975, v. 67, No 1, p. 317–323.
- 1.81. Денис В., Канцлерис Ж., Мартунас З. Теплые электроны. – Вильнюс: Мокелас, 1983. 144 с.
- 1.82. Weinreich G., Sanders T. M., White H. G. Acoustoelectric effect in  $n$ -type germanium // *Phys. Rev.*, 1959, v. 114, No 1, p. 33–44.
- 1.83. Dargys A., Banys T. Dependence of the phenomenological energy relaxation time on electric field in  $n$ -Si and  $n$ -Ge at 77 K // *Phys. Stat. Sol. (b)*, 1972, v. 52, No 2, p. 699–706.
- 1.84. Барейкис В. А., Гальдикас А. П., Пожела Ю. К. Шумы, время релаксации энергии и диффузия горячих дырок в  $p$ -Ge в магнитном поле // *ФТП*, 1977, т. 11, вып. 2, с. 365–372.
- 1.85. Morin F. J., Geballe T. H., Herring C. Temperature dependence of the piezoresistance of high-purity silicon and germanium // *Phys. Rev.*, 1957, v. 105, No 2, p. 525–539.
- 1.86. Шадрин В. С., Городецкий А. Ф. Пьезосопротивление германия // *ФТТ*, 1963, т. 5, вып. 11, с. 3081–3087.
- 1.87. Pollak M. Piezoresistance in heavily doped  $n$ -type germanium // *Phys. Rev.*, 1958, v. 111, No 3, p. 798–802.
- 1.88. Geballe T. H., Hull G. W. Seebeck effect in germanium // *Phys. Rev.*, 1954, v. 94, No 5, p. 1134–1140.
- 1.89. Hudgens S., Kastner M., Fritzsche H. Diamagnetic susceptibility of tetrahedral semiconductors // *Phys. Rev. Lett.*, 1974, v. 33, No 26, p. 1552–1555.
- 1.90. Stevens D. K., Cleland J. W., Crawford J. H., Schweinler H. C. Magnetic susceptibility of germanium // *Phys. Rev.*, 1955, v. 100, No 4, p. 1084–1093.
- 1.91. Бабич В. М., Баранский П. И., Даховский И. В., Самойлович А. Г. Концентрационная зависимость коэффициента Холла в  $n$ -Ge в слабых магнитных полях // *УФЖ*, 1969, т. 14, № 3, с. 418–422.
- 1.92. Алексеенко М. В., Андреев А. Г., Забродский А. Г., Попов В. В. Экспериментальное определение Холл-фактора в сложной валентной зоне  $p$ -Ge // *ФТП*, 1988, т. 22, вып. 1, с. 140–143.
- 1.93. Pearson G. L., Suhl H. The magneto-resistance effect in oriented single crystals of germanium // *Phys. Rev.*, 1951, v. 83, No 4, p. 768–776.
- 1.94. Babich V. M., Baranskii P. I., Korolyuk S. L., Samoilovich A. G., Chelova T. N. Transverse magnetoresistance of  $n$ -type Ge in quantizing magnetic fields // *Phys. Stat. Sol. (b)*, 1973, v. 55, No 1, p. 457–466.
- 1.95. Reuszer J. H., Fisher P. An optical determination of the ground-state splittings of group V impurities in germanium // *Phys. Rev.*, 1964, v. 135, No 4A, p. 1125–1132.
- 1.96. Aggarwal R. L., Fisher P., Mourzine V., Ramdas A. K. Excitation spectra of lithium donors in silicon and germanium // *Phys. Rev.*, 1965, v. 138, No 3A, p. 882–893.
- 1.97. Grimmeiss H. G., Montelius L., Larsson K. Chalcogens in germanium // *Phys. Rev. B*, 1988, v. 37, No 12, p. 6916–6928.
- 1.98. Jones R. L., Fisher P. Excitation spectra of group III impurities in germanium // *J. Phys. Chem. Solids*, 1965, v. 26, No 7, p. 1125–1131.
- 1.99. Soepangkat H. P., Fisher P. Transverse Zeeman effect of the excitation spectra of boron and thallium impurities in germanium // *Phys. Rev. B*, 1973, v. 8, No 2, p. 870–893.
- 1.100. Cross J. W., Ho L. T., Ramdas A. K., Sauer R., Haller E. E. Excitation spectra of group-II acceptors in Ge: Ge (Be<sup>0</sup>), Ge (Be<sup>-</sup>), and Ge (Mg<sup>0</sup>) // *Phys. Rev. B*, 1983, v. 28, No 12, p. 6953–6960.

- 1.101. Salib E. H., Fisher P., Simmonds P. E. Quantitative piezospectroscopy of neutral copper in germanium // *Phys. Rev. B*, 1985, v. 32, No 4, p. 2424–2438.
- 1.102. Tyler W. W. Deep level impurities in germanium // *J. Phys. Chem. Solids*, 1959, v. 8, p. 59–65.
- 1.103. Chapman R. A., Hutchinson W. G. Excited states of mercury-induced double-acceptors in germanium // *Solid State Commun.*, 1965, v. 3, No 9, p. 293–296.
- 1.104. Chapman R. A., Hutchinson W. G. Excitation spectra and photo-ionization of neutral mercury centers in germanium // *Phys. Rev.*, 1967, v. 157, No 3, p. 615–622.
- 1.105. Borello S. R., Levinstein H. Preparation and properties of mercury-doped germanium // *J. Appl. Phys.*, 1962, v. 33, No 10, p. 2947–2950.
- 1.106. Johnson L., Levinstein H. Infrared properties of gold in germanium // *Phys. Rev.*, 1960, v. 117, No 5, p. 1191–1203.
- 1.107. Остробородова В. В. Факторы вырождения примесных уровней и анализ электрических свойств германия с золотом // *ФТТ*, 1965, т. 7, вып. 2, с. 610–618.
- 1.108. Kogan Sh. M., Lifshits T. M. Photoelectric spectroscopy — a new method of analysis of impurities in semiconductors // *Phys. Stat. Sol. (a)*, 1977, v. 39, No 1, p. 11–39.
- 1.109. Rotsaert E., Clauws P., Vennik J., Van Goethem L. Absorption cross sections in the far-IR spectrum of elemental shallow donors and acceptors in germanium // *J. Appl. Phys.*, 1989, v. 65, No 2, p. 730–735.
- 1.110. Ramdas A. K., Rodriguez S. Spectroscopy of the solid-state analogues of the hydrogen atom: donors and acceptors in semiconductors // *Rep. Prog. Phys.*, 1981, v. 44, No 12, p. 1297–1387.
- 1.111. Абакумов В. Н., Перель В. И., Ясневич И. Н. Захват носителей заряда на притягивающие центры в полупроводниках // *ФТП*, 1978, т. 12, вып. 1, с. 3–32.
- 1.112. Котина И. М., Куряков В. В., Новиков С. Р., Пирожкова Т. И. Емкостная спектроскопия глубоких центров Cu, Au, Ag и Ni в германии // *ФТП*, 1987, т. 21, вып. 6, с. 1039–1043.
- 1.113. Dargys A., Žurauskas S., Žurauskienė N. High electric field impact ionization of shallow donors in Ge(Sb) // *Liet. Fiz. Rink.*, 1989, v. 29, No 3, p. 323–328. [*Lithuanian J. Phys.*, 1989, v. 29, No 3, p. 46–50.]
- 1.114. Аснина Ж. С., Межебовский Б. Е., Парицкий Л. Г. Кинетика ударной ионизации мелких примесных центров в германии // *ФТП*, 1985, т. 19, вып. 6, с. 1064–1069.
- 1.115. Даргис А. Ю., Жураускас С. В. Динамика пробоя мелких акцепторов в германии в сильных электрических полях // *ФТП*, 1988, т. 22, вып. 3, с. 455–460.

## Si

- 2.1. Yim W. M., Paff R. J. Thermal expansion of AlN, sapphire, and silicon // *J. Appl. Phys.*, 1974, v. 45, No 3, p. 1456–1457.
- 2.2. Красюк Б. А., Грибов А. И. Полупроводники — германий и кремний. — Москва: Металлургиздат, 1961. 266 с.
- 2.3. Piermarini G. J., Block S. Ultrahigh pressure diamond-anvil cell and several semiconductor phase transition pressures in relation to the fixed point pressure scale // *Rev. Sci. Instrum.*, 1975, v. 46, No 8, p. 973–979.
- 2.4. McSkimin H. J., Andreatch P. Elastic moduli of silicon vs hydrostatic pressure at 25.0 °C and —195.8 °C // *J. Appl. Phys.*, 1964, v. 35, No 7, p. 2161–2165.
- 2.5. Temple P. A., Hathaway C. E. Multiphonon Raman spectrum of silicon // *Phys. Rev. B*, 1973, v. 7, No 8, p. 3685–3697.
- 2.6. Dolling G. Lattice vibrations in crystals with the diamond structure // *Proc. Symp. Inelastic Scattering Neutrons in Solids and Liquids*. Chalk River, 1962. IAEA, Vienna, 1963, v. 2, p. 37–48.
- 2.7. Asche M., Sarbei O. G. Electron-phonon interaction in *n*-Si // *Phys. Stat. Sol. (b)*, 1981, v. 103, No 1, p. 11–50.
- 2.8. Streitwolf H. W. Intervalley scattering selection rules for Si and Ge // *Phys. Stat. Sol.*, 1970, v. 37, No 1, p. K47–K49.
- 2.9. Hart T. R., Aggarwal R. L., Lax B. Temperature dependence of Raman scattering in silicon // *Phys. Rev. B*, 1970, v. 1, No 2, p. 638–642.
- 2.10. Weinstein B. A., Piermarini G. J. Raman scattering and phonon dispersion in Si and GaP at very high pressure // *Phys. Rev. B*, 1975, v. 12, No 4, p. 1172–1186.

- 2.11. Rao K. V., Smakula A. Dielectric anomalies in silicon single crystals // *J. Appl. Phys.*, 1966, v. 37, No 7, p. 2840—2842.
- 2.12. Vetter R. The pressure coefficient of the infra-red refractive index of silicon // *Phys. Stat. Sol. (a)*, 1971, v. 8, No 2, p. 443—447.
- 2.13. Lamb J., Redwood M., Shteinshleifer Z. Absorption of compressional waves in solids from 100 to 1000 Mc/sec // *Phys. Rev. Lett.*, 1959, v. 3, No 1, p. 28—29.
- 2.14. Lyon K. G., Salinger G. L., Swenson C. A., White G. K. Linear thermal expansion measurements on silicon from 6 to 340 K // *J. Appl. Phys.*, 1977, v. 48, No 3, p. 865—868.
- 2.15. Okada Y., Tokumaru Y. Precise determination of lattice parameter and thermal expansion coefficient of silicon between 300 and 1500 K // *J. Appl. Phys.*, 1984, v. 56, No 2, p. 314—320.
- 2.16. Sparks P. W., Swenson C. A. Thermal expansions from 2 to 40 K of Ge, Si, and four III—V compounds // *Phys. Rev.*, 1967, v. 163, No 3, p. 779—790.
- 2.17. Lautenschlager P., Garriga M., Viña L., Cardona M. Temperature dependence of the dielectric function and interband critical points in silicon // *Phys. Rev. B*, 1987, v. 36, No 9, p. 4821—4830.
- 2.18. Bludau W., Onton A., Heinke W. Temperature dependence of the band gap of silicon // *J. Appl. Phys.*, 1974, v. 45, No 4, p. 1846—1848.
- 2.19. Yu Z., Huang Y. X., Shen S. C. Spin-orbit splitting of the valence bands in silicon determined by means of high-resolution photoconductive spectroscopy // *Phys. Rev. B*, 1989, v. 39, No 9, p. 6287—6289.
- 2.20. Daunois A., Aspnès D. E. Electoreflectance and ellipsometry of silicon from 3 to 6 eV // *Phys. Rev. B*, 1978, v. 18, No 4, p. 1824—1839.
- 2.21. Welber B., Kim C. K., Cardona M., Rodriguez S. Dependence of the indirect energy gap of silicon on hydrostatic pressure // *Solid State Commun.*, 1975, v. 17, No 8, p. 1021—1024.
- 2.22. Schmidt E., Vedam K. Electoreflectance in GeSi alloys under hydrostatic pressure // *Solid State Commun.*, 1971, v. 9, No 13, p. 1187—1191.
- 2.23. Cardona M., Pollak F. H. Energy-band structure of germanium and silicon: The  $k \cdot p$  method // *Phys. Rev.*, 1966, v. 142, No 2, p. 530—543.
- 2.24. Hensei J. C., Hasegawa H., Nakayama M. Cyclotron resonance in uniaxially stressed silicon. II. Nature of the covalent bond // *Phys. Rev.*, 1965, v. 138, No 1A, p. 225—238.
- 2.25. Tekippe V. J., Chandrasekhar H. R., Fisher P., Ramdas A. K. Determination of the deformation-potential constant of the conduction band of silicon from the piezospectroscopy of donors // *Phys. Rev. B*, 1972, v. 6, No 6, p. 2348—2356.
- 2.26. Feher G. Electron spin resonance experiments on donors in silicon. I. Electronic structure of donors by the electron nuclear double resonance technique // *Phys. Rev.*, 1959, v. 114, No 5, p. 1219—1244.
- 2.27. Бобровников Ю. А., Казакова В. М., Фистуль В. И. Квантовый гармонический резонанс в кремнии // *ФТП*, 1988, т. 22, вып. 2, с. 301—306.
- 2.28. Leotin J., Poirier A., Carrere G., Askenazy S., Rössler U., Braun M. Quantum cyclotron resonance in silicon // *Int. J. of Infrared and Millimeter Waves*, 1983, v. 4, No 4, p. 575—589.
- 2.29. Chandrasekhar H. R., Fisher P., Ramdas A. K., Rodriguez S. Quantitative piezospectroscopy of the ground and excited states of acceptors in silicon // *Phys. Rev. B*, 1973, v. 8, No 8, p. 3836—3851.
- 2.30. Ohyama T., Yoshihara T., Murase K., Otsuka E. Observation of cyclotron resonance at the split-off valence band in silicon // *Phys. Lett.*, 1970, v. 33A, No 1, p. 55—56.
- 2.31. Wagner J. Photoluminescence and excitation spectroscopy in heavily doped *n*- and *p*-type silicon // *Phys. Rev. B*, 1984, v. 29, No 4, p. 2002—2009.
- 2.32. Balkanski M., Aziza A., Amzallag E. Infrared absorption in heavily doped *n*-type Si // *Phys. Stat. Sol.*, 1969, v. 31, No 1, p. 323—330.
- 2.33. Вольфсон А. А., Субашнев В. К. Край собственного поглощения кремния, сильно легированного донорными или акцепторными примесями // *ФТП*, 1967, т. 1, вып. 3, с. 397—404.
- 2.34. Schmid P. E. Optical absorption in heavily doped silicon // *Phys. Rev. B*, 1981, v. 23, No 10, p. 5531—5536.
- 2.35. Philipp H. R., Taft E. A. Optical constants of silicon in the region 1 to 10 eV // *Phys. Rev.*, 1960, v. 120, No 1, p. 37—38.
- 2.36. Edwards D. F., Ochoa E. Infrared refractive index of silicon // *Appl. Opt.*, 1980, v. 19, No 24, p. 4130—4131.
- 2.37. Hultén R. Optical constants of epitaxial silicon in the region 1—3.3 eV // *Physica Scr.*, 1975, v. 12, No 6, p. 342—344.
- 2.38. Geist J., Migdall A., Baltes H. P. Analytic representation of the silicon absorption coefficient in the indirect transition region // *Appl. Opt.*, 1988, v. 27, No 18, p. 3777—3779.

- 2.39. Weakliem H. A., Redfield D. Temperature dependence of the optical properties of silicon // *J. Appl. Phys.*, 1979, v. 50, No 3, p. 1491–1493.
- 2.40. Macfarlane G. G., McLean T. P., Quarrington J. E., Roberts V. Fine structure in the absorption-edge spectrum of Si // *Phys. Rev.*, 1958, v. 111, No 5, p. 1245–1254.
- 2.41. Johnson F. A. Lattice absorption bands in silicon // *Proc. Phys. Soc.*, 1959, v. 73, No 470, pt 2, p. 265–272.
- 2.42. Soref R. A., Bennett B. R. Electrooptical effects in silicon // *IEEE J. Quantum Electron.*, 1987, v. QE-23, No 1, p. 123–129.
- 2.43. Spitzer W., Fan H. Y. Infrared absorption in *n*-type silicon // *Phys. Rev.*, 1957, v. 108, No 2, p. 268–271.
- 2.44. Thewalt M. L. W., Rostworowski J. A. Biexcitons in Si // *Solid State Commun.*, 1978, v. 25, No 12, p. 991–993.
- 2.45. Kosai K., Gershenson M. New photoluminescence line-series spectra attributed to decay of multiexciton complexes bound to Li, B, and P centers in Si // *Phys. Rev. B*, 1974, v. 9, No 2, p. 723–736.
- 2.46. Hammond R. B., Silver R. N. Temperature dependence of the exciton lifetime in high-purity silicon // *Appl. Phys. Lett.*, 1980, v. 36, No 1, p. 68–71.
- 2.47. Gourley P. L., Wolfe J. P. Experimental determination of equilibrium constants for excitonic systems in stressed, ultrapure silicon // *Phys. Rev. B*, 1982, v. 25, No 10, p. 6338–6348.
- 2.48. Hunter A. T., Lyon S. A., Smith D. L., McGill T. C. Transient decay of satellite lines of bound excitons in Si:P // *Phys. Rev. B*, 1979, v. 20, No 6, p. 2431–2437.
- 2.49. Каминский А. С., Карасюк В. А., Покровский Я. Е. Многочастичные примесные комплексы в кремнии, легированном бором, фосфором и сурьмой // *ЖЭТФ*, 1978, т. 74, вып. 6, с. 2234–2243.
- 2.50. Elliott K. R., McGill T. C. Systematics of bound excitons and bound multiexciton complexes for shallow donors in silicon // *Solid State Commun.*, 1978, v. 28, No 7, p. 491–496.
- 2.51. Dean P. J., Haynes J. R., Flood W. F. New radiative recombination processes involving neutral donors and acceptors in silicon and germanium // *Phys. Rev.*, 1967, v. 161, No 3, p. 711–729.
- 2.52. Schmid W. Auger lifetimes for excitons bound to neutral donors and acceptors in Si // *Phys. Stat. Sol. (b)*, 1977, v. 84, No 2, p. 529–540.
- 2.53. Vonk M. A., Lightowers E. C. A high resolution investigation of the recombination radiation from Si containing the acceptors B, Al, Ga, In and Tl // *J. Luminesc.*, 1977, v. 15, No 4, p. 357–384.
- 2.54. Lyon S. A., Osbourn G. C., Smith D. L., McGill T. C. Bound exciton lifetimes for acceptors in Si // *Solid State Commun.*, 1977, v. 23, No 7, p. 425–428.
- 2.55. Lyon S. A., Smith D. L., McGill T. C. Edge luminescence spectra of acceptors in Si: Implications for multiexciton complexes // *Phys. Rev. B*, 1978, v. 17, No 6, p. 2620–2624.
- 2.56. Thewalt M. L. W., Watkins S. P., Ziemelis U. O., Lightowers E. C., Henry M. O. Photoluminescence lifetime, absorption and excitation spectroscopy measurements on isoelectronic bound excitons in beryllium-doped silicon // *Solid State Commun.*, 1982, v. 44, No 5, p. 573–577.
- 2.57. Тьюэлл М. Л. В. Связанные многоэкситонно-примесные комплексы // *Экситоны* / Под ред. Э. И. Рашба, М. Д. Стерджа. — Москва: Наука, 1985, с. 284–332.
- 2.57a. Shaklee K. L., Nahory R. E. Valley orbit splitting of free excitons? The absorption edge of Si // *Phys. Rev. Lett.*, 1970, v. 24, No 17, p. 942–945.
- 2.58. Grimsditch M., Cardona M. Absolute cross-section for Raman scattering by phonons in silicon // *Phys. Stat. Sol. (b)*, 1980, v. 102, No 1, p. 155–161.
- 2.59. Biegelsen D. K. Photoelastic tensor of silicon and the volume dependence of the average gap // *Phys. Rev. Lett.*, 1974, v. 32, No 21, p. 1196–1199.
- 2.60. Chandrasekhar M., Grimsditch M. H., Cardona M. Piezobirefringence above the fundamental edge in Si // *Phys. Rev. B*, 1978, v. 18, No 8, p. 4301–4311.
- 2.61. Long D., Myers J. Ionized-impurity scattering mobility of electrons in silicon // *Phys. Rev.*, 1959, v. 115, No 5, p. 1107–1118.
- 2.62. Morin F. J., Maita J. P. Electrical properties of silicon containing arsenic and boron // *Phys. Rev.*, 1954, v. 96, No 1, p. 28–35.
- 2.63. Fulkerson W., Moore J. P., Williams R. K., Graves R. S., McElroy D. L. Thermal conductivity, electrical resistivity, and Seebeck coefficient of silicon from 100 to 1300 K // *Phys. Rev.*, 1968, v. 167, No 3, p. 765–782.
- 2.64. Wasserrab Th. Die Temperaturabhängigkeit der elektronischen Kenngrößen des eigenleitenden Siliciums // *Z. Naturforsch.*, 1977, Bd 32a, S. 746–749.
- 2.65. VLSI Technology / Ed. by S. M. Sze. — New York: McGraw-Hill, 1983.



- Технология СБИС: В 2-х кн. Кн. 1/Под ред. С. Зи. — Москва: Мир, 1986. 404 с.
- 2.66. Jacoboni C., Canali C., Ottaviani G., Alberigi Quaranta A. A review of some charge transport properties of silicon // *Solid State Electron.*, 1977, v. 20, No 2, p. 77–89.
  - 2.67. Canali C., Jacoboni C., Nava F., Ottaviani G., Alberigi Quaranta A. Electron drift velocity in silicon // *Phys. Rev. B*, 1975, v. 12, No 6, p. 2265–2284.
  - 2.68. Ottaviani G., Reggiani L., Canali C., Nava F., Alberigi Quaranta A. Hole drift velocity in silicon // *Phys. Rev. B*, 1975, v. 12, No 8, p. 3318–3329.
  - 2.69. Smith P. M., Inoue M., Frey J. Electron velocity in Si and GaAs at very high electric fields // *Appl. Phys. Lett.*, 1980, v. 37, No 9, p. 797–798.
  - 2.70. Smith P. M., Frey J., Chatterjee P. High-field transport of holes in silicon // *Appl. Phys. Lett.*, 1981, v. 39, No 4, p. 332–333.
  - 2.71. Van Overstraeten R., de Man H. Measurement of the ionization rates in diffused silicon *p-n* junctions // *Solid State Electron.*, 1970, v. 13, No 5, p. 583–608.
  - 2.72. Ашмонтас С. П., Олекас А. П. Концентрационная зависимость феноменологического времени релаксации энергии электронов в *n-Si* // *ФТП*, 1980, т. 14, вып. 3, с. 546–549.
  - 2.73. Гинтилас Ш. З., Денис В. И., Мартунас З. И., Шеткус А. П. Температурная зависимость времени междолинной релаксации в электронном кремнии // *ФТП*, 1984, т. 18, вып. 2, с. 324–326.
  - 2.74. Borghesi A., Stella A., Bottazzi P., Guizzetti G., Reggiani L. Optical determination of Si conduction-band nonparabolicity // *J. Appl. Phys.*, 1990, v. 67, No 6, p. 3102–3106.
  - 2.75. Tufte O. N., Stelzer E. L. Piezoresistive properties of heavily doped *n*-type silicon // *Phys. Rev.*, 1964, v. 133, No 6A, p. 1705–1716.
  - 2.76. Matsuda K., Kanda Y., Suzuki K. Second-order piezoresistance coefficients of *n*-type silicon // *Jpn. J. Appl. Phys.*, 1989, v. 28, No 10, p. L1676–L1677.
  - 2.77. Курбатов Л. Н., Фромсой И. М., Шахиджанов С. С. Полный тензор пьезосопротивления *p*-кремния в широком интервале температур // *ФТП*, 1977, т. 11, вып. 5, с. 991–993.
  - 2.78. Paul W., Pearson G. L. Pressure dependence of the resistivity of silicon // *Phys. Rev.*, 1955, v. 98, No 6, p. 1755–1757.
  - 2.79. Brinson M. E., Dunstan W. Thermal conductivity and thermoelectric power of heavily doped *n*-type silicon // *J. Phys. C: Solid State Phys.*, 1970, v. 3, No 3, p. 483–491.
  - 2.80. Geballe T. H., Hull G. W. Seebeck effect in silicon // *Phys. Rev.*, 1955, v. 98, No 4, p. 940–947.
  - 2.81. Sasaki W., Kinoshita J. Piezoresistance and magnetic susceptibility in heavily doped *n*-type silicon // *J. Phys. Soc. Jpn.*, 1968, v. 25, No 6, p. 1622–1629.
  - 2.82. Kirnas I. G., Kurilo P. M., Litovchenko P. G., Lutsyak V. S., Nitsovich V. M. Concentration dependence of the Hall factor in *n*-type silicon // *Phys. Stat. Sol. (a)*, 1974, v. 23, No 2, p. K123–K127.
  - 2.83. Szmulowicz F. Acoustic and optical-phonon-limited mobilities in *p*-type silicon within the deformation-potential theory // *Appl. Phys. Lett.*, 1983, v. 43, No 5, p. 485–487.
  - 2.84. Krag W. E. Galvanomagnetic effects in *n*-type silicon // *Phys. Rev.*, 1960, v. 118, No 2, p. 435–450.
  - 2.85. Long D. Galvanomagnetic effects in *p*-type silicon // *Phys. Rev.*, 1957, v. 107, No 3, p. 672–677.
  - 2.86. Jagannath C., Grabowski Z. W., Ramdas A. K. Linewidths of the electronic excitation spectra of donors in silicon // *Phys. Rev. B*, 1981, v. 23, No 5, p. 2082–2098.
  - 2.87. Baron R., Young M. H., Neeland J. K., Marsh O. J. A new acceptor level in indium-doped silicon // *Appl. Phys. Lett.*, 1977, v. 30, No 11, p. 594–596.
  - 2.88. Picus G., Burstein E., Hennis B. Absorption spectra of impurities in silicon — II. Group-V donors // *J. Phys. Chem. Solids*, 1956, v. 1, Nos 1/2, p. 75–81.
  - 2.89. Sclar N. Extrinsic silicon detectors for 3–5 and 8–14  $\mu\text{m}$  // *Infrared Phys.*, 1976, v. 16, No 4, p. 435–448.
  - 2.90. Olajos J., Nielsen B. B., Kleverman M., Omling P., Emanuelsson P., Grimmer H. G. Line spectrum of the interstitial iron donor in silicon // *Appl. Phys. Lett.*, 1988, v. 53, No 25, p. 2507–2509.
  - 2.91. Ho L. T., Ramdas A. K. Excitation spectra and piezospectroscopic effects of magnesium donors in silicon // *Phys. Rev. B*, 1972, v. 5, No 2, p. 462–474.
  - 2.92. Aggarwal R. L., Ramdas A. K. Effect of uniaxial stress on the excitation spectra of donors in silicon // *Phys. Rev.*, 1965, v. 137, No 2A, p. 602–612.
  - 2.93. Grimmer H. G., Janzén E., Ennen H., Schirmer O., Schneider J., Wörner R., Holm C., Sirtl E., Wagner P. Tellurium donors in silicon // *Phys. Rev. B*, 1981, v. 24, No 8, p. 4571–4586.

- 2.94. Ning T. H., Sah C. T. Photoionization cross sections of a two-electron donor center in silicon // *Phys. Rev. B*, 1976, v. 14, No 6, p. 2528–2533.
- 2.95. Rosier L. L., Sah C. T. Photoionization of electrons at sulfur centers in silicon // *J. Appl. Phys.*, 1971, v. 42, No 10, p. 4000–4005.
- 2.96. Grimmeiss H. G., Skarstam B. Excited states at deep centers in Si:S and Si:Se // *Phys. Rev. B*, 1981, v. 23, No 4, p. 1947–1960.
- 2.97. Janzén E., Stedman R., Grossmann G., Grimmeiss H. G. High-resolution studies of sulfur- and selenium-related donor centers in silicon // *Phys. Rev. B*, 1984, v. 29, No 4, p. 1907–1918.
- 2.98. Burstein E., Picus G., Hennis B., Wallis R. Absorption spectra of impurities in silicon — I. Group-III acceptors // *J. Phys. Chem. Solids*, 1956, v. 1, Nos 1/2, p. 65–74.
- 2.99. Anderson W. W. Shallow impurity states in semiconductors: Absorption cross-sections, excitation rates, and capture cross-sections // *Solid State Electron.*, 1975, v. 18, No 3, p. 235–245.
- 2.100. Migliorato P., Elliott C. T., Vere A. W. Photo-excitation of electrons from ionized silver acceptors in silicon // *Solid State Commun.*, 1977, v. 24, No 1, p. 117–119.
- 2.101. Sclar N. Survey of dopants in silicon for 2–2.7 and 3–5  $\mu\text{m}$  infrared detector application // *Infrared Phys.*, 1977, v. 17, No 1, p. 71–82.
- 2.102. Зубиц Ю. А., Парицкий Л. Г., Рывкин С. М., Дохолян Ж. Г. Фотоэлектрические свойства кремния с примесями меди, вольфрама и платины // *ФТТ*, 1966, т. 8, вып. 9, с. 2549–2557.
- 2.103. Onton A., Fisher P., Ramdas A. K. Spectroscopic investigation of group-III acceptor states in silicon // *Phys. Rev.*, 1967, v. 163, No 3, p. 686–703.
- 2.104. Messenger R. A., Blakemore J. S. The photo-ionization cross-section of indium acceptors in silicon // *Solid State Commun.*, 1971, v. 9, No 5, p. 319–322.
- 2.105. Scott W., Schmit J. L. Infrared excitation spectrum of thallium-doped silicon // *Appl. Phys. Lett.*, 1978, v. 33, No 4, p. 294–295.
- 2.106. Herman J. M., Sah C. T. Photoionization cross sections of holes at zinc centers in silicon // *J. Appl. Phys.*, 1973, v. 44, No 3, p. 1259–1262.
- 2.107. Weman H., Henry A., Begum T., Monemar B., Awadelkarim O. O., Lindström J. L. Electrical and optical properties of gold-doped *n*-type silicon // *J. Appl. Phys.*, 1989, v. 65, No 1, p. 137–145.
- 2.108. Parker W. C., Forbes L. Experimental characterization of gold-doped infrared-sensing MOSFET's // *IEEE Trans. Electron Devices*, 1975, v. ED-22, No 10, p. 916–924.
- 2.109. Bever T., Emanuelsson P., Kleverman M., Grimmeiss H. G. Identification of hole transitions at the neutral interstitial manganese center in silicon // *Appl. Phys. Lett.*, 1989, v. 55, No 24, p. 2541–2543.
- 2.110. Mayo S., Lowney J. R. Photoionization cross-section studies of the platinum-donor center in silicon // *J. Appl. Phys.*, 1987, v. 61, No 7, p. 2626–2632.
- 2.111. Braun S., Grimmeiss H. G., Spann K. Photoionization cross sections in platinum-doped silicon // *J. Appl. Phys.*, 1977, v. 48, No 9, p. 3883–3887.
- 2.112. Печин Н. А., Журкин Б. Г., Волков Б. А. Влияние концентрации доноров и акцепторов на электропроводность сильно легированного кремния *n*-типа // *ФТТ*, 1965, т. 7, вып. 11, с. 3188–3193.
- 2.113. Swartz G. A. Low-temperature Hall coefficient and conductivity in heavily doped silicon // *J. Phys. Chem. Solids*, 1960, v. 12, Nos 3/4, p. 245–259.
- 2.114. Wu R. H., Peaker A. R. Capture cross sections of the gold donor and acceptor states in *n*-type Czochralski silicon // *Solid State Electron.*, 1982, v. 25, No 7, p. 643–649.
- 2.115. Kunio T., Yamazaki T., Ohta E., Sakata M. Defect levels in chromium-doped silicon // *Solid State Electron.*, 1983, v. 26, No 2, p. 155–160.
- 2.116. Brotherton S. D., Ayres J. R., Gill A., van Kesteren H. W., Greidanus F. J. A. M. Deep levels of copper in silicon // *J. Appl. Phys.*, 1987, v. 62, No 5, p. 1826–1832.
- 2.117. Eywaraye A. O. The defect levels in *p*-type silicon doped with manganese // *J. Appl. Phys.*, 1977, v. 48, No 9, p. 3813–3818.
- 2.118. Абдурахманов К. П., Лебедев А. А., Крейсль Й., Утамурадова Ш. Б. Глубокие уровни в кремнии, связанные с марганцем // *ФТП*, 1985, т. 19, вып. 2, с. 213–216.
- 2.119. Rohatgi A., Hopkins R. H., Davis J. R., Campbell R. B., Mollenkopf H. C. The impact of molybdenum on silicon and silicon solar cell performance // *Solid State Electron.*, 1980, v. 23, No 11, p. 1185–1190.
- 2.120. Kitagawa H., Nakashima H. Nickel-related donor level in silicon // *Phys. Stat. Sol. (a)*, 1987, v. 102, No 1, p. K23–K27.

- 2.121. Brotherton S. D., Bradley P., Bicknell J. Electrical properties of platinum in silicon // J. Appl. Phys., 1979, v. 50, No 5, p. 3396–3403.
- 2.122. Thurber W. R., Lowney J. R. Methods for accurate determination of emission rate and trap concentration with application to platinum-doped silicon // J. Appl. Phys., 1987, v. 62, No 2, p. 534–540.
- 2.123. Grimmeiss H. G., Janzén E., Skarstam B. Deep sulfur-related centers in silicon // J. Appl. Phys., 1980, v. 51, No 8, p. 4212–4217.
- 2.124. Grimmeiss H. G., Janzén E., Skarstam B. Electronic properties of selenium-doped silicon // J. Appl. Phys., 1980, v. 51, No 7, p. 3740–3745.
- 2.125. Chen J.-W., Milnes A. G., Rohatgi A. Titanium in silicon as a deep level impurity // Solid State Electron., 1979, v. 22, No 9, p. 801–808.
- 2.126. Brotherton S. D., Gill A. The energy level of thallium in silicon // Appl. Phys. Lett., 1978, v. 33, No 11, p. 953–955.
- 2.127. Fujisaki Y., Ando T., Kozuka H., Takano Y. Characterization of tungsten-related deep levels in bulk silicon crystal // J. Appl. Phys., 1988, v. 63, No 7, p. 2304–2306.
- 2.128. Asche M., Kostial H., Sarbey O. G. Ionization of low donor levels and recombination of hot electrons in *n*-Si at low temperatures // Phys. Stat. Sol. (b), 1979, v. 91, No 2, p. 521–530.
- 2.129. Dargys A., Žurauskas S. Observation of the transition from impact-ionization-dominated to field-ionization-dominated impurity breakdown in silicon // Solid State Commun., 1984, v. 52, No 2, p. 139–142.

## GaAs

- 3.1. Von Piesbergen U. Die durchschnittlichen Atomwärmen der  $A^{III}B^V$  – Halbleiter AlSb, GaSb, GaP, InP, InAs, InSb und die Atomwärme des Elements Germanium zwischen 12 und 273 K // Z. Naturforsch., 1963, Bd 18a, H. 2, S. 141–147.
- 3.2. Sajovec F., Wolf R., Fattah A., Bickmann K., Wenzl H., Nagel G., Rüfer H., Tomzig E., De Bièvre P. Defect analysis on GaAs crystals by precision measurements of density and lattice parameter // Phys. Stat. Sol. (a), 1990, v. 122, No 1, p. 139–152.
- 3.3. Richman D. Dissociation pressures of GaAs, GaP and InP and the nature of III–V melts // J. Phys. Chem. Solids, 1963, v. 24, No 9, p. 1131–1139.
- 3.4. Baublitz M., Ruoff A. L. Diffraction studies of the high pressure phases of GaAs and GaP // J. Appl. Phys., 1982, v. 53, No 9, p. 6179–6185.
- 3.5. Cottam R. I., Saunders G. A. The elastic constants of GaAs from 2 K to 320 K // J. Phys. C: Solid State Phys., 1973, v. 6, No 13, p. 2105–2118.
- 3.6. McSkimin H. J., Jayaraman A., Andreatch P. Elastic moduli of GaAs at moderate pressures and the evaluation of compression to 250 kbar // J. Appl. Phys., 1967, v. 38, No 5, p. 2362–2364.
- 3.7. Waugh J. L. T., Dolling G. Crystal dynamics of gallium arsenide // Phys. Rev., 1963, v. 132, No 6, p. 2410–2412.
- 3.8. Von der Linde D., Kuhl J., Klingenberg H. Raman scattering from nonequilibrium LO phonons with picosecond resolution // Phys. Rev. Lett., 1980, v. 44, No 23, p. 1505–1508.
- 3.9. Mooradian A., Wright G. B. First order Raman effect in III–V compounds // Solid State Commun., 1966, v. 4, No 9, p. 431–434.
- 3.10. Soma T., Satoh J., Matsuo H. Thermal expansion coefficient of GaAs and InP // Solid State Commun., 1982, v. 42, No 12, p. 889–892.
- 3.11. Seeger K. Temperature dependence of the dielectric constants of semi-insulating III–V compounds // Appl. Phys. Lett., 1989, v. 54, No 13, p. 1268–1269.
- 3.12. Samara G. A. Temperature and pressure dependences of the dielectric constants of semiconductors // Phys. Rev. B, 1983, v. 27, No 6, p. 3494–3505.
- 3.13. Иванов С. Н., Котелянский И. М., Мансфельд Г. Д., Хазанов Е. Н. Поглощение ультразвуковых волн в кристаллах арсенида галлия и антимонида индия // ФТТ, 1971, т. 13, вып. 2, с. 620–623.
- 3.14. Cottam R. I., Saunders G. A. Ultrasonic attenuation in GaAs from 2 K to 300 K // J. Phys. C: Solid State Phys., 1974, v. 7, No 14, p. 2447–2456.
- 3.15. Blakemore J. S. Semiconducting and other major properties of gallium arsenide // J. Appl. Phys., 1982, v. 53, No 10, p. R123–R181.
- 3.16. Cetas T. C., Tilford C. R., Swenson C. A. Specific heats of Cu, GaAs, GaSb, InAs, and InSb from 1 to 30 K // Phys. Rev., 1968, v. 174, No 3, p. 835–844.

- 3.17. Lichter B. D., Sommelet P. Thermal properties of  $A^{III}B^V$  compounds: II. High-temperature heat contents and heats of fusion of InAs and GaAs // Trans. Metal. Soc. AIME, 1969, v. 245, p. 1021–1027.
- 3.18. Carlson R. O., Slack G. A., Silverman S. J. Thermal conductivity of GaAs and  $GaAs_{1-x}P_x$  laser semiconductors // J. Appl. Phys., 1965, v. 36, No 2, p. 505–507.
- 3.19. Новикова С. И. Исследование теплового расширения GaAs и ZnSe // ФТТ, 1961, т. 3, вып. 1, с. 178–179.
- 3.20. Feder R., Light T. Precision thermal expansion measurements of semi-insulating GaAs // J. Appl. Phys., 1968, v. 39, No 10, p. 4870–4871.
- 3.21. Lautenschlager P., Garriga M., Logothetidis S., Cardona M. Interband critical points of GaAs and their temperature dependence // Phys. Rev. B, 1987, v. 35, No 17, p. 9174–9189.
- 3.22. Drouhin H.-J., Hermann C., Lampel G. Photoemission from activated arsenide. I. Very-high-resolution energy distribution curves // Phys. Rev. B, 1985, v. 31, No 6, p. 3859–3871.
- 3.23. Aspnes D. E. GaAs lower conduction-band minima: Ordering and properties // Phys. Rev. B, 1976, v. 14, No 12, p. 5331–5343.
- 3.24. Williams E. W., Rehn V. Electroreflectance studies of InAs, GaAs, and (Ga, In)As alloys // Phys. Rev., 1968, v. 172, No 3, p. 798–810.
- 3.25. Goñi A. R., Strössner K., Syassen K., Cardona M. Pressure dependence of direct and indirect optical absorption in GaAs // Phys. Rev. B, 1987, v. 36, No 3, p. 1581–1587.
- 3.26. Goñi A. R., Cantarero A., Syassen K., Cardona M. Effect of pressure on the low-temperature exciton absorption in GaAs // Phys. Rev. B, 1990, v. 41, No 14, p. 10111–10119.
- 3.27. Wolford D. J., Bradley J. A. Pressure dependence of shallow bound states in gallium arsenide // Solid State Commun., 1985, v. 53, No 12, p. 1069–1076.
- 3.28. Mirlin D. N., Sapega V. F., Karlik I. Ya., Katilius R. Hot photoluminescence spectroscopy investigations of  $L$ -valley splitting and intervalley scattering in uniaxially stressed gallium arsenide // Solid State Commun., 1987, v. 61, No 12, p. 799–802.
- 3.29. Bendorius R., Shileika A. Electroreflectance spectra of GaAs at hydrostatic pressure // Solid State Commun., 1970, v. 8, No 14, p. 1111–1113.
- 3.30. Stradling R. A., Wood R. A. The temperature dependence of the band-edge effective masses of InSb, InAs and GaAs as deduced from magnetophonon magnetoresistance measurements // J. Phys. C: Solid State Phys., 1970, v. 3, No 5, p. L94–L99.
- 3.31. Stillman G. E., Wolfe C. M., Dimmock J. O. Magnetospectroscopy of shallow donors in GaAs // Solid State Commun., 1969, v. 7, No 13, p. 921–925.
- 3.32. Brennan K., Hess K. High field transport in GaAs, InP and InAs // Solid State Electron., 1984, v. 27, No 4, p. 347–357.
- 3.33. Weisbuch C., Hermann C. Optical detection of conduction-electron spin resonance in GaAs,  $Ga_{1-x}In_xAs$  and  $Ga_{1-x}Al_xAs$  // Phys. Rev. B, 1977, v. 15, No 2, p. 816–822.
- 3.34. Skolnick M. S., Jain A. K., Stradling R. A., Leotin J., Ousset J. C., Askenazy S. An investigation of the anisotropy of the valence band of GaAs by cyclotron resonance // J. Phys. C: Solid State Phys., 1976, v. 9, No 14, p. 2809–2821.
- 3.35. Hess K., Bimberg D., Lipari N. O., Fischbach J. U., Altarelli M. Band parameter determination of III–V compounds from high-field magnetoreflectance of excitons // Proc. 13th Int. Conf. on Physics of Semiconductors / Ed. by F. G. Fumi. Rome, 1976, p. 142–145.
- 3.36. Chandrasekhar M., Pollak F. H. Effects of uniaxial stress on the electroreflectance spectrum of Ge and GaAs // Phys. Rev. B, 1977, v. 15, No 4, p. 2127–2144.
- 3.37. Aspnes D. E., Studna A. A. Schottky-barrier electroreflectance: Application to GaAs // Phys. Rev. B, 1973, v. 7, No 10, p. 4605–4625.
- 3.38. Reine M., Aggarwal R. L., Lax B. Split-off valence-band parameters for GaAs from stress-modulated magnetoreflexivity // Phys. Rev. B, 1970, v. 2, No 2, p. 458–463.
- 3.39. Olego D., Cardona M. Photoluminescence in heavily doped GaAs. I. Temperature and hole-concentration dependence // Phys. Rev. B, 1980, v. 22, No 2, p. 886–893.
- 3.40. Haufe A., Schwabe R., Fieseler H., Ilegems M. The luminescence lineshape of highly doped direct-gap III–V compounds // J. Phys. C: Solid State Phys., 1988, v. 21, No 15, p. 2951–2968.
- 3.41. Borghs G., Bhattacharyya K., Deneffe K., Van Mieghem P., Mertens R. Band-gap narrowing in highly doped  $n$ - and  $p$ -type GaAs studied by photoluminescence spectroscopy // J. Appl. Phys., 1989, v. 66, No 9, p. 4381–4386.
- 3.42. Jiang De-Sheng, Makita Y., Ploog K., Queisser H. J. Electrical properties and photoluminescence of Te-doped GaAs grown by molecular beam epitaxy // J. Appl. Phys., 1982, v. 53, No 2, p. 999–1006.

- 3.43. Casey H. C. Concentration-dependent absorption and spontaneous emission of heavily doped GaAs // *J. Appl. Phys.*, 1976, v. 47, No 2, p. 631–643.
- 3.44. Yao H., Compaan A. Plasmons, photoluminescence, and band-gap narrowing in very heavily doped *n*-GaAs // *Appl. Phys. Lett.*, 1990, v. 57, No 2, p. 147–149.
- 3.45. Sturge M. D. Optical absorption of gallium arsenide between 0.6 and 2.75 eV // *Phys. Rev.*, 1962, v. 127, No 3, p. 768–773.
- 3.46. Campi D., Papuzza C. Refractive index dispersion in group IV and binary III–V semiconductors: Comparison of calculated and experimental values // *J. Appl. Phys.*, 1985, v. 57, No 4, p. 1305–1310.
- 3.47. Casey H. C., Sell D. D., Wecht K. W. Concentration dependence of the absorption coefficient for *n*- and *p*-type GaAs between 1.3 and 1.6 eV // *J. Appl. Phys.*, 1975, v. 46, No 1, p. 250–257.
- 3.48. Holm R. T., Gibson J. W., Palik E. D. Infrared reflectance studies of bulk and epitaxial-film *n*-type GaAs // *J. Appl. Phys.*, 1977, v. 48, No 1, p. 212–223.
- 3.49. Cochran W., Fray S. J., Johnson F. A., Quarrington J. E., Williams N. Lattice absorption in gallium arsenide // *J. Appl. Phys.*, 1961, suppl. to v. 32, No 10, p. 2102–2106.
- 3.50. Spitzer W. G., Whelan J. M. Infrared absorption and electron effective mass in *n*-type gallium arsenide // *Phys. Rev.*, 1959, v. 114, No 1, p. 59–63.
- 3.51. Osamura K., Murakami Y. Free carrier absorption in *n*-GaAs // *Jpn. J. Appl. Phys.*, 1972, v. 11, No 3, p. 365–371.
- 3.52. Braunstein R. Intervalence band transitions in gallium arsenide // *J. Phys. Chem. Solids*, 1959, v. 8, p. 280–282.
- 3.53. Henry C. H., Logan R. A., Merritt F. R., Luongo J. P. The effect of intervalence band absorption on the thermal behavior of InGaAsP lasers // *IEEE J. Quantum Electron.*, 1983, v. QE-19, No 6, p. 947–952.
- 3.54. Takeshima M. Green's-function formalism of electronic states in heavily doped semiconductors and its application to a problem of inter-valence-band absorption // *Phys. Rev. B*, 1985, v. 32, No 12, p. 8066–8070.
- 3.55. Nam S. B., Reynolds D. C., Litton C. W., Almasy R. J., Collins T. C., Wolfe C. M. Free-exciton energy spectrum in GaAs // *Phys. Rev. B*, 1976, v. 13, No 2, p. 761–766.
- 3.56. 't Hooft G. W., van der Poel W. A. J. A., Molenkamp J. W., Foxon C. T. Giant oscillator strength of free excitons in GaAs // *Phys. Rev. B*, 1987, v. 35, No 15, p. 8281–8284.
- 3.57. Reynolds D. C., Bajaj K. K., Litton C. W. Study of shallow impurity states in compound semiconductors using high resolution photoluminescence spectroscopy // *Solid State Commun.*, 1985, v. 53, No 12, p. 1061–1067.
- 3.58. Bludau W., Wagner E. Impact ionization of excitons in GaAs // *Phys. Rev. B*, 1976, v. 13, No 12, p. 5410–5414.
- 3.59. Hwang C. J. Lifetimes of free and bound excitons in high-purity GaAs // *Phys. Rev. B*, 1973, v. 8, No 2, p. 646–652.
- 3.60. Schairer W., Bimberg D., Kottler W., Cho K., Schmidt M. Piezospectroscopic and magneto-optical study of the Sn-acceptor in GaAs // *Phys. Rev. B*, 1976, v. 13, No 8, p. 3452–3467.
- 3.61. Ashen D. J., Dean P. J., Hurler D. T. J., Mullin J. B., White A. M. The incorporation and characterisation of acceptors in epitaxial GaAs // *J. Phys. Chem. Solids*, 1975, v. 36, No 10, p. 1041–1053.
- 3.62. Montelius L., Nilsson S., Samuelson L. Hole ionization of Mn-doped GaAs: Photoluminescence versus space-charge techniques // *Phys. Rev. B*, 1989, v. 40, No 8, p. 5598–5601.
- 3.63. Bois D., Beaudet D. Photoluminescence study of the shallow acceptor states in *n*-type GaAs // *J. Appl. Phys.*, 1975, v. 46, No 9, p. 3882–3884.
- 3.64. Mendez E. E., Heiblum M., Fisher R., Klem J., Thorne R. E., Morkoç H. Photoluminescence study of the incorporation of silicon in GaAs grown by molecular beam epitaxy // *J. Appl. Phys.*, 1983, v. 54, No 7, p. 4202–4204.
- 3.65. Dixon R. W. Photoelastic properties of selected materials and their relevance for applications to acoustic light modulators and scanners // *J. Appl. Phys.*, 1967, v. 38, No 13, p. 5149–5153.
- 3.66. Yariv A., Yeh P. *Optical Waves in Crystals*. — New York: John Wiley, 1984.  
Ярив А., Юх П. *Оптические волны в кристаллах*. — Москва: Мир, 1987. 616 с.
- 3.67. Sugie M., Tada K. Measurements of the linear electrooptic coefficients and analysis of the nonlinear susceptibilities in cubic GaAs and hexagonal CdS // *Jpn. J. Appl. Phys.*, 1976, v. 15, No 3, p. 421–431.
- 3.68. McFee J. H., Boyd G. D., Schmidt P. H. Redetermination of the nonlinear optical coefficients of Te and GaAs by comparison with Ag<sub>3</sub>SbS<sub>3</sub> // *Appl. Phys. Lett.*, 1970, v. 17, No 2, p. 57–59.

- 3.69. Mayer A., Keilmann F. Far-infrared nonlinear optics. I.  $\chi^{(2)}$  near ionic resonance // *Phys. Rev. B*, 1986, v. 33, No 10, p. 6954–6961.
- 3.70. Stillman G. E., Wolfe C. M., Dimmock J. O. Hall coefficient factor for polar mode scattering in *n*-type GaAs // *J. Phys. Chem. Solids*, 1970, v. 31, No 6, p. 1199–1204.
- 3.71. Nichols K. H., Yee C. M. L., Wolfe C. M. High-temperature carrier transport in *n*-type epitaxial GaAs // *Solid State Electron.*, 1980, v. 23, No 2, p. 109–116.
- 3.72. Hill D. E. Activation energy of holes in Zn-doped GaAs // *J. Appl. Phys.*, 1970, v. 41, No 4, p. 1815–1818.
- 3.73. Blakemore J. S. Intrinsic density  $n_i(T)$  in GaAs: Deduced from band gap and effective mass parameters and derived independently from Cr acceptor capture and emission coefficients // *J. Appl. Phys.*, 1982, v. 53, No 1, p. 520–531.
- 3.74. Anderson D. A., Apsley N. The Hall effect in III–V semiconductor assessment // *Semicond. Sci. Technol.*, 1986, v. 1, No 3, p. 187–202.
- 3.75. Poth H., Bruch H., Heyen M., Balk P. Electron mobility in vapor-grown GaAs films // *J. Appl. Phys.*, 1978, v. 49, No 1, p. 285–288.
- 3.76. Kuphal E., Schlachetzki A., Pöcker A. Incorporation of Sn into epitaxial GaAs grown from the liquid phase // *Appl. Phys.*, 1978, v. 17, No 1, p. 63–72.
- 3.77. Wiley J. Y. D. Mobility of holes in III–V compounds // *Semiconductors and Semimetals* / Ed. by R. K. Willardson, A. C. Beer. — New York: Academic Press, 1975, v. 10, p. 91–174.
- 3.78. Ruch J. G., Kino G. S. Transport properties of GaAs // *Phys. Rev.*, 1968, v. 174, No 3, p. 921–931.
- 3.79. Chang C. S., Fetterman H. R. Electron drift velocity versus electric field in GaAs // *Solid State Electron.*, 1986, v. 29, No 12, p. 1295–1296.
- 3.80. Hill G., Robson P. N. Electron drift velocity in GaAs using a variable frequency microwave time-of-flight technique // *Solid State Electron.*, 1982, v. 25, No 7, p. 589–597.
- 3.81. Dalal V. L., Dreeben A. B., Triano A. Temperature dependence of hole velocity in *p*-GaAs // *J. Appl. Phys.*, 1971, v. 42, No 7, p. 2864–2867.
- 3.82. Bulman G. E., Robbins V. M., Brennan K. F., Hess K., Stillman G. E. Experimental determination of impact ionization coefficients in (100) GaAs // *IEEE Electron Device Lett.*, 1983, v. EDL-4, No 6, p. 181–185.
- 3.83. Philipp A., Kuchar F., Seeger K. Submillimeter conductivity of thermal and warm electrons in GaAs and InP // *Phys. Stat. Sol. (b)*, 1977, v. 79, No 1, p. 115–124.
- 3.84. Glover G. H. Study of electron energy relaxation times in GaAs and InP // *J. Appl. Phys.*, 1973, v. 44, No 3, p. 1295–1301.
- 3.85. Ulbrich R. G., Kash J. A., Tsang J. C. Hot-electron recombination at neutral acceptors in GaAs: A cw probe of femtosecond intervalley scattering // *Phys. Rev. Lett.*, 1989, v. 62, No 8, p. 949–952.
- 3.86. Mickevičius R., Reklaitis A. Electron intervalley scattering in gallium arsenide // *Semicond. Sci. Technol.*, 1990, v. 5, No 8, p. 805–812.
- 3.87. Arlt G., Quadflieg P. Piezoelectricity in III–V compounds with a phenomenological analysis of the piezoelectric effect // *Phys. Stat. Sol.*, 1968, v. 25, No 1, p. 323–330.
- 3.88. Sagar A. Piezoresistance in *n*-type GaAs // *Phys. Rev.*, 1958, v. 112, No 5, p. 1533.
- 3.89. Козеев Е. В., Кравченко А. Ф. Исследование пьезосопротивления в арсениде галлия дырочной проводимости // *ФТП*, 1978, т. 12, вып. 6, с. 1041–1046.
- 3.90. Pitt G. D. Developments in high pressure physics // *Contemp. Phys.*, 1977, v. 18, No 2, p. 137–164.
- 3.91. Leroux M., Pelous G., Raymond F., Verie C. Minority-carrier lifetime study of the pressure induced  $\Gamma$ - $X$  crossover in GaAs // *Appl. Phys. Lett.*, 1985, v. 46, No 3, p. 288–290.
- 3.92. Арсенид галлия. Получение, свойства и применение / Под ред. Ф. П. Кесаманлы и Д. Н. Наследова. — Москва: Наука, 1973. 471 с.
- 3.93. Pöddör B. Magnetoresistance and electron scattering mechanisms in gallium arsenide // *Acta Phys. Hung.*, 1983, v. 54, Nos 1–2, p. 125–137.
- 3.94. Борисова Л. А., Кравченко А. Ф., Кот К. Н., Скок Э. М. Холл-фактор в арсениде галлия // *ФТП*, 1972, т. 6, вып. 5, с. 799–801.
- 3.95. Rode D. L. Theory of electron galvanomagnetism in crystals: Hall effect in semiconductors and semimetals // *Phys. Stat. Sol. (b)*, 1973, v. 55, No 2, p. 687–696.
- 3.96. Шишияну Ф. С., Болтакс Б. И. Об энергетических уровнях Ag и Au в GaAs // *ФТП*, 1966, т. 8, вып. 4, с. 1312–1314.
- 3.97. Blätte M., Schairer W., Willmann F. Photoluminescence of Ag-doped *p*-type GaAs // *Solid State Commun.*, 1970, v. 8, No 16, p. 1265–1268.
- 3.98. Cooke R. A., Hoult R. A., Kirkman R. F., Stradling R. A. The characterisation of the donors in GaAs epitaxial films by far-infrared photoconductive techniques // *J. Phys. D: Appl. Phys.*, 1978, v. 11, No 6, p. 945–953.

- 3.99. Kisker D. W., Tews H., Rehm W. Luminescence study of C, Zn, Si, and Ge acceptors in GaAs // *J. Appl. Phys.*, 1983, v. 54, No 3, p. 1332–1336.
- 3.100. Haisty R. W., Cronin G. R. A comparison of doping effects of transition elements in gallium arsenide // *Proc. 7th Intern. Conf. Phys. Semiconductors*. Dunod, Paris, 1964, p. 1161–1167.
- 3.101. Rosi F. D., Meyerhofer D., Jensen R. V. Properties of *p*-type GaAs prepared by copper diffusion // *J. Appl. Phys.*, 1960, v. 31, No 6, p. 1105–1108.
- 3.102. Baxter R. D., Reid F. J. Heat treatment of GaAs containing copper // *J. Electrochem. Soc.*, 1963, v. 110, No 8, p. 187C.
- 3.103. Kirkman R. F., Stradling R. A., Lin-Chung P. J. An infrared study of the shallow acceptor states in GaAs // *J. Phys. C: Solid State Phys.*, 1978, v. 11, No 2, p. 419–433.
- 3.104. Hegems M., Dingle R. Acceptor incorporation in GaAs grown by beam epitaxy // *Gallium Arsenide and Related Compounds, 1974 Symp. Proc.*, Inst. Phys., London, 1975, p. 1–9.
- 3.105. Schairer W., Schmidt M. Strongly quenched deformation potentials of the Mn acceptor in GaAs // *Phys. Rev. B*, 1974, v. 10, No 6, p. 2501–2506.
- 3.106. Haisty R. W., Mehal E. W., Stratton R. Preparation and characterization of high resistivity GaAs // *J. Phys. Chem. Solids*, 1962, v. 23, No 7, p. 829–836.
- 3.107. Fetterman H. R., Waldman J., Wolfe C. M., Stillman G. E., Parker C. D. Identification of donor species in high-purity GaAs using optically pumped submillimeter lasers // *Appl. Phys. Lett.*, 1972, v. 21, No 9, p. 434–436.
- 3.108. Brandt C. D., Hennel A. M., Bryskiewicz T., Ko K. Y., Pawlosicz L. M., Gatos H. C. Electronic and optical properties of Ti-doped GaAs and InP; semi-insulating InP // *J. Appl. Phys.*, 1989, v. 65, No 9, p. 3459–3469.
- 3.109. Summers C. J., Dingle R., Hill D. E. Far-infrared donor absorption and photoconductivity in epitaxial *n*-type GaAs // *Phys. Rev. B*, 1970, v. 1, No 4, p. 1603–1606.
- 3.110. Stillman G. E., Wolfe C. M., Dimmock J. O. Far-infrared photoconductivity in high purity GaAs // *Semiconductors and Semimetals* / Ed. by R. K. Willardson, A. C. Beer. — New York: Academic Press, 1977, v. 12, p. 169–290.
- 3.111. Kundrotas J., Čėsna A., Dargys A. Impurity impact ionization and electron recombination rates in *n*-GaAs // *Liet. Fiz. Rink.*, 1991, v. 31, No 5, p. 485–487. [*Lithuanian J. Phys.*, 1991, v. 31, No 5, p. 282–283.]
- 3.112. Said M., Kanehisa M. A. Excited acceptor states in II–VI and III–V semiconductors // *Phys. Stat. Sol. (b)*, 1990, v. 157, No 1, p. 311–321.
- 3.113. Ermanis F., Wolfstirn K. Hall effect and resistivity of Zn-doped GaAs // *J. Appl. Phys.*, 1966, v. 37, No 5, p. 1963–1966.
- 3.114. Martin G. M., Mitonneau A., Mircea A. Electron traps in bulk and epitaxial GaAs crystals // *Electron. Lett.*, 1977, v. 13, No 7, p. 191–193.
- 3.115. Mitonneau A., Martin G. M., Mircea A. Hole traps in bulk and epitaxial GaAs crystals // *Electron. Lett.*, 1977, v. 13, No 22, p. 666–668.
- 3.116. Dargys A., Čėsna A., Kundrotas J. Shallow impurity impact ionization transients in *n*-type InP and GaAs // *Semicond. Sci. Technol.*, 1992, v. 7, No 2, p. 210–217.

## InP

- 4.1. Deus P., Schneider H. A., Voland U., Stiehler K. Low temperature thermal expansion of InP // *Phys. Stat. Sol. (a)*, 1987, v. 103, No 2, p. 443–447.
- 4.2. Bachmann K. J. Properties, preparation and device applications of indium phosphide // *Ann. Rev. Mater. Sci.*, 1981, v. 11, p. 441–484.
- 4.3. Tozer S. W., Wolford D. J., Bradley J. A., Bour D., Stringfellow G. B. InP and  $\text{Ga}_x\text{In}_{1-x}\text{P}$  band structure under pressure // *19th Int. Conf. Physics of Semiconductors*, Warsaw, 1988, v. 2, p. 881–884.
- 4.4. Nichols D. N., Rimai D. S., Sladek R. J. Elastic anharmonicity of InP: Its relationship to the high pressure transition // *Solid State Commun.*, 1980, v. 36, No 8, p. 667–669.
- 4.5. Hilsom C., Fray S., Smith C. The optical frequencies and dielectric constants of InP // *Solid State Commun.*, 1969, v. 7, No 15, p. 1057–1059.
- 4.6. Borchers P. H., Alfrey G. F., Saunderson D. H., Woods A. D. B. Phonon dispersion curves in indium phosphide // *J. Phys. C: Solid State Phys.*, 1975, v. 8, No 13, p. 2022–2030.
- 4.7. Trommer R., Müller H., Cardona M., Vogl P. Dependence of the phonon spectrum of InP on hydrostatic pressure // *Phys. Rev. B*, 1980, v. 21, No 10, p. 4869–4878.

- 4.8. Boyle W. F., Sladck R. J. Piezoelectric constant and conductivity relaxation in *n*-type InP from ultrasonic attenuation measurements // *Solid State Commun.*, 1975, v. 16, No 3, p. 323–326.
- 4.9. Алиев С. А., Намельский А. Я., Шалыт С. С. Теплопроводность и термоэдс фосфида индия *n*-типа при низких температурах // *ФТТ*, 1965, т. 7, вып. 5, с. 1590–1592.
- 4.10. Kudman I., Steigmeier E. F. Thermal conductivity and Seebeck coefficient of InP // *Phys. Rev.*, 1964, v. 133, No 6A, p. 1665–1667.
- 4.11. Haruna K., Maeta H., Ohashi K., Koike T. The thermal expansion coefficient and Grüneisen parameter of InP crystal at low temperatures // *J. Phys. C: Solid State Phys.*, 1987, v. 20, No 32, p. 5275–5279.
- 4.12. Lautenschlager P., Garriga M., Cardona M. Temperature dependence of the interband critical-point parameters of InP // *Phys. Rev. B*, 1987, v. 36, No 9, p. 4813–4820.
- 4.13. Bugajski M., Lewandowski W. Concentration-dependent absorption and photoluminescence of *n*-type InP // *J. Appl. Phys.*, 1985, v. 57, No 2, p. 521–530.
- 4.14. Onton A., Chicotka R. J., Yacoby Y. Subsidiary indirect conduction band minima and their donor levels in GaAs and InP // *Proc. 11th Int. Conf. on Physics of Semiconductors*, Warszawa, 1972, v. 2, p. 1023–1029.
- 4.15. Alekseev M. A., Karlik I. Ya., Mirlin D. N., Saepa V. F., Sirenko A. A. Intra and inter-valley electron scattering in the conduction band of InP. The valence band warping // *19th Int. Conf. Physics of Semiconductors*, Warsaw, 1988, p. 1423–1426.
- 4.16. Camassel J., Merle P., Bayo L., Mathieu H. Deformation potentials of the fundamental exciton spectrum of InP // *Phys. Rev. B*, 1980, v. 22, No 4, p. 2020–2024.
- 4.17. Zurawsky W. P., Littman J. E., Drickamer H. G. Pressure induced conduction and valence band shifts in InP and GaAs from measurements at semiconductor-electrolyte interfaces // *J. Appl. Phys.*, 1983, v. 54, No 6, p. 3216–3219.
- 4.18. Бендориус Р. А., Шилейка А. Ю. Влияние гидростатического давления на спектры электроотражения InP // *ФТП*, 1972, т. 6, вып. 6, с. 1185–1186.
- 4.19. Eaves L., Stradling R. A., Askenazy S., Lectin J., Portal J. C., Ulmet J. P. The magneto-phonon effect in epitaxial films of *n*-type InP // *J. Phys. C: Solid State Phys.*, 1971, v. 4, No 2, p. L42–L47.
- 4.20. Chamberlain J. M., Simmonds P. E., Stradling R. A., Bradley C. C. Cyclotron resonance with epitaxial films of *n*-type InP // *J. Phys. C: Solid State Phys.*, 1971, v. 4, No 2, p. L33–L42.
- 4.21. Bimberg D., Hess K., Lipari N. O., Fischbach J. U., Altarelli M. Free excitons in InP in high magnetic fields // *Physica B*, 1977, v. 89, p. 139–142.
- 4.22. Alekseev M. A., Karlik I. Ya., Merkulov I. A., Mirlin D. N., Saepa V. F. Hot photoluminescence and valence band warping in GaAs and InP crystals // *Phys. Lett. A*, 1988, v. 127, Nos 6/7, p. 373–378.
- 4.23. Аверкиев Н. С., Гореленок А. Т., Тарасов И. С. Особенности поляризации люминесценции и константы деформационного потенциала в InP *n*- и *p*-типа проводимости // *ФТП*, 1983, т. 17, вып. 6, с. 997–1002.
- 4.24. Rochon P., Fortin E. Photovoltaic effect and interband magneto-optical transitions in InP // *Phys. Rev. B*, 1975, v. 12, No 12, p. 5803–5810.
- 4.25. Hang Z., Shen H., Pollak F. H. Temperature dependence of the  $E_0$  and  $E_0 + \Delta_0$  gaps of InP up to 600 °C // *Solid State Commun.*, 1990, v. 73, No 1, p. 15–18.
- 4.26. Schwabe R., Haufe A., Gottschalch V., Unger K. Photoluminescence of heavily doped *n*-InP // *Solid State Commun.*, 1986, v. 58, No 7, p. 485–491.
- 4.27. Turner W. J., Reese W. E., Pettit G. D. Exciton absorption and emission in InP // *Phys. Rev.*, 1964, v. 136, No 5A, p. 1467–1470.
- 4.28. Burkhard H., Dinges H. W., Kuphal E. Optical properties of  $\text{In}_{1-x}\text{Ga}_x\text{P}_{1-y}\text{As}_y$ , InP, GaAs, and GaP determined by ellipsometry // *J. Appl. Phys.*, 1982, v. 53, No 1, p. 655–662.
- 4.29. Hass M., Hennis B. W. Infrared lattice reflection spectra of III–V compound semiconductors // *J. Phys. Chem. Solids*, 1962, v. 23, No 8, p. 1099–1104.
- 4.30. Newman R. Optical properties of *n*-type InP // *Phys. Rev.*, 1958, v. 111, No 6, p. 1518–1521.
- 4.31. Dumke W. P., Lorenz M. R., Pettit G. D. Intra- and interband free-carrier absorption and the fundamental absorption edge in *n*-type InP // *Phys. Rev. B*, 1970, v. 1, No 12, p. 4668–4673.
- 4.32. Mathieu H., Chen Y., Camassel J., Allegre J., Robertson D. S. Excitons and polaritons in InP // *Phys. Rev. B*, 1985, v. 32, No 6, p. 4042–4051.
- 4.33. Skolnick M. S., Dean P. J. Near-gap energy levels of InP – luminescence and photoconductivity study // *J. Phys. C: Solid State Phys.*, 1982, v. 15, No 28, p. 5863–5874.
- 4.34. Heim U. Lifetimes of bound excitons in InP // *Phys. Stat. Sol. (b)*, 1971, v. 48, No 2, p. 629–633.



- 4.35. Rühle W., Schmid W., Meck R., Stath N., Fischbach J. U., Strottner I., Benz K. W., Pilkuhn M. Isoelectronic impurity states in direct-gap III—V compounds: The case of InP: Bi // *Phys. Rev. B*, 1978, v. 18, No 12, p. 7022—7032.
- 4.36. Mathieu H., Camassel J., Chekroun F. B. Stress effects on excitons bound to neutral acceptors in InP // *Phys. Rev. B*, 1984, v. 29, No 6, p. 3438—3448.
- 4.37. Skromme B. J., Stillman G. E. Impact ionization of excitons and shallow donors in InP // *Phys. Rev. B*, 1983, v. 28, No 8, p. 4602—4607.
- 4.38. Beye A. C., Yamada A., Kamijoh T., Tanoue H., Mayer K. M., Ohnishi N., Shibata H., Makita Y. Excited-state spectroscopy of identified Mg acceptor in InP // *Appl. Phys. Lett.*, 1990, v. 56, No 4, p. 349—351.
- 4.39. Pomrenke G. S., Reynolds D. C., Park Y. S. Near-edge emission of unimplanted and Mg-implanted VPE InP // *J. Lumin.*, 1981, v. 24/25, pt 1, p. 189—192.
- 4.40. Skromme B. J., Stillman G. E., Oberstar J. D., Chan S. S. Identification of the residual acceptors in undoped high purity InP // *Appl. Phys. Lett.*, 1984, v. 44, No 3, p. 319—321.
- 4.41. Yamaguchi M., Yamamoto A., Shinoyama S., Sugiura H. Photoluminescence and infrared absorption studies of liquid encapsulated Czochralski-grown InP single crystals // *J. Appl. Phys.*, 1982, v. 53, No 1, p. 633—638.
- 4.42. Skromme B. J., Stillman G. E. Excited-state-donor-to-acceptor transitions in the photoluminescence spectrum of GaAs and InP // *Phys. Rev. B*, 1984, v. 29, No 4, p. 1982—1992.
- 4.43. Inoue T., Kainosho K., Hiranō R., Shimakura H., Kanazawa T., Oda O. Characterization of high-purity InP by photoluminescence // *J. Appl. Phys.*, 1990, v. 67, No 11, p. 7165—7168.
- 4.44. Uwai K., Yamada S., Takahei K. Identification of acceptors and donors in high-purity InP grown by metalorganic chemical vapor deposition // *J. Appl. Phys.*, 1987, v. 61, No 3, p. 1059—1062.
- 4.45. Tada K., Suzuki N. Linear electrooptic properties of InP // *Jpn. J. Appl. Phys.*, 1980, v. 19, No 11, p. 2295—2296.
- 4.46. Canal F., Grimditch M., Cardona M. Piezobirefringence in GaP and InP // *Solid State Commun.*, 1979, v. 29, No 7, p. 523—526.
- 4.47. Lee C. C., Fan H. Y. Second-harmonic generation in InSb, InP, and AlSb // *Phys. Rev. B*, 1974, v. 10, No 2, p. 703—709.
- 4.48. Blood P., Orton J. W. The electrical properties of *n*-type epitaxial InP in the temperature range 5 K to 700 K // *J. Phys. C: Solid State Phys.*, 1974, v. 7, No 5, p. 893—904.
- 4.49. Коханюк М. Б., Ляху Г. Л., Молодян И. П., Руссу Е. В. Электрические свойства фосфида индия, легированного цинком // *Фосфид индия в полупроводниковой электронике* / Под ред. С. И. Радауцана. — Кишинев: Штиинца, 1988, с. 200—222.
- 4.50. Von Folberth O. G., Weiss H. Herstellung und elektrische Eigenschaften von InP und GaAs // *Z. Naturforsch.*, 1953, Bd 10a, H. 8, S. 615—619.
- 4.51. Кесаманлы Ф. П., Наследов Д. Н., Нашельский А. Я., Скрипкин В. А. Зависимость эффективной массы электронов от их концентрации в кристаллах фосфида индия // *ФТП*, 1968, т. 2, вып. 10, с. 1463—1466.
- 4.52. Galayanov V. V., Siukaev N. V. On mechanism of electron scattering in InP // *Phys. Stat. Sol.*, 1970, v. 38, No 2, p. 523—530.
- 4.53. Hilsum C., Rees H. D., Wilgoss W. The scattering factor in *n*-type InP // *Phys. Stat. Sol. (b)*, 1973, v. 56, No 2, p. K93—K96.
- 4.54. Walukiewicz W., Lagowski J., Jastrzebski L., Rava P., Lichtensteiger M., Gatos C. H., Gatos H. C. Electron mobility and free-carrier absorption in InP; determination of the compensation ratio // *J. Appl. Phys.*, 1980, v. 51, No 5, p. 2659—2668.
- 4.55. Anderson D. A., Apsley N., Davies P., Giles P. L. Compensation in heavily doped *n*-type InP and GaAs // *J. Appl. Phys.*, 1985, v. 58, No 8, p. 3059—3067.
- 4.56. Zhu L. D., Chan K. T., Ballantyne J. M. Very high mobility InP grown by low pressure metalorganic vapor phase epitaxy using solid trimethylindium source // *Appl. Phys. Lett.*, 1985, v. 47, No 1, p. 47—48.
- 4.57. Benzaquen M., Walsh D., Mazuruk K. High-temperature mobility of pure *n*-type InP epitaxial layers // *Phys. Rev. B*, 1987, v. 36, No 8, p. 4388—4393.
- 4.58. Apsley N., Anderson D. A., Morrison J. B. The Hall scattering factor in InP // *Semicond. Sci. Technol.*, 1987, v. 2, No 1, p. 44—49.
- 4.59. Glicksman M., Weiser K. Electrical properties of *p*-type InP // *Phys. Chem. Solids*, 1959, v. 10, No 4, p. 337—340.
- 4.60. Галаванов В. В., Метрелеви С. Г., Сиукаев Н. В., Старосельцева С. П. Электрические свойства *p*-InP // *ФТП*, 1969, т. 3, вып. 1, с. 120—122.
- 4.61. Наследов Д. Н., Попов Ю. Г., Сиукаев Н. В., Старосельцева С. П. Электрические свойства *p*-InP при низких температурах // *ФТП*, 1969, т. 3, вып. 3, с. 454—456.

- 4.62. Галаванов В. В., Метревели С. Г., Старосельцева С. П. Термоздс в  $p$ -InP // ФТП, 1969, т. 3, вып. 9, с. 1391–1393.
- 4.63. Tuck B., Zahari M. D. Electrical measurements on homogeneous diffused  $p$ -type InP // J. Phys. D: Appl. Phys., 1977, v. 10, No 18, p. 2473–2479.
- 4.64. Majerfeld A., Potter K. E., Robson P. N. Subthreshold velocity-field characteristics for bulk and epitaxial InP // J. Appl. Phys., 1974, v. 45, No 8, p. 3681–3682.
- 4.65. Windhorn T. H., Cook L. W., Haase M. A., Stillman G. E. Electron transport in InP at high electric fields // Appl. Phys. Lett., 1983, v. 42, No 8, p. 725–727.
- 4.66. Brennan K., Hess K. Theory of high-field transport of holes in GaAs and InP // Phys. Rev. B, 1984, v. 29, No 10, p. 5581–5590.
- 4.67. Tabatabaie N., Robbins V. M., Pan N., Stillman G. E. Impact ionization coefficients in (111) InP // Appl. Phys. Lett., 1985, v. 46, No 2, p. 182–184.
- 4.68. Барейкис В., Билькис Ж., Либерис Ю., Сакалас П., Шальтис Р. Шумы и диффузия в коротких  $n^+-n-n^+$  InP структурах // ФТП, 1988, т. 22, вып. 6, с. 1040–1044.
- 4.69. Rottner K., Helbig R., Müller G. Piezoelectric constant of InP // Appl. Phys. Lett., 1993, v. 62, No 4, p. 352–353.
- 4.70. Sagar A. Piezoresistance in  $n$ -type InP // Phys. Rev., 1960, v. 117, No 1, p. 101.
- 4.71. von Busch G. A., Kern R. Die magnetischen Eigenschaften der  $A^{III}B^V$  – Verbindungen // Helv. Phys. Acta, 1959, v. 32, No 1, p. 24–57.
- 4.72. Дахно А. Н., Емельяненко О. В., Лагунова Т. С., Старосельцева С. П. Особенности переноса электронов в компенсированных кристаллах  $n$ -InP // ФТП, 1979, т. 13, вып. 9, с. 1788–1794.
- 4.73. Williams E. W., Elder W., Astles M. G., Webb M., Mullin J. B., Straughan B., Tufton P. J. Indium phosphide. I. A photoluminescence materials study // J. Electrochem. Soc., 1973, v. 120, No 12, p. 1741–1749.
- 4.74. Dean P. J., Robbins D. J., Bishop S. G. Dye laser selective spectroscopy in bulk-grown indium phosphide // J. Phys. C: Solid State Phys., 1979, v. 12, No 24, p. 5567–5575.
- 4.75. Rojo P., Leyral P., Nouailhat A., Guillot G., Lambert B., Deveaud B., Coquille R. Deep levels related to Co in InP // J. Appl. Phys., 1984, v. 55, No 2, p. 395–401.
- 4.76. Ledebø L.-Å., Ridley B. K. On the position of energy levels related to transition-metal impurities in III–V semiconductors // J. Phys. C: Solid State Phys., 1982, v. 15, No 27, p. L961–L964.
- 4.77. Kullendorff N., Jansson L., Ledebø L.-Å. Copper-related deep level defects in III–V semiconductors // J. Appl. Phys., 1983, v. 54, No 6, p. 3203–3212.
- 4.78. Eaves L., Smith A. W., Skolnick M. S., Cockayne B. An investigation of the deep level photoluminescence spectra of InP (Mn), InP (Fe), and of undoped InP // J. Appl. Phys., 1982, v. 53, No 7, p. 4955–4963.
- 4.79. Chiao S. H., Antypas G. A. Photocapacitance effects of deep traps in  $n$ -type InP // J. Appl. Phys., 1978, v. 49, No 1, p. 466–468.
- 4.80. Deveaud B., Plot B., Lambert B., Bremond G., Guillot G., Nouailhat A., Clerjaud B., Naud C. The donor level of vanadium in InP // J. Appl. Phys., 1986, v. 59, No 9, p. 3126–3130.
- 4.81. Reeder A. A., Chamberlain J. M., Turner R. J., Hill G. Shallow-donor profiles and zero magnetic field FIR photoconductivity spectra of high purity indium phosphide // Solid State Commun., 1986, v. 57, No 5, p. 355–359.
- 4.82. Lau K. M., Wilson W. L. FIR photoconductivity in epitaxial InP // Infrared Phys., 1983, v. 23, No 6, p. 311–319.
- 4.83. Rikken G. L. J. A., Wyder P., Chamberlain J. M., Grimes R. T., Taylor L. L. Time-resolved recombination dynamics of photoionized hydrogenlike impurities // Phys. Rev. B, 1988, v. 38, No 6, p. 4156–4164.
- 4.84. Dean P. J., Robbins D. J., Bishop S. G. Acceptor excited states in indium phosphide // Solid State Commun., 1979, v. 32, No 5, p. 379–384.
- 4.85. Whitney P. S., Uwai K. Compensation ratios in high-purity InP using an improved Hall measurement technique // J. Appl. Phys., 1988, v. 63, No 5, p. 1585–1590.
- 4.86. Lim H., Sagnes G., Bastide G., Rouzeyre M. Deep level transient spectroscopy study in  $n$ -type InP // J. Appl. Phys., 1982, v. 53, No 4, p. 3317–3320.
- 4.87. Bremond G., Nouailhat A., Guillot G., Cockayne B. Deep level spectroscopy in InP:Fe // Electron. Lett., 1981, v. 17, No 1, p. 55–56.
- 4.88. Dargys A., Kundrotas J., Paršellūnas J., Čėsna A. Impact ionization of shallow donors in  $n$ -InP // Liet. Fiz. Rink., 1991, v. 31, No 3, p. 326–332. [Lithuanian J. Phys., 1991, v. 31, No 3, p. 189–192.]

## 2. Subject index

	Definition	Ge	Si	GaAs	InP
<b>A</b>					
<b>A, B, C parameters</b>	15				
<b>Absorption coefficient</b>	17				
at high photon energies		46	98	158	202
by free electrons			102	161, 163	205
by free holes			102	161	204
by lattice		49	101	163	205
near band gap edge		47, 48	100	159, 161	203, 204
<b>Absorption cross section</b>	17				
acceptor		73	131		
amphoteric impurity		74	131		
donor		73	130, 136		
free electron		50	103	164	206
free hole		50		164	206
<b>B</b>					
<b>Band structure</b>		38	91	150	196
<b>Brillouin zone</b>	10				
high symmetry points and lines					
diamond lattice	13	13	13		
zinc blende lattice	14			14	14
<b>Bulk modulus</b>	10	32	84	144	190
<b>C</b>					
<b>Capture</b>					
time, rate	25				
cross section	25				
acceptor		78, 80	137, 139		226
donor		78, 80	137, 139	183	223
trap				185, 186	225
<b>Cleavage</b>		31	83	143	189
<b>Compliance tensor</b>	9				
<b>Compressibility</b>	10				
<b>Concentration vs. temperature</b>					
electron			111	170, 171	211
hole			113		
intrinsic		58	114	173	213

	Definition	Ge	Si	GaAs	InP
<b>Conductivity vs. temperature</b> ( <i>see also</i> resistivity)					
<i>n</i> -type			110		
<i>p</i> -type			112		
intrinsic		58	114		
<b>Conduction band parameters</b>	12	40	93	153	198
<b>Constant energy surface</b>					
spherical	14				
ellipsoidal	14	42	95		
warped	15	42	94	155	199
<b>Critical points</b>					
energetic distances		39	92	152	197
nomenclature		38	91	151	196
pressure coefficients		39	92	152	197
vs. temperature		44	96	156	200
<b>D</b>					
<b>D-A transition</b>	18			166	208
<b>Debye temperature</b>	12	35	88	147	193
<b>Deformation potential</b>					
acoustic scattering		65	123	178	218
optical scattering		65	123	178	218
uniaxial					
conduction band	43	40	93	153	
valence band	16, 43	41	94	154	199
<b>Density</b>		31	83	143	189
<b>Dielectric permittivity</b>					
high frequency				145	191
static		33	86	145	191
vs. pressure		33	86	145	
vs. temperature		33	86	145	191
<b>Diffusion coefficient</b> ( <i>see</i> diffusivity)					
<b>Diffusion length</b>	22				
<b>Diffusivity</b>	22				
electron		62	119	177	217
hole		62	120		
<b>Dispersion curves</b>					
electron	14	38	91	150	196
hole	15	42	91	155	196
phonon	9	34	87	146	192
<b>Dispersion relation</b>					
electron	14				
hole	15				
<b>Drift velocity</b>	21				
electron		61	117, 119	175	215
hole		62	118, 119	176	216

	Definition	Ge	Si	GaAs	InP
<b>E</b>					
<b><i>e</i>-A transition</b>	18			166	208
<b>Effective mass</b>					
electron					
conductivity	15	40	93		
density-of-states	15	40	93	153	198
longitudinal	14	40	93	153	
scalar	14	40	93	153	198
transverse	14	40	93	153	
hole					
density-of-states	15	41	94	154	199
heavy	15	41	94	154	199
light	15	41	94	154	199
split-off band		41	94	154	199
<b>Elastic anisotropy factor</b>	10	32	84	144	190
<b>Elastic coefficient (tensor)</b>	9				
<b>Elastic constants</b>	9	32	84	144	190
<b>Elastooptic coefficient</b>	19	53	106	167	
<b>Elastoresistance tensor (coefficient)</b>	23				
<b>Electrooptic coefficient (tensor)</b>	20	53	107	167	209
<b>Emission rate</b>					
electron	26	79	138	185	225, 226
hole	26	79	138	186	225, 226
<b>Empirical formula</b>					
absorption coefficient			100		
conductivity			114		
critical point energy		44	96	156	200
differential expansivity			90		
drift velocity			118	175	
energy gap		44	96	156	200
impact ionization coefficient for donors		81		187	227
intrinsic concentration		58	114	173	213
ionization energy					
acceptor			135	184	224
donor		77	135	184	224
lattice constant			83		
mobility			115, 116		
refractive index			99	160	
<b>Energy relaxation time</b>	23				
electron					
vs. concentration		63	121		
vs. electric field		64	122	177	217
vs. temperature		63	121	177	217
hole					
vs. concentration		63			
vs. electric field		64			
vs. temperature			121		

	Definition	Ge	Si	GaAs	InP
<b>Energy levels</b>					
acceptor		75, 77	133	184	224
donor		74	132, 136	183	223
<b>Exciton</b>	18				
bound to acceptor		51	105	165	207
bound to donor		50	104	165	207
free		50	104	165	207
lifetime					
bound		50	104	165	207
free			104	165	
luminescence spectra		52	106	166	209
<b>F</b>					
<b>Fermi energy</b>		45	97	157	201
<b>Forbidden energy gap</b>					
pressure coefficient		39	92	152	197
vs. impurity concentration		45	97	157	201
vs. temperature		44	96	156	200
<b>G</b>					
<b>g-factor</b>					
conduction band	16	40	93	153	198
split-off band		41	94	154	199
valence band	16	41		154	199
$\gamma_1, \gamma_2, \gamma_3$ parameters	15	41	94	154	199
<b>Grüneisen parameter</b>					
average	11	37	90	149	191
phonon branch	11	33	86	145	195
<b>H</b>					
<b><i>h</i>-D transition</b>	19				208
<b>Hall coefficient</b>	22				
vs. temperature					
electron		55	109, 110		
hole		56	112	172	212
<b>Hall factor</b>	22				
electron		70	128	181	221
hole		71	128	181	
vs. magnetic induction				181	221
<b>Heat capacity</b>	12	35	88	147	193
<b>Hot electrons (holes)</b>	23				
<b>I</b>					
<b>Impact ionization</b>					
band-band	22	63	120	176	216
coefficient	26				

	Definition	Ge	Si	GaAs	InP
acceptor		81			
donor		81	140	187	227
Impermeability tensor	19				
Intervalley relaxation time	23	64	122	177	217
Intervalley coupling constants		65	123	178	218
Intravalley scattering parameters		65	123	178	218
Ionization energy					
acceptor		73	131	182	222
vs. concentration			135	184	224
amphoteric impurity		74	131		
donor		73	130	182	222
vs. concentration		77	135	184	224
trap				185, 186	225
<b>K</b>					
Kerr coefficient	20				
<b>L</b>					
Lattice					
atomic, molecular weight		31	83	143	189
cleavage		31	83	143	189
constant		31	83	143	189
density		31	83	143	189
isotopes		31	83	143	189
melting temperature		31	83	143	189
number of atoms		31	83	143	189
phase transition		31	83	143	189
space group		31	83	143	189
symmetry formula		31	83	143	189
tensorial properties	26				
Luttinger parameters	15	41	94	154	199
<b>M</b>					
Magnetic permeability	25				
Magnetic susceptibility	25	70	128	180	220
Magnetoresistance	25				
electron		71, 72	129	181	221
hole		72	129		
Melting temperature		31	83	143	189
Mobility	21				
electron					
vs. concentration		59	115	174	214
vs. temperature		56, 60	109, 116	170, 171	212
hole					
vs. concentration		60	115	174	214

	Definition	Ge	Si	GaAs	InP
vs. temperature		56, 60	113, 116	172	212
lattice limited		60	116	170	
<b>Murnaghan equation</b>	10				
<b>N</b>					
<b>Nonparabolicity parameter</b>	16				
conduction band		65	123	153, 178	198, 218
valence band		41			
<b>Nonsphericity parameter</b>	15	41	94	154	199
<b>O</b>					
<b>Optical absorption spectra</b>					
acceptor		76	134		
band-band		46, 48	98, 100	158, 159	202, 203
donor		76	134		
<b>Optical transition nomenclature</b>					
band-band		38	91	151	196
impurity		74, 75	132, 133	183, 184	223, 224
<b>P</b>					
<b>Parameters for high electric field transport calculation</b>		65	123	178	218
<b>Phonon</b>					
branches	9	34	87	146	192
Brillouin zone	9				
dispersion relation	9	34	87	146	192
energies for high symmetry points		33	85	144	190
energy vs. temperature		33	86		
high symmetry points and lines	9				
intervalley <i>f</i> -, <i>g</i> -type	95		85		
lifetime		33	86	145	191
Raman activity		33	86	145	191
<b>Physical constants</b>	28				
<b>Piezoelectric tensor</b> (coefficient)	24	66	124	179	219
<b>Piezooptic coefficient</b> (tensor)	19	53	106		
<b>Piezooptic effect</b>	19	53	107	168	210
<b>Piezoresistance tensor</b> (coefficient)	23	66	124	179	219
<b>Pockels coefficient</b>	20	53	107	167	209
<b>Poisson ratio</b>	10	32	84	144	190
<b>Polarization</b> (dielectric)	20				
<b>Pressure coefficient</b>					
band gap		39	92	152	197
critical energy points		39	92	152	197
dielectric permittivity		33	86	145	
refractive index		52	106	167	



	Definition	Ge	Si	GaAs	InP
<b>R</b>					
<b>Raman activity</b>		33	86	145	191
<b>Recombination channels</b>	18				
<b>Reflection coefficient</b>	17				
at high photon energies		46	98	158	202
in reststrahlen region				161	205
<b>Refractive index</b>	17	52	99, 106	167	209
at band edge		48	99	160	204
vs. pressure		52	106	167	
vs. temperature		52	106	167	209
<b>Resistivity</b> ( <i>see also</i> conductivity)					
vs. impurity concentration		59	114	173	213
vs. magnetic induction					
electron		71, 72	129	181	221
hole		72	129		
vs. pressure		66	124	179	219
hydrostatic	24	68	126	179	219
uniaxial	24	68	126		
vs. temperature		55, 56			
<b>S</b>					
<b>Seebeck coefficient</b>	25				
electron		69	126	180	220
hole		69	127	180	220
intrinsic		70	127		
<b>Sound velocity</b>	11	32	84	144	190
<b>Space group</b>		31	83	143	189
<b>Split-off valence band separation</b>		41	94	154	199
<b>Splitting under uniaxial stress</b>					
<i>L</i> valleys	43	43			
valence band	43	43	95	155	200
<i>X</i> valleys	95		95		
<b>Strain, stress tensor</b> (coefficient)	9				
<b>Susceptibility</b>	20				
anisotropy	21	54	108	169	
vs. electron concentration		54	108	169	
vs. hole concentration		54	108		
2nd, 3d order	20	54	108	168, 169	210
<b>Symbols of particles and complexes</b>	18				
<b>Symmetry points and lines</b>		13	13	14	14
<b>T</b>					
<b>Temperature dependence</b>					
critical energy points		44	96	156	200
dielectric permittivity		33	86	145	191
forbidden energy gap		44	96	156	200
refractive index		52	106	167	209

# Subject index

	Definition	Ge	Si	GaAs	InP
<b>Tensors in cubic semiconductors</b>	26				
<b>Thermal conductivity</b>	12	35	89	148	194
<b>Thermal expansivity</b>		36	89	148	194
differential	12	36	90	149	195
<b>Thermal velocity</b>	25				
<b>Thermoelectric power</b> ( <i>see</i> Seebeck coefficient)					
<b>Translation from CGS to SI units</b>	29				
<b>U</b>					
<b>Ultrasound acoustic wave attenuation</b>	11	34	87	146	192
<b>V</b>					
<b>Valence band parameters</b>	15	41	94	154	199
<b>Valley energy separation</b>		39	92	152	197
<b>Valleys <math>\Gamma</math>, X, L</b>		40	93	153	198
<b>W</b>					
<b>Warm electrons (holes)</b>	23				
<b>Y</b>					
<b>Young's modulus</b>	10	32	84	144	190

### 3. Subject index in Lithuanian

#### Rodyklė

	Apibrėži- mas	Ge	Si	GaAs	InP
<b>A</b>					
<i>A, B, C</i> parametrai	15				
Absorbcijos koeficientas	17				
prie draustinės energijos tarpo		47, 48	100	159, 161	203, 204
didelės energijos fotonų		46	98	158	202
gardelės		49	101	163	205
laisvųjų elektronų			102	161, 163	205
laisvųjų skylių			102	161	204
Absorbcijos skerspjūvis	17				
akceptorių		73	131		
amfoterinių priemaišų		74	131		
donorų		73	130, 136		
laisvųjų elektronų		50	103	164	206
laisvųjų skylių		50		164	206
Atskilusios valentinės juostos tarpas		41	94	154	199
Atspindžio koeficientas					
didelės energijos fotonų		46	98	158	202
liktinių spindulių srityje				161	205
Atstumas tarp slėnių		39	92	152	197
<b>B</b>					
Brillouino zona	10				
aukštos simetrijos taškai ir ašys					
cinko blizgio gardelei	14			14	14
deimanto gardelei	13	13	13		
<b>D</b>					
<i>D-A</i> šuolis	18			166	208
Dalelių ir kompleksų simboliai	18				
Debye temperatūra	12	35	88	147	193
Deformacijos tenzorius (koeficientas)	9				
Deformacinis potencialas					
akustinės sklaidos		65	123	178	218
optinės sklaidos		65	123	178	218
vienaašis					
laidumo juostos	43	40	93	153	
valentinės juostos	16, 43	41	94	154	199

	Apibrėži- mas	Ge	Si	GaAs	InP
<b>Dielektrinė skvarba</b>					
aukštojo dažnio				145	191
priklausomybė nuo slėgio		33	86	145	
temperatūros		33	86	145	191
statinė		33	86	145	191
<b>Difuzijos koeficientas</b>	22				
elektronų		62	119	177	217
skylių		62	120		
<b>Difuzijos nuotolis</b>	22				
<b>Dispersijos kreivės</b>					
elektronų	14	38	91	150	196
fononų	9	34	87	146	192
skylių	15	42	91	155	196
<b>Dispersijos sąryšiai</b>					
elektronų	14				
skylių	15				
<b>Draustinės energijos tarpas</b>					
priklausomybė nuo					
priemaišų koncentracijos		45	97	157	201
temperatūros		44	96	156	200
slėgio koeficientas		39	92	152	197
<b>Dreifo greitis</b>	21				
elektronų		61	117, 119	175	215
skylių		62	118, 119	176	216
<b>E</b>					
<i>e-A</i> šuolis	18			166	208
<b>Efektinė masė</b>					
elektronų					
išilginė	14	40	93	153	
laidumo	15	40	93		
lygmenų tankio	15	40	93	153	198
skaliarinė	14	40	93	153	198
skersinė	14	40	93	153	
skylių					
atskilusios juostos		41	94	154	199
lengvųjų	15	41	94	154	199
lygmenų tankio	15	41	94	154	199
sunkiųjų	15	41	94	154	199
<b>Eksitonas</b>	18				
gyvavimo trukmė					
laisvojo			104	165	
surištojo		50	104	165	207
laisvasis		50	104	165	207
surištasis su akceptoriumi		51	105	165	207
surištasis su donoru		50	104	165	207
<b>Eksitonų luminescencijos spektras</b>		52	106	166	209
<b>Elastooptinis koeficientas</b>	19	53	106	167	

	Apibrėži- mas	Ge	Si	GaAs	InP
<b>Elastovaržos tenzorius (koeficientas)</b>	23				
<b>Elektrooptinis koeficientas (tenzorius)</b>	20	53	107	167	209
<b>Emisijos sparta</b>					
elektronų	26	79	138	185	225, 226
skylių	26	79	138	185	225, 226
<b>Empyrinė formulė</b>					
absorbcijos koeficiento			100		
diferencialinio plėtrumo			90		
donorų smūginės jonizacijos koe- ficiento		81		187	227
dreifo greičio			118	175	
gardelės konstantos			83		
jonizacijos energijos					
akceptorų			135	184	224
donorų		77	135	184	224
judrumo			115, 116		
juostos tarpo		44	96	156	200
krizinių taškų energijos		44	96	156	200
laidumo			114		
lūžio rodiklio			99	160	
savosios koncentracijos		58	114	173	213
<b>Energijos lygmenys</b>					
akceptorų		75, 77	133	184	224
donorų		74	132, 136	183	223
<b>Energijos relaksacijos trukmė</b>	23				
elektronų priklausomybė nuo					
elektrinio lauko		64	122	177	217
koncentracijos		63	121		
temperatūros		63	121	177	217
skylių priklausomybė nuo					
elektrinio lauko		64			
koncentracijos		63			
temperatūros			121		
<b>Erdvinė grupė</b>		31	83	143	189
<b>F</b>					
<b>Fermi energija</b>		45	97	157	201
<b>Fizikinės konstantos</b>	28				
<b>Fononai</b>					
aukštos simetrijos taškai ir ašys	9				
Brillouino zona	9				
dispersijos sąryšiai	9	34	87	146	192
energija aukštos simetrijos taškuose		33	85	144	190
<i>f</i> ir <i>g</i> tipo	95		85		
gyvavimo trukmė		33	86	145	191
Ramano aktyvumas		33	86	145	191
šakos	9	34	87	146	192

	Apibrėži- mas	Ge	Si	GaAs	InP
<b>G</b>					
<b>g faktorius</b>					
atskilusios juostos		41	94	154	199
laidumo juostos	16	40	93	153	198
valentinės juostos	16	41		154	199
$\gamma_1, \gamma_2, \gamma_3$ parametrai	15	41	94	154	199
<b>Gardelė</b>					
atominė, molekulinė masė		31	83	143	189
atomų kiekis		31	83	143	189
erdvinė grupė		31	83	143	189
fazinis virsmas		31	83	143	189
izotopai		31	83	143	189
konstanta		31	83	143	189
lydymosi temperatūra		31	83	143	189
simetrijos formulė		31	83	143	189
skalumas		31	83	143	189
tankis		31	83	143	189
tenzorinės savybės	26				
Garso greitis	11	32	84	144	190
<b>Grūneiseno parametras</b>					
fononinių šakų	11	33	86	145	195
vidutinis	11	37	90	149	191
<b>H</b>					
<i>h-D</i> šuolis	19				
<b>Hallo faktorius</b>					
elektronų	22	70	128	181	221
priklausomybė nuo magnetinės indukcijos				181	221
skylių		71	128	181	
<b>Hallo koeficientas</b>					
priklausomybė nuo temperatūros	22				
<i>n</i> tipo		55	109, 110		
<i>p</i> tipo		56	112	172	212
<b>I</b>					
Įtempimo tenzorius (koeficientas)	9				
<b>Y</b>					
Youngo modulis	10	32	84	144	190
<b>J</b>					
<b>Jonizacijos energija</b>					
akceptoriaus		73	131	182	222
priklausomybė nuo koncentracijos			135	184	224

	Apibrėži- mas	Ge	Si	GaAs	InP
amfoterinės priemonės		74	131		
donoro		73	130	182	222
priklausomybė nuo koncentracijos		77	135	184	224
spąsto				185, 186	225
<b>Judrumas</b>	21				
elektronų priklausomybė nuo					
koncentracijos		59	115	174	214
temperatūros		56, 60	109, 116	170, 171	212
gardelės ribotas		60	116	170	
skylių priklausomybė nuo					
koncentracijos		60	115	174	214
temperatūros		56, 60	113, 116	172	212
<b>Juostinė sandara</b>		38	91	150	196
<b>K</b>					
<b>Karštieji elektronai (skylės)</b>	23				
<b>Kerro koeficientas</b>	20				
<b>Koncentracija</b>					
elektronų			111	170, 171	211
savoji		58	114	173	213
skylių			113		
<b>Kriziniai taškai</b>					
energijų tarpai		39	92	152	197
nomenklatūra		38	91	151	196
priklausomybė nuo temperatūros		44	96	156	200
slėgio koeficientai		39	92	152	197
<b>L</b>					
<b>Laidumo juostos parametrai</b>	12	40	93	153	198
<b>Laidumas (taip pat žr. savitoji varža)</b>					
<i>n</i> tipo			110		
<i>p</i> tipo			112		
savasis		58	114		
<b>Lydimosi temperatūra</b>		31	83	143	189
<b>Luttingerio parametrai</b>	15	41	94	154	199
<b>Lūžio rodiklis</b>	17	52	99, 106	167	209
draustinės juostos srityje		48	99	160	204
priklausomybė nuo					
slėgio		52	106	167	
temperatūros		52	106	167	209
<b>M</b>					
<b>Magnetinė skvarba</b>	25				
<b>Magnetinis jautris</b>	25	70	128	180	220

	Apibrėži- mas	Ge	Si	GaAs	InP
<b>Magnetovarža</b>	25				
elektronų		71, 72	129	181	221
skylių		72	129		
<b>Murnaghano lygtis</b>	10				
<b>N</b>					
<b>Nesferiškumo parametras</b>	15	41	94	154	199
<b>Neskvarbumo tenzorius</b>	19				
<b>Neparaboliškumo parametras</b>	16				
laidumo juostos		65	123	153, 178	198, 218
valentinės juostos		41			
<b>Netiesinis optinis jautris</b>	20				
anizotropija	21	54	108	169	
priklausomybė nuo					
elektronų koncentracijos		54	108	169	
skylių koncentracijos		54	108		
2-os, 3-os eilės	20	54	108	168, 169	210
<b>O</b>					
<b>Optinės absorbcijos spektras</b>					
akceptorų		76	134		
donorų		76	134		
tarpuostinis		46, 48	98, 100	158, 159	202, 203
<b>Optinių šuolių nomenklatūra</b>					
priemaišinių		74, 75	132, 133	183, 184	223, 224
tarpuostinių		38	91	151	196
<b>P</b>					
<b>Pagavimo skerspjuvis</b>	25				
akceptoriais		78, 80	137, 139		226
donorais		78, 80	137, 139	183	223
spąstais				185, 186	225
<b>Pagavimo trukmė, sparta</b>	25				
<b>Parametrai stipraus elektrinio lauko</b>					
kinetiniams reiškiniams skaičiuoti		65	123	178	218
<b>Pastoviosios energijos paviršiai</b>					
elipsoidiniai	14	42	95		
gofruotieji	15	42	94	155	199
sferiniai	14				
<b>Pjezoelektrinis tenzorius (koeficientas)</b>	24	66	124	179	219
<b>Pjezooptinis efektas</b>	19	53	107	168	210
<b>Pjezooptinis koeficientas (tenzorius)</b>	19	53	106		
<b>Pjezovaržos tenzorius (koeficientas)</b>	23	66	124	179	219
<b>Pockelso koeficientas</b>	20	53	107	167	209
<b>Poissono koeficientas</b>	10	32	84	144	190
<b>Poliarizacija (dielektrinė)</b>	20				

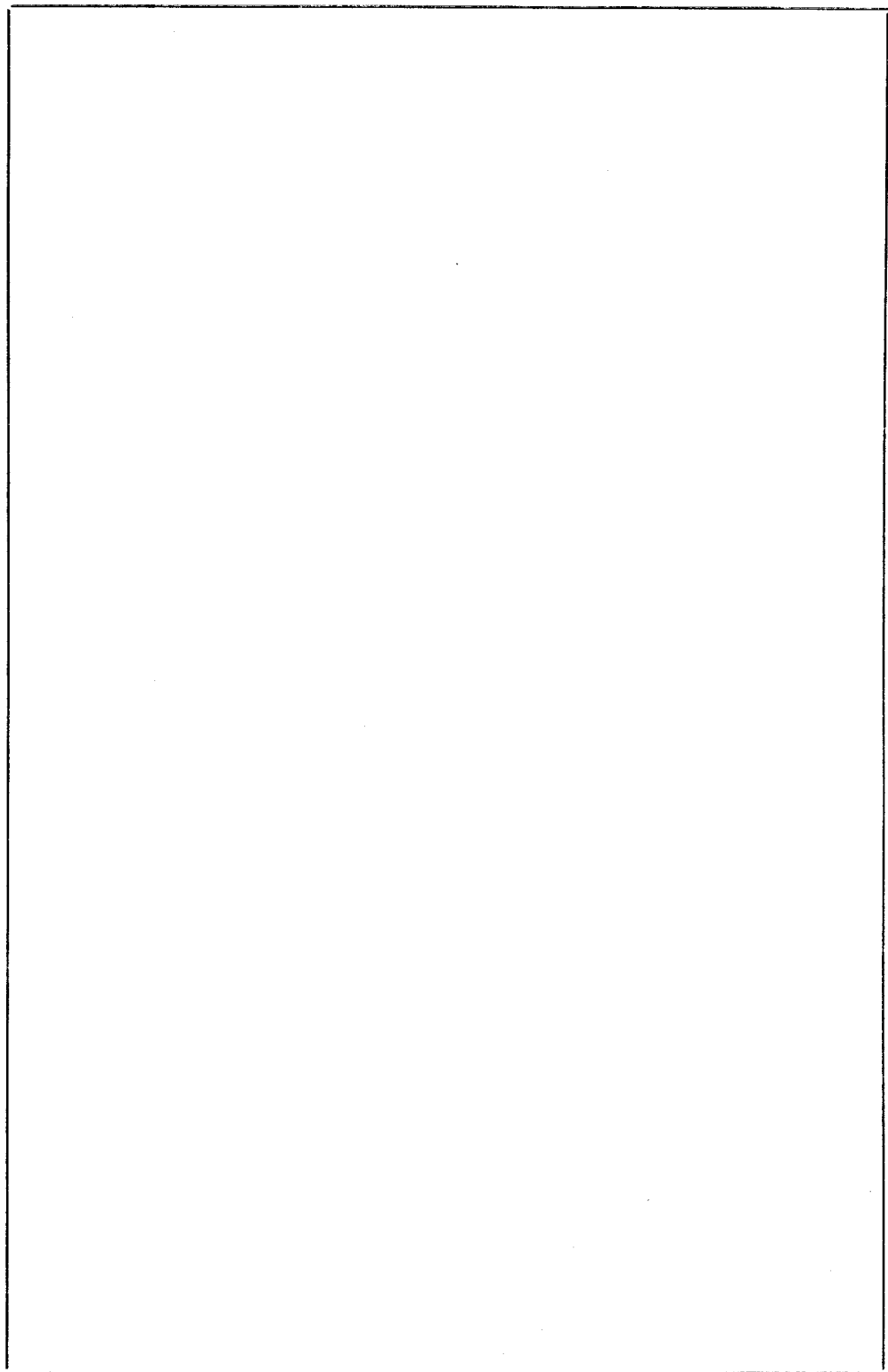


	Apibrėži- mas	Ge	Si	GaAs	InP
<b>R</b>					
Ramano aktyvumas		33	86	145	191
Rekombinacijos kanalai	18				
Ryšys tarp CGS ir SI sistemų	29				
<b>S</b>					
Savitoji varža ( <i>taip pat žr. laidumas</i> )					
priklausomybė nuo magnetinės indukcijos					
elektronų		71, 72	129	181	221
skylių		72	129		
priklausomybė nuo priemaišų koncentracijos		59	114	173	213
priklausomybė nuo slėgio		66	124	179	219
hidrostatinio	24	68	126	179	219
vienašio	24	68	126		
priklausomybė nuo temperatūros		55, 56			
Seebecko koeficientas	25				
elektronų		69	126	180	220
savasis		70	127		
skylių		69	127	180	220
Simetrijos taškai ir ašys		13	13	14	14
Skalumas		31	83	143	189
Skilimas veikiant vienašiam slėgiui					
<i>L</i> slėnių	43	43			
<i>X</i> slėnių	95		95		
valentinės juostos	43	43	95	155	200
Sklaida					
slėnyje		65	123	178	218
tarp slėnių		65	123	178	218
Slankumo tenzorius	9				
Slėgio koeficientas					
dielektrinės skvarbos		33	86	145	
krizinių taškų energijos		39	92	152	197
draustinės juostos tarpo		39	92	152	197
lūžio rodiklio		52	106	167	
Slėniai $\Gamma$ , <i>X</i> , <i>L</i>		40	93	153	198
Smūginė jonizacija					
koeficientas	26				
akceptorinių		81			
donorinių		81	140	187	227
tarpjuostinė	22	63	120	176	216
Spūdumas	10				
Spūdumo modulis	10	32	84	144	190

	Apibrėži- mas	Ge	Si	GaAs	InP
<b>Š</b>					
Šiltieji elektronai (skylės)	23				
Šiluminė talpa	12	35	88	147	193
Šiluminis greitis	25				
Šiluminis laidumas	12	35	89	148	194
Šiluminis plėtrumas		36	89	148	194
diferencialinis	12	36	90	149	195
<b>T</b>					
Tamprumo anizotropijos koeficientas	10	32	84	144	190
Tamprumo konstantos	9	32	84	144	190
Tankis		31	83	143	189
Temperatūrinė priklausomybė					
dielektrinės skvarbos		33	86	145	191
draustinės juostos tarpo		44	96	156	200
krizinių taškų energijos		44	96	156	200
lūžio rodiklio		52	106	167	209
Tenzoriai	26				
Termoelektrovaros jėga (žr. Seebecko koeficientas)					
Tarpslėnė relaksacijos trukmė	23	64	122	177	217
Tarpslėnės sklaidos konstantos		65	123	178	218
<b>U</b>					
Ultragarso slopimas	11	34	87	146	192
<b>V</b>					
Valentinės juostos parametrai	15	41	94	154	199

Informacinis leidinys  
Adolfas **Dargys**, Jurgis **Kundrotas**  
HANDBOOK ON PHYSICAL PROPERTIES OF Ge, Si, GaAs and InP  
Žinynas

Redaktorius **G. Miklaševskis**, **A. Zimanienė**,  
Dailininkas **V. Kudaba**,  
Meninis redaktorius **V. Ajauskas**,  
Techninė redaktorė **J. Dunauskienė**  
Korektorės: **N. Kolpigina** ir **N. Semionova**





**Parameters of Ge, Si, GaAs and InP at room temperature**

Parameter	Ge	Si	GaAs	InP
Atomic, molecular weight	72.59	28.08	144.63	145.8
Lattice constant, nm	0.5658	0.5431	0.5654	0.5869
Density, g/cm <sup>3</sup>	5.327	2.329	5.316	4.81
Melting temperature, K	1210	1685	1511	1335
Longitudinal sound velocity:				
[100] direction, cm/s	$4.9 \cdot 10^5$	$8.4 \cdot 10^5$	$4.7 \cdot 10^5$	$4.6 \cdot 10^5$
[111] direction, cm/s	$5.5 \cdot 10^5$	$9.3 \cdot 10^5$	$5.4 \cdot 10^5$	$5.2 \cdot 10^5$
Heat capacity, J/(g·K)	0.32	0.71	0.33	0.31
Thermal conductivity, W/(cm·K)	0.60	1.56	0.58	0.70
Differential thermal expansivity, K <sup>-1</sup>	$5.9 \cdot 10^{-6}$	$2.6 \cdot 10^{-6}$	$5.7 \cdot 10^{-6}$	$4.5 \cdot 10^{-6}$
Lattice dielectric permittivity:				
relative static $\epsilon/\epsilon_0$	15.94	11.9	12.8	12.5
relative high frequency $\epsilon_\infty/\epsilon_0$			10.92	9.52
Forbidden energy gap, eV	0.665	1.124	1.429	1.344
Intrinsic carrier				
concentration, cm <sup>-3</sup>	$2.3 \cdot 10^{13}$	$1.0 \cdot 10^{10}$	$1.8 \cdot 10^6$	$1.2 \cdot 10^8$
Intrinsic resistivity, $\Omega \cdot \text{cm}$	47	$3.2 \cdot 10^5$	$3.9 \cdot 10^8$	$1.0 \cdot 10^7$
Conduction band edge:				
axis of the energy minimum (valley)	$\langle 111 \rangle$	$\langle 100 \rangle$	$\langle 000 \rangle$	$\langle 000 \rangle$
valley symmetry	L	$\Delta$	$\Gamma$	$\Gamma$
number of valleys	4	6	1	1
electron mass $m_c/m_0$	0.12	0.26	0.064	0.078
electron mobility, cm <sup>2</sup> /(V·s)	3900	1450	8500	4800
density-of-states $N_c$ , cm <sup>-3</sup>	$1.0 \cdot 10^{19}$	$2.7 \cdot 10^{19}$	$4.0 \cdot 10^{17}$	$5.5 \cdot 10^{17}$
Valence band edge:				
spin-orbit splitting $\Delta_0$ , eV	0.29	0.043	0.34	0.11
heavy hole mass $m_h/m_0$	0.32	0.47	0.59	0.83
light hole mass $m_l/m_0$	0.042	0.16	0.083	0.11
hole mobility, cm <sup>2</sup> /(V·s)	1900	450	400	160
density of states $N_v$ , cm <sup>-3</sup>	$4.7 \cdot 10^{18}$	$1.0 \cdot 10^{19}$	$1.2 \cdot 10^{19}$	$2.0 \cdot 10^{19}$

# Translation of electrical quantities from CGS to SI units

Quantity	CGS	SI
Relative dielectric permittivity	$\varepsilon^*$	$\rightarrow \varepsilon_r$
Relative magnetic permeability	$\mu^*$	$\rightarrow \mu_r$
Electric field intensity	$E^*$	$\rightarrow E \cdot (4\pi\varepsilon_0)^{1/2}$
Electric induction	$D^*$	$\rightarrow D \cdot (4\pi/\varepsilon_0)^{1/2}$
Magnetic field intensity	$H^*$	$\rightarrow H \cdot (4\pi/\mu_0)^{1/2}$
Magnetic induction	$B^*$	$\rightarrow B \cdot (4\pi/\mu_0)^{1/2}$
Electron charge	$e^*$	$\rightarrow e/(4\pi\varepsilon_0)^{1/2}$
Charge	$Q^*$	$\rightarrow Q/(4\pi\varepsilon_0)^{1/2}$
Current density	$J^*$	$\rightarrow J/(4\pi\varepsilon_0)^{1/2}$
Current	$I^*$	$\rightarrow I/(4\pi\varepsilon_0)^{1/2}$
Voltage	$U^*$	$\rightarrow U \cdot (4\pi\varepsilon_0)^{1/2}$
Vector potential	$A^*$	$\rightarrow A \cdot (4\pi/\mu_0)^{1/2}$
Polarization vector	$P^*$	$\rightarrow P/(4\pi\varepsilon_0)^{1/2}$
Magnetization vector	$M^*$	$\rightarrow M/(4\pi/\mu_0)^{1/2}$
Resistance	$R^*$	$\rightarrow R \cdot (4\pi\varepsilon_0)$
Conductivity	$\sigma^*$	$\rightarrow \sigma/(4\pi\varepsilon_0)$
Capacity	$C^*$	$\rightarrow C/(4\pi\varepsilon_0)$
Inductance	$L^*$	$\rightarrow L \cdot (4\pi/\mu_0)$
Mobility	$\mu^*$	$\rightarrow \mu/(4\pi\varepsilon_0)^{1/2}$
Dielectric susceptibility	$\chi_e^*$	$\rightarrow \chi_e/(4\pi)$
Magnetic susceptibility	$\chi_m^*$	$\rightarrow \chi_m/(4\pi)$
Bohr magneton	$\mu_B^*$	$\rightarrow \mu_B/(4\pi/\mu_0)$
Light velocity in vacuum		$c = 1/(\varepsilon_0 \mu_0)^{1/2}$





# Handbook on the physical properties of Ge, Si, GaAs and InP

## by A Dargys and J Kundrotas

**Handbook on the physical properties of Ge, Si, GaAs and InP.** A Dargys, J Kundrotas (Vilnius, Lithuania: Science and Encyclopedia Publishers, 1994) 262 pp.

PACS numbers: 73.61.–r, 72.80.Ey, 78.30.Fs

The handbook under review provides up-to-date information on the basic physical parameters of two elementary (Ge and Si) and two compound (GaAs and InP) semiconductors.

The introductory section presents a reasonably detailed discussion of the current view of the band structure and major electrical and physical properties of crystalline semiconductors; tables of major physical properties and the relation between CGS and SI numerical values are also given. The publication of this introduction as a brochure or an appendix to Soviet Physics-Semiconductors, whether in the original English or in a Russian translation, is likely to attract considerable specialist interest in Russia.

The semiconductors covered are quite a natural choice as far as Ge, Si, and GaAs are concerned, because many remarkable properties of germanium made it a very convenient material at the early stages of modern semiconductor physics and solid-state electronics. [The electrical and physical data on Ge open the main part of the book (pp. 31 – 73)]. Perhaps the most favourable factor was the relative ease of growing large pure single Ge: crystals a research area, parenthetically, in which the reviewer himself was involved from 1952–55. For many years since then, and indeed in the course of the 1990s, single crystalline Ge has been the most suitable object for the fundamental studies of phenomena such as the condensation of nonequilibrium charge carriers to 'electron-hole drops', predicted by L V Keldysh. Compared to the well-known handbook of Landolt-Börnstein†, the present volume contains new important data for many researchers who continue to investigate the fundamental phenomena in semiconductors. It should be noted that while covering single crystalline properties of Ge, Si, GaAs and InP, the handbook fails to include the properties of their amorphous phases. This should not be considered a shortcoming, though, since unlike perfect single crystals, amorphous phases exhibit a wide variety of forms whose study has not yet reached a level at which reliable quantitative parameters could be given.

At the end of the single crystalline Ge section, detailed tables of the energy levels of major electrically active impurities are given together with appropriate literature references (from p. 73 on).

Section II (pp. 83 – 130) presents data on the band structure and energy spectrum of single crystalline silicon.

At present, about 98% of all active elements of solid state electronics are known to be manufactured on the basis of this material. The technology of growing huge Si single crystals (up to 150 mm in diameter and 57 – 75 cm in length) has nowadays achieved a high level of perfection. The content of this section will undoubtedly be of much use for specialists in Russia and Belarus', where extensive work is being carried out on the design of silicon devices. As is the case with the Introduction, it seems that modern electrical and physical parameters data on silicon should also be made accessible to a wide range of Russian specialists in the near future, whether through publishing this section in Russian or re-editing it in the English original. It should be noted that the book fails to cover the technologically important data now available on major point defects occurring in Si and on their complexes with impurities, nor does it contain information about the energy spectra of local centres at silicon interfaces with SiO<sub>2</sub> and other substances. Since almost all silicon devices are planar structures at present, the energy spectra of near-surface local centres are of crucial importance for practical applications.

GaAs is known to be the material on the basis of which the early injection lasers were developed. The technological problems in growing large single crystals or preparing epitaxy films of GaAs has proved to be extremely difficult, and although much progress has been made, this semiconductor remains in some respects unpredictable, especially as far as long-service devices are concerned. Nevertheless, the remarkable properties of GaAs has made it attractive for interesting and practically important applications. Of particular interest is that part of Section 3 containing very detailed data on GaAs luminescence spectra. Unlike the silicon section, in the section on GaAs there is Table 3.2 presenting quite detailed data on capture centres (traps) whose nature is not yet completely understood. Note that the table fails to give literature references (the authors' own data, 3.116, seem to have been used).

The final fourth section of the book contains band-structure, electrical, and physical data on indium phosphide InP which, like GaAs, is also an A<sub>3</sub>B<sub>5</sub> compound. In terms of layout, this section is similar to the preceding one. The data it presents will probably have a narrower readership compared with the previous, particularly second and third, sections.

At the end of the book there is an extensive list of references, including original publications appearing up to 1992. On the latest pages, a brief summary in Lithuanian is given. The book is of high technical quality and would undoubtedly be a welcome library addition for major scientific centres in Russia.

The reviewer has visited the Lithuanian scientific centres in Vilnius and Kaunas on many occasions and is well acquainted with the great achievements of Lithuanian physicists. The book under review is a result of serious and highly labour-consuming work. The authors are to be congratulated on the appearance of the book and wished continuing success in their future efforts.

† Landolt-Börnstein *Zahlenwerte und Funktionen in Naturwissenschaften und Technik. Neue Serie* (Ed. O Madelung) Band 17 *Halbleiter* (Eds M Schulz, H Weiss) (Berlin, Heidelberg, New York: Springer-Verlag, 1982).

scattering. Each chapter is written by experts in the field, and is supported by a suite of programs (in FORTRAN), and a set of problems. These generally seem to be well thought out and realistic; they cover exactly the mixture of basic theory, numerical analysis and computer trickery that occurs in reality. The programs themselves of course make some concession to the fact that their source codes must all fit onto one DOS diskette, so in many cases they represent truncated versions of the state of the art. I had no difficulty in compiling a sample on a fairly standard PC, but, in one case, had problems reproducing the sample output. The contributors, however, have made themselves hostage to fortune by supplying their e-mail addresses, so I was able to obtain advice within about 20 minutes. (The problem came from one of these irritating, but no doubt useful tests which the writers of mathematical subroutines like to use to make sure that their numerical approximations to special functions actually achieve machine accuracy; a further example of the educational value of this book).

In summary, this is a very good introduction to the real world of electron-atom-scattering theory. It would be useful for graduate students and research workers, but probably assumes too much background experience in atomic physics generally to serve unsupported as an introductory text.

P. T. GREENLAND  
(Imperial College, London)

***Handbook on Physical Properties of Ge, Si, GaAs and InP***

By A. DARGYS and J. KUNDROTAS

1995, US\$30.00 (hbk), pp. 264. Vilnius, Science and Encyclopedia Publishers, ISBN 5 420 01088 7. Scope: reference. Level: specialist.

Data on the fundamental bulk properties of single crystal semiconductors have been collated by the authors and summarised in the form of 80 tables and 249 figures within 196 pages. The book contains four main sections each dealing with one semi-conducting material. Within a section the data is arranged under six main headings, dealing in turn with lattice; band; optical; electrical; piezoelectric, thermoelectric and magnetic properties; and impurity properties. In addition there is an introductory chapter which gives a summary of semiconductor properties together with their definition, an extensive list of 477 references and an index in both English and Lithuanian.

Germanium, silicon, gallium arsenide and indium phosphide have been chosen because their physical properties are well characterised and they are important materials for the device fabrication industry. This restriction to four semiconductors results in a comprehensive and detailed

summary of their properties. The book will serve as a quick source of reference for both solid state physicists and engineers working in the field of semiconductor device technology. It will be beneficial as a laboratory reference guide and will serve as the first step in a more comprehensive literature search. In common with other handbooks of a similar format it will only be useful when it contains the information a reader is looking for.

D. I. JONES  
(University of Dundee)

***Introduction to Partial Differential Equations. 2nd Edn***

By G. B. FOLLAND

1995, £27.50, US\$39.50 (hbk), pp. xi+ 324. Princeton University Press, ISBN 0 691 0436 1 2. Scope: textbook. Level: advanced undergraduate and postgraduate.

The mathematical literature is awash with books on partial differential equations, covering many different approaches. There are the very practical approaches of specific problem solving, involving for instance the method of characteristics, series solutions, separation of variables, etc. or transformation methods and Green's functions. Mostly, such books are restricted to looking at linear equations, this is due either to keeping things reasonably simple (also many of the equations with physical application are indeed linear!) or as in the case of Green's functions, dealing with linear equations is generally a necessity because of the involvement of distribution theory.

The second main approach found in books is more theoretical. In such books the basic structure of the theory is examined and the question of uniqueness and existence of solutions is considered. This approach would usually be thought of as more difficult as it requires a more substantial understanding of real and complex analysis.

There is a third, more modern, approach which uses more recent developments in the theory, for example pseudo-differential operators. This approach includes many powerful techniques for dealing with PDEs in a more general setting.

*An Introduction to Partial Differential Equations* by Gerald Folland lies perhaps toward the more theoretical end of the spectrum, but even so about a third of the book is devoted to important partial differential operators from theoretical physics such as the Laplacian and the heat operator. The book also incorporates both the 'traditional' and 'modern' approaches to the subject, placed in a modern setting.

It is in fact, the second edition of a book that has been available for several years. This edition has some rewriting and notational changes, but more importantly, some additional material inserted throughout the text, including